Novel techniques for a Strontium Optical Lattice Clock

Doctoral Dissertation
Doctoral Program in Metrology (31.st cycle)

Novel techniques for a Strontium Optical Lattice Clock

Matteo Barbiero
* * * * * *

Supervisors
Prof. Gabriele Ferrari, CNR-INO BEC Center and Università di Trento
Dr. Filippo Levi, Istituto Nazionale di Ricerca Metrologica

Doctoral Examination Committee:
Dr. Luca Lorini, Referee, LNE-SYRTE Observatoire de Paris
Prof. Michał Zawada, Referee, Nicolaus Copernicus University
Dr. Chiara D'Errico, CNR-INO, LENS and Università di Firenze
Prof. Giovanni Costanzo, Politecnico di Torino
Dr. Marco Pizzocaro, Istituto Nazionale di Ricerca Metrologica

Politecnico di Torino
September 2, 2019

I hereby declare that, the contents and organisation of this dissertation constitute my own original work and does not compromise in any way the rights of third parties, including those relating to the security of personal data.

. . . . . .

Matteo Barbiero
Turin, September 2, 2019

Summary

In this dissertation I present the building of a new optical lattice clock with Sr atoms at Time and Frequency division of *Istituto Nazionale di Ricerca Metrologica* (INRIM) at Turin. This work was possible thanks to the joint collaboration between the BEC-center of *Università di Trento* (UNITN) and the INRIM. The goal of the project is to investigate and implement new experimental techniques that may enhance the metrological performances of the current state-of-the-art optical lattice clocks. Using the know-how offered by experiment with cold atoms, a compact and efficient new atomic source is designed complying with metrological requirements. The atomic source employs a novel design based on *two dimensional magnetic optical trap* (2D-MOT) where it is transversally loaded from a thermal beam of Sr atoms. Atoms trapped in the 2D-MOT region are then moved toward the final MOT by means of a push optical beam. This double loading stage of the MOT offers some metrological advantages like a complete optical control of the cold atomic flux generated from the atomic source, a suppression of hot-background collisions among atoms in final MOT and atoms in thermal beams, and a reduction of black body radiation shift of the oven. During this thesis, a new trapping scheme based on two frequencies 2D-MOT is introduced. This method is used in order to enhance the performance of the atomic flux production of the atomic source. Atomic source and the sideband enhanced 2D-MOT performances were experimental characterized and quantitatively compared with a fully 3D atomic trajectories simulation based on Monte Carlo approach. Finally, the development and the characterization of new lasers sources that address second stage MOT, repumping and clock transitions are presented and their related lasers stabilization techniques are also discussed. During my PhD I spent the first two years at UNITN where I developed preliminary numeric simulations about atomic source performances and I assembled the main components of the experimental apparatus. During the time at UNITN, I had also the opportunity to be involved in the building of a similar apparatus for production of a Bose Einstein condensate. Once it was finally possible to obtained a stable first stage MOT, the entire apparatus was moved from UNITN to INRIM where final characterizations were performed. At INRIM we are now assembling the laser stabilization system for the second MOT stage.

Acknowledgements

Ringrazio Gabriele Ferrari, Filippo Levi, e Davide Calonico per l'importante opportunità offertami di poter lavorare in un settore scientifico altamente stimolante e innovativo. Ringrazio tutti i miei colleghi per questi tre anni di lavoro insieme. Sperando di non dimenticare nessuno ringrazio Giacomo Lamporesi, Giacomo Colzi, Carmelo Mordini, Eleonora Fava, Simone Serafini, Simone Donadello, Tom Bienaimé, Arturo Farolfi, Stefano Signorini, Simone Bolognini, Marco Tarallo, Filippo Bregolin, Anna Tampellini, Hai Xiao Lin, Piero Barbieri, Michele Gozzelino, Martina Gertosio, Gianmaria Milani, Benjamin Rauf, Marco Pizzocaro, Cecilia Clivati, Giacomo Cappelini, Elio Bertacco, Claudio Calosso, Alberto Mura, Salvatore Michalizio e tutto il personale del servizio di elettronica e progettazione di Trento. Un ringraziamento forte va alla mia compagna Federica, alla mia famiglia e persone a me care, Domenico, Paola, Riccardo, Michele, Maristella, Giuseppe, Adriano, Gianna, Francesca, e a tutti i miei amici. Vi ringrazio per avermi sostenuto e aiutato in tutto questo periodo.

This work has been funded by the "European Metrology Program for Innovation and Research" (EMPIR) projects 15SIB03 OC18 and 17FUN03 USOQS. This project has received funding from the EMPIR programme co-financed by the participating states and from the European Union's Horizon 2020 research and innovation programme. This work has been also supported by the Provincia Autonoma di Trento.

Contents

Chapter 1

Introduction

If we think about the dynamics of a modern society, we will realize that accurate measures of time play a fundamental and almost unavoidable role in many aspects of social, civil, defence and scientific sectors of a society. The clock is the instrument created by humans civilization that allows to quantify and measure the time interval between two events. From a theoretical perspective, a clock is made by two components: a periodic phenomenon with a well defined frequency that generates an oscillating signal, and a system that counts the cycles of this periodic phenomenon generating regulars time intervals. Atomic clocks are nowadays the most precise timekeeping instruments ever created. In these clocks, a laser stabilized to a specific atomic resonance is used as periodic phenomena and with dedicated electronic reading system it is possible to count the laser frequency and convert it into a time intervals.

As international common agreement [1, 2], 1 second , the unit of time, is now defined as the duration of 9 192 631 770 periods of the radiation corresponding to the transition between the two hyperfine levels of the unperturbed ground state of the ^{133}Cs atom. This number was chosen in order to remain consistent with the previous definitions of the second where 1 second was defined as 1/86 400 th part of the solar day until the 1956 and where 1 second was defined as 1/31 556 925.9747 th of the tropical year from 1956 to 1967.

1.1 Atomic clocks

The atom has the main role in the definition of the second. Such important role is given by quantum mechanics laws that impose to atoms or molecules to have only discrete values of energy among its internal states. The transition between two different states with different energies, E_g and E_e, is observed by the absorption or emission of electromagnetic waves with precise frequency of $\nu_{eg} = |E_e - E_g|/h$ where

h is the Plank's constant. The frequency ν_{eg} can be measured and, once corrected for external perturbation, this value is only defined by quantum mechanics laws. An atomic clock is realized by matching an external oscillator ν to the atomic frequency ν_{eg}. The transition ν_{eg} is also called clock transition. Once the external oscillator ν is referred to the clock transition, ν is called frequency standard.

In order to know how precise a frequency standard is, its related uncertainty has to be quantified. In the field of time and frequency metrology, the frequency uncertainty is estimated in term of fractional frequency $\delta\nu/\nu_{eg}$, where $\delta\nu$ is the frequency mismatch between ν and clock transition ν_{eg}. The uncertainty contribution of a measure is dived in two types [3]: statistical errors (type A) and systematics errors (type B). In our case, the systematic error is estimated considering how our knowledge of frequency deviates from the unperturbed value ν_{eg} by means of external factors. This frequency discrepancy is also called accuracy of the frequency standard. Statistical errors of frequency measurements are usually quantified by means of the Allan deviation $\sigma_y(\tau)$ estimator [4, 5]. The parameter y is defined as $y = (\nu - \nu_0)/\nu_{eg}$, where ν_0 is the frequency of the atomic transition which can be shifted from ν_{eg} because of systematics effects. Allan deviation is a two sampled deviation of the fractional frequencies y as a function of the averaging time τ. The quantity $\sigma_y(\tau)$ is also called instability of the frequency standard.

Fundamental limit of the instability of an atomic clock is given by *quantum projection noise* (QPN) [6]. The QPN is a noise arising during the estimation of the number of atoms in a defined quantum state during the measurement process. During the atomic clock operation, the atomic sample is prepared in its ground state $|g\rangle$. After the clock excitation and depending on the frequency of the clock radiation, the atom can be written as linear superposition $|\Psi\rangle = c_e\,|e\rangle + c_g\,|g\rangle$ where the $|c_e|^2$ and $|c_g|^2$ are the associated probabilities to find the atom in the state $|e\rangle$ or in the state $|g\rangle$. Such values satisfy the relation $|c_e|^2 + |c_g|^2 = 1$. Due to the measure process of quantum states, the detection of the atom in the state $|e\rangle$ is described by the projection operator $\Pi_e = |e\rangle\langle e|$ which it will collapse the wave function $|\Psi\rangle$ the state $|e\rangle$. The mean value and the variance of the measurement process is estimated as $\langle\Pi_e\rangle = |c_e|^2$ and $\langle\Delta\Pi_e\rangle^2 = |c_e|^2(1-|c_e|^2)$. The fact that for a single measure of atomic state we have an associated variance is the physical origin of the quantum projection noise. Having an ensemble of N independent atoms we obtain a $\langle\Pi_e\rangle = N|c_e|^2$ and $\langle\Delta\Pi_e\rangle^2 = N|c_e|^2(1-|c_e|^2)$. From these observations we conclude that the signal to noise ratio of the measurement process scales as $\sim\sqrt{N}$ and the fundamental limit of the instability generated by the QPN is estimated as:

$$\sigma_y(\tau) \simeq \frac{1}{Q}\frac{\eta}{(S/N)\sqrt{\tau}} \tag{1.1}$$

where the ratio $Q = \nu_{eg}/\Delta\nu$ is also called quality factor of the resonance ν_{eg} and $\Delta\nu$

is the linewidth associated to ν_{eg}, the value τ is the measure averaging time, η is a factor close to 1 and it describes the spectroscopic method adopted for the atomic interrogation and S/N is the signal to noise ratio which depends on the number of interrogated atoms N as $S/N \sim \sqrt{N}$ for the case of QPN. The linewidth of the transition scales as $\Delta\nu \sim 1/T$, where T is the interaction time between radiation and atoms. The ultimate value of the quality factor Q is given considering the natural linewidth of the atom in the excited state. According to the formula expressed in Eq.1.1, increasing the quality factor Q, the number of atom interrogated N and the interrogation time T will reduce the instability of the atomic clock.

History of atomic clocks

The idea of using the light-matter interaction to realize frequency reference came from molecular spectroscopy experiments in the microwave domain. At the beginning, in these type of experiments the atoms were excited by microwave signal inside a cavity where a magnetic field was applied. The first experimental evidence was observed by single and broad absorption signal in the microwave regime for the NH_3 molecules [7]. The Doppler shift of the molecular beam and the limited interaction time between the atoms and the microwave signal inside the cavity were the major limitations for the experimental linewidth reduction. These limitations were solved after the introduction of a new interrogation method proposed by Norman Ramsey in 1950 [8]. This interrogation protocol consists into a controlled interactions between molecular beam with a double oscillating fields spatial separated in two different microwave cavities. The spatial separation of the interrogations regions with the molecular beam induce a dark time T_R of the atom between the two microwaves interactions; tuning opportunely the microwave fields it is possible to reduce the experimental linewidth of $\Delta\nu \sim 1/T_R$ [9]. Using this new interrogation method it was successfully realize a first clock of NH_3 molecular beam [10] and then it was realized a more stable clock based on Cs atom in 1955 by Essen and Parry [11].

Further technological advancement of the atomic clock design was related to the discover of laser cooling techniques by Chu, Cohen-Tannoudji and Phillips in the 1990s [12]. For this contribution to the science the three authors were awarded of the Nobel Prize in Physics in 1997. With this cooling method a thermal atomic beam can be slowed down at few cm/s with a temperature of the order of few µK suppressing Doppler effects. In a Ramsey interrogation, a slower atomic beam will also increase the interaction time between atom cavity increasing the dark time between two cavities. In order to avoid complications deriving from the deflection of the atomic beam by gravity and the use of two different microwave cavities, vertical systems were proposed instead of the usual horizontal approach. These systems,

called atomic fountain clocks, were first suggested by Zacharias in 1953 and experimentally demonstrated only in 1989 with Na atoms employing the laser cooling techniques [13]. In the atomic fountain system, an ensemble of atoms are cooled by means of optical molasses and launched vertically. During their free fly, by gravity atoms pass trough a single microwave twice where the Ramsey scheme is applied.

Nowadays, the atomic fountains are spread in many metrological institutes and used as a primary frequency standards. It is also demonstrated that the atomic fountains reached the instability limit of the QPN [14]. The latest versions of atomic fountains reached accuracies of few 1×10^{-16} and instabilities of the order of $\sigma_y(\tau) \simeq 2 - 5 \times 10^{-14}/\sqrt{\tau/\mathrm{s}}$ [15–18].

1.2 Optical atomic clocks

As introduced in the Eq.1.1, lower instability can be achieved choosing a specific transition with larger quality factor Q compare to the microwave transition. For a given transition linewidth $\Delta\nu$, the optical transition ($\nu_{eg} \sim 10^{14}\,\mathrm{Hz}$) instead of microwave transition ($\nu_{eg} \sim 10^{10}\,\mathrm{Hz}$) has a larger quality factor. Moreover, because of the presence of slightly admitted transitions, some atoms possess optical narrow transitions which are considered as a good candidates to be clock transitions with high Q. Nowadays, the most widespread optical frequency standards are based on trapped single ions and trapped neutral atoms [19]. Common feature of these two groups is the possibility to trap the single ion, or the neutral atoms, in a tight potential able to decouple the external and internal degree of freedom of the atom. In this way the Doppler and recoil shift are suppressed and it is possible to perform precise clock spectroscopy of motional frozen atoms.

Another important point is the experimental capability to count the optical transition oscillations. Before the introduction of the frequency comb, the microwave oscillations were easily counted with apposite electronic but it was difficult to measure the frequency of optical radiation. At that time, the optical frequency measurement was possible only by means of complicated frequency chain systems able to fill the gap between the optical domain and the microwave domain [20]. The introduction of the frequency comb opened the possibility to directly link the optical radiation with microwave domain [21, 22]. Thanks to this technological improvement in the laser precision spectroscopy, John Hall and Theodor Hänsch were awarded in Nobel Prize in Physics in 2005.

The frequency comb down-converts our optical frequency standard in the radiofrequency domain. The optical frequency comb spectrum is described by frequency components distributed according to the following relation:

$$\nu_n = f_{\mathrm{CEO}} + n f_{\mathrm{rep}} \tag{1.2}$$

where ν_n is the optical frequency of the n-tooth comb line, n is an integer number, f_{rep} is the frequency separation between the comb teeth which is also the repetition frequency of the mode-lock laser, and f_{CEO} is the carrier-envelope offset [23]. Both frequencies, f_{rep} and f_{CEO}, are in the radiofrequency domain and performing the beatnote between the optical frequency ν_{eg} and comb's tooth ν_n, the generated beatnote f_{beat} can be counted by means of a frequency-counter.

The working principle of optical atomic clock is reported in the Fig.1.1. As explained for atomic clock, a clock laser frequency ν is stabilized to the absorption profile of the clock transition ν_{eg}. The clock laser frequency is converted in the radiofrequency domain by beating it with the closest frequency comb tooth. The radiofrequency beating is then measured with dead-time-free electronics counters [24]. Before the atomic interrogation, the linewidth of the clock laser frequency is usually reduced by locking it to high ultrastable Faby-Perot cavity made by low expansion material [25].

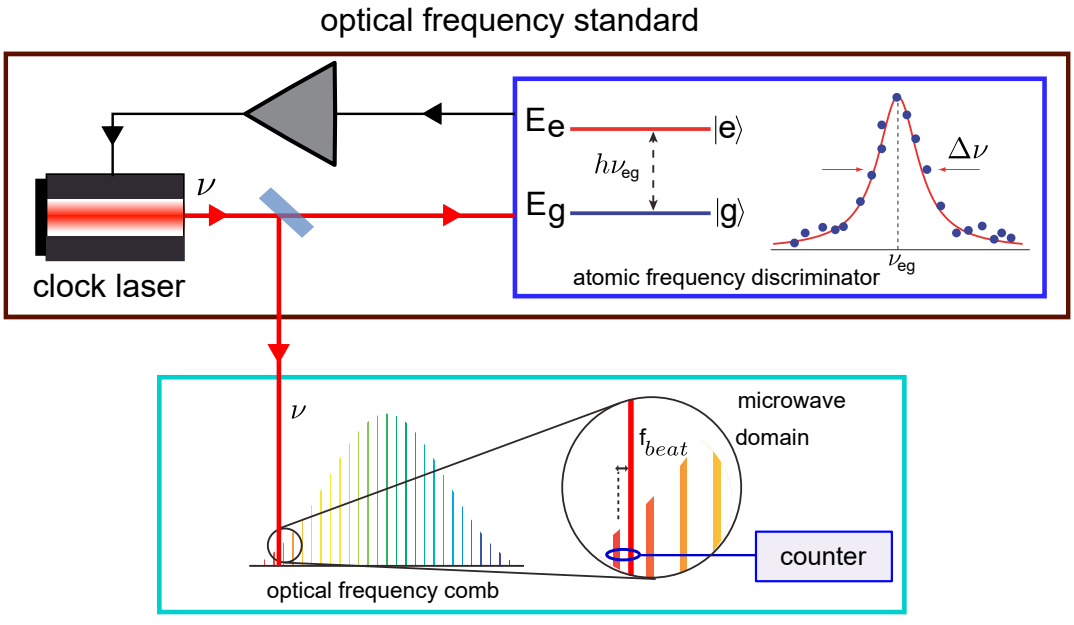

Figure 1.1: Structure of optical atomic clock

In the case of single ion clocks, the ion is trapped by mean of both static oscillating electric fields and laser radiation [26, 27]. Ion clocks are realized in different

institutes with different atomic species like Yb^+ [28, 29] , Sr^+ [30], Al^+ [31, 32], Hg^+ [33], Ca^+ [34] , In^+ [35]. The best reported fractional accuracies of these type of clocks is 9.5×10^{-19} with an instability of $\sigma_y(\tau) = 1.2 \times 10^{-15}/\sqrt{\tau/\mathrm{s}}$ [32]. For the development and the precision reached by the single ion clock, in 1989 Wolfgang Paul and Hans Dehmelt were awarded of the Nobel Prize in Physics for the development of ion traps and in 2012 and David Wineland and Serge Haroche introducing experimental methods that enable measuring and manipulation of individual quantum systems.

In the optical clock with neutral atoms, the trapping exploits optical lattice in order to suppress the motional effects. This configuration freezes the atomic motion along the optical lattice direction. As first suggested by Katori in 2003 [36], the perturbations on the clock transition due to the high intensity laser fields can be removed by appropriately choosing the wavelength of the optical lattice. Considering the internal structure of atoms and the wavelength of the optical lattice, it is possible to remove to the first order, the non-uniform perturbation induced by the optical lattice to the energy levels of the clock transition. Optical lattice clocks are realized in different metrology institutes with different atomic species like Sr [37–42], Yb [43–48], Hg [49, 50] and other possible candidates as Mg [51] and Cd [52]. The best reported fractional accuracies of these type of clocks are $\sim 10^{-18}$ with an instability of $\sigma_y(\tau) \sim 4 \times 10^{-17}/\sqrt{\tau/\mathrm{s}}$ [48, 53, 54].

Fig.1.2 compares the fractional uncertainty advancement of different atomic clocks and optical atomic clocks. It it possible to appreciated how the optical frequency standard trend has surpassed the microwave frequency standard in terms of fractional uncertainty. Scientific applications of these ultra-precise instruments are many. One possibility is to study the deviation from the geoid level by making remote clocks comparison exploiting recent advancement in fiber link technology [55–57]. Others fundamental applications that exploit the precision of the optical atomic clock are testing of the Lorentz symmetry [58], probing possible Higgs-like forces between different atomic isotopes [59], dark matter detection [60], and testing theories beyond the Standard Model by measuring the variation of the fundamental constant as a function of the time [61].

Toward a quantum enhanced optical lattice clock

This thesis is only the first step of a long term goal project where the final goal is to understand the quantum frontier of the time measurements exploiting state-of-the-art optical lattice clocks and systems where atoms are strongly coupled with electromagnetic radiation by means of a mechanical cavity [62]. The strong interaction between atoms and photons is described by *cavity quantum electrodynamics* theory (CQED) [63]

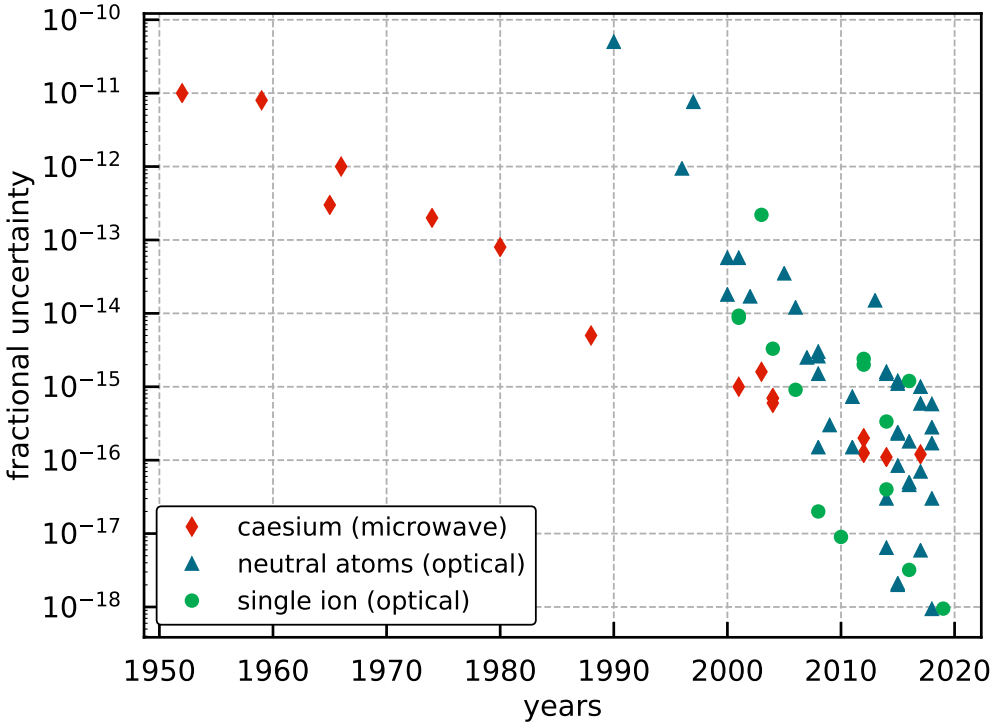

Figure 1.2: Comparison of fractional uncertainty of the atomic clocks and optical atomic clocks. Advancement during the years

The astonishing performances reached by recent optical lattice clocks are mainly limited by few factors. One limit is imposed by the clock laser noise induced by the ultrastable cavity. The recent progresses underline the fact that we are reaching the fundamental limits imposed by the Brownian motion of the cavity material. Thermal noise of this system can be reduced by employing cryogenic cavity [64]. Another possibility to reduce the clock laser noise generated by the ultratable cavity is to change completely the perspective of clock as a passive system and use superradiance effect [65, 66] where the clock laser radiation is generated actively. With strong coupling between atoms and electromagnetic radiation, it is possible to exploit cavity-induced long range coherence among the atomic dipoles which subsequently radiate coherently in the superradiant regime. Above a power threshold and in the bad cavity regime, where the cavity linewidth is larger than the clock laser linewidth, it is possible to generate a stable ultra-narrow clock radiation insensitive to the cavity length fluctuations [67, 68]. From the metrological point of view, this ultra-narrow laser is only limited by the clock transition linewidth and can be used as active optical frequency standard. Such active system will offer the possibility to supress the Dick-effect which is the frequency noise induced by the finite interrogation time of atoms by clock laser [69].

Another limit is given by the QPN where the scaling factor between the clock instability and the number of interrogated atom is $\sigma_y \sim 1/\sqrt{N}$. A possibility to reduce the QPN is to use squeezed states [70]. The ultimate instability limit of the optical clock is related to the Heisemberg limits which scales as $\sigma_y \sim 1/N$ [71, 72]. Squeezed states in a CQED system can be generated through *quantum non demolition measurement* (QND) of the collective atomic state. One of the possible QND protocol can be achieved by probing the atoms trapped in the lattice with far-detuned laser beam [73]. One of the objective of the project at INRIM is to understand if the squeezing has beneficial effects in the field of the time and frequency metrology

1.3 Thesis overview

The work presented in this dissertation reports the development of a new optical lattice clock with Sr atoms. This work is a collaboration between the BEC center of *Università di Trento* (UNITN) and the Time and Frequency division of the *Istituto Nazionale di Ricerca Metrologica* (INRIM) in Turin. Once the Sr clock will operate, the INRIM will have a set of optical lattice clocks composed by an already operating clock with neutral Yb atoms and a clock with Cd atoms, which is under construction, opening the possibility of novel metrological and physical investigations. At the moment, we have characterized the atomic source of the Sr apparatus and we successfully load the atoms into the final blue MOT. We also study the feasibility and reliability of a novel cooling method that enhance the atomic flux provided by the atomic source preserving the compactness and robustness criteria of the apparatus. We also build the red laser source used for the rempumping transition, second cooling stage and clock laser spectroscopy. Nowadays, we are working to achieve the red MOT cooling stage of the system.

I spent the first two years of my PhD at UNITN where the main experimental components of the Sr atomic source were assembled. During the period at UNITN I also had the opportunity to follow and contribute to the development of a new experimental apparatus for the production of the Bose-Einstein-Condensate with Na atoms [74, 75]. Both systems share same atomic source design and same hardware and software for the electronic experimental control. Once the system was able to produce the first stable magneto optical trapping of Sr atoms, the apparatus was moved to INRIM. In Turin I performed the final characterization of the atomic source and I studied a new method to enhance the performances of the Sr atomic source.

The thesis is organized as follow:

- Chapter 2 introduces the basic concepts of laser cooling and dipole trapping. In this chapter it is also reported the main spectroscopic properties of the Sr atom and the suitable transitions used for the optical lattice clock operation.
- Chapter 3 reports the main features of the experimental apparatus underlining the metrological advantages offered by the novel atomic source design. The main experimental elements for the production of first MOT stage are presented. At the end of the chapter, the characterization of new lasers sources for the second stage MOT, repumping and clock transitions are reported and the related lasers stabilization techniques are also discussed.
- Chapter 4 describes the full 3D atomic trajectories simulation used to predict the best experimental trapping configuration for Sr atoms.
- Chapter 5 reports the experimental characterization of the atomic source and the comparison with respect to numerical simulation. We also present the performances of the new scheme proposed for enhancing the atomic flux of the atomic source.

Chapter 2

Atom manipulation

After introducing the general theory of atom-light interaction [63], we expose the laser cooling theory for neutral atoms. The idea to slow down and cool atoms by means of laser radiation was first proposed on 1975 independently by Hänsch and Schawlow for neutral atoms [76], and by Wineland and Dehmelt for ions [77]. We also introduce the magneto optical trapping technique used to spatially confine and trap neutral atoms. This technique was proposed by Jean Dalibard [78] and experimental demonstrated by Raab *et. al* [79]. In the second part of the chapter, we discuss about the neutral atom trapping by means of the optical potential and we highlight the main trapping features of an optical lattice clock. In the last part of the chapter, the Sr proprieties and its relevant transitions for the laser cooling are presented.

2.1 Atom-light interaction

The atom is approximated as a point-like object with an internal structure given by two-level system, $|g\rangle$ and $|e\rangle$. We consider the energy separation between the exited state and the ground state $E = \hbar\omega_{eg}$ and Γ as the rate of the spontaneous emission. The atom interacts with a monochromatic laser beam with frequency $\omega_L = 2\pi c/\lambda_L$ and a defined wave-vector $\mathbf{k}_L = c/\omega_L\hat{\mathbf{k}}$, where the unitary vector $\hat{\mathbf{k}}$ express the laser prorogation direction. The *Optical-Bloch-Equation* (OBE) is adopted in order to describe the internal dynamics of two-level system [12, 80, 81].

In the OBE approach, the laser field is approximated as a classical external field. Considering the plane-wave approximation, the electric field is written as:

$$\mathbf{E}(\mathbf{r}, t) = \mathbf{e}E_0(\mathbf{r})\cos(\omega_L t - \mathbf{k}_L \cdot \mathbf{r}) \tag{2.1}$$

where $\mathbf{e}$ is the wave polarization. The Hamiltonian of the two-level system coupled

with external radiation is described as:

$$H = \hbar\omega_{eg} \left|e\right\rangle\!\left\langle e\right| + U(\mathbf{r}, t) \tag{2.2}$$

where U is the atom-light coupling described as:

$$U(\mathbf{r}, t) = -\mathbf{d} \cdot \mathbf{E} \tag{2.3}$$

where $\mathbf{d} = d_{\mathrm{eg}} \left(\left|e\right\rangle\!\left\langle g\right| + \left|g\right\rangle\!\left\langle e\right|\right)$ is the atomic dipole operator, $d_{eg} = \langle e|\mathbf{d}|g\rangle$ is the dipole matrix element and $\mathbf{E}(\mathbf{r})$ is the electromagnetic field described by Eq.2.1. Atom-light coupling is expressed with the Rabi frequency defined as $\Omega = -\mathbf{d} \cdot \mathbf{E}/\hbar$. Defining the rising operator $\sigma^+ = \left|e\right\rangle\!\left\langle g\right|$ and the lowering operator $\sigma^- = \left|g\right\rangle\!\left\langle e\right|$, the dipole moment can be rewritten as $\mathbf{d} = d_{eg} \left(\sigma^+ + \sigma^-\right)$. The equation of motion of the atomic density matrix is regulated by the Master equation [63, 82]:

$$\frac{\mathrm{d}\rho}{\mathrm{d}t} = -\frac{i}{\hbar}[H, \rho] + \left(\frac{\mathrm{d}\rho}{\mathrm{d}t}\right)_{\mathrm{sp}} \tag{2.4}$$

where the damping term takes into account the spontaneous emission process. The corresponding rate of density the matrix element can be written as:

$$\left(\frac{\mathrm{d}\rho_{ee}}{\mathrm{d}t}\right)_{\mathrm{sp}} = -\Gamma\rho_{ee} \qquad \left(\frac{\mathrm{d}\rho_{eg}}{\mathrm{d}t}\right)_{\mathrm{sp}} = -\frac{\Gamma}{2}\rho_{eg} \qquad \left(\frac{\mathrm{d}\rho_{gg}}{\mathrm{d}t}\right)_{\mathrm{sp}} = \Gamma\rho_{ee} \tag{2.5}$$

The interpretation of these equations are the following. The first equation describes the decay of the population of excited state $|e\rangle$ with a rate Γ, the second equation describes the damping of the coherence between the state $|e\rangle$ and $|g\rangle$ with a rate $\Gamma/2$ and the third one describes the increment of the ground state population $|g\rangle$ due to the spontaneous emission with a rate Γ. In Eq.2.4 the commutator describes the evolution of the density matrix as a function of system Hamiltonian H of the system while the last term expressed in the Eq.2.5 describes a damping term on density matrix evolution.

In order to derive an explicit expression for the mean force acting on the atom, we introduce three important approximations:

- assuming a close resonance condition $\omega_L \sim \omega_{eg}$ of the electric field described with the Eq.2.1, the evolution of the density matrix ρ is regulated by a slow dynamic, with a factor of $e^{i(\omega_L - \omega_{eg})t}$, and by a fast dynamics, with a factor of $e^{i(\omega_L + \omega_{eg})t}$. If the faster contribution is averaged, we are using the so called *rotating wave approximation* (RWA) With the RWA, Eq.2.4 can be solved analytically.

- we consider the evolution of the internal atomic degree of freedom, such as the dipole moment, faster compare to the external one, such as the atom

position and velocity. As a consequence, for a time scale of $t \gg \Gamma^{-1}$, the variation of the slow external variables are neglected in the resolution of the Eq.2.4. In this framework, we can solve the equation Eq.2.4 in its stationary case ($\frac{\mathrm{d}\rho}{\mathrm{d}t} = 0$) and considering only the stationary case for the internal atomic variables, ρ^{st} and d_{eg}^{st}.

- In all the treatment above, we are approximating the atom as a point-like object. Considering a diluted gas of atoms at temperature T and mean distance a, the point-like approximation is legitimated if the laser wavelength λ_L is larger compare to the thermal de Broglie wavelength defined as:

$$\lambda_{\mathrm{dB}} = \sqrt{\frac{2\pi\hbar^2}{mk_BT}} \tag{2.6}$$

  Under this approximation, the spatial distribution of the atom wavepacket is small compare to λ_L. At temperature close to the absolute zero where $\lambda_{\mathrm{dB}} \sim a$, atoms are no more simple point-like object and their spatial wavefunctions size become important [83].

Under these approximation, the mean mechanical force induced by the electromagnetic radiation on the atom can be written as [81, 82]

$$\mathbf{F} = -\mathrm{Tr}(\rho^{\mathrm{st}}\boldsymbol{\nabla}U) = \mathbf{F}_{\mathrm{diss}} + \mathbf{F}_{\mathrm{react}} \tag{2.7}$$

where the dissipative force component is

$$\mathbf{F}_{\mathrm{diss}} = \hbar\mathbf{k}_L\frac{\Gamma}{2}\frac{s}{1+s+4(\Delta/\Gamma)^2} \tag{2.8}$$

and the reactive force component is

$$\mathbf{F}_{\mathrm{reac}} = -\frac{\hbar\Delta}{2}\frac{\boldsymbol{\nabla}s}{1+s+4(\Delta/\Gamma)^2} \tag{2.9}$$

In both Eq.2.8 and Eq.2.9 we introduce two experimental relevant quantities: the laser detuning, $\Delta = \omega_L - \omega_{eg}$ and the saturation parameter $s = I/I_0$ where I is the intensity of the electric field and I_0 is the saturation intensity of the two level system. The saturation parameter s and the Rabi frequency Ω are related by the following relation [80]:

$$\Omega^2 = s\frac{\Gamma^2}{2} = I\frac{3}{4\pi^2}\frac{\lambda_{eg}^3\Gamma}{\hbar c} \qquad I_0 = \frac{2\pi^2}{3}\frac{\hbar c\Gamma}{\lambda_{eg}^3} \tag{2.10}$$

where c is the light speed and $\lambda_{eg} = 2\pi c/\omega_{eg}$ is the transition wavelength.

2.2 The radiation pressure

Close to laser resonance condition $\Delta/\Gamma \ll 1$, the dissipative force contribution expressed with Eq.2.8 is dominant compared to the reactive force of Eq.2.9. Considering cycles of absorption-spontaneous emission events during a time scale $\Delta t \gg \Gamma^{-1}$, the average momentum transferred to the atoms can be written as:

$$\langle \Delta \mathbf{p} \rangle = \langle \Delta \mathbf{p}_{\text{abs}} \rangle + \langle \Delta \mathbf{p}_{\text{sp.e}} \rangle \tag{2.11}$$

where $\langle \Delta \mathbf{p}_{\text{abs}} \rangle$ is the average momentum transferred to the atoms by absorption processes and $\langle \Delta \mathbf{p}_{\text{sp.e}} \rangle$ is the average momentum transferred to the atoms by spontaneous emission processes. In single absorption process the atom change momentum in the direction of absorbed photon. In the single spontaneous emission event the atom change momentum in the direction of the emitted photon which is random. If we consider cycles of N_{abs} absorbed photons, the Eq.2.11 can be written as:

$$\langle \Delta \mathbf{p} \rangle = \langle \Delta \mathbf{p}_{\text{abs}} \rangle = \langle N_{\text{abs}} \rangle \, \hbar \mathbf{k}_L \tag{2.12}$$

where the average momentum of spontaneous emission processes is null. Using a semi-classical interpretation of the atom-light interaction, Eq.2.12 can be written as [84]:

$$\mathbf{F} = \frac{\mathrm{d} \langle \Delta \mathbf{p} \rangle}{\mathrm{d}t} = \hbar \mathbf{k} \frac{\mathrm{d}}{\mathrm{d}t} \langle N_{\text{abs}} \rangle = \hbar \mathbf{k}_L R \tag{2.13}$$

where R is the rate scattering events. Equating the Eq.2.8 with the Eq.2.13, the scattering rate R can be estimated as:

$$R = \frac{\Gamma}{2} \frac{s}{1 + s + 4(\Delta/\Gamma)^2} \tag{2.14}$$

where s is the saturation parameter and Δ is the laser beam detuning defined as $\Delta = \omega_L - \omega_{eg}$. This parameter estimates the rate of photon absorbed (or scattered) by means of atom-light coupling.

As a function of laser frequency ω_L, the dissipative force described with Eq.2.8 has a Lorentzian shape centered at $\omega_L = \omega_{eg}$ ($\Delta = 0$) with a full width half maximum of $\Delta\omega = \Gamma\sqrt{1+s}$. The parameter $\Delta\omega$ describes the atomic resonance broadening considering the atom-light coupling. We analyse two important limits:

- In the high intensity limit, $s \gg \Delta/\Gamma$, the force converges at its maximum value of $\mathbf{F}_{\text{max}} = \frac{\Gamma}{2}\hbar\mathbf{k}_L$. In the same limit the broadening of the resonance increases as $\Delta\omega \simeq \Gamma\sqrt{s}$.
- In the limit of low intensity, $s \ll \Delta/\Gamma$, the force in proportional to the laser intensity s and the transition broadening converges to its minimum value $\Delta\omega = \Gamma$.

Up to this point we did not consider the velocity $\mathbf{v}$ of the atom. Because of Doppler effect the laser frequency perceived by the atom, moving at velocity $\mathbf{v}$, is $\omega_L - \mathbf{k}_L \cdot \mathbf{v}$. If $\mathbf{k}_L$ and $\mathbf{v}$ have opposite direction (same direction), the resonance condition is fulfilled at $\omega_L < \omega_{eg}$ ($\omega_L > \omega_{eg}$). In this framework, the total force acting on the atom can be written as

$$\mathbf{F} = \hbar \mathbf{k}_L \frac{\Gamma}{2} \frac{s}{1 + s + 4(\Delta - \mathbf{k}_L \cdot \mathbf{v})^2/\Gamma^2} \tag{2.15}$$

The force expressed in Eq.2.15 has a Lorentzian shape with the center of the resonance at $\Delta = -\mathbf{k}_L \cdot \mathbf{v}$ as shown in the Fig.2.1(a). Eq.2.15 can be also Taylor-expanded for small velocity and for low saturation regime $s \ll 1$ as:

$$\mathbf{F}(\mathbf{v}) \simeq \mathbf{F}(0) - \frac{1}{2}\beta \mathbf{v} \qquad \beta = 8\hbar k_L^2 s \frac{-\Delta/\Gamma}{(1 + 4\Delta^2/\Gamma^2)^2} \tag{2.16}$$

At small velocity, the radiation pressure is described as a pure friction force proportional to $\mathbf{v}$ and a constant term $\mathbf{F}(0)$ given by radiation pressure. The radiation pressure of Eq.2.16 can be exploited to decelerate an atom using a counter-propagating light beam respect to the atom's velocity.

2.3 Optical molasses

Exploiting the Eq.2.16, it is possible to use two counter propagating beams with same detuning and same saturation intensity in order to generate a configuration where atoms are cooled and viscously confined. Assuming that the two forces act independently on the atom, the total average force is given by the sum of the two optical forces contributions. This assumption is valid for small value of saturation parameter $s \ll 1$ [85]. Adding a counter-propagating beam, the force of Eq.2.16 becomes a pure friction force:

$$\mathbf{F} = \mathbf{F}_-(\Delta_-) + \mathbf{F}_-(\Delta_+) \tag{2.17}$$

$$= \hbar \mathbf{k}_L \frac{\Gamma}{2} \left[\frac{s}{1 + s + 4\Delta_-^2/\Gamma^2} - \frac{s}{1 + s + 4\Delta_+^2/\Gamma^2} \right] \tag{2.18}$$

$$\simeq -\beta \mathbf{v} \tag{2.19}$$

where the detunings perceived by the atoms is:

$$\Delta_\pm = \Delta \pm \mathbf{k}_L \cdot \mathbf{v} \tag{2.20}$$

With this laser beam configuration, the constant terms of radiations pressure contributions cancel out. A simple 1D situation is depicted in the Fig.2.1(b). Let's consider an atom with velocity near to $\mathbf{v} \sim 0$. At $\Delta > 0$ ($\beta > 0$), the Eq.2.19 describes an atomic acceleration which is is not useful for cooling process. At $\Delta < 0$

($\beta < 0$), the Eq.2.19 describes a deceleration given by a friction force. This force configuration is also called the molasses force and it is used for cooling an ensamble of atoms. The maximum damping coefficient β is obtained at $\Delta/\Gamma = -1/2\sqrt{3}$.

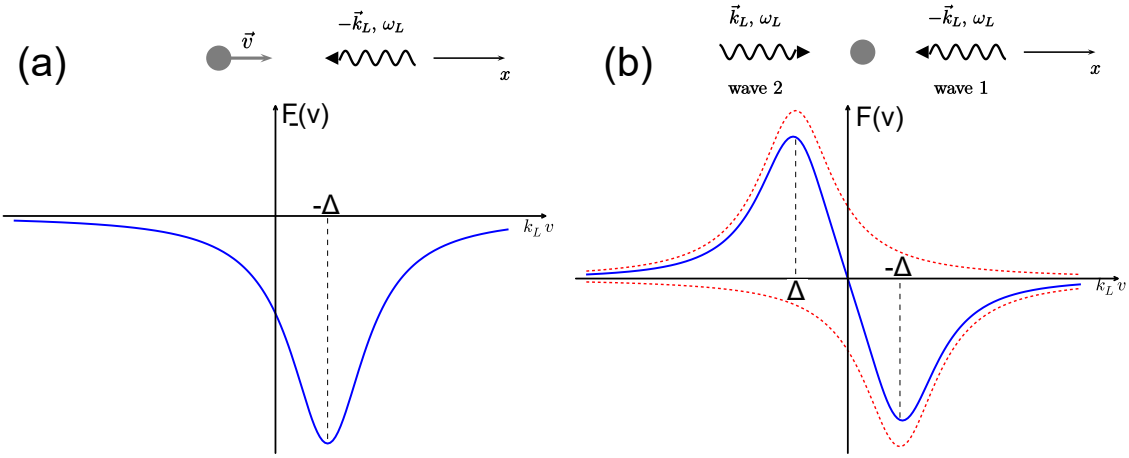

Figure 2.1: Atom-light interaction. **(a)** Single beam interaction with atom. The force has a finite component when the atomic velocity is zero. **(b)** Optical molasses. Two counter-propagating beam interact with an atom. The force is linear with the velocity and no constant component is present

2.3.1 Doppler limit temperature

Considering this one-dimensional problem, we can estimate the temperature in the optical molasses. In the optimal molasses we have two competing processes: a cooling process, induced by the pure friction force, and a heating process, induced by the fluctuation of the dissipative force. The temperature of the atomic gas is computed considering the stationary condition between these two opposite effects. The cooling mechanism is simply obtained considering the reduction of the kinetic energy of the atom via the Eq.2.19:

$$\left.\frac{\mathrm{d}E_k}{\mathrm{d}t}\right|_{\text{cooling}} = \mathbf{F}\cdot\mathbf{v} = -\beta v^2 \tag{2.21}$$

The heating mechanism is computed considering the fluctuation of the absorbed photons and the fluctuation of the atomic momentum removed by the photon during the spontaneous emission process. Taking into account these effects, the diffusion constant $\mathcal{D}$ is computed as [86, 87]:

$$\mathcal{D} = \hbar^2 k_L^2 R \tag{2.22}$$

where R is the scattering rate. In one dimensional case, the variation of the mean square momentum of the atom grows according to [85, 86]:

$$\frac{\mathrm{d}p^2}{\mathrm{d}t} = 2\mathcal{D} \tag{2.23}$$

the factor 2 takes into account both the absorption and the spontaneous emission process. The growth of the atomic kinetic energy due to the heating process can be written as:

$$\left.\frac{\mathrm{d}E_k}{\mathrm{d}t}\right|_{\text{heating}} = \frac{1}{2m}\frac{\mathrm{d}p^2}{\mathrm{d}t} = \frac{2\mathcal{D}}{m} \tag{2.24}$$

At equilibrium, the heating and the cooling rate are equal. The thermalization condition is expressed with the following equation:

$$\left.\frac{\mathrm{d}E_k}{\mathrm{d}t}\right|_{\text{cooling}} + \left.\frac{\mathrm{d}E_k}{\mathrm{d}t}\right|_{\text{heating}} = 0 \tag{2.25}$$

This condition imposes the value of the mean square velocity $\langle v \rangle^2$. In the low saturation regime $s \ll 1$ and using the expressions given by Eq.2.21,Eq.2.24 and Eq.2.16 we can write:

$$\left\langle v^2 \right\rangle = \frac{2\mathcal{D}}{m\beta} \tag{2.26}$$

Using the virial theorem we finally obtain:

$$k_B T = \frac{\mathcal{D}}{\beta} = \frac{\hbar\Gamma}{8}\frac{1 + 4\Delta^2/\Gamma^2}{|\Delta|/\Gamma} \tag{2.27}$$

at $\Delta = -\Gamma/2$ the temperature T reaches the minimum value of:

$$k_B T_D = \frac{\hbar\Gamma}{2} \tag{2.28}$$

This temperature T_D is also called Doppler-limit temperature. The Eq.2.28 says that the the minimum kinetic energy of the atom is given by the energy linewidth of the cooling transition $|g\rangle - - |e\rangle$. In this section, the Doppler limit temperature was computed using the semi-classical approach. A complete quantum treatment of one-dimensional laser cooling of free atom using the transition $J = 0$ and $J = 1$ can be found in [88, 89].

The temperature expressed in the Eq.2.28 is not the lowest temperature achievable in a optical molasses. Sub-Doppler temperature regime can be reached with alkali atoms. In the case of alkali atoms, which have several Zemman sublevels in the ground state, they can be cooled in a optical molasses with even lower temperatures. Atoms can be cooled for instance by means of polarization gradient induced by the optical molasses and the Zemman sublevels. This kind of laser cooling is called *Sisyphus* cooling [90–92] and brings the temperature of the system close to the recoil temperature $T_R = \hbar^2 k_L^2 / 2m k_B$.

2.3.2 Generalization at higher dimension

In this section I discuss the case of 3D or 2D optical molasses. In this configuration, the friction force acts in all directions of the space. If we consider the presence of N counter-propagating beams (N = 2,3), the total saturation parameter $2Ns$ perceived from atoms starts to become non negligible. A possible way to include the saturation effects $2Ns$ induced by multiple beams is to add it by hand in the denominator of the friction force of Eq.2.16. With these considerations, the friction coefficient β can be rewritten as:

$$\beta = 8\hbar k_L^2 s \frac{-\Delta/\Gamma}{(1 + 2Ns + 4\Delta^2/\Gamma^2)^2} \tag{2.29}$$

It is possible observe that the friction coefficient β of Eq.2.29 has an extra factor $2Ns$ in the denominator compare to unidimensional case of Eq.2.19. This is a good approximation until the total saturation intensity perceived by the atom is $2Ns \sim 1$ [85]. With this reformulation of the β coefficient, the scattering rate R can be rewritten as

$$R = \frac{\Gamma}{2} \frac{2Ns}{1 + 2Ns + 4(\Delta/\Gamma)^2} \tag{2.30}$$

Repeating the calculation for the minimum Doppler temperature expressed in Sec.2.3.1 and considering the role of the dimensionality N in the diffusion coefficient $\mathcal{D}$ and also in the virial theorem, we obtain:

$$k_B T_D = \frac{\hbar\Gamma}{8} \frac{1 + 2Ns + 4(\Delta/\Gamma)^2}{|\Delta|/\Gamma} \tag{2.31}$$

2.4 Magneto Optical Trapping

The viscous force exerted by the optical molasses is space invariant. This means that atoms are slowed down but it is not possible to trap them in a well defined region of space. To trap an atom by radiation pressure, we have to generate a force that depends on the atom spatial position. This can be accomplished with the Zeeman effect that combines the viscous force of the red-detuned, circular polarized and counter propagating laser beams and magnetic field gradient [79]. The configuration used to trap the atom is called *magneto optical trap* (MOT). Let's consider the one dimensional case reported in Fig.2.2. Suppose that our states $|g\rangle, |e\rangle$ are described with the quantum number $J = 0$ and $J = 1$. This atomic configuration is the typical atomic configuration of the lowest energy levels of alkaline earth atoms. In the center position $\mathbf{z} = 0$ of Fig.2.2, the magnetic field is $\mathbf{B} = \mathbf{0}$ and it increases linearly along the $\mathbf{z}$ direction. Close to the $\mathbf{z} = \mathbf{0}$, the magnetic field can be described as $\mathbf{B} = b\mathbf{z}$ where b is the magnetic field gradient. The inhomogeneous magnetic field generates a Zeeman splitting in the $J = 1$

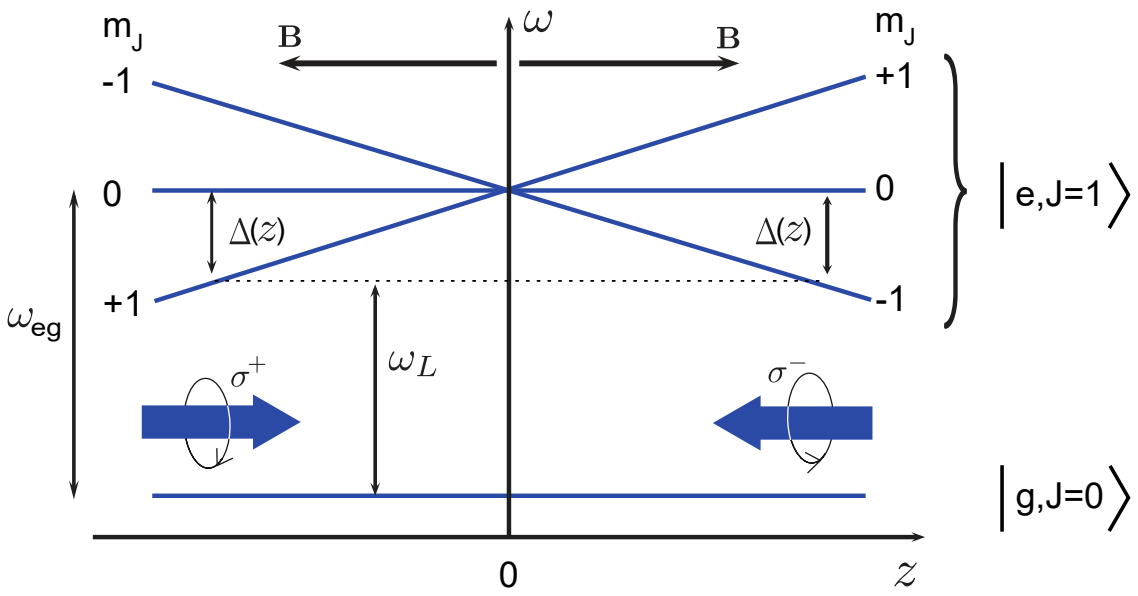

Figure 2.2: Zeeman sublevels in MOT as a function of the atomic position. The center of the magnetic field coincides with the zero position.

state of the atoms as a function of atomic position relative to the center of the magnetic field. This energy splitting, and relative detuning, is calculated according the following relation:

$$\Delta E(z) = g_J m_J \mu_B |\mathbf{B}| \qquad \Longrightarrow \qquad \omega_{eg}(z) = \omega_{eg} + \hbar^{-1} g_J m_J \mu_B |\mathbf{B}| \tag{2.32}$$

where $\mu_B = 9.274 \times 10^{-24}\,\mathrm{J/T}$ is the Born magneton, g_J is the Landé factor and m_J is the Zeeman sub-level quantum number. For the selection rules, the σ^+ drives only a transition where $\Delta M_J = 1$, and the σ^- drives only a transition where $\Delta M_J = -1$. An atom with velocity $\mathbf{v} = 0$ and position $\mathbf{z} > 0$ ($\mathbf{z} < 0$) will see a $\sigma^-(\sigma^+)$ beam closer to the resonance depending on the magnitude of z. The atom perceives a force that pulls it back to the center of the trap. Summing the contributions from the two beams and taking into account the splitting induced by the magnetic field described in Eq.2.32, the MOT force can be written as:

$$\mathbf{F}_{\mathrm{MOT}} = \mathbf{F}_+(\Delta_+) + \mathbf{F}_-(\Delta_-) \tag{2.33}$$

where the detunings are:

$$\Delta_\pm = \Delta \pm \mathbf{k}_L \cdot \mathbf{v} \pm \frac{1}{\hbar} g_J \mu_B b |\mathbf{z}| \tag{2.34}$$

It is possible to demonstrate that for small velocity and small displacement, the MOT force can be approximate as:

$$\mathbf{F}_{\mathrm{MOT}} = -\beta \mathbf{v} - \kappa \mathbf{z} \qquad \kappa = \frac{g_J \mu_B b}{\hbar k_L} \beta \tag{2.35}$$

The force in the Eq.2.35 describes the dynamics of a damped harmonic oscillator. This force generates the trapping of the atom in a well defined spatial region. From a theoretical point of view, the conservative component $-\kappa\mathbf{z}$ of the Eq.2.35 does not induce any cooling or dissipation mechanism. This means that the minimum temperature achieved by the MOT is defined only by optical molasses parameter of Eq.2.27.

2.4.1 The capture velocity

Atoms in the MOT are generally loaded from atomic vapour or from thermal atomic beam where their velocities are distributed according the 3D Maxwell-Boltzmann distribution:

$$f(v) = \sqrt{\frac{2}{\pi}} \frac{v^2}{v_{\text{th}}^2} \exp\left(-v^2/2v_{\text{th}}^2\right) \tag{2.36}$$

where $v_{\text{th}} = \sqrt{k_B T/m}$ is the root mean squared velocity of thermal atoms with mass m at temperature T. Because of the finite dimension of the laser beams, not all the atomic velocities can be trapped in the MOT. This means that exists a maximum atom's velocity captured by the MOT, which is called capture velocity v_{cap}, and it is also related to the beam dimension w_0. A reasonable estimation of the capture velocity is provided with the following consideration. In the MOT, atom is decelerated by scattering R photons per second and for each scattering processes atom is slowed by a recoil velocity $v_r = \hbar k_L/m$. If we want to stop the atom after a distance w_0, the capture velocity can be estimated as [93]:

$$v_{\text{cap}} \simeq \sqrt{2 w_0 R v_r} \tag{2.37}$$

It is possible to demonstrate that the MOT loading rate L_{MOT} is strictly related to the MOT capture velocity with the following relation:

$$L_{\text{MOT}} = nS \int_0^{v_{\text{capt}}} v f(v) dv \tag{2.38}$$

$$\simeq nS v_{\text{th}} \left(\frac{v_{\text{cap}}}{v_{\text{th}}}\right)^4 \tag{2.39}$$

where n is the atomic density of the atomic vapour or thermal beam and S is the trap surface area. The last passage of the Eq.2.39 is valid until $v_{\text{cap}} \ll v_{\text{th}}$. This relation is usually fulfilled in many atomic physics experiments where $v_{\text{cap}} \sim 40\,\text{m/s}$ and v_{th} is one order of magnitude larger (In the case of Sr atoms, $v_{\text{th}} = 160\,\text{m/s}$ at room temperature $T = 300\,\text{K}$). Considering the Eq.2.39, the capture velocity is related with a power law relation to the number of atoms in MOT. Having a tool

that estimates and predicts the capture velocity v_{cap} as a function of the experimental parameters, such as $s, \Delta/\Gamma, b$, is important in order to properly design the MOT.

A more precise estimation of the capture velocity considering also a non negligible magnetic field is also provided by [94]. If we want to figure out a correct estimation of the capture velocity, without introducing any approximation of the force given by Eq.2.33, a numeric approach has to be implemented [95]. In this section we perform the numeric capture velocity estimation considering the complete MOT force of Eq.2.33 acting on ^{88}Sr atoms. Numerically simulating atomic trajectories at different starting velocities, the capture velocity is extrapolated considering the trajectory with higher starting velocity trapped by the MOT. An example of the 1D trajectories simulations are reported in Fig.2.3 and Fig.2.4. Inputs parameters and numeric capture velocities estimation are reported in Tab.2.1.

		Fig.2.3	Fig.2.4
atomic mass	m	88 u	88 u
wavelength	λ	461 nm	461 nm
linewidth	$\Gamma/2\pi$	30.5 MHz	30.5 MHz
beam waist	w_0	9 mm	9 mm
saturation parameter	s_0	0.5	0.5
detuning	Δ/Γ	-0.5	-2
magnetic gradient	b	0.2 T/m	0.4 T/m
estimated capture velocity	v_{cap}	60.5 m/s	22.8 m/s
numeric capture velocity	$v_{\text{cap}}^{\text{num}}$	43(1) m/s	72(1) m/s

Table 2.1: Parameters used for the numeric estimation of the capture velocities. The estimated capture velocity is provided by Eq.2.37

The background color maps of Fig.2.3 and Fig.2.4 are accelerations expressed by Eq.2.35 at different positions and velocities of the atom and with different experimental parameters given by Tab.2.1. Each acceleration maps show two defined regions with opposite accelerations. The separation of these two region is proportional to the detuning Δ/Γ of the optical beam. At larger detuning, the separation increases. Rotation of the regions are related to the magnetic gradient b of the MOT, the higher is the gradient, the higher is the rotation induced. In the end, the broadening of the regions are related to the optical saturation s. In these simulations we also include finite size of the Gaussian intensity relation $s(x) = s_0 e^{-2x^2/w_0^2}$, where x is the atomic position, w_0 is the beam waist and s_0 in the saturation parameter of the single beam. Each white line of the plots is a simulated atomic trajectory of ^{88}Sr. Trajectories started at $x = -0.02$ m with different starting velocities spanning from 10 m/s to 110 m/s. Starting velocities are directed toward

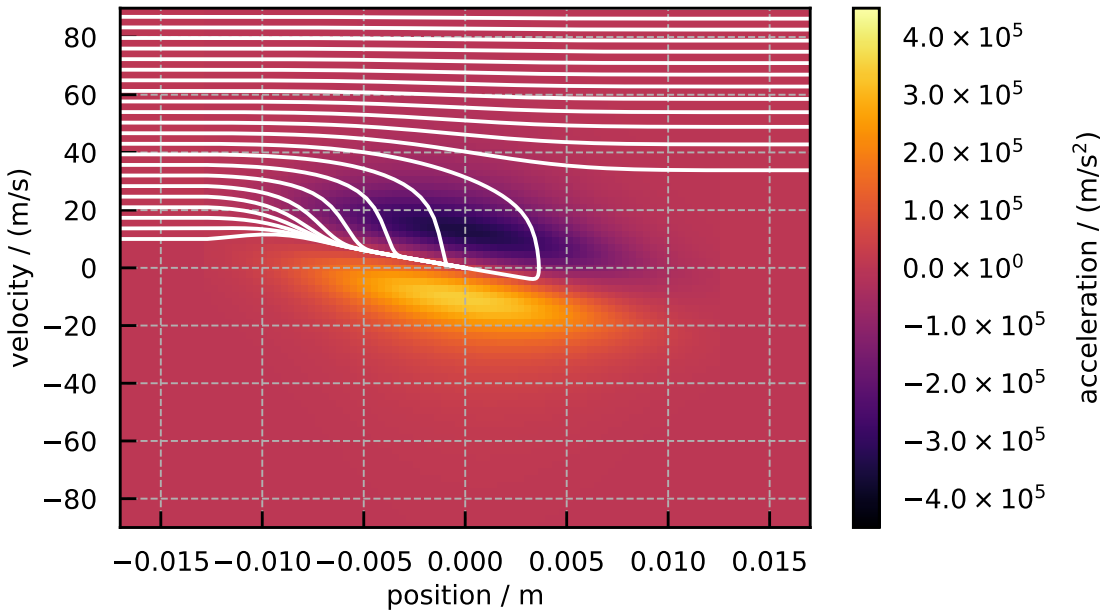

Figure 2.3: Capture velocity with $s = 0.5$, $\Delta/\Gamma = -0.5$ and $b = 20\,\mathrm{G/cm}$. Close to the center of the trap, the phase-space trajectories describe an over-damped harmonic oscillator dynamics

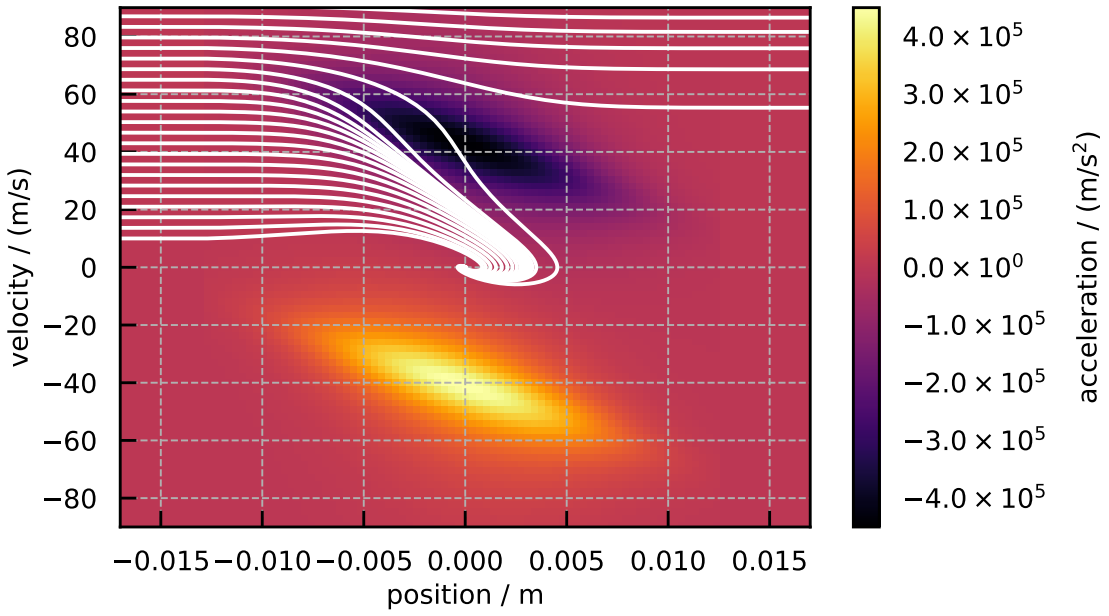

Figure 2.4: Capture velocity with $s = 0.5$, $\Delta/\Gamma = -2$ and $b = 40\,\mathrm{G/cm}$ Close to the center of the trap, the phase-space trajectories describe a damped harmonic oscillator dynamics

the trapping center $x = 0$. From Fig.2.3 and Fig.2.4 it is possible to appreciated the velocity range that contributes to the MOT loading process. As shown in the Tab.2.1, the estimation provided by Eq.2.37 is not accurate at higher magnetic field gradient compare to the numerical one.

The capture velocity parameter gives a reasonable estimation concerning the MOT efficiency and it is an important tool in order to get the main feature of the trapping process during the MOT design. The capture velocity v_{cap} defined in the Eq.2.37 is atomic parameter and it is a 1D estimation of a complicated volumetric loading process L_{MOT} where the capture velocity v_{cap} may be dependent to initial atomic position and velocity [96] and the loading geometry. As will be reported in Ch.4, a fully 3D atomic trajectory simulation directly estimate the MOT loading process L_{MOT} instead of v_{cap}.

2.4.2 3D magneto optical trap

Even if we do not discuss the complete 3D theory of the MOT [97, 98], the 1D model captures the main physical features and the dynamics of the trapping process. An example of a possible experimental 3D realization of the MOT is reported in the Fig.2.5. The optical molasses is generated by three counter-propagating beams with same detuning and saturation intensity. The magnetic field gradient is generated by a pair of coils in the Anti-Helmholtz configuration where the current circulates in opposite directions. The magnetic field generated is linear for small displacements around the center of the trap and can be written as:

$$\mathbf{B} = b\mathbf{x} + b\mathbf{y} - 2b\mathbf{z} \tag{2.40}$$

The gradient of the magnetic field generated by the coils has to fulfil the Maxwell equation $\boldsymbol{\nabla} \cdot \mathbf{B} = 0$. Taking into account the cylindrical symmetry of the system around $\hat{\mathbf{z}}$, the magnetic field components have to fulfil the following relation:

$$\frac{\mathrm{d}B}{\mathrm{d}x} = \frac{\mathrm{d}B}{\mathrm{d}y} = -\frac{1}{2}\frac{\mathrm{d}B}{\mathrm{d}z} \tag{2.41}$$

The knowledge of the magnetic field direction is used to set the right polarization of each optical beams. As show in the Fig.2.5, in each laser reference of frame, the beam polarization has to point in the opposite direction of the magnetic field orientation .

2.4.3 2D magneto optical trap

Another interesting trapping geometry is provided by the 2D magneto optical trap. As show in the Fig.2.6, the trapping process is spatial limited in a plane

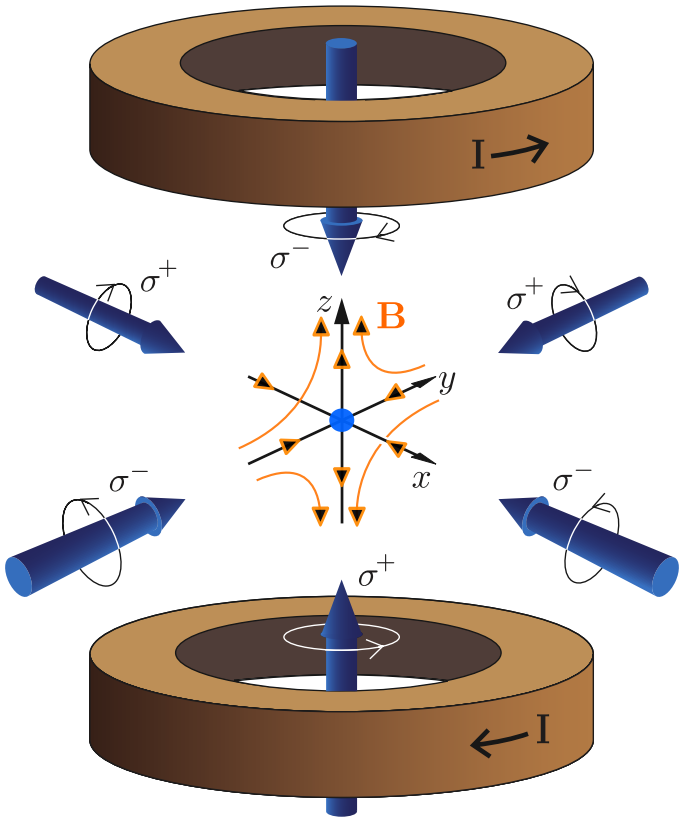

Figure 2.5: Three dimensional MOT representation. Magnetic quadrupole is generated by a pair of coils in Anti-Helmohltz. Optical molasses is generated by 3 counter-propagating circular beams with specific polarization σ. Each σ polarizations beams are chosen considering magnetic field direction. Magnetic field direction in the MOT are depicted with orange arrow-lines. Atoms are trapped in the center of the 3D-MOT showing a spherical geometry.

of the beams while in the other direction the atoms remain unperturbed. Optical molasses is generated by 2 counter propagating beams with same detunings and saturation parameters . In the Fig.2.6, a possible magnetic field configuration that generated a 2D-MOT is made by a 2 pair of coils in Anti-Heltmoltz configuration. The magnetic field generated by the coils close to the center of the trap can be approximated as:

$$\mathbf{B} = b\mathbf{x} - b\mathbf{z} \tag{2.42}$$

where b is the magnetic gradient. This formula says that there is no magnetic field along the y direction and the gradient along the x direction is inverse to the gradient along the z direction because of the Maxwell equation. This trapping geometry generate a cold atomic ensemble with a cigar shape along y direction where the amplitude of the magnetic field is null.

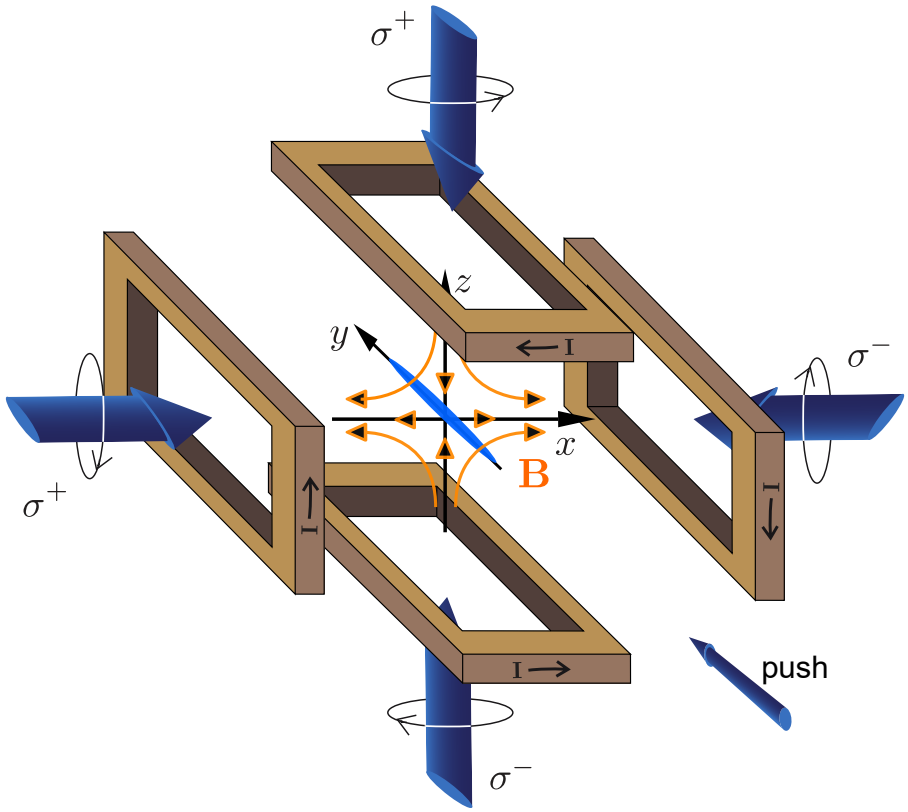

Figure 2.6: Example of Two dimensional MOT representation usually employed for K and Rb experiments. Magnetic quadrupole is generated by two pair of coils in Anti-Helmohltz configurations. Optical molasses is generated by 2 counter-propagating beams with specific polarization σ. The MOT beams have and elliptical shape along the free direction of the 2D-MOT in order to increase the capture process of the atoms in the 2D-MOT. Each σ polarizations beams are chosen considering magnetic field direction. In the atomic source design, the push beam is usually add in the y direction where the magnetic field is null. Magnetic field direction in the 2D-MOT are depicted with orange arrow-lines. Atoms are trapped in the center of the 2D-MOT showing a cigar shape geometry along the y direction.

Adding a resonant low power beam along the y direction, the entire system can be saw as an atomic source of slow atoms. The thermal atoms, coming from thermal vapour or by thermal beam, are loaded to the 2D-MOT and emitted along the push direction. Because of the trapping in the 2D-MOT plane, the radial velocity of the atoms (along x and z) are reduced close to the Doppler limit while along the y direction, the velocity of the atoms are tuned by means of the optical parameter of the push beam. The result of the entire process can be saw as an atomic funnel [99] where a thermal atomic distribution is collimated to a cold and slow atomic flux.

A lot of experiments are found in the literature where the 2D-MOT and push beam are employed as atomic source system. This experiments employs different atomic species like Rb [99, 100], K [101, 102] , Li [103], Na [75, 104] , Yb [105, 106] and Sr [107] and also double species components Rb-K [108]. In our system we use a 2D-MOT as atomic source of our optical lattice clock. In the Ch.3 we will discuss the metrological and technical advantages offer by this solution.

Sideband enhanced 2D-MOT

In our system we also investigate the possibility to enhance the atomic flux generated by the 2D-MOT atomic source adding a sideband beams to the standard 2D-MOT beams. Sideband beams have the same polarization of the 2D-MOT and they are red-shifted compared to the 2D-MOT beam generating a two-colors 2D-MOT. The physics behind this sideband-ehnacend 2D-MOT is simple: the red detuned sideband beams interact with thermal atoms with higher velocity class, once the faster atoms are slowed down by the sideband beam interaction, they will be captured by the standard 2D-MOT beams.

Having a fixed optical power we engineer the optical power redistribution between the sideband beam and the 2D-MOT beam at different detunings to find a possible increment on the atomic flux provided by the atomic source. The result of this experimental investigation with the quantitative simulation comparison will be discussed in Ch.5.

2.5 Dipole force

In this section we focus on the reactive component of the force described with Eq.2.9 and we analyze the proprieties of the optical dipole trap. The loading of the neutral atoms in the optical potential is a mandatory step to produce a optical lattice clock. First evidence of the neutral atoms trapped in a optical potential was performed by Chu *et. al* [109]. Suppose that we are in the far-off resonant regime where $\Delta/\Gamma \gg 1$, the Eq.2.9 is approximated as:

$$\mathbf{F}(\mathbf{r}) = -\frac{\hbar\Gamma}{8}\left(\frac{\Gamma}{\Delta}\right)\boldsymbol{\nabla} s(\mathbf{r}) \tag{2.43}$$

Where $\mathbf{r}$ is the atom position. This force is a conservative force and its associated potential energy is given by:

$$U_{\text{dip}}(\mathbf{r}) = \frac{\hbar\Gamma}{8}\left(\frac{\Gamma}{\Delta}\right) s(\mathbf{r}) \tag{2.44}$$

This is the so called optical dipole potential. From Eq.2.44 we observe that the sign of the dipole potential depends on the sign of the detuning Δ. If the laser light

is below the resonance, $\Delta < 0$, the dipole potential is negative and atoms tend to be attracted in the region of higher intensity. In the positive detuning case, $\Delta > 0$, the dipole potential is positive and the atoms are repelled from regions with high intensity field. In order to load atoms in the optical trap, the temperature of the MOT and the lattice depth have to match. For the case of the Sr atoms, the single stage cooling with $^1S_0 - {}^1P_1$ transition is not sufficient and a second stage cooling with $^1S_0 - {}^3P_1$ transition is usually employed to efficiently load atoms in the optical dipole trap.

Using the relation expressed in Eq.2.10 between the Rabi frequency Ω and the saturation parameter s, we can rewrite the saturation parameter s as:

$$s = 2\frac{\Omega^2}{\Gamma^2} = \frac{d_{eg}^2 E_0^2}{2\Gamma^2\hbar} \tag{2.45}$$

Combining the Eq.2.44 with Eq.2.45, the dipole potential can be rewritten as:

$$U_{\text{dip}} = \frac{1}{4}\frac{d_{eg}^2}{\hbar\Delta}E_0^2 = -\frac{1}{2}\alpha(\omega_L)E_0^2 \tag{2.46}$$

in the last reformulation, we introduce the coefficient α that described the polarizability of the atomic system. According the Eq.2.46, dipole porizzability is defined as:

$$\alpha(\omega_L) = \frac{1}{2\hbar}\frac{d_{eg}^2}{\omega_{eg} - \omega_L} \tag{2.47}$$

Classically the concept of the polarizability describes the linear response of the electric dipole moment to the external electrical field $\mathbf{d} = \alpha\mathbf{E}$. The energy shift induced to the atomic transition energy $\hbar\omega_{eg}$ by means of the dipole potential is called AC Stark shift and can be estimated according the following relation:

$$\delta\omega_{eg} = -\frac{1}{4\hbar^2}\alpha(\omega_L)E_0^2 \tag{2.48}$$

Eq.2.47 is valid under two assumptions. The first assumption concerns the fact that we are dealing with the RWA approximation. This approximation is no longer valid if we are in the far-off resonance regime ($|\Delta| \lesssim \omega_{eg}$). Another approximation is provided considering that we are assuming the atomic internal structure as a perfect two levels system. Removing the RWA approximation and considering the multi-level structure of the atom, the dipole porizability and the frequency shift a of the state $|n\rangle$ can be expressed as: [81, 110]:

$$\alpha_n(\omega_L) = \frac{1}{2\hbar}\sum_k \left[\frac{d_{kn}^2}{\omega_{kn} - \omega_L} - \frac{d_{kn}^2}{\omega_{kn} + \omega_L}\right] \tag{2.49}$$

$$\delta\omega_n = \frac{1}{2\hbar}\alpha_n(\omega_L)E_0^2 \tag{2.50}$$

where $|k\rangle$ labels different states of the internal atomic structure and ω_{kn} are the transitions frequencies among the states $|k\rangle$ relative to the state $|n\rangle$.

2.5.1 Optical lattice

The easiest method to generate an optical lattice is to making interfere two counter propagating laser beams of the same detuning Δ and saturation parameter s. In this configuration, the 1D electric field and the dipole potential are described as:

$$E(z) = E_0 \left(e^{-i\omega_L t - ik_L z} + e^{-i\omega_L t + ik_L z}\right) = 2E_0 e^{-i\omega_L t} \cos\left(2\pi z/\lambda_L\right) \tag{2.51}$$

$$U_{\text{dip}} = -\alpha E_0^2 \cos^2\left(2\pi z/\lambda_L\right) = -U_0 \cos^2\left(2\pi z/\lambda_L\right) \tag{2.52}$$

$$\tag{2.53}$$

With this method, a standing wave along the laser propagation direction z is generated with an intensity modulation with periodicity $\lambda_L/2$. Consider the 3D case, the laser beam is better described as a Gaussian beam rather than a plane wave. The single beam spatial intensity distribution is described as:

$$I(r,z) = \frac{2P_0}{\pi w(z)} \exp\left(-2r^2/w^2(z)\right) \tag{2.54}$$

where z is the propagation direction of the laser beam and r is the transversal direction. The e^{-2} radius of the laser beam is defined as $w(z) = w_0\sqrt{1+(z/z_R)^2}$ where w_0 is the minimum radius and $z_R = \pi w_0^2/\lambda_L$ is the Rayleigh range. In the region where $z \ll z_R$, the radius beam is approximate to $w(z) \simeq w_0$ and the dipole potential is written as:

$$U_{\text{dip}} = -U_0 \exp\left(-2r^2/w_0^2\right) \cos^2(2\pi z/\lambda) \tag{2.55}$$

In the deep lattice approximation and close to the minima points of the optical intensity, Eq.2.55 can be further approximate as an harmonic oscillator potential:

$$U_{\text{dip}} \simeq U_0 \left[\left(\frac{2\pi z}{\lambda_L}\right)^2 + \left(\frac{2r}{w_0}\right)^2\right] = \frac{1}{2}m\omega_z^2 z^2 + \frac{1}{2}m\omega_r^2 r^2 \tag{2.56}$$

where the trapping frequency are defined as:

$$f_z = \frac{\omega_z}{2\pi} = \frac{1}{\lambda_L}\sqrt{\frac{2U_0}{m}} = \frac{2}{\hbar}\sqrt{U_0 E_r} \qquad f_r = \frac{\omega_r}{2\pi} = \frac{1}{2\pi}\sqrt{\frac{4U_0}{m w_0^2}} = \frac{\lambda_L}{2\pi w_0} f_z \tag{2.57}$$

where $E_r = \hbar k_L^2/2m$ is the photon recoil energy. From the relations of the trap frequencies given by Eq.2.57, the ratio between the two trapping frequencies is $f_r/f_z = w_0/2z_R$ where z_R is the Rayleigh range. This ratio is always smaller than one, therefore the potential along the axial direction is steeper that the radial one.

2.5.2 Lamb-Dicke regime

Once the atoms are successfully trapped in the optical lattice, their clock transition are usually probed with a laser beam propagating along the z direction. If so, the main motional effects are related to the dynamics along the z direction. Along the the longitudinal direction z, the harmonic confinement give the quantum energy spectrum described as:

$$E_n = \hbar\omega_z \left(n + \frac{1}{2}\right) \tag{2.58}$$

where n is the integer number that labels the vibrational state. In this configuration, the atom wavefunction can be factorized into an electronic wavefunction, $|g\rangle$ or $|e\rangle$, and into a vibrational wavefunction, $|n\rangle$. As sketched in the Fig.2.7(a), During the excitation from the ground state to clock state an atom trapped in the lattice can make a pure electronic transition $|g, n\rangle \rightarrow |e, n\rangle$ absorbing a photon ω_{eg}, or it can also exchange quanta of vibrations as $|g, n\rangle \rightarrow |e, m\rangle$. On the bottom of the Fig.2.7(a), a possible excitation spectrum is depicted: the central peak corresponds to a pure electronic excitation while the sidebands peaks corresponds to a mixing among the electronic and the vibrational excitations.

Because we are interested to probe the pure electronic transition, the transitions of different vibrational states have to be suppressed. Let's consider the localization factor η defined as:

$$\eta = \frac{k_L z_{\text{ho}}}{\sqrt{2}} = \sqrt{\frac{\omega_z}{\omega_R}} \tag{2.59}$$

where $z_{\text{ho}} = \sqrt{\hbar/m\omega_z}$ is quantum harmonic oscillator radius and $k_L = 2\pi/\lambda_L$ wavenumber of the probing light. As show in the spectrum of Fig.2.7(b), At large value of η, the carrier frequency is not well discriminated from the sidebands frequency while at lower values of η the central peak, which is the pure electronic transition, becomes well resolved respect to the sidebands peaks. The Lamd-Dicke regime is achieved at $\eta \ll 1$ where the size of the spatial wavefunction of the atom is smaller than the probing wavelength [111]. In this strong confinement regime, the recoil energy $E_r \ll \hbar\omega_z$ is small compared to the spacing among the vibrational levels: the recoil energy induced during the atom interrogation is taken by the confining potential leaving unperturbed the atoms transition. Trapping the atom in the in the Lamb-Dicke regime is the key strategy to suppress the Doppler and the recoil shifts.

2.5.3 Magic wavelength

As explained in the 2.50, the interaction of the atom with the optical lattice induces a light shift (or also called AC Stark shift) on the the atomic energy levels.

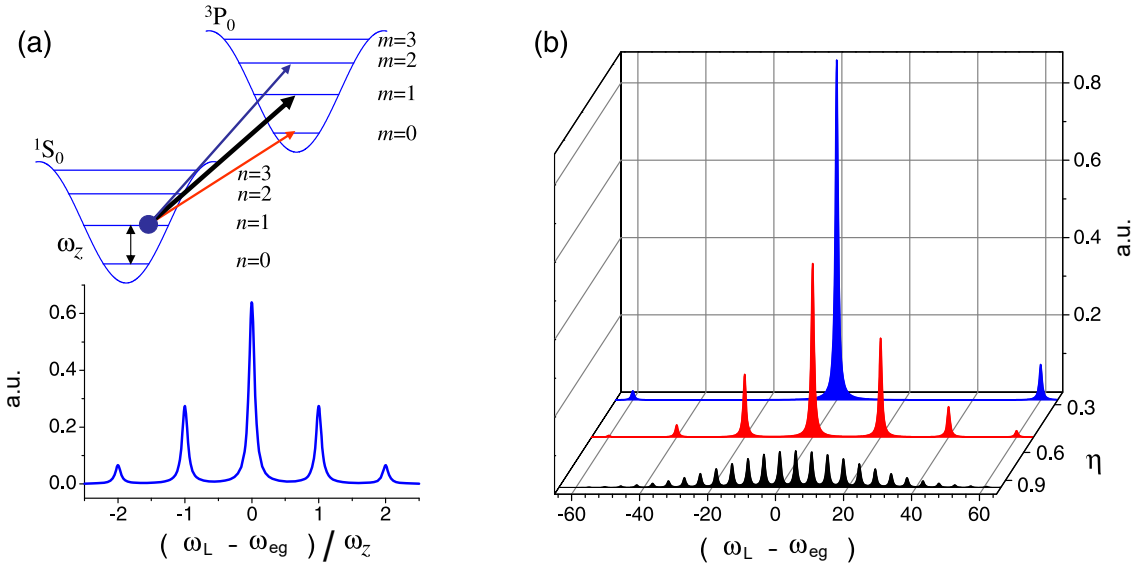

Figure 2.7: Lamb-Dicke regime. **(a)** Atom in the lattice potential in and its possible spectrum during the clock laser excitation. **(b)** Absorption spectrum of the atoms after the clock laser probing in the lattice potential at different η. In the Lamb-Dicke regime, lower *eta*, the spectral lines are clearly resolved and the carrier frequency are well discriminated. Figure taken from [19]

As a consequence, the frequency between excited state $|e\rangle$ of the clock transition and its ground state $|g\rangle$ is shifted by a factor of:

$$\omega_{eg}^{*} = \omega_{eg} - \frac{1}{4\hbar}\Delta\alpha_{eg}(\omega_L)E_0^2 \tag{2.60}$$

where $\Delta\alpha_{eg}(\omega_L) = \alpha_e(\omega_L) - \alpha_g(\omega_L)$ is the differential polarizability between the ground state and the excited state.

Katori proposal was to cancel the first order light shift by inducing the same AC Stark perturbation on both the ground and the excited states [36, 112]. This phenomena is achieved by tuning the lattice laser frequency at the so called magic frequency $\omega_L = \omega_{\text{magic}}$ where:

$$\alpha_g(\omega_{\text{magic}}) = \alpha_e(\omega_{\text{magic}}) \qquad \Longrightarrow \qquad \Delta\alpha_{eg}(\omega_{\text{magic}}) = 0 \tag{2.61}$$

For given atomic system and clock transition $|g\rangle - |e\rangle$, more than one wavelengths ω_{magic} can fulfil Eq.2.61. From all the possible magic wavelengths it usually choose the one which the variation of the polarizabilities $\alpha_g(\omega_{\text{magic}})$ and $\alpha_e(\omega_{\text{magic}})$ as a function of the trapping frequency are lower. Because we are dealing with a simple 1D-optical lattice, the trapping is performed only with a red-detuned optical trap, which means that the selected magic wavelength has to be red detuned respect to

the clock transition and the atoms are trapped in the maximum intensity regions of the lattice. Experimentally, also the possibility to develop a high power stabilization system at ω_{magic} can play a role in the choice of a possible ω_{magic}.

The Eq.2.60 does not take into account higher order correction terms, such as the hyperpolarizability term, which can not be removed at magic wavelength [113, 114]. Because we employing a red-detuned trap, these correction terms can not be cancelled at high optical intensity of the trap. In the literature it is possible to find some proposal of blue-detuned optical trap where the atoms are trapped in the minima intensity regions of the lattice and in order to be less perturbed by the lattice trap [115].

2.6 The Strontium atom

The Strontium a is chemical element with symbol Sr and it is placed on the second group and fifth period of the Mendeleev periodic table. Strontium has physical and chemical properties similar with its two vertical neighbours in the periodic table, the Calcium and the Barium. Sr is silvery metal at room temperature, it oxidises rapidly when exposes to air forming a dark oxide layer. Sr has a density of $2.64\,\text{g/cm}^3$ with a melting point at 777 °C and a boiling point at 1382 °C [116]. Sr has an atomic number $Z = 38$ and atomic mass $m = 87.62\,\text{u}$, where u is the atomic mass unit ($1\,\text{u} = 1.66 \times 10^{-27}\,\text{kg}$). The ground state of the neutral strontium is $[\text{Kr}]5s^2\,{}^1S_0$.

As reported in Tab.2.2, Sr has four stable isotopes plus one, the ^{90}Sr, which has a lifetime of 29.1 year. Except the ^{87}Sr, all the Sr isotopes are boson with spin 0. The isotope ^{87}Sr is a fermion with a nuclear spin $I = 9/2$ and it posses an hyperfine structure. All the boson isotopes have the same electronic structure, the isotopic shift is the only difference among them.

Isotope	mass / u	Abundance / %	Spin	μ/μ_N
^{84}Sr	83.913425(3)	0.56(1)	0	
^{86}Sr	85.9092602(12)	9.86(1)	0	
^{87}Sr	86.908871(12)	7.00(1)	9/2	-1.0936030(13)
^{88}Sr	87.9056121(12)	82.58(1)	0	

Table 2.2: mass, natural abundance, an nuclear spin of stable Sr isotopes [116]. Nuclear magneton is $\mu_N = 5.050\,783\,699(31) \times 10^{-27}\,\text{J/T}$

2.6.1 Relevant spectral lines of Sr

As the other alkaline earth metals, the Sr has two valence electrons. The presence of the second valence electron divides the electronic spectrum of the Sr in two distinct groups: the energy levels group with total spin $S = 0$ (singlet states) and the energy levels group with total spin $S = 1$ (triplet states). In the case of the alkaline earth metal, the spin orbit coupling between the spin S and the electronic angular momentum L is low compared to the electrostatic interaction. This means that n, L and S are good quantum numbers to identify the state of the Sr. Using the Russell-Saunders notation ${}^{2S+1}L_J$, the Fig.2.8 reports the relevant lower energy levels of the ^{88}Sr.

The possibility to perform a transition from a state to another state are defined by the selection rules. In the case for the electric dipole transition, the selections rules are the following:

$$\Delta L = \pm 1 \tag{2.62a}$$
$$\Delta S = 0 \tag{2.62b}$$
$$\Delta J = 0,\ \pm 1 \quad (0 \nrightarrow 0) \tag{2.62c}$$
$$\Delta M_J = 0,\ \pm 1 \tag{2.62d}$$

The first two rules expressed in Eq.2.62a and Eq.2.62b are valid at zero spin orbit coupling. These rules are responsible of the strong transitions of states with same quantum number S. These transitions have generally a large linewidth Γ. The last two rules expressed in Eq.2.62c and Eq.2.62d are used when the spin-orbit coupling is not zero. These rule are responsible for the inter-combination transitions ($\Delta S \neq 0$) and they have smaller linewidth.

Cooling transitions

As show in the Fig.2.8, the ground state of the ^{88}Sr atoms is ${}^1\mathrm{S}_0$. This state has $J = 0$ and it has a strong dipole allowed transition with the state ${}^1\mathrm{P}_1$, which has $J = 1$. The transition wavelength is 461 nm and the excited state ${}^1\mathrm{P}_1$ has a relative short life time ($\tau = 5.22\,\mathrm{ns}$) [117, 118]. Because of the large scattering rate and suitable atomic structure of the levels where $\Delta J = 1$, the ${}^1\mathrm{S}_0 - {}^1\mathrm{P}_1$ is a valid transition for cooling and trapping atoms in a MOT. This MOT stage is also called blue MOT. Unfortunately, the ${}^1\mathrm{S}_0 - {}^1\mathrm{P}_1$ transition is not a perfect two levels system. In fact, the state ${}^1\mathrm{P}_1$ has a non negligible decay rate of 620 Hz ($\tau = 256\,\mu\mathrm{s}$) toward the state ${}^1\mathrm{D}_2$ [119]. Atoms in the state ${}^1\mathrm{D}_2$ can then decay in the sub-levels of the triplet state: ${}^3\mathrm{P}_2$ and ${}^3\mathrm{P}_1$. From the state ${}^3\mathrm{P}_1$, the electrons can rapidly ($\tau = 20\,\mu\mathrm{s}$) decay in the ground state ${}^1\mathrm{S}_0$ closing the loop [116]. On the other hand, the electrons in the state ${}^3\mathrm{P}_2$ decay in the ground state after a longer time.

The state $^3P_2$ is also called metastable state. Experiment shows the $^3P_2$ decay time of $\tau = 520\,s$ [120] which partially agree with the theoretical value $\tau = 1020\,s$ [121]. Because of the long decay time of the atoms in the metastable state, large part of atom are lost in the blue MOT. This losses also limit the MOT loading rate to a few $\sim$10 ms [122]. The losses in the cooling process of the $^1S_0 - {}^1P_1$ can be overcome exploiting the repumping transitions of the Sr. As we are going explain, these transitions can close the $^1S_0 - {}^1P_1$ transition and increase the number of atoms trapped and its loading rate. By cooling on the 461 nm laser light it is possible to achieve temperature of the atomic sample of the order of few mK. In the case of the fermionic isotope ^{87}Sr, the presence of sub-Zeeman levels offer the possibility to achieve lower temperatures for the $^1S_0 - {}^1P_1$ transition by means of Sisyphus cooling [122].

A second laser at 689 nm is usually employed in order to cool further the atomic sample. This laser light addresses the transition $^1S_0 - {}^3P_1$ which has a lower linewidth as compared to the $^1S_0 - {}^1P_1$ transition. As reported in the Tab.2.3, even if the Doppler temperature is low because of the lower linewidth of the red transition, at same detuning and saturation parameter, the optical acceleration to the atoms of the $^1S_0 - {}^3P_1$ transition is lower compared to the $^1S_0 - {}^1P_1$ transition. This means that the direct capture process of atoms from a thermal beam almost impossible and a blue MOT is a necessary stage to increment the loading efficiency in the red MOT. Starting from an atomic sample of few mK given by the blue MOT, this second cooling stage can further reduce the atomic sample temperature to few µK [123, 124]. Relevant parameters of blue and red cooling processes are reported on Tab.2.3. Some differences between the ^{88}Sr and the ^{87}Sr second stage cooling are mainly related to the isotopic shift and the hyperfine structure present in the in the fermionic isotope [125].

Repumping transitions

In order to increase the number of atoms in the MOT, it is necessary to optically pump the atoms accumulated on the metastable state $^3P_2$ during the operation of the blue MOT, towards the ground state. There are several possibilities to close the transition $^1S_0 - {}^1P_1$. One possibility is to use two lasers of 707 nm and 679 nm that address respectively the transitions $^3P_2 - {}^3S_1$ and $^3P_0 - {}^3S_1$ [126]. The 707 nm pumps the atoms from $^3P_2$ to the state $^3S_1$ and then they decay into $^3S_1 - {}^3P_{0,1}$. If the atoms decay in the $^3P_1$, the atoms rapidly decay to the state $^1S_0$. If the atom decay on $^3P_0$, because of the selection rules it can not decay in the ground state $^1S_0$. The repumper light at 679 nm pumps the atom from $^3P_0$ to $^3S_1$ repeating the decay path explained before. With this two lasers configuration, atoms are induced to populate the state $^1P_3$ which decay rapidly in the ground state closing the $^1S_0 - {}^1P_1$ transition. The main consequence of the repumping process is the gain in the

		$^1S_0 - {}^1P_1$	$^1S_0 - {}^3P_1$
wavelength	λ	460.86 nm	689.45 nm
wavenumber	$k/2\pi = \lambda^{-1}$	21 698.452 cm^{-1}	14 504.334 cm^{-1}
frequency	$\nu = c/\lambda$	650.51 THz	434.83 THz
transition probability	A	1.92×10^8 Hz	4.69×10^4 Hz
linewidth	$\Gamma = A$	$2\pi \times 30.5$ MHz	$2\pi \times 7.6$ kHz
decay time	$\tau = A^{-1}$	5.22 ns	21 µs
Landè factor	g_J	1	1.5
saturation intensity	$I_0 = \pi hc/3\lambda^3\tau$	41 mW/cm^2	3 $\mu W/cm^2$
maximum acceleration	$a_{max} = \Gamma\hbar k/2m$	9.3×10^5 m/s^2	155 m/s^2
recoil frequency	$\omega_r = \hbar k^2/2m$	$2\pi \times 11$ kHz	$2\pi \times 4.8$ kHz
Doppler temperature	$T_D = \hbar\Gamma/2k_B$	731 µK	182 nK
Recoil temperature	$T_R = \hbar^2k^2/2mk_B$	1.02 µK	454 nK

Table 2.3: Parameters of the two cooling transitions of ^{88}Sr

number of atoms in the MOT and a longer loading rate compared to the single blue MOT [122]. Parameters of the repumping transition are reported in Tab.2.4.

		$^3P_2 - {}^3S_1$	$^3P_0 - {}^3S_1$
wavelength	λ	707.20 nm	679.29 nm
wavenumber	$k/2\pi = \lambda^{-1}$	14 140.271 cm^{-1}	14 721.253 cm^{-1}
frequency	$\nu = c/\lambda$	423.91 THz	441.32 THz
transition probability	A	2.89×10^8 Hz	5.65×10^7 Hz
linewidth	$\Gamma = A$	$2\pi \times 46$ MHz	$2\pi \times 9$ MHz
decay time	$\tau = A^{-1}$	3.4 ns	0.17 ns
saturation intensity	$I_0 = \pi hc/3\lambda^3\tau$	17 mW/cm^2	3.7 mW/cm^2

Table 2.4: Parameters of the two repumping transition of ^{88}Sr

Another possibility is to use a single repumper laser scheme in order to close the $^1S_0 - {}^1P_1$ transition. All of these schemes repump the atom from the $^3P_2$ to another state that can decay in the $^3P_1$ state. One possibility is to pump the the atom from $5s5p\,{}^3P_2$ to $5s5p\,{}^3D_2$ via the laser transition 497 nm [127–129]. Another possibility is use a 403 nm to pump the atom from $5s5p\,{}^3P_2$ to $5s6d\,{}^3D_2$ [129]. Also the mid-infrared light of 3012 nm can be employed to pump the atom from $5s5p\,{}^3P_2$ to $5s4d\,{}^3D_2$ [130] . More recently, a repumper schemer of 481 nm was proposed to pump the atom from $5s5p\,{}^3P_2$ to $5p^2\,{}^3P_2$ [131]. Historically, it was also tested the possibility to repump the atom from $5s4d\,{}^1D_2$ to $5s6p\,{}^1D_2$ by means of 717 nm laser radiation [132].

In these we decide to repump the Sr atom with the transitions $^3P_2 - {}^3S_1$ at 707 nm and $^3P_0 - {}^3S_1$ at 679 nm. As we will explain in the Sec.3.7, the light source of these transitions can be generated by cheap commercial lasers diodes and its emitted wavelength can be easily reduced and tuned with a suitable electro-mechanical system.

Clock transition and magic wavelength

The requirements for the clock transition is to posses an high quality factor Q and also to have a low sensitivity to the environmental conditions. For the case of Sr, the best candidate for the clock transition is the $^1S_0 - {}^3P_0$. According to the selection rules given by Eq.2.62b and Eq.2.62c, this transition is double forbidden.

For the bosonic isotope ^{88}Sr it is possible to address this transition by adding and external magnetic field which induces a mixing between the state $^3P_0$ and $^3P_1$ [133–136]. However, a precise knowledge and control of the external magnetic field is required to performer a precise estimation of the induced quadratic Zeeman shift. Moreover, the bosonic nature of the isotope will also add some complications related to the density shift induced by cold collisions [137] . If we consider the fermionic isotope ^{87}Sr, these two problem are limited. Because of the hyperfine interaction in the ^{87}Sr isotope, the state $^3P_0$ is not a pure state but it is mixed with other states generating a small linewidth of 1 mHz [36, 138] that induces the transition from $^1S_0$ to $^3P_0$ and because of the fermionic nature of the ^{87}Sr the cold collisional shift is reduced compared to the boson counterpart [134, 137]. Uncertainty of the clock transition was estimated using atom trapped in a MOT [139] and also atoms trapped in optical lattice at magic wavelength [36, 37]. The magic wavelength of the $^1S_0 - {}^3P_0$ is estimated at $\lambda_{\text{magic}} \simeq 813.427$ nm [140, 141].

The unperturbed clock transition $^1S_0 - {}^3P_0$ of ^{87}Sr is $\nu = 429\,228\,004\,229\,873.0$ Hz with a fractional accuracy of 4×10^{-16} [38, 39, 142–145] This frequency value corresponds to a wavelength of $\lambda = 698\,445\,709.612\,754\,4$ fm. This frequency value is one of recommended ones for the secondary representation of the SI second [146] approved by *Consultative Committee for Time and Frequency* (CCTF) on June 2017 [147].

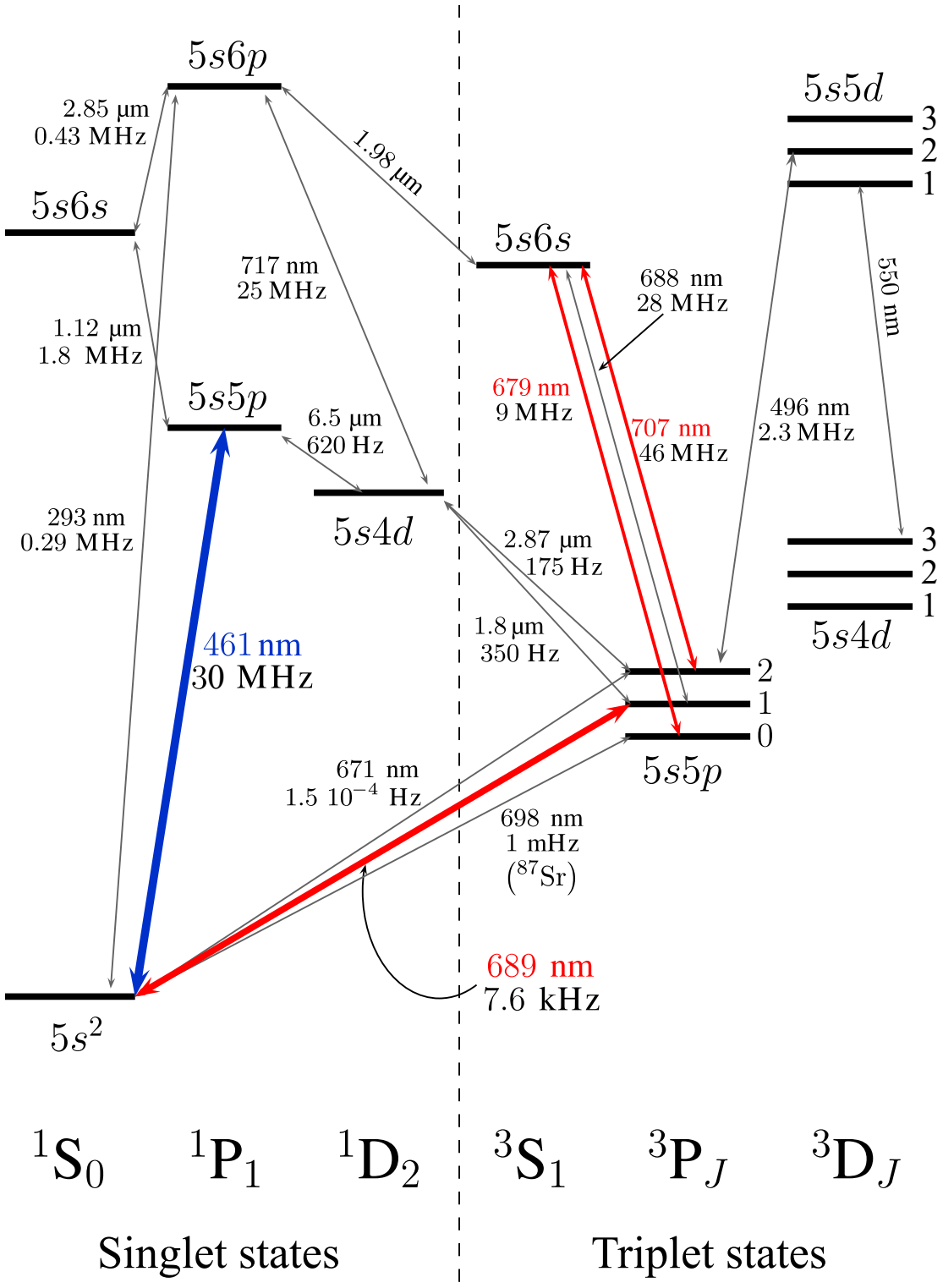

Figure 2.8: ^{88}Sr energy levels

Chapter 3

Building the experimental apparatus

In this chapter, the main building blocks of our experimental apparatus are presented and explained in detail. In Sec.3.1 and Sec.3.2, we present the mechanical design and main vacuum features of our system discussing the experimental steps adopted to generate a high vacuum environment needed for the atomic clock operation. In Sec.3.3 we present the hardware of the electronic experimental control implemented discussing its features. In Sec.3.4 we show the optical setup and the experimental laser stabilization technique of the blue light source to the $^1S_0 - ^1P_1$ atomic transition. In Sec.3.5 and 3.6 we show the design and the simulation of the magnetic systems employed for the 2D-MOT trapping and for the MOT trapping and their related experimental characterizations. In Sec.3.7 we discuss the opto-mechanical design and the experimental characterizations of our home-made laser sources that will address the second cooling stage and the repumping transitions while in the Sec.3.8 we show the preliminary results obtained with our home-made clock laser source and we discuss the laser stabilization method that we will implement. Finally, in the Sec.3.9 we discuss the future implementation of the three colors cavity for the multi-wavelength stabilization.

3.1 General description of atomic source

A schematic drawing of our apparatus is shown in Fig.3.1 and it is also described in [148]. The atomic source employs a novel design based on *two dimensional magnetic optical trapping* (2D-MOT). Atomic source is composed by the oven, that generate the atomic thermal beam, and multi ports vacuum chamber that provides optical access to cool and trap the thermal atomic beam into a 2D-MOT. The magnetic quadrupole of the 2D-MOT is generated by 4 stacks of permanent magnets. A similar atomic source design is already implemented in experiment with Li atoms,

[103], Na atoms [75, 104] and Sr atoms [107]. The push beam interaction with atoms in the 2D-MOT generates a cold atomic beam with a small radial velocity along the 2D-MOT plane and a longitudinal velocity optical controlled by the push beam intensity along the push direction. The cold atomic beam is send toward the science cell where it is trapped in the final MOT.

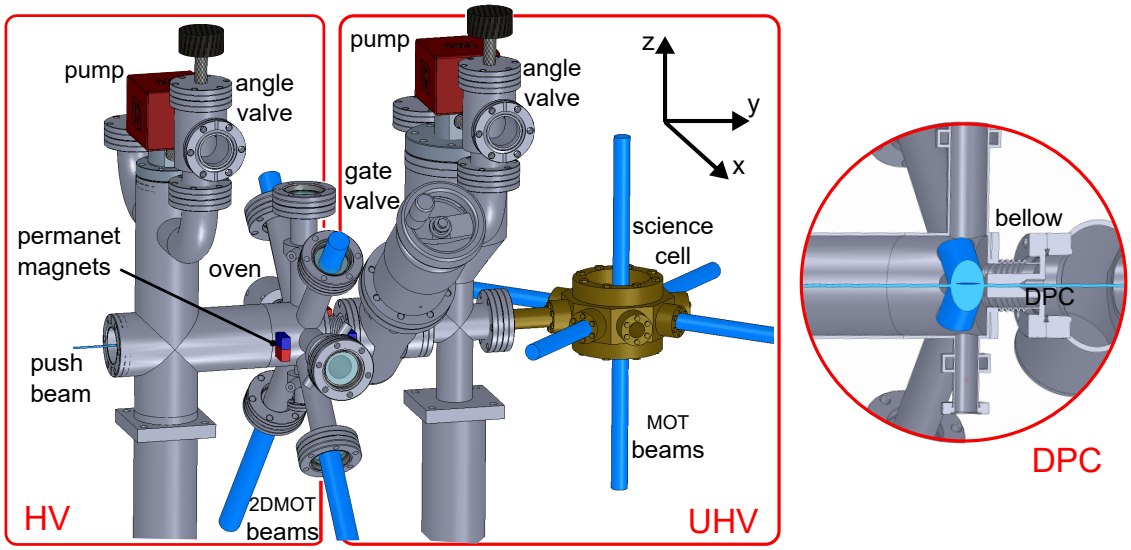

Figure 3.1: Vacuum system overview. Apparatus is divided in HV and UHV region. DPC connects the two regions. The size of entire vacuum apparatus are roughly 70 cm × 70 cm × 45 cm.

The atomic source based on the 2D-MOT ensures important advantages concerning our atomic clock application:

- the push beam offers the possibility to optical control the cold atomic flux of atoms that is accelerated from the 2D-MOT toward the MOT. In the absence of the push almost no MOT fluorescence signal is observed.
- With the presence of the push beam, the 2D-MOT acts as an atomic funnel [99, 149]. Starting with a thermal atomic beam, 2D-MOT and push beams generate a cold atomic beam with a divergence in principle limited by the Doppler temperature of 2D-MOT.
- From geometrical constraints, atoms emitted from the oven have little probability to pass directly in the science cell. This reduces the background of hot atoms in the MOT region.
- From metrological point of view, this transverse loading procedure will reduce the Black Body Radiation shift induced by oven [150, 151]. As the oven is not

in the line of sight of the UHV region and hence we can avoid the presence of mechanical shutter to screen the oven.

- The atomic source design offers the possibility to load simultaneously more atomic species on the same apparatus exploiting the remaining free ports.

3.2 Vacuum system

Collisions between trapped atoms and background gas limit the lifetime of the atomic sample in the optical lattice and can be a source of decoherence and frequency shift for the clock spectroscopy [57, 152]. For this reason, ultra-high vacuum is a demanding factor in an optical lattice clock. The vacuum apparatus has also to offer the possibility to generate a thermal atomic beam, generally by means of a heating process, and to provide the proper optical access to cool and trap atoms via laser cooling techniques.

3.2.1 Vacuum regions and pumping elements

Atomic source region and the science cell have different vacuum levels requirements. In the science cell an ultra-high vacuum levels is needed to efficiently trap the atoms in the optical lattice while in the atomic source region an ultra-high vacuum levels is not mandatory. For these reasons, vacuum system is divided in two main regions: the *high vacuum region* (HV) and the *ultra-high vacuum region* (UHV). The HV hosts the atomic source and the UHV hosts the science cell. A sketch of the vacuum regions and main vacuum elements is reported in Fig.3.1. On the top of both regions, two angle valves (Varian, VAT54132-GE02) are needed to evacuate separately the system by means of external pumping. Because of ultra-high vacuum requirement in the science cell, the UHV region is equipped with a vacuum pump with higher pumping speed compared to HV region. The pumping elements in HV and UHV regions are NexTorr D200 and NexTorr D500 pumps respectively. The NexTorr pumps integrate a *sputter ion pump* element (SIP) and a *non evaporative getter* element (NEG). NEG elements removes the active gas such as H_2, N_2 while the SIP element is effective with non reactive gas such as CH_4 and Ar. During the normal operation, oven reaches $T_{ov} = 460\,°C$ and background pressures of $P_{HV} \simeq 2 \times 10^{-9}\,$mbar and $P_{UHV} \simeq 10^{-10}\,$mbar are measured by pump drivers. Vacuum level of $10^{-10}\,$mbar is the minimum detectable pressures of our pump drivers. Pumps are also covered by µ-metal shield provided by the company in order to reduce possible strays magnetic field on the science chamber. The pumping speed performances for different gases are reported in Tab.3.1.

Differential pressure between HV and UHV is ensured by means of *differential pumping channel* (DPC) with diameter of $a_{DPC} = 2\,$mm and length of

		NexTorr D200	NexTorr D500
weight/Kg		2.2	3.1
volume/L		0.5	0.7
pumping speed / (L/s)	O_2	200	500
	H_2	200	500
	CO	140	340
	N_2	80	200
	CH_4	13	13
	Ar	6	6

Table 3.1: NexTorr encumbrance and pumping performances for different gas at room temperature. Pumping speeds are estimated after the NEG activation.

$L_{\mathrm{DPC}} = 22.8\,\mathrm{mm}$. In order to avoid mechanical strain and to correct any mechanical imperfection alignment of the DCP caused during the assembling, the HV region and the UHV are connected with a flexible bellow. As shown in Fig.3.1, the DPC can be manually closed by means of all-metal gate valve (Varian, VAT 48132-CE01). By closing the all-metal gate valve, the UH and UHV region are sealed respect to each others. The all-metal valve is particular useful if only one region needs to be vented. During the normal operation, the all-metal valve is open and differential pressure between the two region arise because of DPC conductance. Considering a molecular flow regime of N_2 at room temperature and in the long tube approximation ($a_{\mathrm{DPC}} \ll L_{\mathrm{DPC}}$), the DPC conductance can be estimated with the following formula:

$$C_{\mathrm{DPC}} = 12.2\frac{a_{\mathrm{DPC}}^3}{L_{\mathrm{DPC}}} = 4.3 \times 10^{-2}\,\mathrm{L/s} \tag{3.1}$$

where a_{DCP} and L_{DPC} are expressed in cm while C_{DPC} is given in L/s. At given C_{DPC} and pumping speeds $S_{\mathrm{UHV}}, S_{\mathrm{HV}}$ reported in Tab.3.1 for the N_2 gas, the maximum differential pressure sustainable by our system is estimated with flux equation:

$$P_{\mathrm{UHV}}S_{\mathrm{UHV}} = (P_{\mathrm{HV}} - P_{\mathrm{UHV}})C_{\mathrm{DPC}} \qquad \Longrightarrow \qquad \frac{P_{\mathrm{UHV}}}{P_{\mathrm{HV}}} \simeq \frac{C_{DPC}}{S_{\mathrm{UHV}}} = 2.1 \times 10^{-4} \tag{3.2}$$

The final relation of Eq.3.2 says that the influence of the atomic source pressure P_{HV} in the final MOT region P_{UHV} is negligible.

3.2.2 Vacuum materials

The main requirements for the vacuum materials are the low out-gassing rate, the possibility to sustain high temperature stress during the heating process, resistance to corrosion process, minimize eddy currents and reduce possible induced

local magnetizations in the apparatus. For these reasons, the stainless steel, aluminium and titanium materials are reasonable choices. For the out-gassing process, in particular for the hydrogen out-gassing, the stainless steel seems to have worst performances compared to the others materials enumerated [153] This is due to the hydrogen penetration process during the early phases of fabrication and production of the stainless steel. A common procedure to reduce the out-gassing of the stainless steel is to bake the entire system at temperature of 300 °C for a period of time greater than 1 day. Also the aluminium reduces the out-gassing rate by means of bake-out procedure but with lower temperatures of 100 °C and with the same amount of time. Although the stainless steel does not excel in propriety of out-gassing, it has a reasonable cost, it is simple to manufacturing and it is a material compatible with other common materials, such as copper, regarding the tightening among different vacuum flanges for vacuum applications. Considering that the atomic source region has not a severe limitation form the vacuum point of view, we decided to produce the atomic source apparatus with stainless steel alloy (AISI-304) while we temporarily use a stainless steel cell for the UHV region. Because of the high level of vacuum required in the science cell region and the possibility to reduce possible local magnetizations, we are studying and planning to substitution of the stainless steel cell with a titanium cell.

To ensure high vacuum quality, the *conflat* (CF) flanges connections are used and all vacuum components are connected with copper gaskets. Close to the oven, high temperature tolerance is the most important requirement. The oven is mounted to HV region by means of CF of 16 mm of aperture (DN16CF) with a nickel gasket which seals the system at higher temperatures ($\sim 600\,^{\circ}$C) respect to the copper gasket. On the top of the oven, capillaries array is placed in order to generate a collimated thermal atomic beam. The capillaries made out of the high temperature tolerance and chemical stable compound $Ni_{65}Cu_{33}Fe_2$ (GoodFellow, Monel-400).

The glass of the vacuum viewports are made of BK7-silica and they are commercially available and compatible with the CF connections. In the atomic source, the windows of the viewports are treated with anti-reflecting coating for the 461 nm radiation. As depicted in Fig.3.1, optical windows with diameter of 32 mm (DN40CF) are placed in the extremities of the 45° multi cross channels for the 2D-MOT beams optical access, along z-direction of the multi cross channel to observe the 2D-MOT fluorescence, and long the y-direction for the push optical access. The science cell is equipped with 7 vacuum viewports with diameter of 16 mm (DN16CF) and with 2 optical windows with diameter of 64 mm (DN63CF). The optical windows in the science cell are employed for the MOT beam optical access and for the fluorescence detection as it will be described in Sec.3.6.2.

3.2.3 Production of a collimated thermal atomic beam

The oven and heating elements

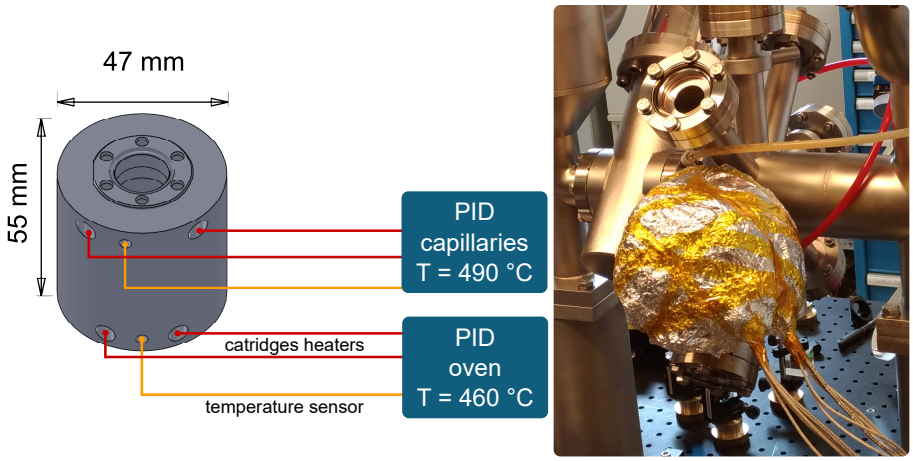

Figure 3.2: Oven heating. On the left side, schematic heating elements of the oven are shown. On the right side, final insulation of the oven from external environment is shown

As schematically shown in Fig.3.2, the oven is a stainless steel hollow cylinder with 47 mm of external diameter, 55 mm of height and internal aperture diameter of 16 mm. Two external pairs of heaters cartridges and K-type thermocouple sensors are inserted in the oven in suitable external mechanical access as shown in the Fig.3.2. Thermocouple sensor and heater cartridges are connected to two industrial PIDs which provide the temperature stabilization of different parts of the oven. The oven is filled with almost 4 g of granular Sr (Sigma-Aldrich, 460346-5G). The evaporation of Sr atoms are induced by means of heaters cartridges placed on the bottom of the oven. Vapour generated is then collimated by mean of capillaries array. Capillaries are held inside a custom holder which is placed in the aperture of the oven. In order to avoid capillaries clogging by Sr atoms, the top pairs of heaters cartridges maintain the capillaries array at higher temperature T_{cap} than vapour generation temperature T_{ov}. For all experimental characterizations we maintain a differential temperature $T_{\mathrm{cap}} - T_{\mathrm{ov}} = 30\,^{\circ}\mathrm{C}$. During the heating phase, each thermal heaters absorb up to 100 W of electric power. As shown on the left panel of Fig:(3.2), oven insulation is ensured by glass wool and covered by several layers of aluminium foils.

Capillaries array manufacturing

We employed 3 capillaries each of 1 m long, internal diameter of 0.4 mm and external diameter of 0.6 mm. We had tackled two main problems related to capillary array manufacturing. The first one was to find a method to cut the capillary tube

into shorter capillaries preserving the capillary hole. The second problem was to design a good capillaries holder that keep fixed and aligned the capillaries

With this small dimension of the tube, pliers cutting will obstruct the hole. We unsuccessfully tried to reduce the resilience of the capillary immersing the capillary into liquid nitrogen during the cut. The idea of this procedure was to favour the breaking of the object without obstructing the capillary hole structure. Unfortunately, following this procedure we simply obtained the bending of the capillary. Even if we are aware about non mechanical cutting processing such as wire-cut electrical discharge machining (EDM), we obtained a satisfactory result with a cheaper home-made procedure.

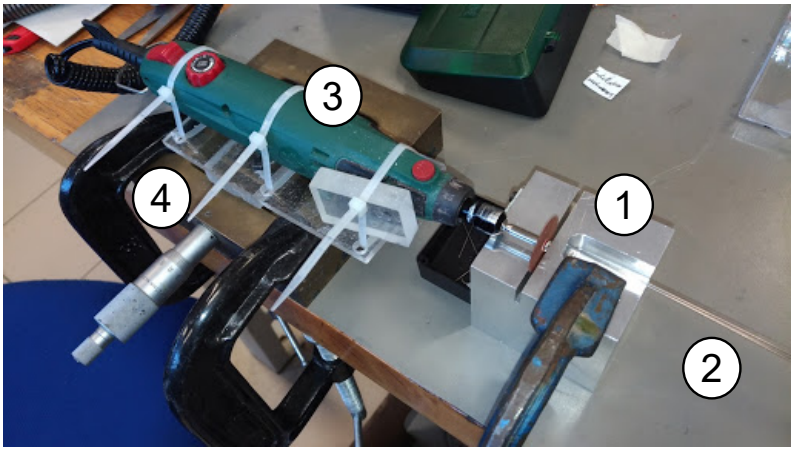

Figure 3.3: Cutting procedure of the capillaries. Elements enumerated are (1) capillary holder, (2) capillary tube, (3) rotatory saw and (4) micro-metric translating steps.

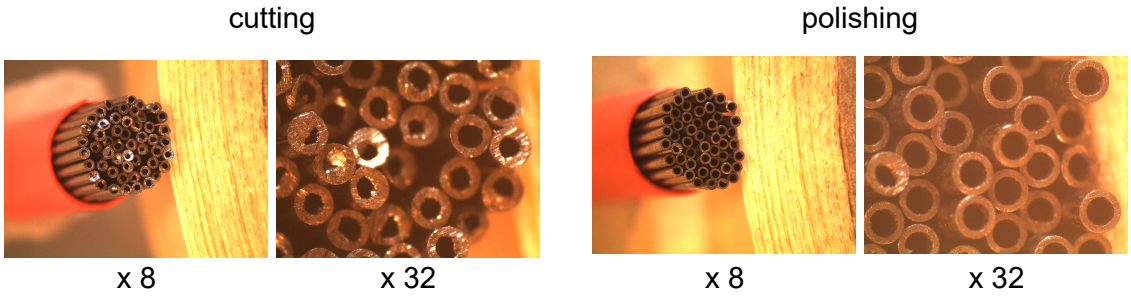

Figure 3.4: Comparison between the capillaries surfaces at different magnification before (left columns) and after (right columns) the polishing procedure.

In Fig.3.3, our home-made cutting procedure is shown: the single capillary tube (2) is inserted inside a custom holder (1) that set the maximum capillary length

Figure 3.5: Final result: capillaries are stuck and aligned inside a cylindrical custom holder compatible with the oven aperture

and offer the possibility to transversally saw the capillary by a generic rotary saw (3) and keeping the capillary tube fixed during the sawing procedure. The rotary saw is mounted on the top of a micro-metric translating stage (4) that transversally moves the rotary saw blade and tunes the velocity of the sawing procedure. On the left columns of Fig.3.4 , pictures of the capillary surface is shown after the cutting procedure. Each capillary tube is cut in several capillaries of 20 mm length, then their end surfaces were polished to remove imperfections by means of extra-fine abrasive sheet. Polishing was performed in a water environment in order to avoid mechanical deformation induced by heating. Remaining polishing scraps inside the capillary were removed by compressed air jets. From right columns of Fig.3.4 it is possible to appreciate the improvement in the quality of the capillary surfaces after the polishing procedure. Fig.3.5 shows the final result: stainless steel holder compliant with the oven design hosts an aligned capillaries array. The capillary holder has an external diameter of 15.8 mm, internal aperture diameter of 8 mm and 12 mm of length. A mechanical insert of 17 mm of diameter and 0.2 mm of length allows the holder to lay on the top of the oven aperture without obstructing during the CF clamping. Because the capillaries are simply stuck inside the holder, we decided to mount the oven along the horizontal direction as shown in the right panel of Fig.3.2. This shrewdness is made to prevent the capillaries falling by gravity.

From the central view of Fig.3.5, it is possible to count almost 150 capillaries and 50 interstices with the capillary diameter dimension. As show in the Fig.3.5, even if the capillaries array is regular and well oriented in the center of the cylindrical holder, it become irregular close to the edge increasing the number of large interstices an slightly misaligned the capillaries orientation. As explained in [154], a triangle or hexagonal geometry of the capillaries holder reduces both the dimensions and the number of interstices and keeps better aligned the capillaries array. Even if the the cylindrical geometry of capillary holder is not the ideal one, it remains

the simplest and fastest manufacturing solution.

3.2.4 Bake-out procedure and pumps activation

The slow out-gassing of impurities present on vacuum components is one of the limiting factor to reach the high vacuum regime. The bake-out procedure consists of enhancing the desorption rate of materials by increasing the temperature of the vacuum components by means of external heating [155]. As a consequence, the pumping time needed to bring a system from the atmospherics pressure to the high vacuum regime, in our case below the 10^{-10} mbar is reduced. Volatile compounds generated during the bake-out are removed by mean of external pumping system. The most common volatile compound removed by the vacuum bake out procedure is the water present in the air that condense in the vacuum components [156]. At ultra high vacuum pressure, the hydrogen out-gassing present inside the steel is the limiting factor [157].

Before assembly the vacuum system, all the vacuum components were carefully cleaned. Using grease-free gloves and optical sheets soaked with acetone, impurities left from components manufacturing were removed. Small vacuum pieces were cleaned using an ultrasonic bath in acetone. The vacuum chamber was assembled after the components were cleaned. In the first assembly, Sr-stone, capillary holder and science cell were not mounted in the vacuum system.

The entire vacuum bake-out procedure is reported in Fig.3.6. First, the apparatus was evacuated connecting the turbo pump (Varian, TPS mobile) through the angle valves reported in Fig.3.1. At this stage, pressure level inside the vacuum chamber was measured by vacuum gauge of turbo pump. At the pressure level of 10^{-7} mbar, we started the bake-out procedure. The heating of the vacuum chamber was made externally by means of heating bands connected to auto-transformers. Each vacuum part was winded up with the heating bands and thermocouples were placed in order to monitor local temperatures of the critical components. All the apparatus was thermally insulated from room environment by means of several aluminium foils layers. By measuring the voltage drop of each bands and monitoring the associated vacuum components temperatures we constantly increased the temperature of vacuum system. In the regions where optical windows were present, we increased the vacuum system temperature with a rate temperature below 20 °C/h. This precaution was taken because the silica and the stainless steel have different thermal expansion coefficient, in this way the different materials of windows flange respond homogeneously to thermal stress avoiding a possible window breaking. Close to the NexTorrs pumps, we kept temperature below 300 °C in order to avoid possible demagnetization of SIP magnets. The entire vacuum system was kept at average temperature of 170 °C during 3 days. Before finish the bake-out

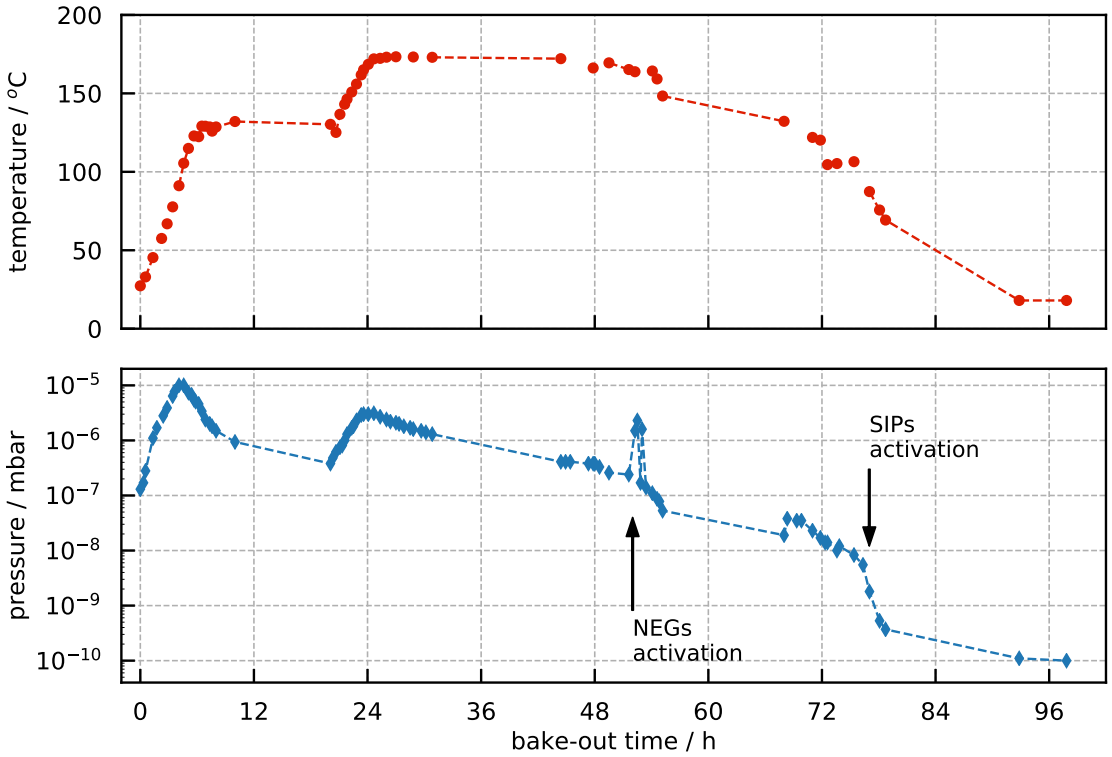

Figure 3.6: Bake-out procedure. On the top panel, the average temperature of the vacuum system during the bake-out procedure. The average temperature is computed considering all temperatures measured with thermocouples. On the bottom panel, the average pressure level measured inside the vacuum system.

procedure, NEGs elements were activated at 500 °C during 1 h by means of internal heating component of the pumps. After the NEGs activation, the SIP elements were switched on and off repetitively causing the SIP degassing. At the end of the bake-out procedure when the average temperature was below the 100 °C, the SIPs element were switched on and the angle valves were closed sealing the vacuum chamber from exterior. With this procedure we were able to reach the 10^{-10} mbar of vacuum pressure both in the HV and UHV regions.

Sr activation

Once reached the target vacuum level, we started the procedure for the Sr activation. We closed the all-metal valve sealing the UHV and we vented the HV region. After loaded the oven with 4 g of granular strontium we put the capillary holder on oven aperture and then we connected them to the vacuum chamber using the DN16CF vacuum connection. This assembly operation was made in a inert gas

(Ar) environment by means of a glove-bag. We repeated the bake-out procedure only for the HV region procedure. Before the final NEGs activation, we increased the oven and capillary region temperature at 520 °C for 1 h in order to remove the possible formation of oxide layer on the surface of Sr sample. After this procedure, we set the $T_{ov} = 460°$ and the atomic flux is detected by means of laser fluorescence. This is a clear indication that Sr vapour was successfully produced.

Bake-out of the cell

The only remaining component to assembly was the science cell. In the Fig.3.7, the assembly phases of the cell are shown. After cleaning the bulk cell, we decided to perform an air baking at 350 °C during 1 day using an external oven. Air baking is another common strategy that reduce the hydrogen out-gassing from the steel walls [158]. After the air baking, science cell appears brass-like as shown in the Fig.3.7(b). We closed the all-metal valve sealing the HV and we vented the UHV region. As shown in the Fig.3.7(c), the octagon cell was mounted to the vacuum chamber and prepared for the bake-out procedure. For the presence of a lot of windows element, the bake-out procedure for the science cell was made at lower temperatures 100 °C for 3 days.

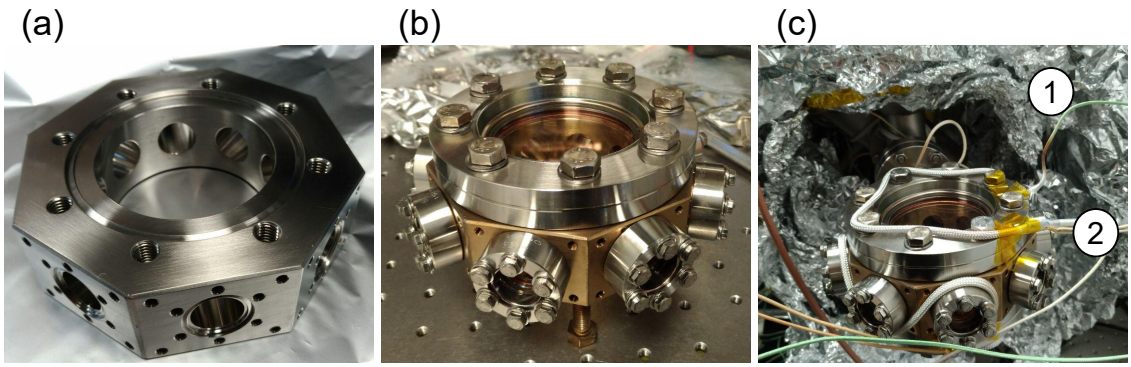

Figure 3.7: Science cell with octagon geometry and its assembly procedure to the vacuum chamber. **(a)** Bulk cell before the air baking **(b)** Bulk cell after air bake-out with mounted optical accesses. **(c)** Science prepared for the final bake-out. In the figure some elements of the bake-out process are shown: (1) temperature sensor and (2) heating band

3.2.5 Expected atomic flux

In this section we estimate the atomic flux generated from the oven considering the atomic beam collimation properties and geometrical constraints imposed

by the capillaries. Geometrical constraints induced by capillaries set a maximum atomic beam divergence. Maximum geometrical divergence θ_{cap} and solid angle Ω_{cap} admitted with capillaries is estimated as:

$$\theta_{\text{cap}} = \arctan\left(\frac{a_{\text{cap}}}{L_{\text{cap}}}\right) = 20\,\text{mrad} \qquad \Omega_{\text{cap}} = \frac{\pi a_{\text{cap}}^2}{L_{\text{cap}}^2} = 1.25 \times 10^{-3}\,\text{sr} \tag{3.3}$$

where $a_{\text{cap}} = 0.4\,\text{mm}$ is the internal capillaries diameter and $L_{\text{cap}} = 20\,\text{mm}$ is the capillaries length . The longitudinal velocity distribution in the thermal atomic beam is generally described by [12]:

$$f(v_L) = \frac{v_L^3}{2v_{th}^4}\exp\left(-\frac{v_L^2}{2v_{th}^2}\right) \tag{3.4}$$

where $v_{th} = \sqrt{k_B T_{\text{ov}}/m_{\text{Sr}}}$. For a given longitudinal velocity v_L, an upper limit in the transverse direction v_T is set by $v_T = v_L \tan\theta_{\text{cap}}$. The distance between the oven aperture and the center of the 2D-MOT is $d = 128\,\text{mm}$. From all these considerations it is possible to estimate the thermal atomic beam width.

Adding the capillaries, two new length scales have to be considered: the capillary aperture a_{cap} and the capillary length L_{cap}. Comparing these length scales with the Sr-Sr mean free path inside the oven λ_{ov}, we can enumerate two possible regimes [159, 160] :

- if $a_{\text{cap}} < L_{\text{cap}} < \lambda_{\text{ov}}$ the presence of the capillaries does not affect the atomic flux and the atomic collision inside the capillary are unlikely. In this flow regime the capillary is considered "transparent" and the atomic flux emitted by capillaries is proportional to pressure inside the oven;
- if $a_{\text{cap}} < \lambda_{\text{ov}} < L_{\text{cap}}$ the presence of the capillaries affects the atomic flux and the atomic collision inside the capillary became more probable. In this flow regime the capillary is considered "opaque" and the atomic flux emitted by capillaries is no more proportional to pressure inside the oven.

Using the ideal gas law, we can predict the oven temperature value at which the atomic flux regime is perturbed by the presence of the capillaries. As a function of the oven temperature T_{ov}, the vapour pressure of solid Sr is estimated with the following equation [161]:

$$\log_{10} P_{\text{Sr}}(T_{\text{ov}}) = A + \frac{B}{T_{\text{ov}}} + C\log_{10} T_{\text{ov}} \tag{3.5}$$

where $A = 14.232$, $B = -8572\,\text{K}$ and $C = -1.1926$. P_{ov} is expressed in Pa and T_{ov} in K. At $T_{\text{ov}} = 460\,°\text{C}$ we get $P_{\text{Sr}}(T_{\text{ov}}) = 0.133\,\text{Pa}$. Considering Sr-Sr collisions as

hard sphere collisions, the atomic density and the mean free path can be estimated as:

$$n_{\mathrm{ov}} = \frac{P_{\mathrm{Sr}}(T_{\mathrm{ov}})}{k_B T_{\mathrm{ov}}} = 1.31 \times 10^{19}\,\mathrm{atoms/m^3} \tag{3.6}$$

$$\sigma_{\mathrm{Sr}} = \pi(2r_{\mathrm{Sr}})^2 = 7.85 \times 10^{-19}\,\mathrm{m^2} \tag{3.7}$$

$$\lambda_{\mathrm{ov}} = (\sqrt{2} n_{\mathrm{ov}} \sigma_{\mathrm{Sr}})^{-1} = 6.89 \times 10^{-2}\,\mathrm{m} \tag{3.8}$$

where $r_{\mathrm{Sr}} = 2.5 \times 10^{-10}\,\mathrm{m}$ is the estimated Sr Van der Waals atomic radius [162].

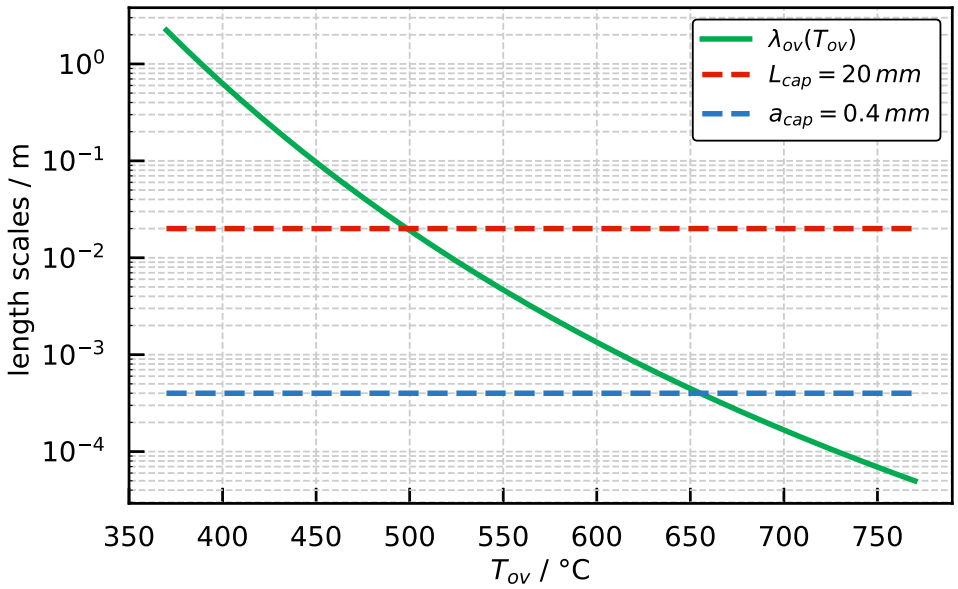

Figure 3.8: Comparison among atomic mean free path inside the oven λ_{ov} and capillary length scales $a_{\mathrm{cap}}, L_{\mathrm{cap}}$

The Fig.3.8 reports the mean free path λ_{ov} as a function of oven temperature computed according Eq.3.8. after the $T_{\mathrm{ov}} > 500\,^{\circ}\mathrm{C}$ the capillary is considered "opaque" and the collision events among Sr atoms start to be become probable along the capillary. According our estimations, at $T_{\mathrm{ov}} = 460\,^{\circ}\mathrm{C}$ capillaries are considered "transparent".

In the transparent regime is possible to give analytical estimation of atomic flux effused from the capillary [160]. At $T_{\mathrm{ov}} = 460\,^{\circ}\mathrm{C}$, atomic flux that enter in the 2D-MOT region is estimated according the following equation:

$$\Phi_{\mathrm{ov}} = a_{88} \frac{1}{4} n_{\mathrm{ov}} \bar{v} W S_{\mathrm{cap}} \tag{3.9}$$

$$= a_{88} n_{\mathrm{ov}} \bar{v} \frac{2\pi}{3} \frac{r_{\mathrm{cap}}^3}{L_{\mathrm{cap}}} N_{\mathrm{cap}} = 5.8 \times 10^{14}\,\mathrm{atoms/s} \tag{3.10}$$

where $a_{88} = 0.82$ is the isotope abundance of ^{88}Sr [116], $r_{\text{cap}} = 2 \times 10^{-4}\,\text{m}$ is the internal capillary radius, $L_{\text{cap}} = 2 \times 10^{-2}\,\text{m}$ is the capillary length, $W \simeq 8r_{\text{cap}}/3L_{\text{cap}} = 0.026$ is the Clausing factor which describes the transmission probability of atoms through a single long capillary in the long tube approximation ($L_{\text{cap}} \gg a_{\text{cap}}$), S_{cap} is the total surface described by the capillaries array computed as $S_{\text{cap}} = N_{\text{cap}}\pi r_{\text{cap}}^2 = 1.88 \times 10^{-5}\,\text{m}^2$ where N_{cap} is the number of capillaries and interstices of same capillary dimension ($N_{\text{cap}} \simeq 150$) and $\bar{v}$ is the mean velocity of the atoms inside the oven given by $\bar{v} = \sqrt{8k_B T_{\text{ov}}/\pi m_{\text{Sr}}} = 427\,\text{m/s}$.

3.3 Experiment control system

Atomic optical clock and in general many atomic physics experiments need a precise timing sequence for the production and sampling of the cold atomic sample. In our experiment we use the digital control system and related firmware designed by Prof. Marco Prevedelli. Fig.3.9 depicts the simplified diagram of the experimental control system. The heart of this experimental control is the motherboard equipped with a FPGA (Xilinx, Spartan XC3S250E) clocked at 10 MHz with a peak to peak voltage $V_{\text{pp}} = 5\,\text{V}$ sine wave. Motherboard and slave-boards are connected via 32-bit bus channel. Via PC, the user can set the the slave-boards state and their timing sequentially in a tabular form thanks to a dedicated Python software [163]. The software also converts instructions into a bit-stream file readable from the motherboard via USB serial connection. At specific timimg set by the user, the motherboard sends the instructions to slave-boards via 24-bit bus. Bus communication via motherboard and slave boards has the following convention: 1-bit is used as strobe pulse, 7-bit for the slave-board address and 16-bit define the state of slave-board. Each slave-boards are uniquely identified by 7-bit address, each board is allowed to read only its own instruction and its state is updated synchronously with a 1-bit strobe pulse for precise timing. The minimum timing between two consecutive instructions sustained by FPGA is 500 ns with a maximum instruction rate of 2.5 MHz. Motherboard and slave-boards are voltage supplied by $\pm 15\,\text{V}$ and $+5\,\text{V}$ provided by DC power supply, the voltage is distributed along the bus-channel using extra bus bits.

In our experiment control, three kinds of slave-board are identified:

- **Digital-board:** Each board can provide 16 logical (TTL 5 V) output channels. Each 16 bits are simply buffered by 74HC374 integrated circuit. Digital outputs of this board is used for fast operations such as trigger events,
- **Analog-board:** Each board contains 2 specific addresses and can provide 2 analogic signals ranging from -10 V to +10 V. Analogic signal is generated

from 16-bit parallel DAC712. This board is used to drive the current generator for the MOT and compensation coils.

- **DDS-board:** Each board can generate 2 *radio frequency* signals (RF) ranging from 200 kHz to 140 MHz. The output power of channels can reach +13 dBm. The RF signal is generated by AD9958 chip based on a 10 bit DAC. This board has the possibility to be externally clocked up to 500 MHz. With an external amplification stage, RFs provided by these boards are used to frequency and power drive the acoustic-optic modulators. Considering the time of the generated RF signal by the DDS and the FPGA command time of the board, the board has a fixed programming delay time of 33 µs.

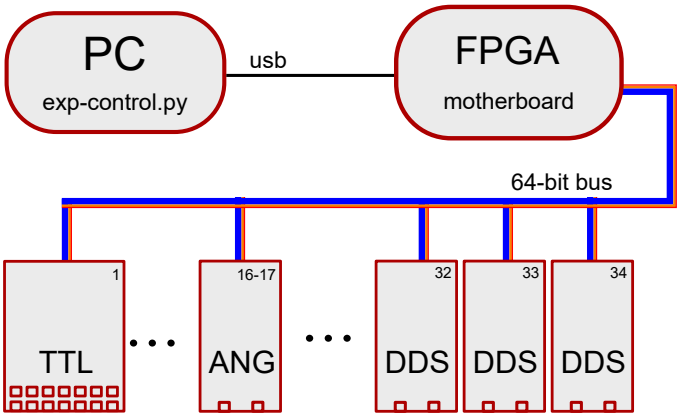

Figure 3.9: Simplified diagram of the experimental control system.

3.4 Blue laser light: Optical setup

The $^1S_0 - ^1P_1$ atomic transition of Sr is used for the first cooling stage. This atomic transition has a wavelength of $\lambda = 460.861\,\text{nm}$, linewidth of $\Gamma = 2\pi \times 30.5\,\text{MHz}$ and saturation intensity of $I_0 = 41\,\text{mW/cm}^2$. In this section, the blue optical set-up and laser stabilization to the atomic resonance are explained in detail.

Blue laser source

We bought a commercial laser system (LEOSolution) as laser source of the λ =460.861 nm. This system is made by an infrared laser source module and a *second harmonic generation* (SHG) system. The infrared laser is composed by master laser source and an infrared *tapered amplifier* (TA). The master is an *external cavity diode laser* (ECDL) in cateye configuration and an internal interference-filter for wavelength selection [164]. At master temperature of 19 °C and current injection of

97 mA we were able to reach the wavelength emission of 921.725 nm. The system has the possibility to extract a small portion of infrared light generated. We usually send this infrared light to a wavelength-meter in order direct to control the lower wavelength. At amplifier's temperature of 18.3 °C and injection current of 3.3 A, the system generates 1.7 W of infrared optical power. Infrared red light is coupled to a second harmonic generation cavity which converts the infrared light into visible light close to the Sr atomic transition. The non linear optical conversion is made by LBO crystal. Calibration curves of TA infrared laser power generated and SHG output power are reported on Fig.3.10 The system is able to generate up to 600 mW of blu optical power with LBO crystal temperature of 39.5 °C. In Fig.3.10, the power conversion between infrared light to blue light is around 35 %.

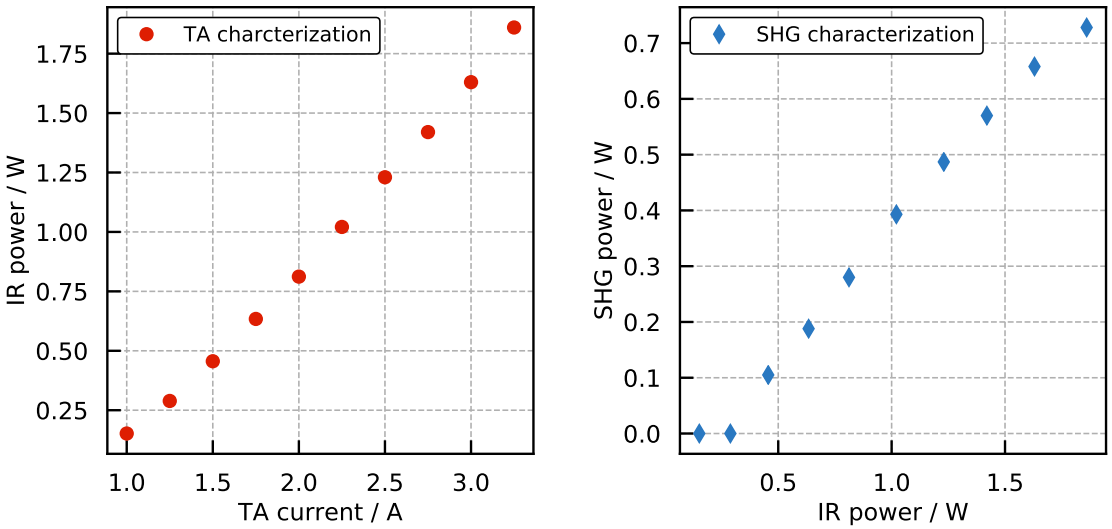

Figure 3.10: Blue laser source characterization

Optical bench

In order to cool and trap the Sr atoms, the blue light has to be properly frequency tuned and polarization controlled. The *acoustic-optic modulator* (AOM) is the main tool used for the frequency manipulation of the light. Our AOM (Gooch & Housego) use the RF signals to shift the light frequency in the MHz regime. RF is generated and controlled by a DDS board. In order to match the injection RF power requirement of AOM, RF amplifiers up to +30 dBm are usually employed. At RF frequency higher that 140 MHz, RF duplication stages are also employed (Minicircuits). Blue light polarization is controlled via polarizing beam splitters (Solid, PBS), $\pi/4$ retarding waveplates (Solid, $\lambda/4$) and $\pi/2$ retarding waveplates (Solid, $\lambda/2$).

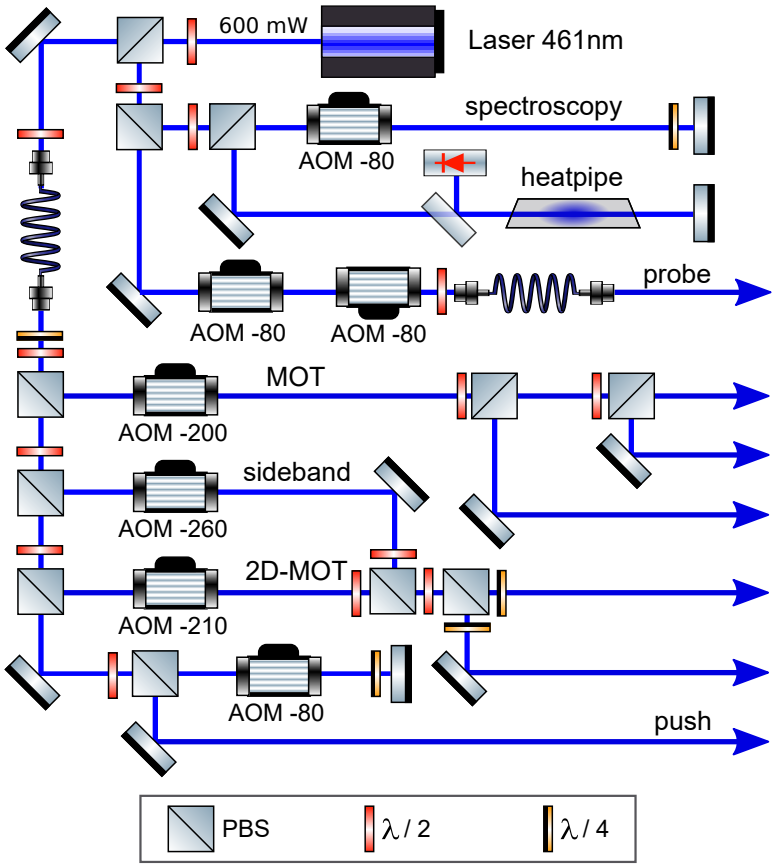

Figure 3.11: Blue optical setup. Beam shaping lenses are omitted

	f_{AOM}/MHz	η_{AOM}/%	Power/mW	waist/mm	s	Δ/Γ
spectroscopy	-80†	50	0.5	0.37	0.11	0.0
2D-MOT	-210	78	100	9.50	3.28*	-1.6
sideband	-260	84	100	9.50	3.28*	-3.13
push	-80†	50	0.15	0.81	0.34	0.0
MOT	-200	85	45	6.20	2.49*	-1.2
probe	-80,-80	76,87	0.5	0.83	1.07	0.0

Table 3.2: Optical parameters. AOMs frequencies and related efficiency are reported in the first and second column respectively. The third column reports the optical power after the AOMs. The others columns report optical beam e^{-2} radius, saturation parameters and the detunings of the optical beam interacting with the Sr atoms. Output power of the blue laser source is about 600 mW. (†) AOMs are considered in double-pass configuration. (*) The calculation of saturation intensity is performed considering the retro-reflected contribution. For the MOT beam, the windows trasmittivity $T_{\mathrm{w}} = 80\,\%$ is considered.

Fig.3.11 and Tab.3.2 report our optical set-up. Blue light is generated by laser system described before and then it is split in two optical paths with a PBS. Almost of all blue power is fiber injected in a singlemode optical fiber (OZ Optics, QSMJ-3S3S-400-3/125-3-5) with 73 % efficiency. The output light is then distributed in different optical path as shown in the Fig.3.11. A large component of the reflected beam is used to generate the probe beam with AOMs in cascade configuration. The probe beam is then fiber coupled in a single mode polarizing optical fiber (Schafter + Kirchhoff, PCM-E-460Si) with efficiency of 35 %. The small part of the reflected component is sent through a heatpipe (spectroscopy cell) where the laser source is frequency stabilized on the Sr atomic transition $^1S_0 - {}^1P_1$. A detailed description of this method and its experimental implementation is given in Sec.3.4.1. As shown in the Fig.3.11 and Tab.3.2, we reach the resonance condition ν_{eg} for a given laser frequency ν_L by shifting the laser frequency with the spectroscopy AOM. The final relation can be written as:

$$\nu_{eg} = \nu_L + f_{\mathrm{AOM}}^{\mathrm{spec}} \tag{3.11}$$

where ν_{eg} is the resonant optical transition $^1S_0 - {}^1P_1$ of ^{88}Sr and $f_{\mathrm{AOM}}^{\mathrm{spec}} = -160\,\mathrm{MHz}$ is the RF shift of the spectroscopy AOM. In this way, the distributed laser light ν_L is not on resonant with the $^1S_0 - {}^1P_1$ transition and red detuned frequency shift needed for the laser cooling process can be reached by a single pass AOMs with negative RF but with higher absolute RF compare to $f_{\mathrm{AOM}}^{\mathrm{spec}}$. This is useful for our sideband optical path and in other experiments where a higher detuned Zeeman slower beam is usually employed. The sideband beam is combined with the 2D-MOT beam as shown Fig.3.11.

3.4.1 Laser stabilization to $^1S_0 - {}^1P_1$ transition of ^{88}Sr

Dealing with the laser cooling and trapping experiments, the frequency stabilization of the laser source is a necessary step. The high melting point of Sr (∼777 °C) imposes the use of dedicated heatpipe (spectroscopy cell) [165], or a direct spectroscopy on the atomic beam [166]. Locking the laser source to an external passive cavity [167, 168] or using a high-accuracy wavelength meter are also possible [169]. Our approach was to rapidly stabilize the blue laser source using spare heatpipe components already present in the laboratory and tackle in the future a general and definitive multi-lasers stabilization method. The next generation laser stabilization will be discussed in Sec.3.9.

In our experiment, the laser stabilization is performed by *wavelength modulation saturation spectroscopy* (WMSS) technique. This technique is composed by two parts: the *saturation spectroscopy* (SS) [170–172], which gives us an absorption signal with linewidth close to the natural linewidth of the atomic transition, and the *wavelength modulation* (WM) [173, 174], an experimental technique that generates the error signal for the laser stabilization extrapolating the derivative of the

absorption signal.

Wavelength Modulated Saturation Spectroscopy

The working principle of SS can be found in reference [80]. A counter-propagating beam is send through the heatpipe, the propagating beam is called pump and the counter-propagating one is called probe. The absorption coefficient is extracted from the optical beam which passes twice thorough spectroscopy cell (probe beam). If the laser light is detuned from the resonance of the blue strontium transition, the pump and the probe beam interact with atoms having different longitudinal velocity class inside the spectroscopy cell. In this case, the extracted absorption coefficient of the probe beam will be affected by Doppler broadening. If the laser light is on resonance, the probe and the pump beams interact with atoms that have zero velocity along the direction of the pump and probe beams. In this case, the probe beam is less absorbed because the pump beam has already exited the majority part of the atoms. Scanning the frequency of the blue laser by master's piezo tuning, is possible to observe a dip in the absorption profile with a linewidth close to the natural linewidth of the atom transition probed. An example trace of the absorption dip is shown in top panel of Fig.3.14.

Due to a parity symmetry of the trace reported in the top panel of Fig.3.14, the laser source can not be stabilized at the center of the absorption dip profile. If lasers frequency drifts from the dip center, no information of the direction of connection can be obtained and consequently it is not possible to apply a correct feedback to master's piezo. On the other hand, its derivative carries on this feedback information. The derivative of the absorption profile is extracted using WM technique for the probe beam. Introducing the WM modulation in the pump and probe beam, their instantaneous wavelength $\lambda(t)$, and so their instantaneous frequencies $\omega(t)$, can be written as:

$$\omega(t) = \omega_0 + \Omega \sin(\omega_m t) \tag{3.12}$$

where ω_0 is the carrier frequency, Ω is the modulation depth, ω_m is the modulation frequency. In the Fourier space, the modulation described by Eq.3.12 generates sibebands in the probe beam intensity at $\omega_0 \pm \omega_m, \omega_0 \pm 2\omega_m, ...$ with carrier frequency ω_0. Following the calculations described on [174], it is possible to demonstrate that the intensity of the signal I oscillating at frequency ω_m is proportional to:

$$I \sim \Omega \frac{da}{d\omega} \tag{3.13}$$

where $a(\omega)$ is the absorption profile. By demodulating the probe signal at ω_m and apply a low pass filter is possible to reconstruct the derivative of the absorption profile. The choice of the low pass filter time constant has to maximize the signal to noise ratio. During the absorption process, the probe beam acquires also a phase

ϕ with respect to the generated WF signal. During the demodulation process, this acquired phase reduces the extracted signal of component ω_m. This problem can be solved using a phase shifter which compensate the phase mismatch ϕ maximizing the demodulated signal.

The heatpipe

In Fig.3.12(a), the main components of the heatpipe are shown. Bulk material of the heatpipe is stainless steel tube with CF40 flange of the edges. Windows of the cell (Thorlabs, WG12012) are glued to stainless steel tube with CF flange. These supports are cut at the Brewster angle, with this shrewdness and a proper polarization alignment, it is possible to extinguish windows optical reflection of the blue light. Windows are glued to the stainless stell support by an epoxy glue (BI-PAX, BA-2143D). The Sr vapour is generated by means of heater cartridges. The hardware for the heating and for the stabilization temperature is the same as the one of the oven in Sec.3.2.3. The tube is designed with a small lateral connection used for evacuation. A brass valve (Swagelock) gives access for external pumping and gas filling.

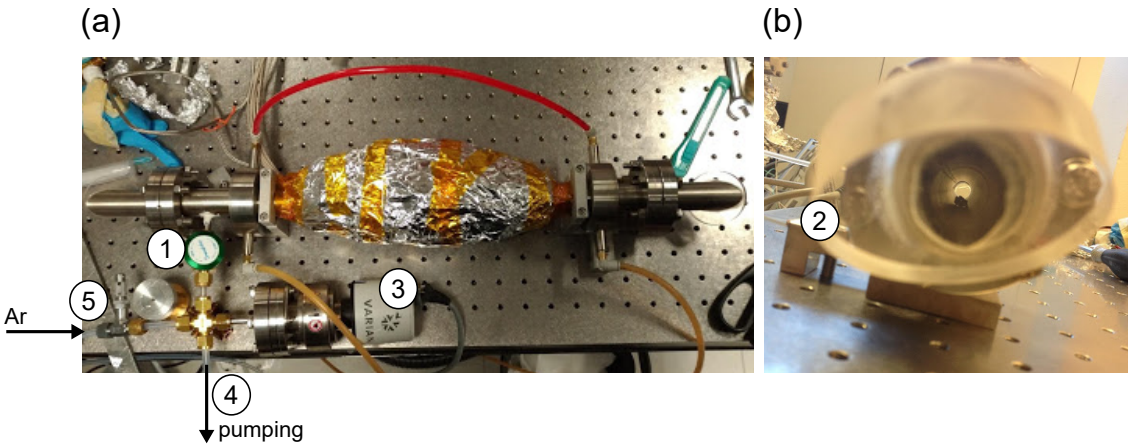

Figure 3.12: Spectorscopy cell. **(a)** Experimental setup for the optimum buffer gas pressure tuning. The figure depicts a brassed valve (1), a pressure gauge sensor (3), the external pumping system (4) and the valve for the buffer gas flux regulation (5). **(b)** Heatpipe side view. The strontium chunk is visible inside the heatpipe.

The Sr metallic chunk is loaded inside the heatpipe with the following procedure. As show in the Fig.3.12(a), we connected on the brass valve (1) a cross junction in order to: measure the local pressure by means of gauge valve (3), evacuate the heatpipe by external turbo-molecular pump (4) and flush some inert Ar gas inside the heatpipe with a proper valve (5). After testing the vacuum seal of the system, we loaded Sr chunk in inert Ar gas environment by means of a glove-bag. In

Fig.3.12(b), is possible to observe 3 g of Sr chunk loaded inside the heapipe. Ar gas acts as a buffer gas reducing the Sr contamination on the spectroscopy windows. Pressure of the buffer gas was optimized in order to increase the signal to noise ratio of the absorption profile and reduce the linewidth of the spectroscopy dip. In the final configuration of P_{Ar}=1 mbar we observe an absorption profile level of 80 % and a dip height of 6 % relative to the absorption profile.

Experimental setup and spectroscopy signal

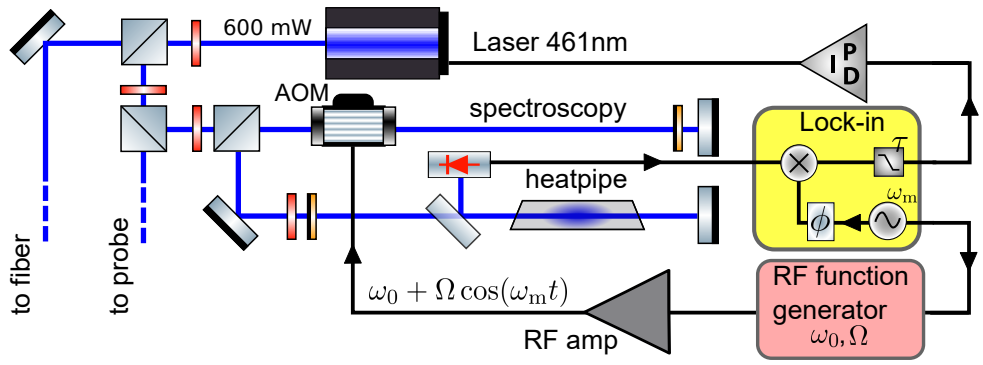

Figure 3.13: Experimental setup of WMSS

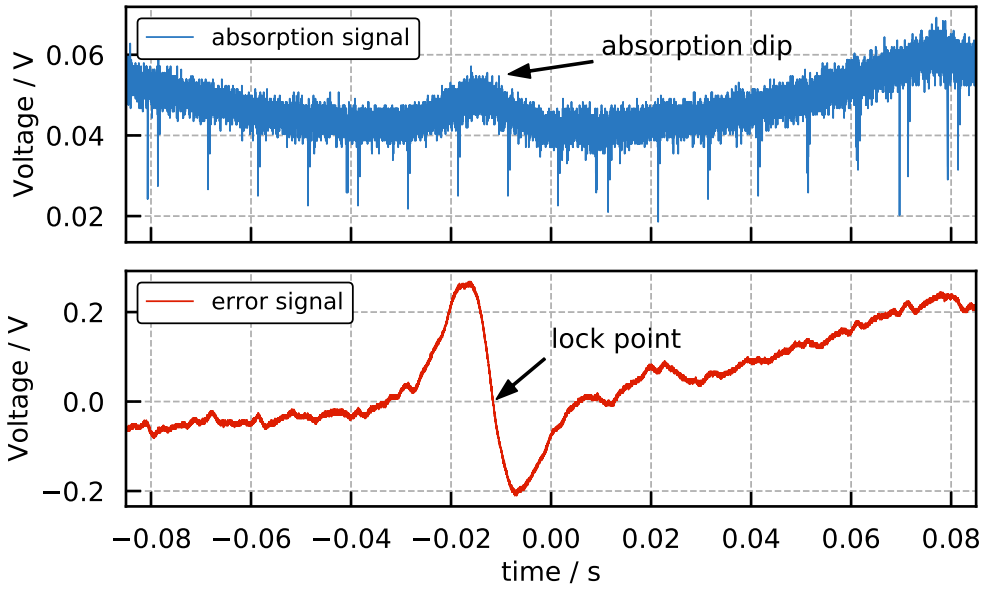

Figure 3.14: Spectroscopy signals obtained with master's piezo sweep. Blue line reports the absroption profile dib obtained with SS method. Red line report the error signal extracted by WM procedure

Demodulation, filter process and phase shifter can be achieved with a lock-in amplifier. The optical and electronic experimental setup for the WMSS is reported in Fig.3.13 A double pass AOM configuration is used to introduce the WM via the first diffraction order of the blue laser. The WM is generated by a frequency synthesizer (Siglent, SDG2122X), the carrier frequency of the AOM was set to $\omega_0 = 2\pi \times 80\,\mathrm{MHz}$ and the modulation depth $\Omega = 2\pi \times 6\,\mathrm{MHz}$. A beam sampler sends the probe light to a Photodiode (Thorlabs, PDA10A-EC). The modulation frequency was generated by the lock-in amplifier (Signal Recovery, 7265) at $\omega_\mathrm{m} = 2\pi \times 77.447\,\mathrm{kHz}$. This value is chosen considering the low frequency noise components of photodiode spectrum. We also choose a prime number of the modulation in order to avoid any higher harmonic coupling of noise spectrum peaks. After the lock-in amplifier demodulation, the error signal shown in the Fig.3.14 is obtained. The time constant of the low pass filter of the lock-in in was set at $\tau = 600\,\mu\mathrm{s}$. The lock-in phase ϕ is set in order to eliminate the in-quadrature component of ω_m maximizing the extracted feedback signal. The experimental strategy to do so consist in finding the phase ϕ that minimizes the error signal and then move to $\phi + \pi/2$ in order obtain best signal. Finally, a PID (SRS, SIM960) with only integrative gain $G_I = 1.1\,\mathrm{s}^{-1}$ that stabilizes the laser frequency using error signal generated from the WMSS technique.

3.5 Pre-cooling stage: Two dimensional magneto optical trapping

As already explained in Sec.3.2.1, the apparatus contains two vacuum regions, HV and UHV, connected by a short differential pumping channel. In the HV region, Sr thermal atomic flux is pre-cooled by means of transversally 2D-MOT loading. 2D-MOT region is defined by the intersection of two orthogonal pairs of counter-propagating beam e^{-2} radius of $\omega_{\text{2D-MOT}} = 9.5\,\mathrm{mm}$ and a maximum beam dimension of 2.5 cm limited by the aperture of most of the optical components. The magnetic field of the 2D-MOT is generated by 4 stacks of permanent magnets. The positions and orientations of the magnets and its induced magnetic field will be described in detail in Sec.3.5.1.

The 2D-MOT mechanical and optical assembly is shown in Fig.3.15. Cooling optical beams are sent from the bottom widows (1) of the atomic source and retro-reflected with a couple of mirrors and $\lambda/4$-waveplates (2) mounted on the lateral breadboard (3). Suitable 3D-printed supports (4) are designed in order to maintain a compact design. These supports are made by ABS-plastic material, they are designed to attach the $\lambda/4$ support to the vacuum system minimizing the total encumbrance. At a first attempt, supports for the retro-reflecting optics were design and implement. Due to heating induced by the close presence of the oven,

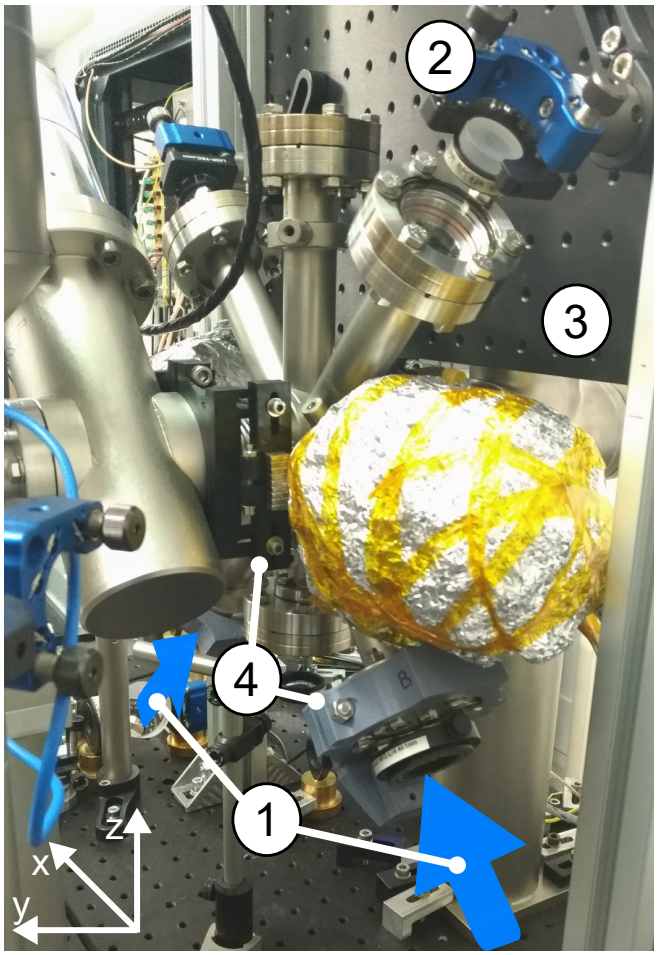

Figure 3.15: Mechanical assembly of the 2D-MOT. **(1)** Optical beams, **(2)** retro-reflecting mirror and $\lambda/4$-waveplates. **(3)** Lateral breadboard. **(4)** 3D-printer supports. Gray supports are waveplate holders. Black ones are a permanent magnet support.

instability on the MOT signal was observed during the day. An improvement in the MOT signal stability was observed by mounting a side breadboard (3).

3.5.1 Permanent magnets configuration

The magnetic field of the 2D-MOT is generated by 4 stacks of permanent neodymium bar magnets (EclipseN750-RB) as reported on [75, 103, 104, 107]. Each magnetic bar has dimension of $10 \times 25 \times 3\,\mathrm{mm}^3$ and magnetization vector of $M = 8.7(1) \times 10^5\,\mathrm{A/m}$. Spatial positions and orientations of the 4 stacks of permanent magnets are reported in the Fig.3.16.

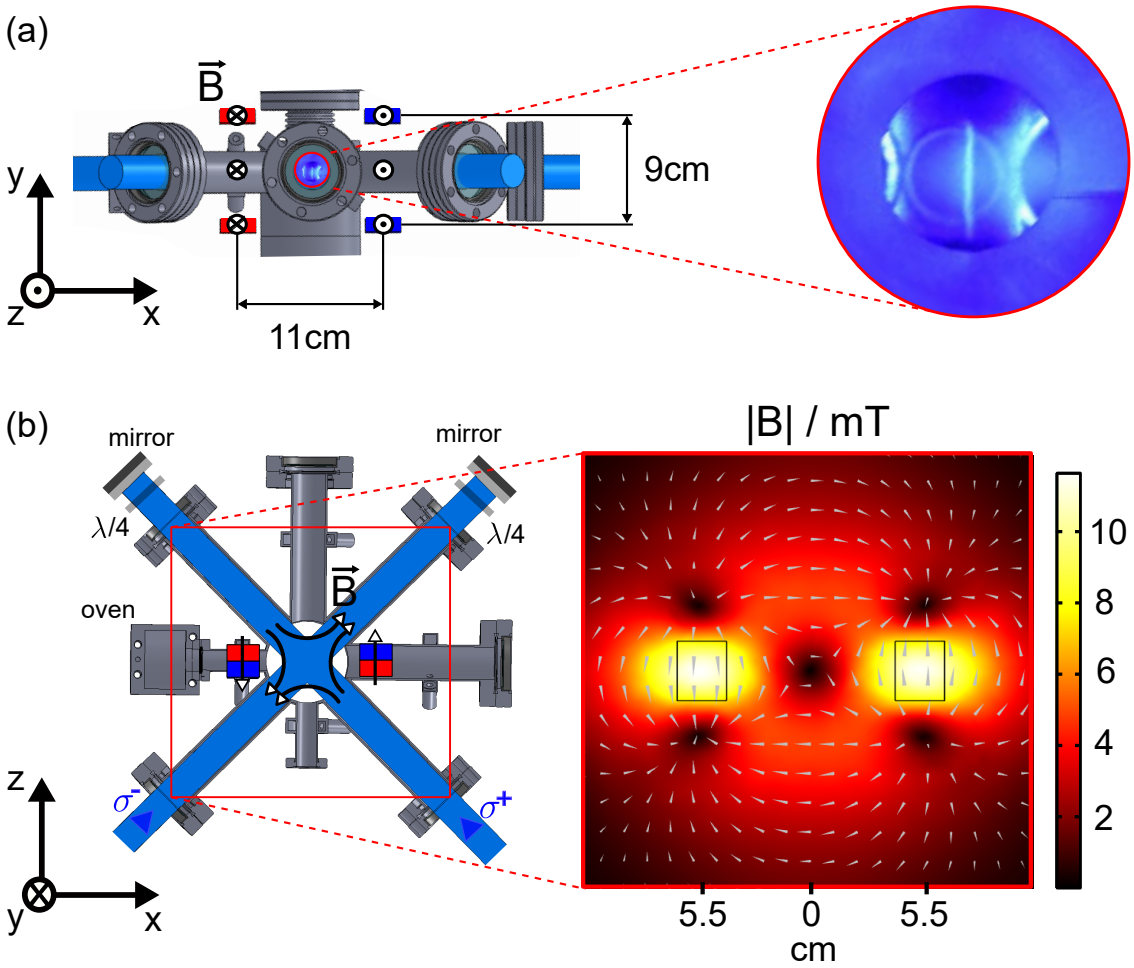

Figure 3.16: Section view of the atomic source showing the permanent magnets orientation and spatial positions. Magnets orientation are outlined with colors (N:blue, S:red). **(a)** Top-view of the atomic source. Insert shows the atomic cloud shape in the 2D-MOT without the push beam. **(b)** Side view of the atomic source. Insert shows the simulation of the magnetic field amplitude and its orientation in the $x - z$ plane.

In Fig.3.16(a), top view of the atomic source is reported. Magnets are placed at the corners of an hypothetical rectangle and centred with respect to the 2D-MOT. The rectangle short side between the magnets is 9 cm and the long side is 11 cm. Along the line of sight of the oven and before the 2D-MOT region, the first magnets pair has the same orientation, while the second pair beyond the 2D-MOT region has opposite direction as compared to the first one. The inset of Fig.3.16(a) shows the stripe shape of the atomic fluorescence in the 2D-MOT. Picture in the insert is taken without the push beam. The side view of the atomic source is reported in the Fig.3.16(b). A pairs of 45° crossed optical beams with a suitable polarizations are sent through the optical access of the multi cross channels. Two

mirrors and two $\lambda/4$-waveplates generate the counter-propagating beams of the 2D-MOT. On the right panel of Fig.3.16(b), the amplitude of the magnetic field and its direction is reported. The magnetic field profile was simulated by Comsol-Multiphysics software. We simulate the magnetic field generated by the magnets in volumetric region of $20 \times 20 \times 20\,\mathrm{cm}^3$ centred with the center of the 2D-MOT. Using the finite element method provided by the software the space is divided into small free meshes and for each meshes the magnetic field is estimated for a given boundary condition imposed by the magnets magnetization. We impose a maximum mesh size of 3 mm close to the magnets and 1 mm along the direction of the atoms emitted from the oven. The magnetic field numerically calculated oscillates with an amplitude error less than $3 \times 10^{-4}\,\mathrm{T}$ along all the push direction where the magnetic field is expected to be null. At position $\mathbf{r}$ smaller than the distance among the magnets, and so within the interaction volume describe by the 2D-MOT beams, the magnetic field vector $\mathbf{B}$ is well approximated with the following equation:

$$\mathbf{B}(\mathbf{r}) = b\mathbf{x} - b\mathbf{z} \tag{3.14}$$

where $\mathbf{r}$ is the generic position $\mathbf{r} = \mathbf{x} + \mathbf{y} + \mathbf{z}$ and b is the magnetic field gradient $b = 0.2245(2)\,\mathrm{T/m}$.

3.6 The 3D magneto optical trap

Final MOT is loaded by the cold atomic beam produced from the atomic source. MOT is located inside the sicence cell and it is realized by means of three pairs of counter-propagating beams with a proper detunings and circular polarization in a quadrupolar magnetic field. In this section, the design and realization of the MOT and compensation coils are described. We also introduce the fluorescence detection on its photodiode calibration used to estimate the number of atoms trapped in the final MOT and also to estimate the atomic flux emitted from the atomic source region.

3.6.1 MOT and compensation coils

The simplest configuration to produce either quadrupole field gradients or a homogeneous magnetic field in a given direction consists of a pair of coaxial twin coils. In Helmholtz configuration (with currents flowing in the same direction rotationwise) constant magnetic field proportional to the current are produced while in the anti-Helmholtz configuration (currents flowing in opposite directions) a quadrupole magnetic field is generated in order to operate the MOT. A good reference for the coils design for atomic physics experiments can be found at [175].

The magnetic field generated from a single coil and its gradient can be estimated as a sum of the single loops contributions. Considering a loop of radius r placed in the $x-y$ plane in the axial position $z = d/2$, the magnetic field along the vertical z direction at the center $x = 0$, $y = 0$ can be estimated with Biot-Savart law:

$$B_z^{\text{loop}}(z, r, d/2) = \frac{\mu_0 I}{2} \frac{r^2}{\left[(z + d/2)^2 + r^2\right]^{3/2}} \tag{3.15}$$

$$b_z^{\text{loop}}(z, r, d/2) = -\frac{3\mu_0 I}{2} \frac{r^2 (z + d/2)}{\left[(z + d/2) + r^2\right]^{5/2}} \tag{3.16}$$

where $\mu_0 = 4\pi \times 1 \times 10^{-7}\,\text{H/m}$ is the magnetic permeability and I is the loop current. The magnetic field of the coil with N winding in the radial direction (in the plane $x-y$) and M winding in the axial direction (along the z direction) can be computed as:

$$B_z^{\text{coil}}(z, r, d/2) = \sum_{n=1}^{N} \sum_{m=1}^{M} B_z^{\text{loop}} \left(z, r_n, \frac{d_m}{2}\right) \tag{3.17}$$

$$b_z^{\text{coil}}(z, r, d/2) = \sum_{n=1}^{N} \sum_{m=1}^{M} b_z^{\text{loop}} \left(z, r_n, \frac{d_m}{2}\right) \tag{3.18}$$

where the radius r_n and the distance d_m of the (n, m)-loop is computed as:

$$r_n = r + a\left(n - \frac{1}{2}\right) \qquad \frac{d_m}{2} = \frac{d}{2} + a\left(m - \frac{1}{2}\right)\text{sgn}(d) \tag{3.19}$$

where a is the diameter of the wire and $\text{sgn}(d)$ is the sign function.

Parameter	symbol	value
density	d_{Cu}	$8.63 \times 10^3\,\text{kg/m}^3$
resistivity	ρ_{Cu}	$1.7 \times 10^{-8}\,\Omega\,\text{m}$
resistance temperature coefficient	α_{Cu}	$3.9 \times 10^{-3}\,\text{K}^{-1}$
heat transfer coefficient with air	h_{air}	$1 \times 10^1\,\text{W/m}^2\text{K}$
emissivity	ε_{Cu}	3×10^{-2}

Table 3.3: Copper coefficients [176]. The copper emissivity ε_{Cu} is refereed to polished copper

It is also possible to compute the temperature reached by the coil as a function of the coil current employed. Considering the power balance between the electric power provided to the coils and their dissipation processes, it is possible to write the following equation at stationary condition:

$$I^2 \frac{\rho_{\text{Cu}} L_{\text{coil}}}{\pi(a/2)^2} \left(1 + \alpha_{\text{Cu}}(T - T_0)\right) = h_{\text{air}} S_{\text{coil}} (T - T_0) + \varepsilon_{\text{Cu}} S_{\text{coil}} \sigma_B (T^4 - T_0^4) \tag{3.20}$$

where L_{coil} is the total length of the wire used for the coil manufacturing, $T_0 = 22.5\,^{\circ}\text{C}$ is the reference temperature of the laboratory, S_{coil} is the total external surface of the coil, and $\sigma_B = 5.67 \times 10^{-8}\,\text{Wm}^{-2}\text{K}^{-4}$ is the Stefan–Boltzmann constant. The remaining copper coefficients are reported in Tab.3.3. The term on the left side of Eq.3.20 describes the electric power provided to the coil at constant current I while the right side terms describe the dissipation of the electric power by convection process between the coil and the air and also by irradiation process. The total wire length L_{coil}, the total mass M_{coil} employed for the coil and the total coil surface S_{coil} can be estimated as:

$$L_{\text{coil}} = M \sum_{n=0}^{N} 2\pi r_n \tag{3.21}$$

$$M_{\text{coil}} = d_{\text{Cu}} \pi (a/2)^2 L_{\text{coil}} \tag{3.22}$$

$$S_{\text{coil}} = 2(\pi r_N^2 - \pi r^2) + 2\pi r (d_M - d) + 2\pi r_N (d_M - d) \tag{3.23}$$

The coil temperature T that fulfils the Eq.3.20 is estimated numerically using the dichotomic procedure. I wrote a Python algorithm that computes the magnetic gradient and the stationary temperature T reached by a system of coils. During the simulation we also tested different higher copper emissivity ε_{Cu} to simulate possible deviation for the polished case of the copper. Coils are design with a compact geometry avoiding the implementation of water cooling system to cool down the temperature of the coils. In the Fig.3.17(a), the coils arrangement respect to the science cell is reported. This coils design is not definitive and it is adopted only for this specific science cell. Once the cell will be replaced with the definitive science cell, all the magnetic coils system will be re-design.

The increment of the coils temperature is not a fast process compared to the time scale of the single clock cycle. This mean that for a single clock operation we are legit to approximate the variation of coils temperature as a constant temperature. The temperature of the coils, or more in general the temperature of and external environment, can coupled to the clock energy levels by means of black body radiation. In the literature there are several methods that allow us to predict black body radiation line-shift induced by the temperature of an external system. One possibility is to model the entire system and perform a numerical estimation of the light shift induced [135, 177], design a science cell with a uniform well characterized black body radiation shift [178], use a in-vacuum thermometer that measure the temperature in the exact position of the atoms [179] or perform a clock interrogation inside a cryogenic chamber [41].

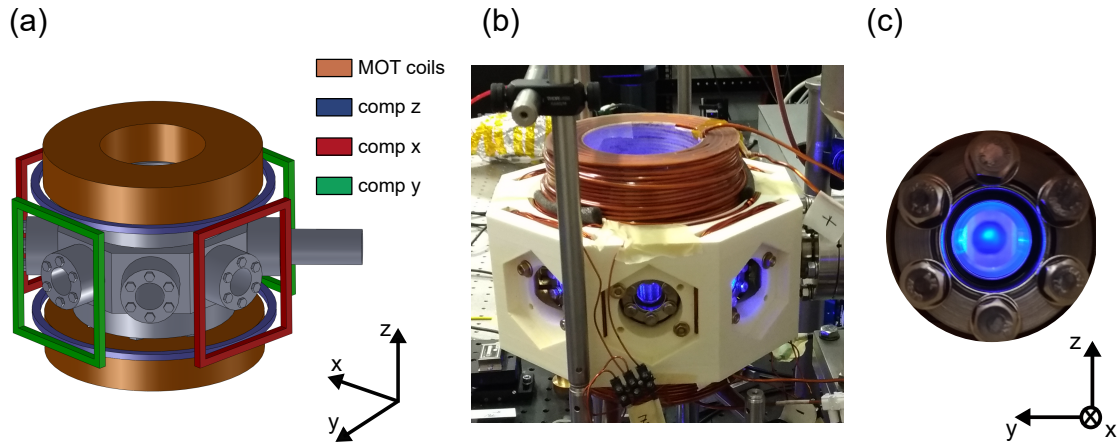

Figure 3.17: MOT and compensating coils. **(a)** Schematic arrangement of MOT coils and compensating coils around the octagon cell. **(b)** Picture of the system. MOT coils and compensating coils are hosted inside a suitable 3D-printed support. **(c)** MOT cloud

Compensation coils

The compensation coils are designed in order to induce a uniform magnetic field of the order of $1 \times 10^{-4}\,\mathrm{T/A}$ ($1\,\mathrm{G/A}$). Compensation coils along the z direction (blue coils) have a radius of $r = 7.5\,\mathrm{cm}$ and they are placed at distance of $d = 7\,\mathrm{cm}$. Each coil is made by 8 windings of circular copper wire with radius of $a/2 = 0.4\,\mathrm{mm}$. The compensating field generated is estimated to be $9.8 \times 10^{-5}\,\mathrm{T/A}$. Compensation coils along the x,y directions (red and green coils) have a side length of $7\,\mathrm{cm}$ and are placed at distance of $15\,\mathrm{cm}$. Each coil is made of 16 windings of circular copper wire of with radius $0.14\,\mathrm{mm}$. The compensating field generated is estimated to be $9.1 \times 10^{-5}\,\mathrm{T/A}$. All compensation coils are power supplied by current source (Delta-Elettronika, ES015-10) capable of driving up to $4\,\mathrm{A}$. As show in the Fig.3.17(b), a custom 3D-printer support is designed to hold the compensation coils positions. This support is fastened directly to the bulk of the octagon cell by screws and it is designed to avoid the obstruction of the optical accesses.

Quadrupolar coils

Considering previous works [122, 123, 180], MOT coils are designed to generate a magnetic field gradient of the order of $0.4\,\mathrm{T/m}$. In order to avoid the presence of a water cooling system, the copper wire diameter a together with radial and axial windings number N, M are chosen opportunely. Using the algorithm described before, we scanned different wire parameters such as the wire diameter, winding configurations (transversal winding and axial windings) and internal coils radius. The only external constraint is the axial distance between the coils $d = 8.5\,\mathrm{cm}$ which is fixed by the science cell size. Among the available choices that maximize

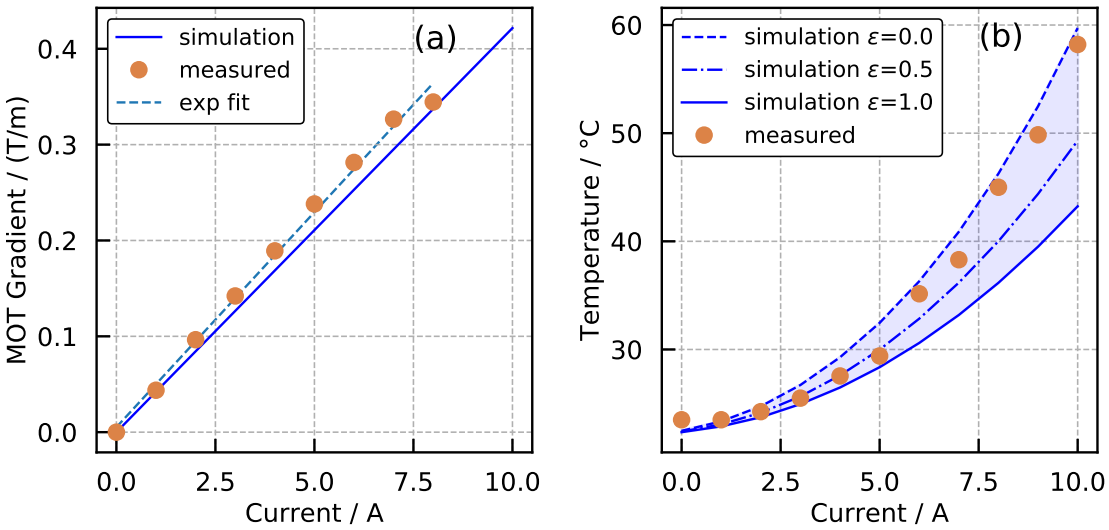

Figure 3.18: Numeric prediction (blu line) and experimental characterization (orange point) of the MOT coils. **(a)** Magnetic field gradient as a function of the current coils. The dashed line show is the experimental characterization fit. **(b)** Temperature of the coils as a function of the current coils

the magnetic gradient and minimize the temperature reached by the coils, we choose a coils geometry with internal radius of $r = 3.7\,\text{cm}$, wire diameter of $a = 2.73\,\text{mm}$, $M = 14$ axial windings and $N = 11$ radial windings.

The MOT coils current is generated from a power supply (Delta-Elettronika, ES015-10) capable to drive 10 A. The power supply is software controlled, the power supply converts the board voltage signal into a coils current. The MOT coils manufacturing was performed by electronic workshop of University of Trento. During the fabrication, a thermally conductive resin was apply on the wire in order to ensure a homogeneous heating dissipation among the internal windings. The coils lay on the top of to the vacuum screws used to fasten the CF63 flanges of the science cell. A small layer of kapton tape (less that 3 mm) was applied on the top of every screws to reduce thermal conduction from coils to the science cell.

Comparison between experimental and simulated gradient sustained by the coils is reported in Fig.3.18(a) We measured the magnetic field generated by the coils as a function of the distance by means of a commercial Hall sensor. We estimate an experimental gradient of 0.045(1) T/Am which is close to the expected value of 0.043 T/Am. Comparison between the temperatures reached of the coil at different currents are with the predicted ones are reported and Fig.3.18(b). We measure a maximum coils temperature of 60 °C at 10 A, this means that we can avoid the introduction of water cooling system for MOT coils. The measured total MOT

coils resistance is around $R = 0.6\,\Omega$. Using the Eq.3.20, we also simulate different emissivity coefficients ε in order to take into account the possible effect in the emissivity of the enamelled layer in the commercial copper wire and the effect of the thermo-conductive resin to the polished copper $\varepsilon_{\mathrm{Cu}}$.

At 5 A of MOT coils current, the characteristic switch-off current of the system is of the order of 20 ms. A reduction of switching-off time is observed by introducing by IGBT (Semikron, SKM150GAL 12T4) in serial configuration with the power supply and the coils. Controlling the gate voltage of the IGBT by a TTL signal it is possible to reduce the switch-off time at 20 µs.

3.6.2 Fluorescence detection

In this section we describe the fluorescence calibration used to determine our atomic source performances. In the first calibration, the collected scattering optical power from the MOT cloud is converted in into a MOT number of atoms N_{MOT}. In the second calibration, collected scattering power coming from the interaction of the probe beam and the cold atomic beam is converted into a atomic flux estimation Φ_{2D} of our atomic source.

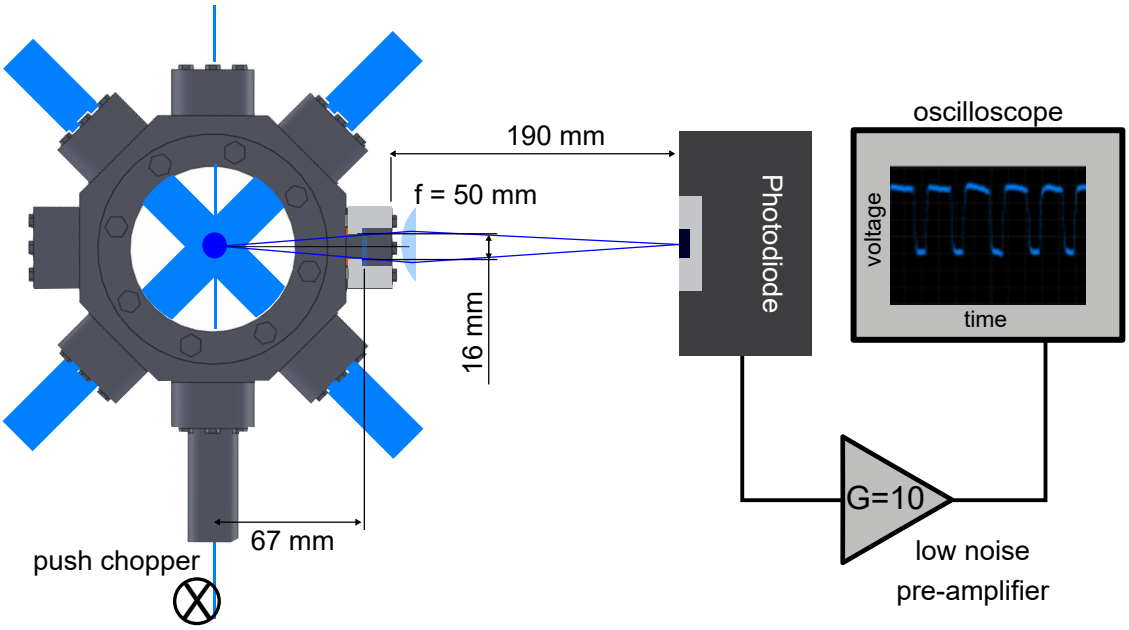

Figure 3.19: Schematic drawing of the experimental setup used to measure the MOT fluorescence signal. Fluorescence signal collected by the photodiode is then amplified by a low noise amplifier.

MOT number of atoms

Figure 3.19 describes the fluorescence collection and measurement system used to detect our Sr MOT. We employed a biased photodetector (Thorlabs, DET36A/M) to generate a photocurrent $I_{\mathrm{PD}} = \mathcal{R}_{\mathrm{PD}} P_{\mathrm{PD}}$, where P_{PD} is the impinging optical scatter power from the MOT and $\mathcal{R}_{\mathrm{PD}}$ is the detector responsivity. Total impinging power to the photodetector P_{PD} can be also rewritten as $P_{\mathrm{PD}} = \tilde{\Omega}_{\mathrm{PD}} T_{\mathrm{w}} P_{\mathrm{sc}} N_{\mathrm{MOT}}$ where N_{MOT} is the total number of atoms in MOT , P_{sc} is single atoms scattering power trapped in MOT, T_{w} is the window transmissivity and $\tilde{\Omega}_{\mathrm{PD}}$ is the fraction of solid angle detected by the photodiode.

First, we calibrated the photodiode responsivity $\mathcal{R}_{\mathrm{PD}}$ at λ =461 nm by measuring for different optical powers impinging on the photodetector the related voltages read from the oscilloscope. Comparing them and performing a linear regression fit, we found that $\mathcal{R}_{\mathrm{PD}} = 0.141(2)\,\mathrm{A/W}$ is the photodiode responsitivity at 461 nm, which is compatible with the datasheet value.

The photodetector current I_{PD} can be converted into a voltage signal either by a load resistor (for instance by means of the input resistance of an oscilloscope) or by a transimpedance amplifier. Because of the weakness of the MOT signal, we decided to employ a low-noise signal pre-amplifier (Stanford research system, SR560 with an overall transimpedance gain $G_{\mathrm{PD}} = G \times R_{\mathrm{amp}} = 10 \times 100\,\mathrm{M\Omega} = 1\,\mathrm{G\Omega}$. Adding this pre-amplifier gain stage, the bandwidth of the photodetector is reduced. The time constant τ_{PD} of the photodetector system is computed considering the load impedance, given by the input pre-amplifier resistance R_{amp}, and the capacitance $C_{\mathrm{amp}} = 25\,\mathrm{pF}$ in parallel to the photodiode capacitance $C_{\mathrm{PD}} = 40\,\mathrm{pF}$. These values give a time constant of $\tau_{\mathrm{PD}} = R_{\mathrm{amp}} \times (C_{\mathrm{amp}} + C_{\mathrm{PD}}) = 6.5\,\mathrm{ms}$.

MOT fluorescence is collected by lens with diameter of 2.54 cm and focal f = 50 mm just outside the vacuum chamber. As shown in Fig. 3.19, the photodiode detects only a fraction of the emitted fluorescence. For circular apertures, the solid angle fraction detected by the photodiode can be estimated according the following formula:

$$\tilde{\Omega}_{\mathrm{PD}} = \frac{1}{4\pi} \frac{\pi r_{\mathrm{w}}^2}{d_{\mathrm{w}}^2} = 3.56(2) \times 10^{-3} \tag{3.24}$$

where $r_{\mathrm{w}} = 8\,\mathrm{mm}$ is the minimum optical access given by the cell window and $d_{\mathrm{w}} = 67\,\mathrm{mm}$ is the distance between cell window and the MOT cloud.

The number of atoms in the MOT N_{MOT} corresponding to a given photodetector

voltage V_{PD} is computed with the following formula:

$$V_{\mathrm{PD}} = (G_{\mathrm{PA}}\mathcal{R}_{\mathrm{PD}}\tilde{\Omega}_{\mathrm{PD}}T_{\mathrm{w}}\ P_{\mathrm{sc}})N_{\mathrm{MOT}} \tag{3.25}$$

$$= k_{\mathrm{PD}}^{-1}N_{\mathrm{MOT}} \tag{3.26}$$

where $T_{\mathrm{w}} = 0.84(8)$ is the measured average window transmissivity and P_{sc} is the single-atom scattered power estimated as:

$$P_{\mathrm{sc}} = \hbar\omega_{\mathrm{eg}}\frac{\Gamma}{2}\frac{s_{\mathrm{MOT}}}{1 + s_{\mathrm{MOT}} + 4\Delta_{\mathrm{MOT}}^2/\Gamma^2} = 1.11 \times 10^{-11}\,\mathrm{W} \tag{3.27}$$

where $\omega_{\mathrm{eg}} = 2\pi c/\lambda$, $\Delta_{\mathrm{MOT}} = -1.2\,\Gamma$ is the MOT beams detuning and s_{MOT} is saturation peak intensity estimate as:

$$s_{\mathrm{MOT}} = T_{\mathrm{w}}(1 + T_{\mathrm{w}}^2) \times \frac{2P_{\mathrm{MOT}}}{\pi w_{\mathrm{MOT}}^2}\frac{1}{I_0} = 2.49 \tag{3.28}$$

where $P_{\mathrm{MOT}} = 45\,\mathrm{mW}$, $w_{\mathrm{MOT}} = 0.62\,\mathrm{cm}$ is the MOT waist, and $I_0 = 41\,\mathrm{mW/cm^2}$ is Sr saturation intensity. Pre-factor $T_{\mathrm{w}}(1+T_{\mathrm{w}}^2)$ takes into account the retro-reflection of the MOT beams. Reversing Eq.3.26 we get

$$k_{\mathrm{PD}} = 0.22(3) \times 10^6\,\mathrm{atoms/V} \tag{3.29}$$

Atomic flux calibration

We also measured the atomic flux delivered from the atomic source before the MOT region. We measured the atomic flux Φ_{2D} emitted from the 2D-MOT region by probing the cold atomic beam with a transverse probe beam. Probe beam is sent along the vertical z direction through the MOT center. Because of the common optical path between the probe beam and the vertical MOT beam, the probe has a circular polarization.

From the collected probe beam fluorescence, the atomic flux can be estimated. According the formula reported in [166]:

$$\Phi_{\mathrm{2D}} = \rho S_{\mathrm{int}} v_L \tag{3.30}$$

$$= \frac{k_{\mathrm{PD}}V_{\mathrm{PD}}}{V_{\mathrm{int}}}\frac{\tilde{\Omega}_\sigma}{F(v_T)}S_{\mathrm{int}}v_L \tag{3.31}$$

where v_L and v_T are longitudinal and transverse velocity of the cold atomic beam emitted from the atomic source. The experimental values of v_L and v_T will be estimated in Sec.5.2. $\tilde{\Omega}_\sigma$ describes the relative solid angle reduction detected by the photodiode considering the radiation pattern induced by the probe polarization along the detection direction. Because of σ polarization has a quasi-uniform spatial

radiation pattern along the detection direction, this number can be reasonably estimated to be $\tilde{\Omega}_\sigma = 1$ [181, 182]. S_{int} is the interaction section between the atomic beam and the probe beam. $F(v_T)$ is a factor that takes into account the Doppler contribution of the transverse components of the cold atomic beam. This factor is estimated according the following equation [166]:

$$F(v_T) = \frac{1}{\sqrt{2\pi}} \int_{-\infty}^{+\infty} \frac{e^{-v^2/2v_T^2}}{1 + 16\pi^2(v/\lambda\Gamma)^2} dv \tag{3.32}$$

The parameter V_{int} is the interaction volume between the probe beam an the cold atomic beam coming from the 2D-MOT. We estimate the interaction volume as $V_{\text{int}} = \pi w_{\text{probe}}^2 a_{\text{DPC}} = 4.22\,\text{mm}^3$ where $a_{\text{DPC}} = 2\,\text{mm}$ is the maximum diameter of the differential pressure channel. We estimate the interaction surface as $S_{\text{int}} = \pi w_{\text{probe}}^2 = 2.11\,\text{mm}^2$, where $w_{\text{probe}} = 0.83\,\text{mm}$ is the probe waist.

The k_{PD} is photodetector voltage-to-atoms conversion factor computed according Eq.3.29. Considering a probe detuning of $\Delta_{\text{probe}}/\Gamma = 0$, a probe saturation intensity $s_{\text{probe}} = 2.74$ and a photodiode transimpedence $G_{\text{PD}} = 10^{10}\,\Omega$ we obtain a conversion factor of $k_{\text{PD}} = 7.88 \times 10^3\,\text{atoms/V}$. Finally, the Eq.3.31 can be rewritten as:

$$\Phi_{\text{2D}} = k_{\text{PD}}^* V_{\text{PD}} \frac{v_L}{F(v_T)} \tag{3.33}$$

where the new photodetector calibration factor is estimated as:

$$k_{\text{PD}}^* = 3.9(5) \times 10^6\,\text{atoms/(Vm)} \tag{3.34}$$

3.7 Red light sources

In this section, the red laser sources needed for the repumping and second cooling stage and clock laser are described. The laser source have home-made assembly using the *External Cavity Diode Laser* (ECDL) design. After highlighting the main advantages of this compact laser source design, characterizations of the laser sources are discussed.

3.7.1 External Cavity Diode Laser

Nowadays, *External Cavity Diode Lasers* (ECDL) represent a common configuration to increase the diode laser wavelength tunability and spectral purity. Our homemade (ECDL) is based on the compact design of [172, 183] which is called Littrow configuration. A theoretical treatment to the resonance conditions of this double cavity system is also called three-mirror cavity model [184, 185].

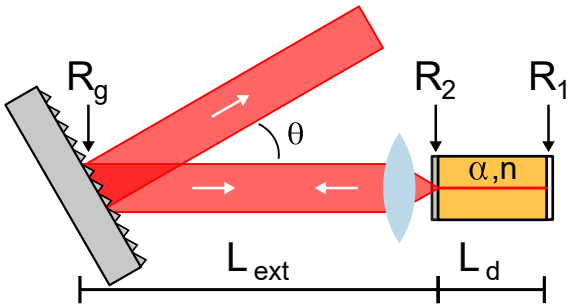

Figure 3.20: Schematic of a Littrow configuration ECDL showing the laser diode, collimating lens, diffraction grating, and output beam. The diode cavity is described by cavity length L_d, facets reflectivity R_1, R_2, chip material optical absorption α and refractive index n. θ is the Littrow angle, L_{ext} is the external cavity length and R_g is the reflectivity of the grating for a selected mode.

Fig.3.20 shows the main components of the ECDL in Littrow configuration. Diode laser is depicted as a small linear cavity with a length L_d with reflecting facet R_1 and partially reflecting facet R_2. Depending on the type of the diode laser, the facet R_2 can be partially reflecting, for the case of the Fabry-Pérot diode, or also anti-reflecting coated. The material of the diode laser is described by a refractive index n, optical absorption coefficient α, and optical gain g. The material gain g is related to the presence of the material doping and the diode laser injection current. Light is out-coupled from diode laser cavity from the less reflective facet R_2, out-coupled light is collimated by a short focal lens and it is coupled with the external cavity generated by the reflectivity of a diffraction grating R_g. Entire system operates as a double cavity laser system, where the first short cavity generates the laser light and the second longer cavity, composed of a diffraction grating, provides a wavelength selective optical feedback. From the experimental point of view, the tunability of the emitted wavelength is performed in two ways:

- A coarse wavelength tuning is performed by geometrical alignment of the diffraction grating. This is usually done by a dedicated mechanical micrometric screw which rotates by an angle θ the grating position, hence changing the wavelength of injected optical feedback.
- A fine wavelength tuning is performed by controlling temperature and the injection current of the diode laser. This is usually performed stabilizing the temperature of the ECDL by means of Thermo-electric cooler (TEC).
- A finale tuning is provided by a piezo-electric element that translates the horizontal position of the grating.

Expected linewidth

The ECDL configuration was designed also to increase the spectral purity of the emitted laser light. In fact, the theoretical limit of laser linewidth $\Delta\nu$ is provided by the Schawlow–Townes formula [186] modified to include the linewidth enhancement factor $(1+\beta^2)$ that is due to coupling between intensity and phase noise in semiconductor diode lasers [187]. With these considerations, the linewidth of the single diode laser can be estimated as [188, 189]:

$$\Delta\nu = \frac{\pi h\nu_0}{P_0}(\Delta\nu^0)^2 n_{\mathrm{sp}}(1+\beta^2) \tag{3.35}$$

where ν_0 is the lasing frequency of the fundamental mode and P_0 is its emitted power. The parameter n_{sp} is the number of spontaneous photons in the mode ν_0, which approach the unity above the threshold [188] and β is the linewidth broadening with a value 3 to 10 [187]. $\Delta\nu^0$ is the passive cavity linewidth. For the *single diode* laser (SD), the cavity linewidth can be estimated as [185]:

$$\Delta\nu^0_{\mathrm{SD}} = \frac{c}{2nL_d}\left(\alpha L_d - \frac{1}{2}\ln\sqrt{R_1R_2}\right) \tag{3.36}$$

Adding the third mirror, the lindewidth of the ECDL system can be written as [185]:

$$\Delta\nu^0_{\mathrm{ECDL}} = \frac{c}{2(nL_d + L_{\mathrm{ext}})}\left(\alpha L_d - \frac{1}{2}\ln\sqrt{R_1R_2k}\right) \tag{3.37}$$

where k takes into account the coupling of the external cavity R_2 - R_g relative to R_2 and it is estimated as:

$$k = 1 + (1-R_2)\sqrt{\frac{R_g}{R_2}} \tag{3.38}$$

The maximum linewidth reduction is estimated considering the spectral linewidth gain of the ECDL system compared to the single diode laser is estimated comparing Schawlow–Townes linewidth with these two different passive cavities [190]

$$\frac{\Delta\nu_{\mathrm{ECDL}}}{\Delta\nu_{\mathrm{SD}}} \simeq \left(\frac{\Delta\nu^0_{\mathrm{ECDL}}}{\Delta\nu^0_{\mathrm{SD}}}\right)^2 \simeq \left(\frac{nL_d}{L_{\mathrm{ext}}}\right)^2 \tag{3.39}$$

Considering a typical chip length $L_d \sim 1\,\mathrm{mm}$ and $L_{\mathrm{ext}} \sim 3\,\mathrm{cm}$ we get a linewidth reduction of the order of 10^{-3}. The last equation is valid for a low coupling regime ($k \sim 1$) where the the grating reflectivity R_g is neglected. As demonstrated in [191], the grating properties do not affect the order of magnitude of the spectral linewidth gain estimated in Eq.3.39.

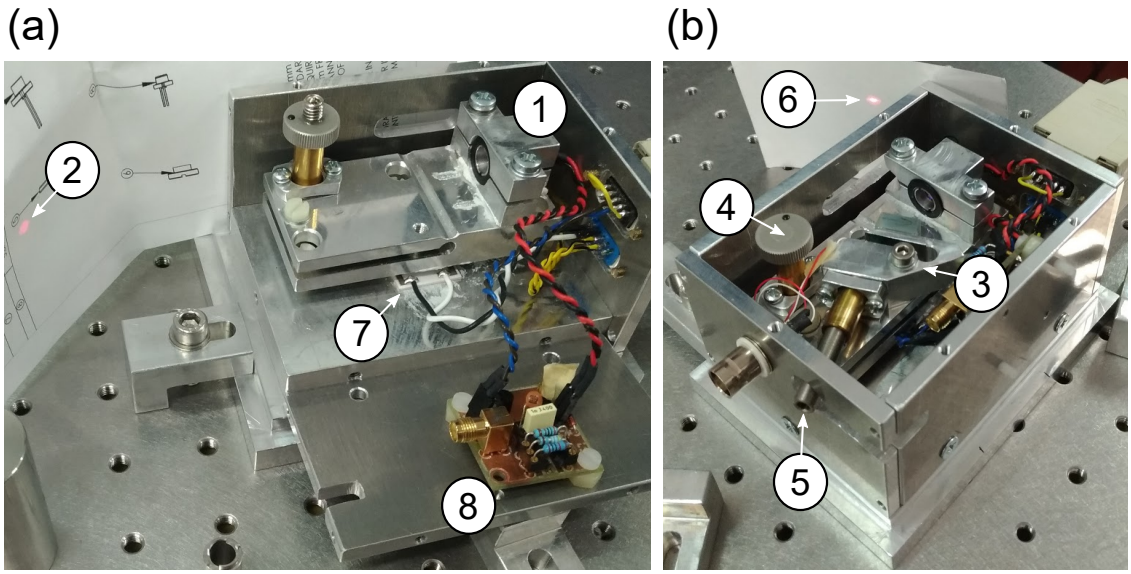

Figure 3.21: ECDL during the two main alignment phases: **(a)** light collimation of the laser diode and **(b)** reduction of the threshold current at specific wavelength during the lasing. Numbers in the figure show the main component of the ECDL. (1) Laser diode and collimating lens clamping system, (2) Collimated light of the laser diode , (3) Grating mechanical support , (4) Screw of the vertical alignment, (5) screw of the horizontal alignment, (6) optical profile of the ECDL, (7) TEC and (8) circuits for laser diode protection and FM modulation. The manufacturing process was made by UNITN and INRIM mechanical workshops.

3.7.2 Second cooling stage and repumpers light sources

Our homemade aluminium mechanical design is depicted in Fig.3.21. Diode laser and the collimating lens holder are fixed inside a collimating tube (Thorlabs, LT230P-B) with a focal lens of $f = 4.5\,\text{mm}$ and numerical aperture of NA=0.55. This holder fixes the diode laser position and offer the possibility to tune the lens position by externally screw the lens holder. This method avoids the use of epoxy glue for lens position fixing. The lens and diode holder is easily clamped externally (1) to the bulk as show in the Fig.3.21. Once the optical mode is collimated (2) in the near and far field we fixed the diffraction grating (Thorlabs, GH13-12V) and its support (3). The grating support hosts a piezo-eletric element (Thorlabs, AE0203D08F) used for fine tune of wavelength emission. Vertical (4) and horizontal (5) coarse alignment of the grating are performed by micro-metric screws.

The output wavelength is selected by changing the angle of incidence on the grating and monitoring it with a wavelength-meter (Burleigh, WA1000). Setting the injection current of the laser diode slightly below its threshold current, optical

feedback is observed by sudden flare of the out-coupling light (6) during the grating vertical alignment. Walk-off between horizontal and vertical alignment is also observed, so the entire procedure is continuously repeated until a reduction of the threshold current at the desired wavelength emission is observed.

Fine tuning of wavelength emission is made by changing the temperature of the laser cavity. The temperature of the system is controlled through a peltier element (Thorlabs, TEC3-6). The thermal contact between the peltier element and the bulk material is ensured by a thermo-conductive paste. A temperature sensor (NTC) is employed in order to monitor the temperature and to stabilize the temperature of the system at the desired value by means of an external PID changing the peltier current source.

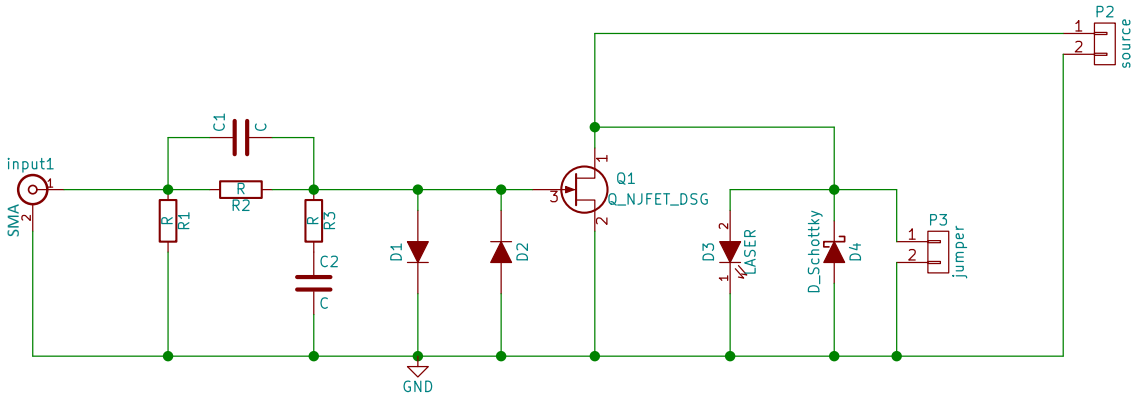

Figure 3.22: Laser diode FM modulation circuits.

A small printed circuit board (8) for the diode laser protection is also present. The schematics of the circuit is reported in Fig.3.22. This circuit offer the possibility to perform a fast *frequency modulation* (FM) of the diode injection current. The RF signal is injected into the SMA connector and after a impedance matching stage, given by resistor and capacitance, the signal goes to the base of a FET element (Fairchild, J113). The FET absorbs the current of the laser diode generating the desired modulation. The circuits clamps any reverse voltage spikes applied to the laser diode by means of a Schottky diode. The printed circuits board was designed using Kicad EDA electronics design automation suite.

ECDL characterizations

Examples of the ECDL characterization are depicted in Fig.3.23,3.24,3.25. These ECDL are designed to address different Sr atomic transitions as the rempumping transitions $^3P_2 - {}^3S_1$, $^3P_0 - {}^3S_1$, and the second cooling stage transition $^1S_0 - {}^3P_1$.

The top panels of Fig.3.23,3.24,3.24 show the emitted power as a function of the injection current of the diode laser. The graphs compare the current-power characterization for the single diode (red-triangles) and for the ECDL configuration of the same diode (blue point). The middle panels of Fig.3.23,3.24,3.24 show the emitted light frequency tuning as a function of diode temperature. The bottom panels show the emitted light frequency as a function of the piezo voltage (PZT voltage). The orange lines are a linear fits used to extrapolate the coefficients $\Delta\nu/\Delta T$ and $\Delta\nu/\Delta V$ of ECDLs. Fit results and summary of the ECDLs characterizations are reported in Tab:3.4.

		$^3P_2 - {}^3S_1$	$^3P_0 - {}^3S_1$	$^1S_0 - {}^3P_1$
DIODE LASER				
	chip type	HL7001MG	HL6750MG	HL6738MG
	λ/nm at T=23 °C	705	685	690
	I_{th} / mA	47.0(5)	45.0(5)	55.0(5)
ECDL				
	I_{th} / mA	41.0(5)	43.0(5)	47.0(5)
	$\Delta\nu/\Delta T$ / GHz/°C	-26(1)	-22.8(6)	-16(1)
	$\Delta\lambda/\Delta T$ / pm/°C	43(2)	35(1)	26(2)
	$\Delta\nu/\Delta V$ / GHz/V	-0.48(6)	-0.53(2)	-0.4(1)
	$\Delta\lambda/\Delta V$ / pm/V	0.8(1)	0.8(1)	0.7(1)
	cavity length /mm	17.4(2)	17.3(2)	15.6(2)
	free spectral range / GHz	8.6(1)	8.6(1)	9.6(1)
	mode hopping / GHz	2.4(2)	1.7(2)	1.9(2)
WORK POINT				
	I / mA	80	70	81
	T / °C	37	7.0	23.5
	P / mW	25.5	13.7	9.04
	λ /nm	707.203	679.290	689.445

Table 3.4: Summary of the ECDLs characterizations.

Repumpers optical bench

The Fig.3.26 reports the repumpers optical setup. The laser lights generated by the ECDLs are superimposed and combined with the blue MOT beam. A small portion of laser lights is also coupled to wavelength-meter to check and calibrate the emitted wavelengths of the lasers. Two optoisolators are also employed in order to avoid optical feedback in the master cavity. Both optoisolators (Crystal, OI-725-03-707, OI-685-03-679) have a transmission efficiency around 75 % and optical isolation of −25 dB. The AOM efficiency is 65 % for both wavelengths.

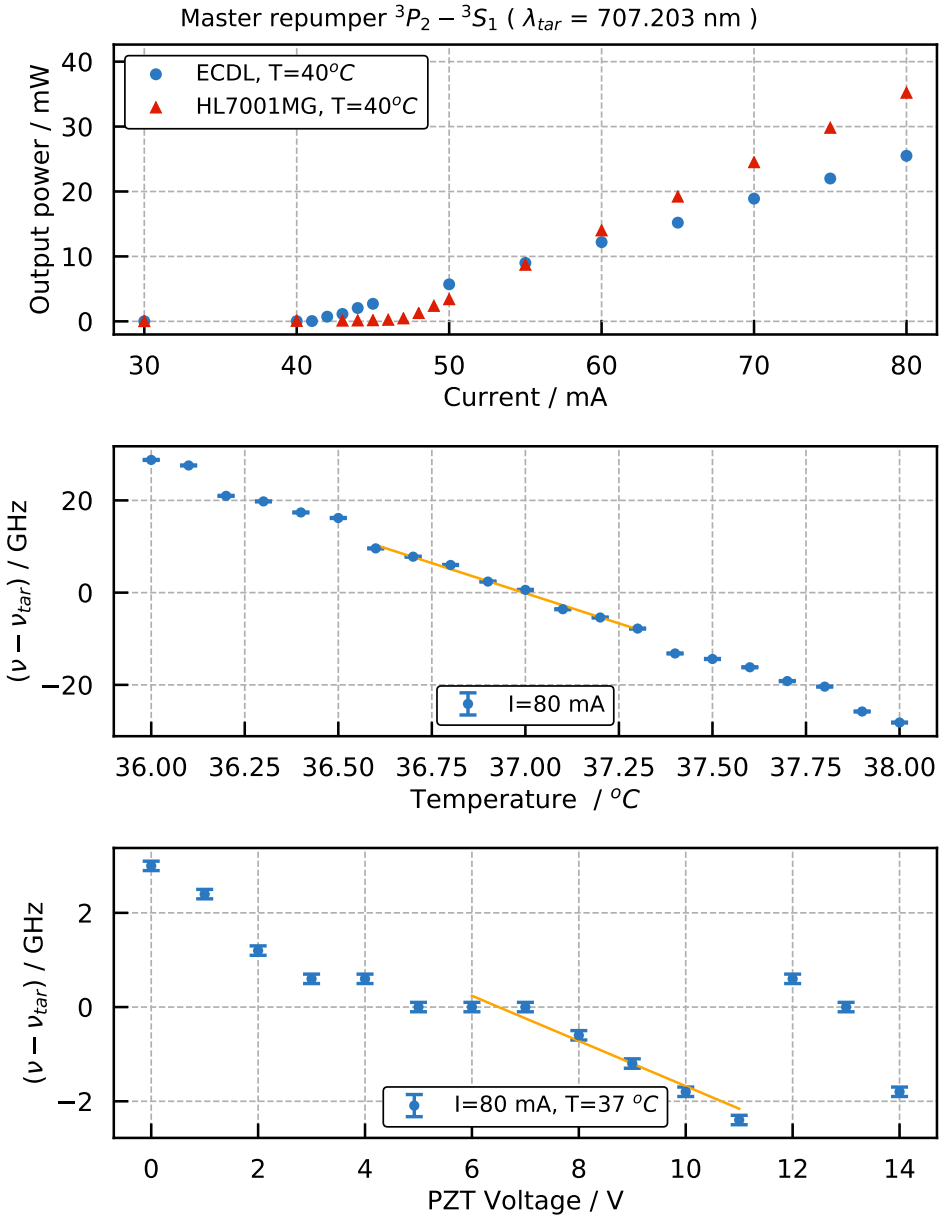

Figure 3.23: Characterization of repumper light source for $^3\mathrm{P}_2 - {}^3\mathrm{S}_1$ ($\lambda_{\mathrm{tar}} = c/\nu_{\mathrm{tar}} =$ 707.203 nm). The top panel reports the optical power as a function of the diode injection current for the single diode laser (red triangles) and with the ECDL design (blu point). The middle panel reports the frequency emission ν to the target frequency ν_{tar} as a function of the temperature of the ECDL (blue point). The bottom panel reports the frequency emission ν to the target frequency ν_{tar} as a function of the PZT voltage (blue point). Orange lines are linear fits used to extrapolate the coefficients $\Delta\nu/\Delta T$ and $\Delta\nu/\Delta V$.

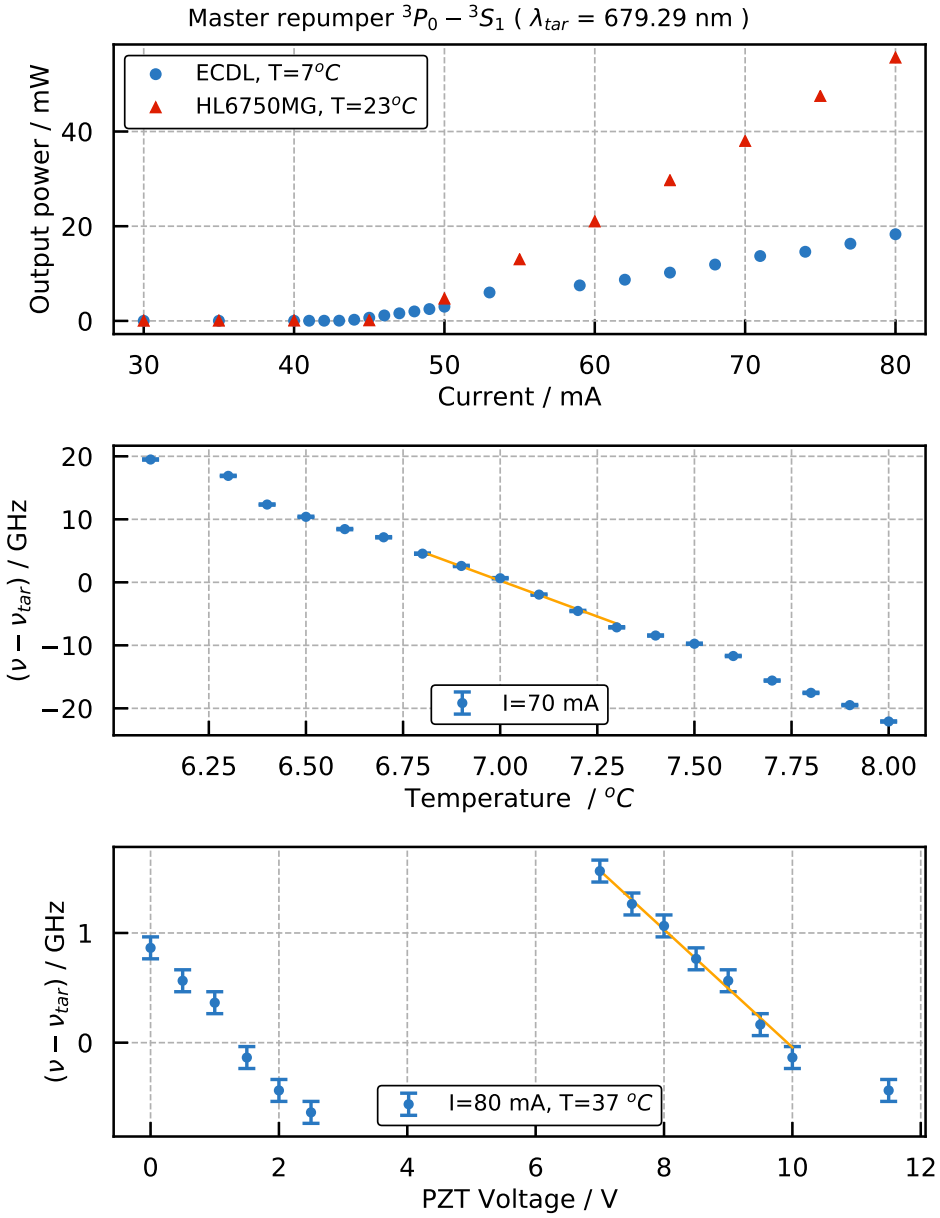

Figure 3.24: Characterization of repumper light source for $^3\mathrm{P}_0 - {}^3\mathrm{S}_1$ ($\lambda_{\mathrm{tar}} = c/\nu_{\mathrm{tar}} =$ 679.290 nm). The top panel reports the optical power as a function of the diode injection current for the single diode laser (red triangles) and with the ECDL design (blu point). The middle panel reports the frequency emission ν to the target frequency ν_{tar} as a function of the temperature of the ECDL (blue point). The bottom panel reports the frequency emission ν to the target frequency ν_{tar} as a function of the PZT voltage (blue point). Orange lines are linear fits used to extrapolate the coefficients $\Delta\nu/\Delta T$ and $\Delta\nu/\Delta V$.

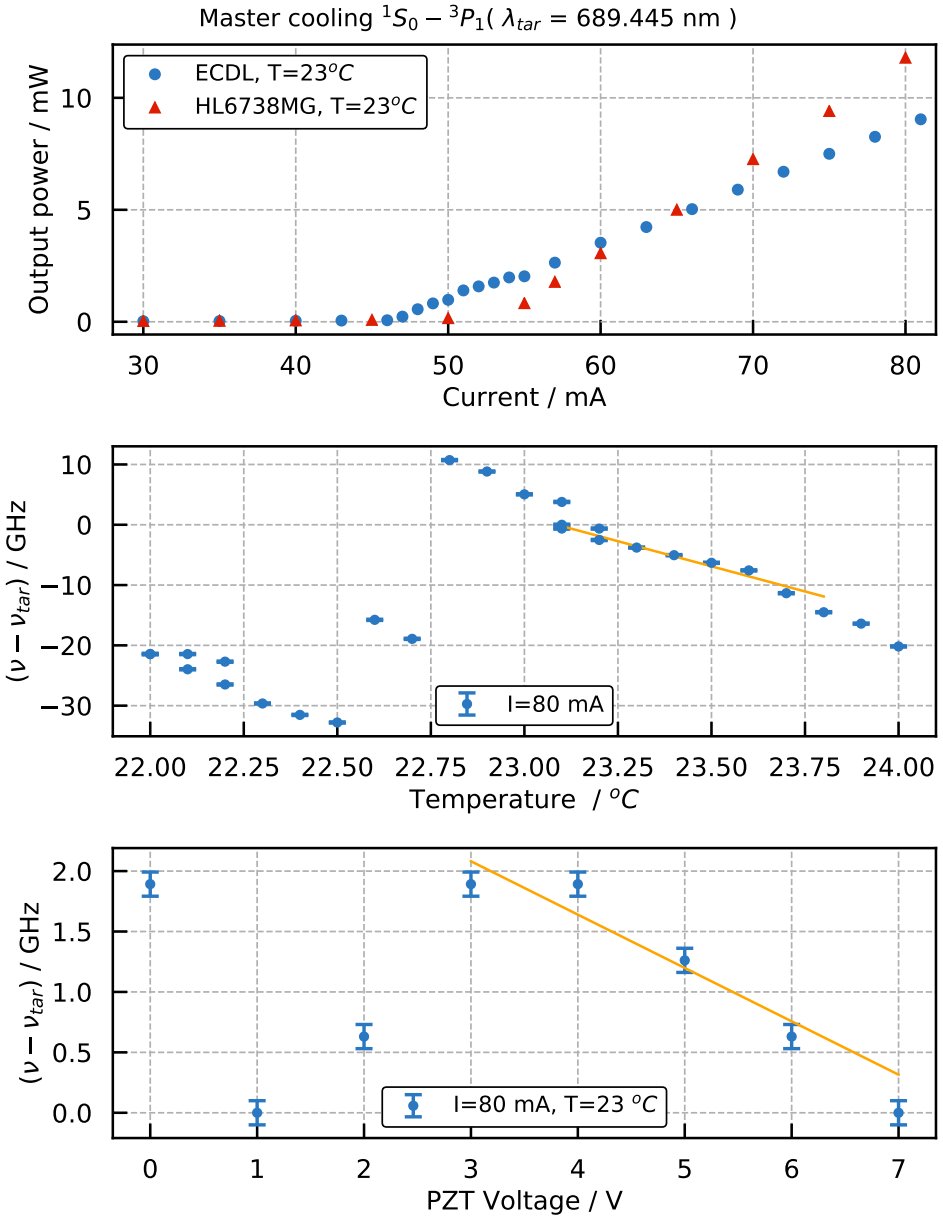

Figure 3.25: Characterization of repumper light source for $^1\mathrm{S}_0 - {}^3\mathrm{P}_1$ ($\lambda_{\mathrm{tar}} = c/\nu_{\mathrm{tar}} =$ 689.445 nm). The top panel reports the optical power as a function of the diode injection current for the single diode laser (red triangles) and with the ECDL design (blu point). The middle panel reports the frequency emission ν to the target frequency ν_{tar} as a function of the temperature of the ECDL (blue point). The bottom panel reports the frequency emission ν to the target frequency ν_{tar} as a function of the PZT voltage (blue point). Orange lines are linear fits used to extrapolate the coefficients $\Delta\nu/\Delta T$ and $\Delta\nu/\Delta V$.

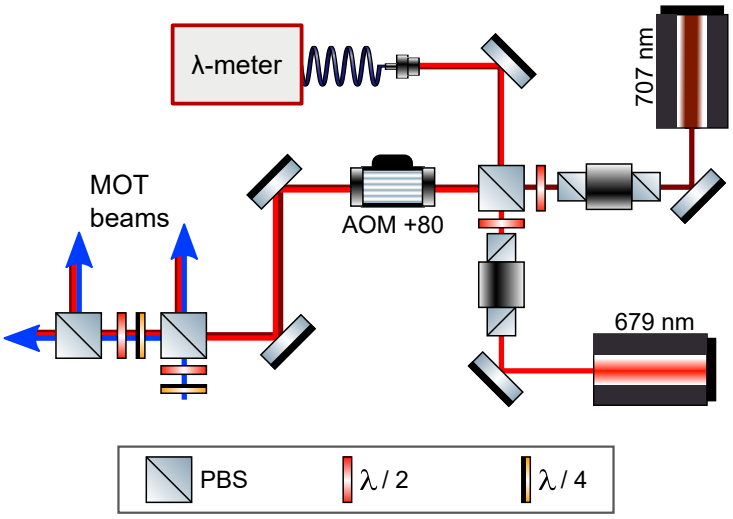

Figure 3.26: Repumpers optical setup

3.8 Clock laser: Universal synthesiser concept

Low level of frequency instability is one of the most important requirement of the clock laser. A high finesse cavity is usually employed as frequency reference for the clock laser. In the infrared domain the best ultrastrable cavities are able to reach the level of 10^{-17} of frequency instability by means of long cavities system [192], crystalline mirrors coating [193] and cryogenic environment with high level of temperature control [64].

In metrological institutes more than one optical atomic clock is usually operating and all of these hold a requirement of high stability. In order to avoid the highly cost of ulstrastable cavities for each atomic clock, the technique based on the spectral purity transfer is employed. The main idea consists in sharing the spectral purity of the ultrastable laser with other region of the optical spectrum by means of a frequency comb [194–196]. With this approach, more reference slave lasers can be locked to one single ulstrastable master laser. This spectral purity transfer of ultrastable laser is also referred as universal synthesizer method.

As depicted in Fig.3.27, our future goal is to stabilize the strontium clock laser by locking it to the Ytterbium ultrastable laser [47]. At INRIM, we successfully stabilize a slave laser to the master Ytterbium clock laser with a locking bandwidth around 60 KHz [197]. Depending on the spectral purity of the strontium clock laser, it will be evaluated a directly stabilized to Ytterbium clock laser without employing a own stabilization cavities.

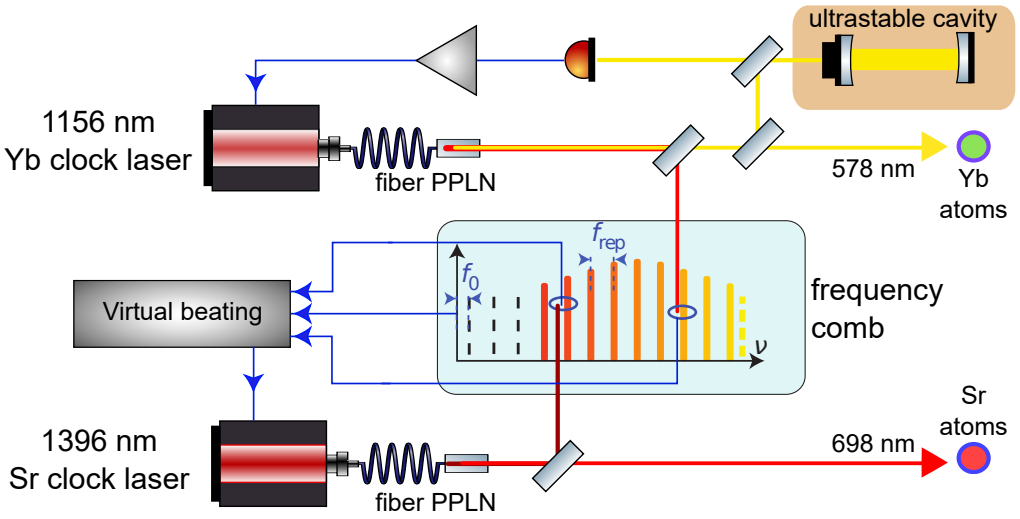

Figure 3.27: Future scheme of INRIM universal synthesizer. The spectral purity of the Yb clock laser source is transferred to the Sr clock laser source by means of a frequency comb. Atomic clock transitions are reached by non-linear fiber duplication of infrared clock laser sources. As shown in the inset of the frequency comb spectrum, spectral purity transfer is performed in the infrared domain. Virtual beatnote method is the analogic error signal generation used to stabilize the Sr clock laser source to the Yb clock laser source.

3.8.1 Laser source design and characterization

As explained in the previous section, the clock laser source at 698 nm is generated from duplication process of 1396 nm laser light, while the stability of the laser will be ensured by the spectra purity transfer method. In this section we present the design of the clock laser source following the work of [198], In this work, the authors were able to generate a laser source system with tunability from 1420 nm to 1620 nm and small linewidth of 5.2 kHz in ECDL configuration. In the following paragraph, the main components of the laser, the mechanical design a preliminary characterization are reported.

Half Butterfly gain chip

The main component of our clock laser is the half-butterfly 20 dB gain chip (Thorlabs, SAF1450S2). Fig.3.28(a) depicts the main components of the chip and Fig.3.28(b) shows the chip front view. Light source is generated inside an angle faced optical waveguide. This waveguide is characterized by a normal facet and and angled facet with different reflectivities $R_1 \sim 10\,\%$(normal facet), and $R_2 \sim 0.005\,\%$ (angle facet). Length of the waveguide is $L_d = 1.5\,\text{mm}$ with a refractive index of $n = 3.5$. The emitted optical power is directly coupled into an integrated optical fiber as shown in Fig.3.28(a), while a small amount of power is emitted on the

angle faced waveguide with and angle of 26° compare to the chip case. The emitted wavelength of this gain chip is centred at 1450 nm with a span of $\Delta\lambda \sim 300$ nm. The chip is also equipped with an internal thermoelectric cooler (TEC) and thermistor which provides the chip temperature stabilization. The chip is controlled by a INRIM's driver current source and temperature stabilization. This system offers a temperature stability of 4 mK and a current noise of 10 µA.

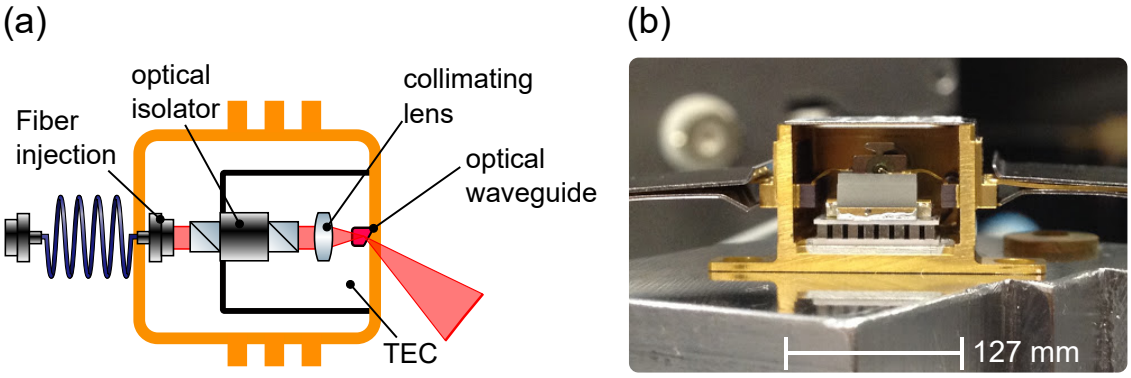

Figure 3.28: half-butterfly gain chip. **(a)** Schematics of internal components of the gain chip. The out-coupled light from the normal surface is collimated by a lens in order to provide the fiber injection. The chip has also an internal optical-isolator in order to suppress optical feed-back. **(b)** Front view of the half-gain chip.

Mechanical design and alignment procedure

The alignment of the external cavity was performed by monitoring at the same time both the optical power and the spectrum profile. By means of unbalanced fiber coupler, the less attenuated component (−1 dB) was send to the power-meter in order to monitor the lasing condition while the highly attenuated component (−14 dB) was sent to *optical spectrum analyser* (OSA) in order to observe the spectrum profile and the central wavelength of the emitted light.

The mechanical design of our ECDL clock laser is shown in the Fig.3.29. The distance between the gain chip (1) and the collimating lens position (2) of $f = 2.97$ (Thorlabs, C660TME-C) was chosen to favourite the lasing of extended cavity. The external diffraction grating (3) (Newport, 33012WCO01-544H) with has a reflectivity of $R_g = 90\,\%$. The grating is glued to an alluminium support to a kinematic mirror holder (Newport) which is fixed to ECDL bulk in two orhogonal points (4-5) as show in the Fig.3.29. For the fine wavelength tuning, a piezo-elettric element (6) was inserted between the horizontal screw and the case of the kinematic mirror. The external cavity length is measured at $L_{\text{ext}} = 5.3$ cm.

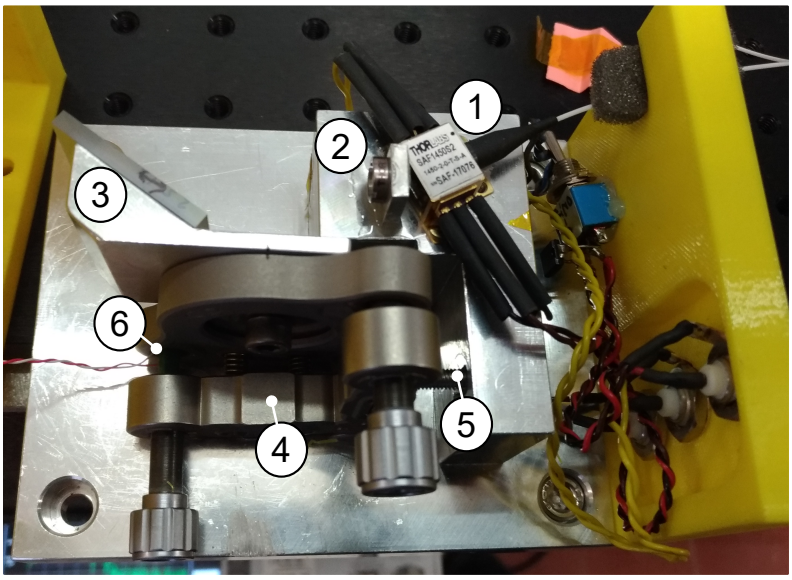

Figure 3.29: Clock laser assembly. The main components in the figure are the gain SAF1450S2 chip (1), collimating lens (2), the diffraction grating and its alluminium support (3), the vertical (4) and the horizontal (5) kinematic mirror fixing points, piezoelectric element (6).

Monitoring the output power on the fiber, collimating lens position was fixed with a triaxial micro-traslator, vertical and horizontal orientations of the grating were aligned in order to observe the ECDL lasing. Once the lasing condition was observed, the desired wavelength was selected by rotating horizontally the grating. Due to the correlations between the lasing alignment and the selection of the specific wavelength, this procedure was iterated until high power emission at desired wavelength was observed. Iterations were performed at different collimation distances in order to find the highest power emission at selected wavelength. The final position of collimation lens was then fixed by bi-components glue (UHU, Endfest) at its best configuration.

ECDL characterization

Fig.3.30(a) shows the spectrum of our ECDL clock laser (red line) as compared to the spectrum of the chip without the diffraction grating (blue line). The resolution bandwidth of the optical spectrum analyser is around $\Delta\lambda_{\mathrm{OSA}} = 1\,\mathrm{nm}1$ with a wavelength range of 1500 nm. In the blue line is possible to appreciate the spontaneous emission gain profile of the single chip. Red line clearly shows the lasing of our clock laser around the target wavelength $\lambda = 1396\,\mathrm{nm}$. In order to figure out the presence of multimode peaks in the lasing profile, we reduced the wavelength range at 5 nm with a resolution of $\Delta\lambda = 0.05\,\mathrm{nm}$. The inset in Fig.3.30(a) shows

the result of this investigation: with a resolution of $\Delta\lambda = 0.05\,\text{nm}$ is possible to observe the absence of the multi-mode peaks in the lasing profile. We also estimate the *Single Mode Suppression Ratio* (SMRS), which quantifies the attenuation between the center longitudinal peak with the nearest noise sideband. From the inset plot of Fig.3.30(a), the estimated SMSR is $-36\,\text{dB}$

.

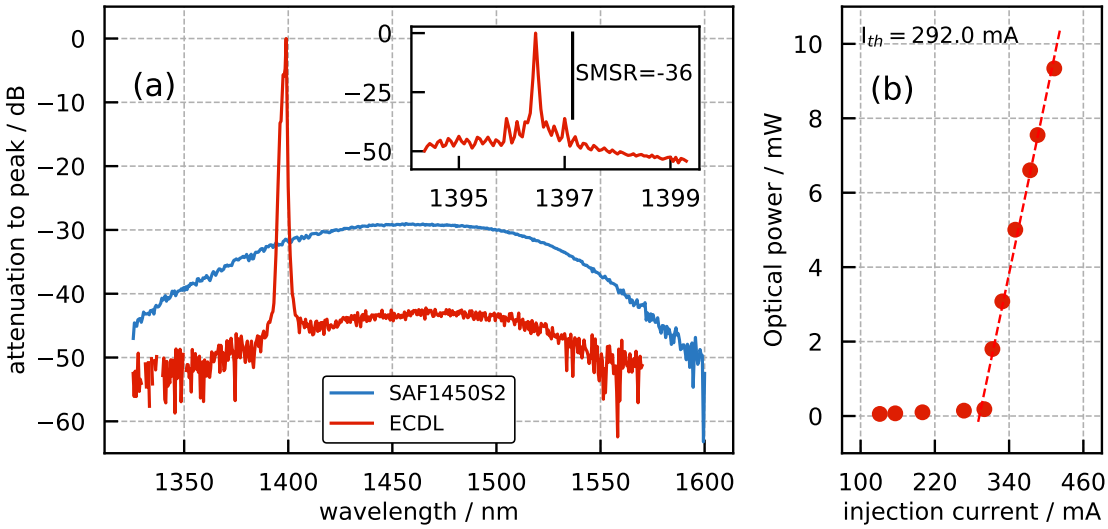

Figure 3.30: **(a)** Optical spectrum comparison between the single waveguide emission (blue line) and with the ECDL configuration (red line). In the inset the lasing profile with a wavelength span of $\Delta\lambda = 4\,\text{nm}$. **(b)** Power emitted as a function of the injection current.

In Fig.3.30(b) the characterization of the clock laser optical power as a function of the injection current is reported, At $I = 411\,\text{mA}$ we get 9 mW of output power with ECDL configuration. From the current-power characterization is possible to estimate a threshold current of $I_{\text{th}} = 292\,\text{mA}$. The power emitted by chip without the grating is $115\,\mu\text{W}$ at $I = 411\,\text{mA}$.

A gain in the output power by lowering the temperature of the chip $T = 15\,^{\circ}\text{C}$ is also observed. Unfortunately, after few hours it seems that lower chip temperature goes to ruin the internal alignment of the fiber chip causing a reduction of the output power less than 1 mW. Returning at $T = 25\,^{\circ}\text{C}$ we were able to restore the 12 mW of output power. This effect suggests us to tune the temperature of the chip less than $2\,^{\circ}\text{C}$.

3.9 Next Lasers stabilizations: multi-wavelengths ultrastable cavity

As already described in Sec.3.4.1, the stabilization of the blue cooling laser is performed using a dedicated spectroscopy cell. In a similar way, the laser light of second cooling stage, provided by a master lasers,it will be first frequency narrowed by locking it to an external optical cavity and then a second heatpipe system will be employed to stabilize the laser frequency to the $^1S_0 - {}^3P_1$ transition [127]. Following this approach, each trapping lasers employs an its own heatpipes and a possible stabilization cavities. A more compact solution for the frequencies stabilization is offered by locking the trapping lasers to a single multi-wavelength ultrastable-cavity. This approch is already used as a stabilization method for the trapping lasers of the INRIM Yb optical clock [199] and in the future it will available also for the Sr apparatus. Fig.3.31 shows the main parts of the optical bench for the multiwavelength stabilization system. The trapping lasers at 689 nm, 813 nm, and the infrared source of 461 nm will be offset-locked to the ultrastable cavity with the sideband technique [200] which is a modified version of the Pound-Drever-Hall method.

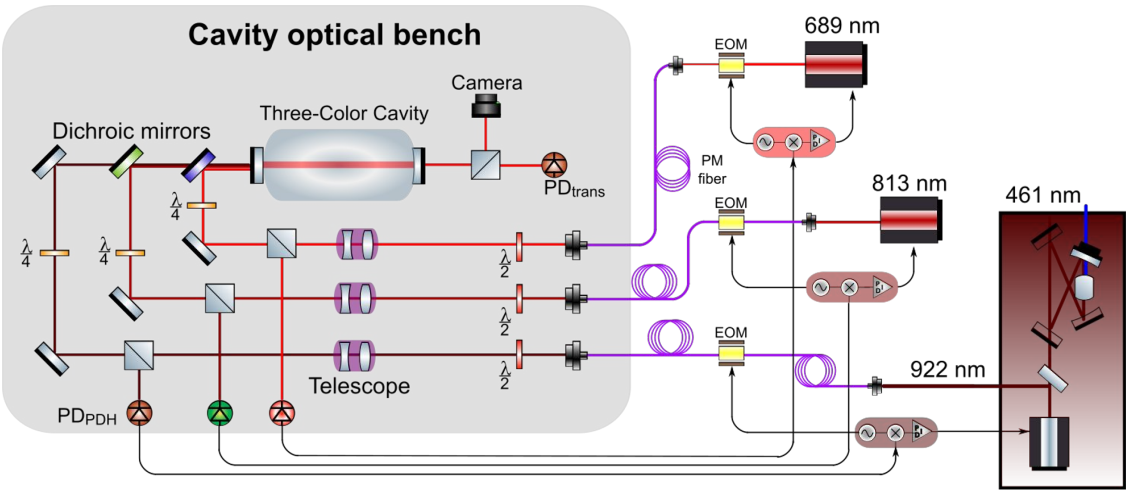

Figure 3.31: Multiwavelength stabilization of the Sr trapping frequency: First cooling stage 461 nm, second cooling stage 689 nm and the dipole trapping 813 nm

At the moment, we are preparing the Vacuum chamber and the temperature control system that will host the ULE cavity. The system is depicted in Fig.3.32. Fig.3.32(a) shows the real vacuum chamber. The Fig.3.32(b) depicts a schematic representation of the system. The ULE cavity will be inserted inside an inner chamber. This chamber is heated externally by two peltier elements. The temperature of the system is monitored by means of several *negative thermal coefficient* resistors

(NTC) placed around the inner chamber.

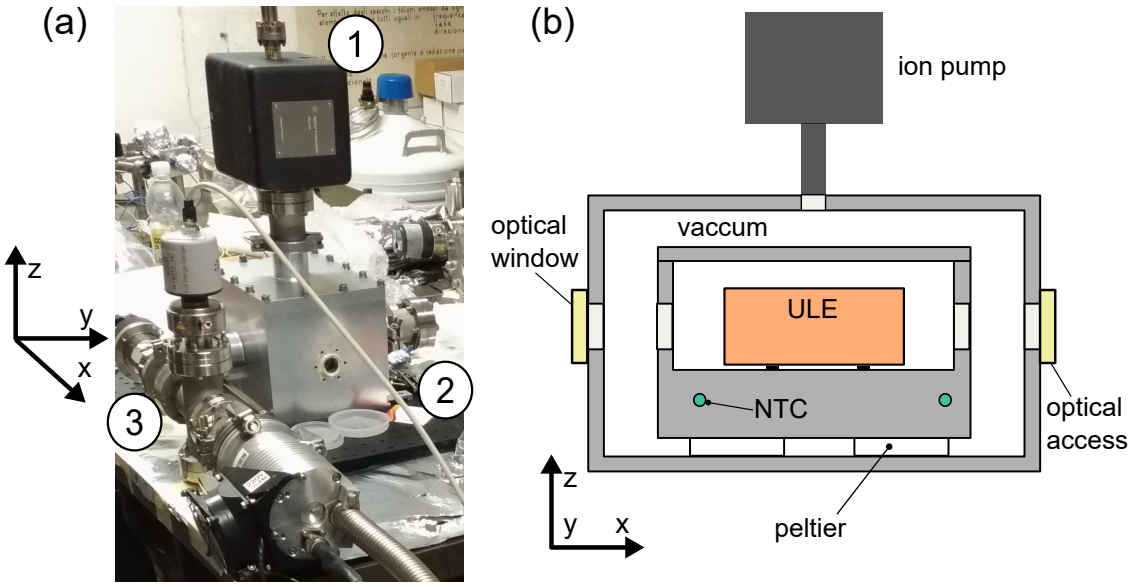

Figure 3.32: Vacuum chamber of the three color cavity. **(a)** real system under evacuation. From the figure is possible observe the main vacuum elements: the ion pump (1), electrical feedthroughs for temperature stabilization (2) and a vacuum valve (3). **(b)** Schematics and main elements of the three color cavity.

Chapter 4

Numerical simulations

Simulating the MOT loading process is used as a tool to understand and design the best trapping configurations [99, 101, 201–205]. The main idea consist in computing atomic trajectories as a function of different MOT trapping parameters. Using the semi-classical treatment of atom-light interaction described in Ch.2, it is possible to simulate the 3D-trajetories of atoms at different trapping configurations. Moreover, this approach is also adopted to explore different trapping system, such as the dipole optical trap [205–207], atoms with higher internal complex structure, such as the molecular MOT [208, 209] and Rydberg-dressed MOT [210].

4.1 Aim of the simulation

The goal of our simulation is to predict and optimize the cold atomic flux produced from our new atomic source as a function of the experimental parameters, such as the 2D-MOT and push beam. Considering our atomic source design described in Ch.3 and reported in the Fig.4.1(a), we want to simulate the atoms trajectories that are generated from the oven, trapped in 2D-MOT region and pushed toward the MOT region by means of the push beam. Knowing the ratio between atomic trajectories that are collected in the final MOT with the overall simulated atomic trajectories, we can predict the MOT loading rate at different atomic source parameters and compare it with the experimental results.

In this thesis we also explored the possibility to enhance the MOT loading rate by adding a sideband beam to the 2D-MOT configuration. Experimental implementation of this method is depicted in Fig.4.1(b) and it allowed the observation of enhancing factor of 2.5 in the MOT loading rate. In order to optimize the sideband and 2D-MOT configuration, we simulated and compared different trapping configurations such as the standard 2D-MOT and the 2D-MOT with sideband beam

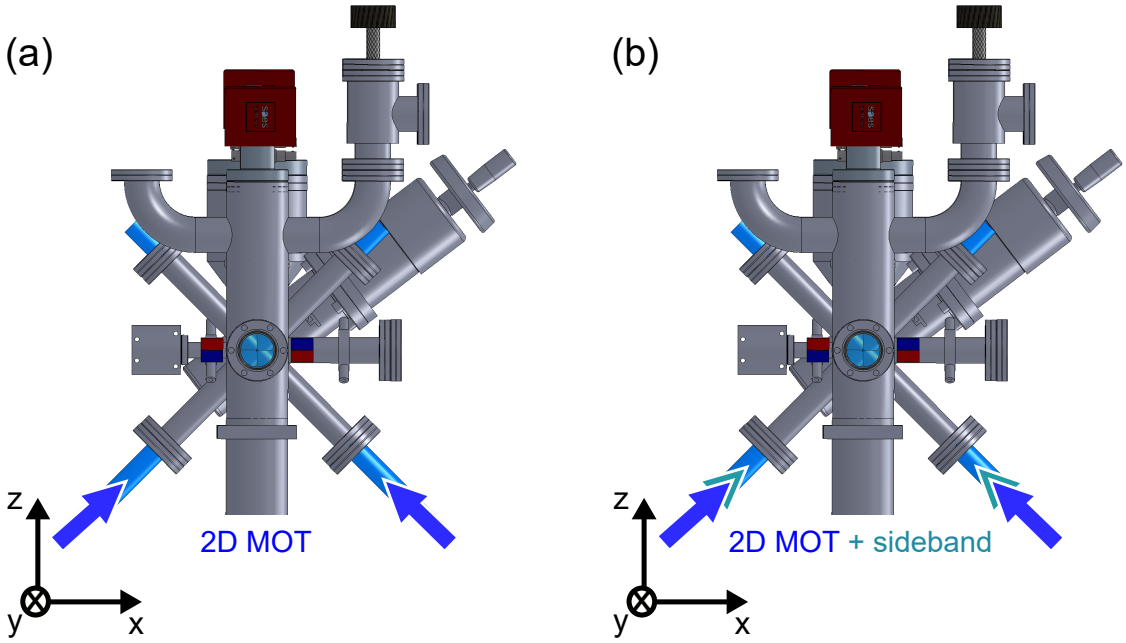

Figure 4.1: Beams configuration for the 2D-MOT trapping **(a)** Standard 2D-MOT trapping, **(b)** Sideband enhancing. Atomic source is reported on the push view.

4.1.1 Capture velocity approach

The capture velocity estimation is a standard tool used in order to access the best MOT configuration. In our atomic source, atoms coming from the oven are loaded transversally in the 2D-MOT region. Performing a numeric integration of the equations of motion along the oven direction, it is possible to simulate atomic trajectories at different starting velocity and different 2D-MOT configuration.

Let's consider the 2D-MOT trapping depicted in Fig.4.1(a). In this configuration, atoms generated from the oven are trapped in the standard 2D-MOT. Fig.4.2 reports the 1D numeric integration of the atomic trajectories along the line of sight of the oven at different initial velocities. The 2D-MOT trapping parameters are reported in the Tab.4.1. In the Fig.4.1(b), we enhance the capture velocity by spatially superimposing a sideband beam to the standard 2D-MOT beam. As reported in the Tab.4.1, the sideband beam is red detuned compared to the standard 2D-MOT and the optical power is equally redistributed between the 2D-MOT and the sideband. The numeric analysis reported in the Fig.4.3 shows the enhancement of the capture velocity from 76(1) m/s to 98(1) m/s. Using the same amount of optical power, the sideband beam adds and extra trapping force in the 2D-MOT region. Using the Eq.2.39, it is possible to estimate an enhancement in the loading rate of the order of $\eta \sim 2.7$.

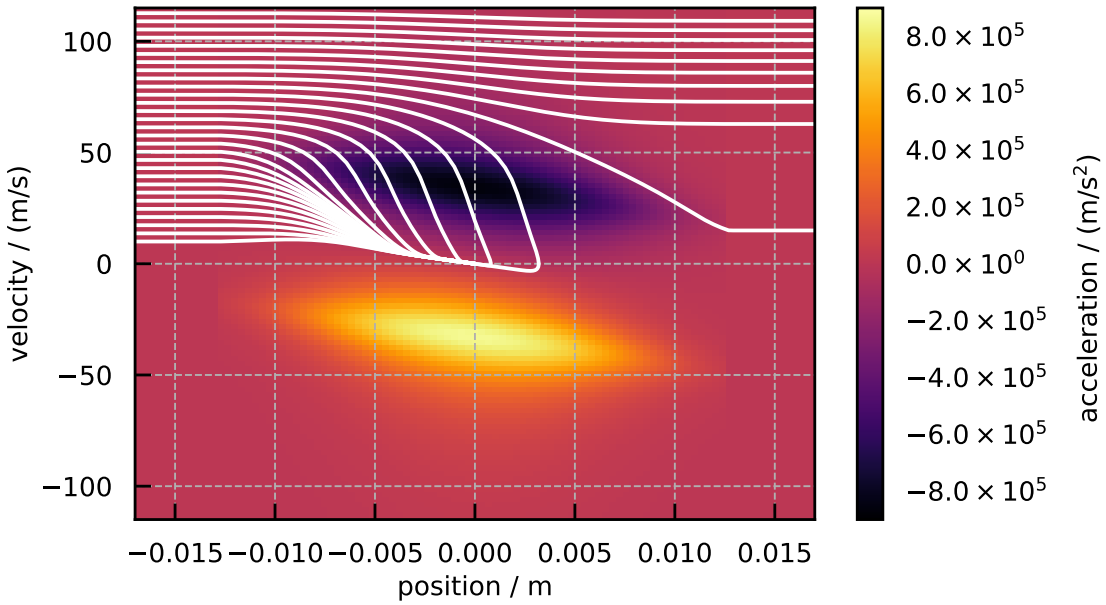

Figure 4.2: Atomic trajectories in the 2D-MOT. Simulation parameters are reported in the Tab.4.1

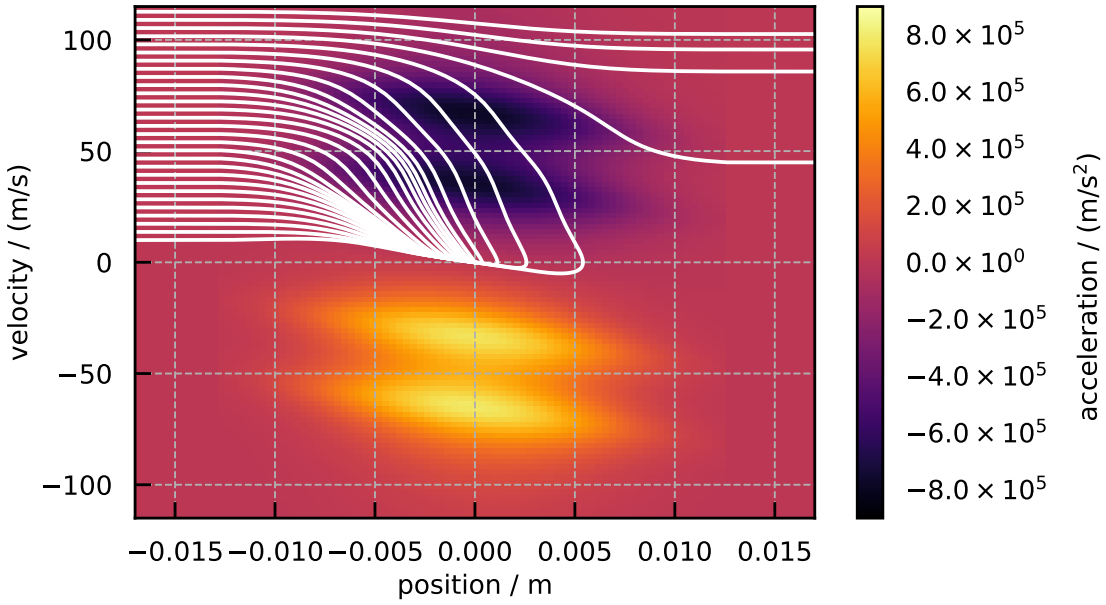

Figure 4.3: Atomic trajectories in the 2D-MOT and sideband beams. Simulation parameters are reported in the Tab.4.1

Even if the capture velocity is a intuitive tool that grasp the physics of sideband enhancing, it can not be used as faithful estimation of the MOT loading process

		Fig.4.2	Fig.4.3
atomic mass	m	88 u	88 u
wavelength	λ	461 nm	461 nm
linewidth	$\Gamma/2\pi$	30.5 MHz	30.5 MHz
beam e^{-2} radius	w_{2DMOT}	9.5 mm	9.5 mm
	w_{side}	/	9.5 mm
saturation parameter	s_{2DMOT}	7.88	3.94
	s_{side}	/	3.94
detuning	$\Delta_{\text{2DMOT}}/\Gamma$	-1.6	-1.6
	$\Delta_{\text{side}}/\Gamma$	/	-3.2
magnetic gradient	b	0.2 T/m	0.2 T/m
numeric capture velocity	$v_{\text{cap}}^{\text{num}}$	76(1) m/s	98(1) m/s

Table 4.1: Parameters used for the numeric estimation of the capture velocities. In this simulation, the saturation parameter s is the total saturation perceived by the atom

because it neglects the geometrical constraints of the capture process. For these reasons, in this chapter we develop an 3D algorithm used to predict the MOT loading rate given by a single 2D-MOT atomic source and we apply it to the sideband method.

4.1.2 Monte Carlo approach

In our simulation we use a stochastic algorithm to estimate some physical process, the so called *Monte Carlo* (MC) method. The MC is a powerful tool used to perform calculations which are too complex for a classical approach [211]. In our simulation, the MC approach is used for the following processes:

- Sampling the starting positions and velocities of atoms. These quantities are randomly sampled according their distributions which are related to the Maxwell-Boltzamnn distribution and the geometry of the capillaries array. This sampling procedure save us for implementing an algorithm where each trajectory is weighted differently as a function of their starting velocity amplitude and divergence induced by capillaries array.

- Simulate the spontaneous emission events. Random sampling is a prefect tool to simulate the spontaneous emission process. During the time of flight of the atom, the probability of the spontaneous emission is computed and the recoil process is simulated by a random sampling of the recoil direction. The ability to simulate this dissipative process offers the possibility to estimate some thermodynamic quantities such as the radial temperature in the 2D-MOT trapping.

- Collision process between the atom capture in the 2D-MOT with the background atoms. The implementation of this events are easily simulated with random sampling.

4.2 Atomic source simulation

In this section we describe in detail the main features of our simulation. The work-flow of the numeric simulation for the single trajectory is the following:

a) First, the starting position and starting velocity are sampled via their probability distributions;

b) Then the atom trajectory is computed considering the interaction among the 2D-MOT beams and the push beam. The integration of the equations of motion is performed using the semi-classical of atom-light interaction equations.

c) At the end of the simulation process and considering the time spent in the 2D-MOT region by the atom, the probability of collision between atom and background atoms is estimated.

d) Finally, we check if the computed trajectory is a valid trajectory to the MOT loading process.

e) The algorithm turns back to point **a)** and the simulation is repeated for another atomic trajectory.

We repeat the entire work-flow until a satisfactory number of trajectories N_{sim} are simulated.

Sampling from a probability distribution

When we are dealing with the MC method, the sampling process of the possible physical events from a defined distribution is a crucial point. In this paragraph, the method for sampling a generic random variable x according the probability distribution f is described. Let's consider a generic distribution $f(x)$ of the random variable $x \in [a, b]$. If the analytic form of f^{-1} exists, the sampling of x is obtained by the following formula:

$$x = f^{-1}(y) \tag{4.1}$$

where y is a random number chosen from a uniform random distribution between the interval $[0, f_{\max}]$. This entire procedure continues until a target number of random variables is generated.

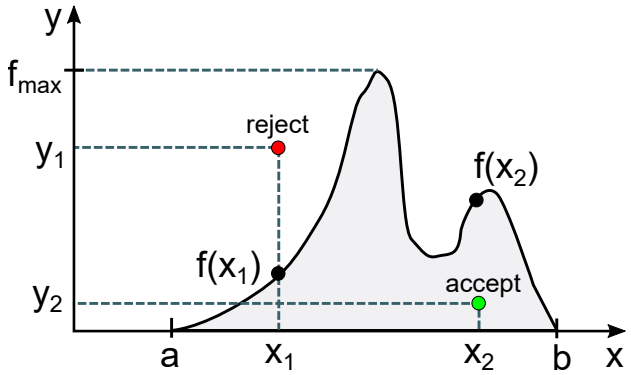

Figure 4.4: Acceptance-rejection cases. The red dot shows the rejection case of variable x_1. The green dot shows the acceptance case of the variable x_2

If the analytic form of f^{-1} does not exist, we can use the rejection-acceptance criteria, also called Von Neumann method [212]. The sampling of random variable x_n according the probability distribution f is summarized in the following steps:

1) First, two random numbers ε_1 and ε_2 are generated via a uniform random distribution between the values [0,1].

2) Then, the value $x_n = a + (b - a)\varepsilon_1$ and the value $y_n = f_{\max}\varepsilon_2$ are computed.

3) A comparison between y_n and $f(x_n)$ is performed. If $y_n \leq f(x_n)$, x_n is accepted as a possible random value form the distribution f. If $y_n > f(x_n)$ the value x_n is rejected. Fig.4.4 shows the rejection case for the random variable x_1 and acceptance case for the random variable x_2.

4) Return to step **1)** until we generate a satisfactory array of values x.

4.2.1 Sampling the starting phase-space domain

The initial space-phase domain is sampled considering the Maxwell-Botlzmann distribution and the geometrical constraints imposed by capillaries.

Sampling the velocities distribution

In this section we illustrate the sampling of the starting velocities effusing from a single capillary. Let's consider the frames of reference reported in the Figs.4.1. Suppose that an atom exits from a capillary along the direction x with velocity amplitude v with and a direction defined by the polar angles θ and ϕ. It is possible to demonstrate that the probability velocity amplitude distribution of an atom

exiting from a capillary is [12, 213]:

$$f(v) = \frac{v^3}{2v_{th}^4} \exp\left(-\frac{v^2}{2v_{th}^2}\right) \tag{4.2}$$

where $v_{th} = \sqrt{k_B T_{\text{oven}}/m_{\text{Sr}}}$ is the thermal velocity computed from a temperature T_{oven}.

Using the acceptance-rejection method with distribution reported on Eq.4.2, it is possible to sample the velocity amplitude v. The angle θ is sampled according a uniform random distribution between the value $\theta = 0$ and $\theta = \theta_{\text{cap}}]$. The angle θ_{cap} is computed as $\theta_{\text{cap}} = a_{\text{cap}}/L_{\text{cap}}$ where a_{cap} is the capillary diameter and L_{cap} is the capillary length. Here we are assuming that the divergence of the thermal atomic beam is mainly related to the divergence of the capillary and we are neglecting a possible extra divergence induced by capillaries misalignments The angle θ_{cap} describes the maximum atom divergence after exit from the capillary without colliding with the capillary walls. The azimuthal angle ϕ can be chosen from a uniform random distribution between the values $[0, 2\pi]$.

After sampling v, θ and ϕ, the Cartesian velocity components v_x, v_y, v_z are computed using the spherical coordinate transformations:

$$v_x = v\cos\theta \tag{4.3}$$
$$v_y = v\sin\theta\cos\phi \tag{4.4}$$
$$v_z = v\sin\theta\sin\phi \tag{4.5}$$

We stress the fact that sampling in the spherical coordinate limits the use of the Von Neumann procedure only for the velocity amplitude instead of all the Cartesian components. Fig.4.5 reports the histograms of the generated velocities v_x, v_y, v_z for $N_{\text{sim}} = 2 \times 10^4$ trajectories and $\theta_{\text{cap}} = 20\,\text{mrad}$. For small atomic beam divergency $\theta \sim 0$, the v_x distribution is well approximated with the Eq.4.2 and the transverses velocities distributions v_y, v_z are well fitted with formula [213, 214]:

$$f(v_\perp) = A|v_\perp| \exp\left(-\frac{v_\perp^2}{2v_{th}^2}\right) \Gamma\left(-\frac{1}{2}, \frac{v_\perp^2}{v_{\text{th}}^2}\frac{1}{\theta_{\text{cap}}^2}\right) \tag{4.6}$$

where A is a normalization constant and Γ is the incomplete Gamma function defined as:

$$\Gamma(\alpha, x) = \int_x^{+\infty} t^{\alpha-1} e^{-t} dt \tag{4.7}$$

In order to speed up the convergence of the MOT flux estimation, we impose a velocity cut-off v_{cutoff} in the sampling process of velocity amplitude v. This cutoff velocity is estimated considering a velocity higher that the 1D capture velocity. In

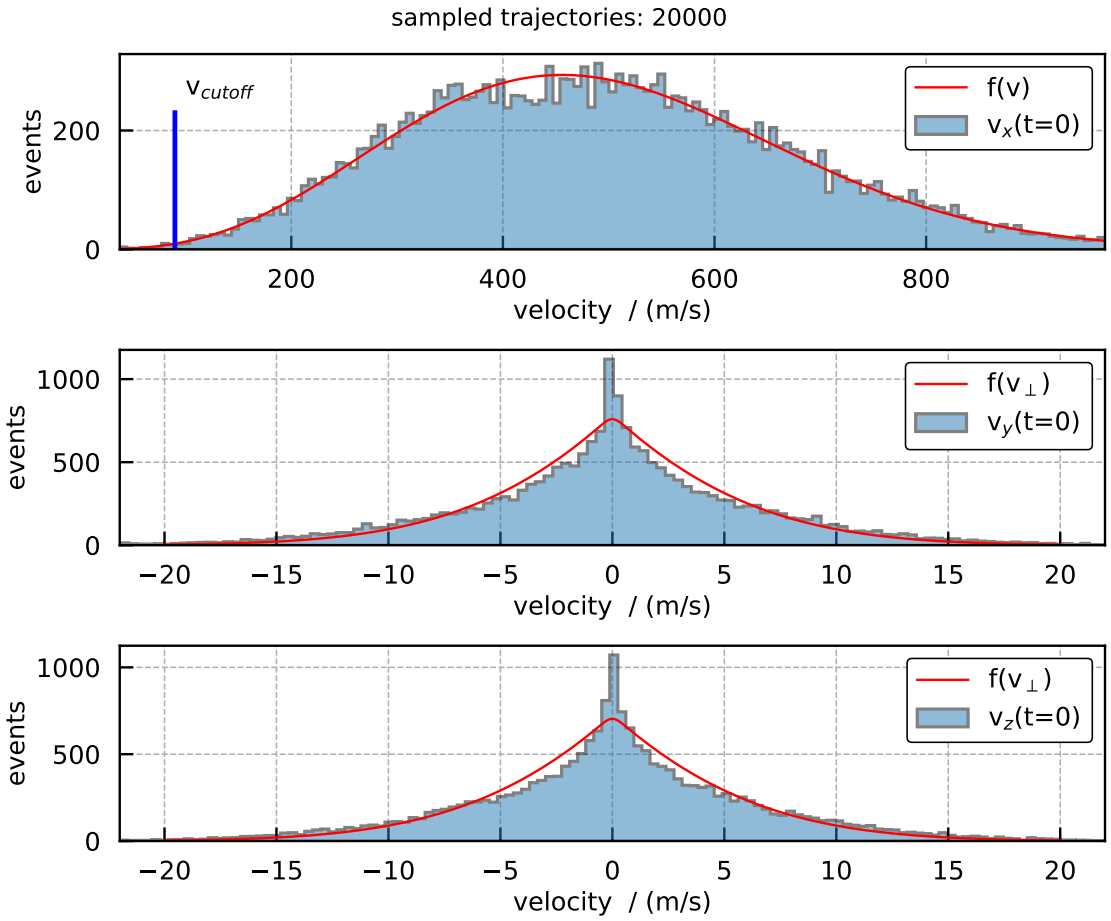

Figure 4.5: Sampled Cartesian velocity distributions (blue bars) are compared with the analytical probability density functions (red dashed lines) considering and oven temperature of $T_{\text{oven}} = 460\,°\text{C}$, and capillary divergence of $\theta_{\text{cap}} = 20\,\text{mrad}$ Histograms are computed for $N_{\text{sim}} = 2 \times 10^4$

fact, we observed that if the starting amplitude velocity is $v > v_{\text{cutoff}}$ the atoms will not trapped. The simulation of all possible starting velocities will simply increase the total computation time without improving the accuracy the trapping efficiency estimation .

Sampling the positions distribution

In this section,we described the sampling of the atoms starting positions exiting from the capillaries. In this sampling procedure we fixed the starting atomic position $x = x_0$ in a plane $y - z$. This means that the atomic position sampling

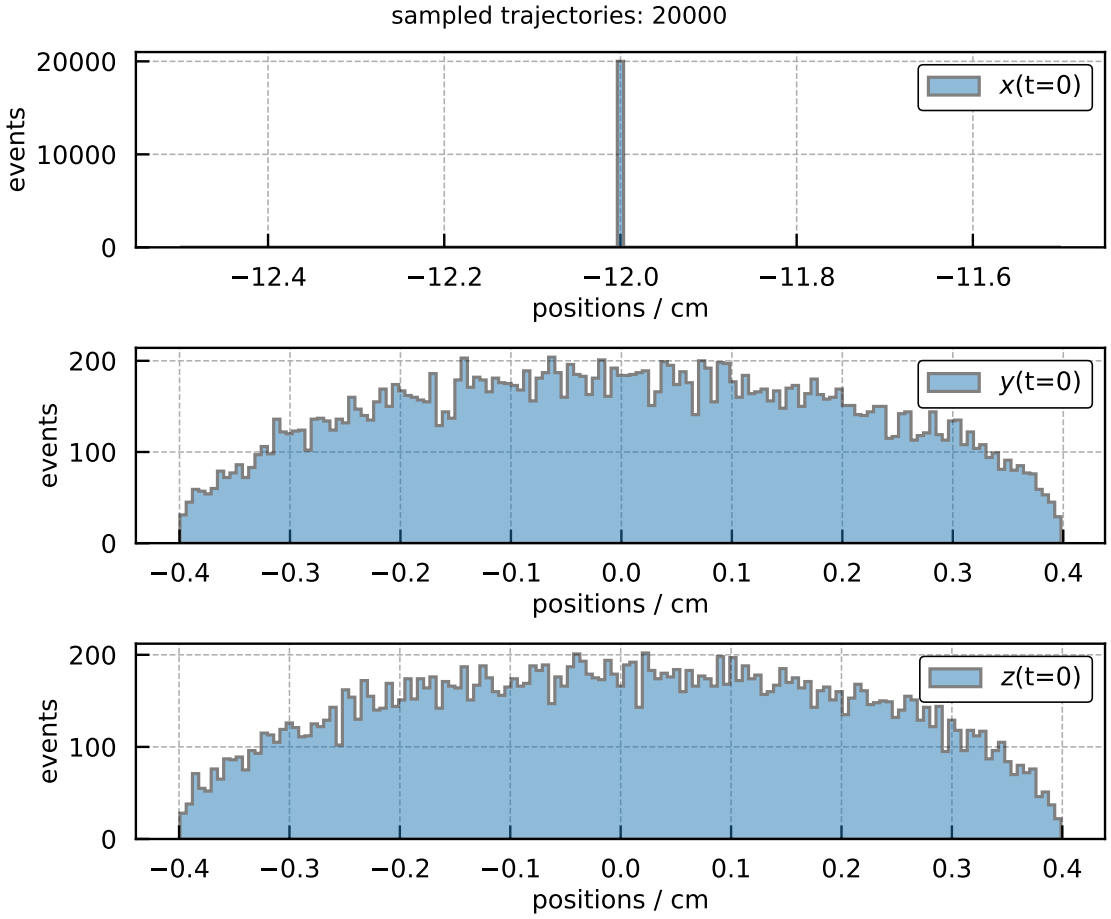

Figure 4.6: Sampled starting spatial distributions. Starting position is fixed at $x_0 = -1.5\,\text{cm}$ and y, z variable are sampled in a disk shape region with maximum radius of $r_{\text{max}} = 0.75\,\text{cm}$. Histograms are computed for $N_{\text{sim}} = 2 \times 10^4$ trajectories

is performed only on the variables y and z. This situation describe reasonably the atoms exit from the capillary where they have the same position along the oven direction by different impact parameter $r = \sqrt{y^2 + z^2}$ relative to the center of the 2D-MOT beams. The sampling of the atomic position (x, y, z), uniformly distributed in a disk shape region with maximum radius r_{max}, is described in the following steps:

1) First, two random number ε_1 and ε_2 uniformly distributed between [0,1] are sampled,

2) Then we compute the values $r = \varepsilon_1 r_{\text{max}}$ and $\alpha = \varepsilon_2 2\pi$.

3) Finally, the starting position x, y, z is computed as:

$$x = x_0 \qquad y = \sqrt{r}\cos\alpha \qquad z = \sqrt{r}\sin\alpha \tag{4.8}$$

The Fig:(4.6) reports the sampled position distributions at $x_0 = -12.0\,\text{cm}$ maximum impact parameter of $r_{\max} = 0.4\,\text{cm}$.

4.2.2 Dynamic: atom-light interaction

Using the semi-classical approximation of atom light-interaction presented in Ch.2, the atom's acceleration due to interaction with an optical beam with saturation intensity s and detuning Δ is computed as

$$\mathbf{a} = \frac{\hbar k_L}{m}\frac{\Gamma}{2}\frac{s}{1+s+4\left(\frac{\Delta_{\text{eff}}}{\Gamma}\right)^2}\hat{\mathbf{k}} \tag{4.9}$$

$$= \frac{\hbar k_L}{m} R\hat{\mathbf{k}} \tag{4.10}$$

$\mathbf{k}_L = 2\pi/\lambda$ is the laser beam momentum, Γ is the scattering rate of the spontaneous emission process and $\hat{\mathbf{k}}$ is the unitary vector of the laser direction. The quantity R in the Eq.4.10 describes the photon scattering rate. At given velocity $\mathbf{v}$ and position $\mathbf{r}$ of the atom, the effective detuning is estimated as:

$$\Delta_{\text{eff}}(\mathbf{r}, \mathbf{v}) = \Delta + \mathbf{k}_L \cdot \mathbf{v} + \hbar^{-1}\mu_B|\mathbf{B}(\mathbf{r})| \tag{4.11}$$

where $\mathbf{B}$ is the 2D-MOT mangetic field estimated with Eq.3.14. The local saturation intensity is computed as:

$$s(\mathbf{r}) = s_0 \exp\left(-\frac{2|\mathbf{r}\times\hat{\mathbf{k}}|^2}{w^2}\right) \tag{4.12}$$

where s_0 is the intensity peak, w is the waist of the optical beam and where the vector product $\mathbf{r}\times\hat{\mathbf{k}}$ is the distance between the atom position and the center of the laser line propagation described by the unitary vector $\hat{\mathbf{k}}$. Considering the aperture of the optics elements, a spatial cut-off of $|\mathbf{r}\times\hat{\mathbf{k}}| < 1.2\,\text{cm}$ in the local saturation intensity s is also applied. Using the acceleration expressed in Eq.4.10, atomic trajectories at given initial conditions $\mathbf{r}(t=0)$ and $\mathbf{v}(t=0)$ are computed via the Runge-Kutta algorithm [215].

In the atom's acceleration, we also consider the spontaneous emissions processes. For each time step Δt, the recoil heating is estimated as [85, 201]:

$$\Delta\mathbf{p} = \sqrt{N_s}\hbar k_L \hat{\mathbf{e}} \tag{4.13}$$

where $\hat{\mathbf{e}}$ is a random unitary vector and $N_s = R\Delta t$ is the total number of absorption-spontaneous emission cycles in the time Δt. After these considerations, the generic atom-light interaction during the time step Δt can be written as:

$$\mathbf{a} = \frac{\hbar k}{m} R_s \hat{\mathbf{k}} + \frac{\hbar k}{m} \frac{\sqrt{N_s}}{\Delta t} \hat{\mathbf{e}} \tag{4.14}$$

$$= \frac{\hbar k}{m} R_s \left[\hat{\mathbf{k}} + \frac{1}{\sqrt{N_s}} \hat{\mathbf{e}} \right] \tag{4.15}$$

The last relation points out that the effect of spontaneous emission in the atom's dynamics is weighted as $N_s^{-1/2}$ in comparison to the dissipative force.

Atom acceleration

Regarding the atom trajectory, the total acceleration in the atomic source is computed considering the atom interaction with the 2D-MOT beam, the possible interaction with the sideband beams and with the push beam. The total acceleration is written as:

$$\mathbf{a} = \mathbf{a}_{\text{2D-MOT}} + \mathbf{a}_{\text{side}} + \mathbf{a}_{\text{push}} \tag{4.16}$$

Considering the generalization at higher saturation intensity exposed in Sec.2.3.2, the atom interaction with the 2D-MOT beams becomes:

$$\mathbf{a}_{\text{2D-MOT}} = \sum_{i=1}^{N_b=4} \left[\frac{\hbar k}{m} \frac{\Gamma}{2} \frac{s_i}{1 + N_b s_i + 4\left(\frac{\Delta_i}{\Gamma}\right)^2} \hat{\mathbf{k}}_i + \frac{\hbar k}{m} \frac{\sqrt{N_s^i}}{\Delta t} \hat{\mathbf{e}}_i \right] \tag{4.17}$$

where $N_b = 4$ is the number of beams and $\hat{\mathbf{k}}_i$ describe all the possible unitary vectors in the $x - z$ plane for the 2D-MOT beams and s_i is the saturation parameter of each beams. The same acceleration is computed for the sidebannd beams. The atom's acceleration by the push beam is written as:

$$\mathbf{a}_{\text{push}} = \frac{\hbar k}{m} \frac{\Gamma}{2} \frac{s}{1 + s + 4\left(\frac{\Delta}{\Gamma}\right)^2} \hat{\mathbf{y}} + \frac{\hbar k}{m} \frac{\sqrt{N_s}}{\Delta t} \hat{\mathbf{e}} \tag{4.18}$$

4.2.3 Background collision probability

In this section we estimate the collision time τ_{coll} among the atoms in the hot atomic beam that load the 2D-MOT. This estimation is performed considering the oven temperature T_{ov}, the Sr collisional cross section σ_{Sr} and taking into account the atomic flow regime out of the capillaries. The idea is to compare the collision time and the time spent by the atom in the 2D-MOT in order to exctract the collision probability of the atomic trajectories with hot atoms effusing from the oven.

The collision probability among the atoms in a molecular beam can be reasonably approximated as one-third of the collision probability among the atom in a ideal gas [216]. As already computed in Eq.3.10, at the oven temperature of $T_{ov} = 460\,°C$ the estimated atomic flux entering in the 2D-MOT region is :

$$\Phi_{ov}(T_{ov}) = 5.8 \times 10^{14}\,\text{atoms/s}$$

Using the ideal gal law, the atomic beam density can be computed according the following equation:

$$n_{beam} = \frac{\Phi_{ov}}{\bar{v} N_{cap} \pi r_{cap}^2} = 1 \times 10^{17}\,\text{atoms/m}^3 \tag{4.19}$$

where $r_{cap} = 0.2\,\text{mm}$ is the radius of the capillary, $N_{cap} = 150$ is the number of capillaries and interstices and $\bar{v}$ is the root mean square velocity of the distribution defined in Eq.4.2 expressed as [12, 216]:

$$\bar{v} = \sqrt{\frac{8\pi}{9}\frac{k_B T_{oven}}{m_{Sr}}} = 503\,\text{m/s} \tag{4.20}$$

From Eq. 4.19 an considering the scaling factor of [216], it is possible to estimate the collision mean free path λ_{coll} and the collision time τ_{coll} of the Sr atoms in the 2D-MOT region as:

$$\lambda_{coll} = 3\lambda = 3(\sqrt{2} n_{beam} \sigma_{Sr})^{-1} = 25\,\text{m} \tag{4.21}$$

$$\tau_{coll} = 3\lambda/\bar{v} = 50\,\text{ms} \tag{4.22}$$

where in this case $\bar{v} = \sqrt{2k_B T_{ov}/m_{Sr}} = 379\,\text{m/s}$ and $\sigma_{Sr} = 8.17 \times 10^{-19}\,\text{m}^2$ is computed according Eq.3.7. The factor 3 comes from the consideration discussed before [216].

Collision probability

Having the collision time τ_{coll}, we can estimate the time scale of collision process between an atom trap in the 2D-MOT region and a hot-atom of the thermal atomic beam. The interaction volume where the collision may happen is enclosed in the 2D-MOT beams intersection. In this treatment, we neglect the cold collision among atoms in the 2D-MOT.

Dealing with hot collisions, the lower is the time τ_{2D} that an atom spend in the 2D-MOT interaction region, the lower is the collision probability with another atom that comes from the oven. Following this simple consideration, a reasonable collision probability can be expressed as [101]

$$f_{coll}(\tau) = 1 - \exp\left(-\frac{\tau}{\tau_{coll}}\right) \tag{4.23}$$

Using the acceptance-rejection method described in Sec.(4.2) the Monte Carlo implementation is straightforward. In this case we use the acceptance-rejection method in order to simulate if the atom during the time spent in the 2D-MOT region τ_{2D} collides with hot atoms:

1) For each particle that goes in the MOT region we compute the factor $f_{\text{coll}}(\tau_{2D})$ defined according Eq.4.23.

2) Then we compute the random number ε between [0,1]. If $f_{\text{coll}}(\tau_{2D}) < \varepsilon$, no collision occurs and the trajectory is considered as a possible trajectory for MOT loading. If $f_{\text{coll}}(\tau_{2D}) \geq \varepsilon$, the trajectory is not considered as a possible trajectory for MOT loading.

4.2.4 Exit conditions

Once the time of atomic trajectory reaches $t = t_{\text{sim}}$, the trajectory evolution stops and the final values $\mathbf{r}(t_{\text{sim}})$ and $\mathbf{v}(t_{\text{sim}})$ are stored. At this point we have to decide if the simulated trajectory is a possible trajectory for the MOT loading process.

An important parameter is the trajectory divergence computed along the push direction (y direction). The trajectory divergence θ_{tr} is defined as:

$$\theta_{\text{tr}} = \arctan\left(\frac{|\mathbf{r}(t_{\text{sim}}) \times \hat{\mathbf{y}}|}{|\mathbf{r}(t_{\text{sim}}) \cdot \hat{\mathbf{y}}|}\right) \tag{4.24}$$

In our simulation, two cases are considered:

- If we are studying the MOT loading rate, the maximum divergency admitted is estimated as

  $$\theta_{\text{geo}} \sim w_{\text{MOT}}/d = 6.2\,\text{mm}/370\,\text{mm} = 16\,\text{mrad}$$

  where w_{MOT} is the MOT waist beam and d is the measured distance between the 2D-MOT center to the MOT center.

- If we are studying only the atomic flux rate without the presence of the MOT capture, the maximum admitted divergency is

  $$\theta_{\text{geo}} \sim a_{\text{DPC}}/L_{\text{DPC}} = 2\,\text{mm}/22.8\,\text{mm} = 88\,\text{mrad}$$

  where a_{DPC} and a_{DPC} are respectively the diameter and the length of the differential channel.

If the final trajectory divergence θ_{tr} computed along the axis y is lower than the geometrical divergence θ_{geo}, the trajectory is consider as a valid process to the MOT loading, otherwise it is rejected.

4.2.5 Simulation parameters and code performance

The input parameters used for the atomic source simulation are reported on Tab.4.2. These parameters are kept fixed during the simulations.

	symbol	value
SAMPLING STARTING ATOMS' VELOCITY		
oven temperature	T_{ov}	460 °C
capillary divergence	θ_{cap}	20 mrad
velocity cut-off	v_{cutoff}	90 m/s
SAMPLING STARTING ATOM'S POSITION		
starting x position	x_0	−12.0 cm
maximum radius	r_{max}	0.4 cm
MOT PARAMETERS		
2D-MOT magnetic gradient	b	0.2245 T/m
2D-MOT e^{-2} beam radius	$w_{\text{2D-MOT}}$	9.5 mm
sideband e^{-2} beam radius	w_{side}	9.5 mm
push e^{-2} beam radius	w_{push}	0.81 mm
COLLISION PROBABILITY		
collision time	τ_{coll}	81 ms
TRAJECTORY COMPUTATION		
time step	Δt	50 µs
simulation time	t_{sim}	4 ms
exit divergence	θ_{geo}	16 mrad
simulated trajectories	N_{sim}	2×10^4

Table 4.2: Input parameter for the atomic source simulation

Our simulation is written in Python . In order to increase the code performance we use the Numba compiler [217]. Code performances are reported in the Fig.4.7 as a function of the number of trajectories simulated. For each N_{sim}, we computed the MOT loading rate as $r = N_{\text{cap}}/N_{\text{sim}}$ where N_{cap} is the number of the trajectories trapped in the MOT. For all trajectories N_{sim}, we run 5 simulations and we estimate the mean ratio $\langle r \rangle$ and its standard deviation σ_r.

The blue line in Fig.4.7 reports the percentage relative error $\sigma_r / \langle r \rangle$. The red line reports the computation time in order to simulate N_{sim} trajectories. For $N_{\text{sim}} = 2 \times 10^4$ we obtain a $\sigma_r / \langle r \rangle \sim 1.5\%$ with a computation time $T_{\text{sim}} \sim 1.5$ min. The hardware used for the MC simulation was a Lenovo Thinkstation, Intel(R) Core(TM) i7-7700 CPU @ 3.60 GHz, with 32.0 GB of RAM.

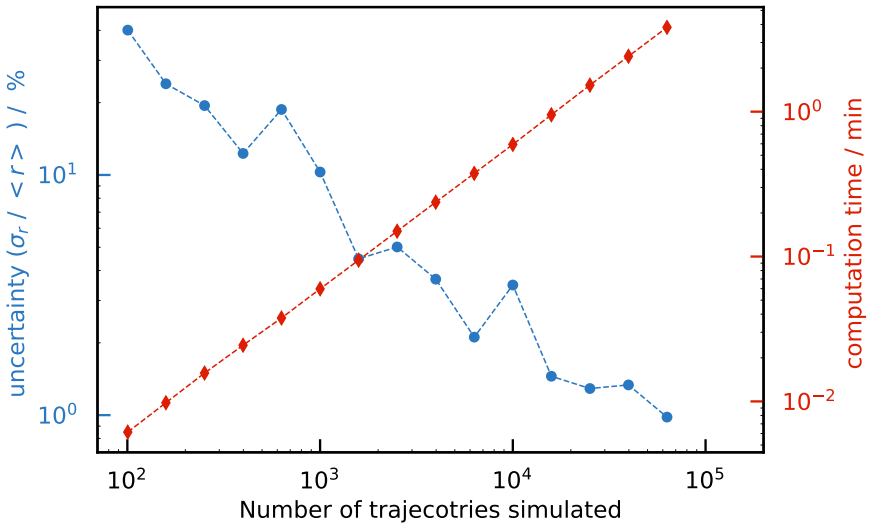

Figure 4.7: Code performance. Blue points represent the relative error of simulation as a function of the number of trajectories simulated. The red points indicate the corresponding time needed to compute the trajectories

4.3 MOT loading rate estimation.

In this section we explain how the simulation results can be linked to the MOT loading rate estimation. After computing the trajectories of N_{sim} atoms, we count the number of the trajectories that fulfil the MOT loading process. After post selecting N_{cap} valid trajectories, the number $r_{\text{MC}} = N_{\text{cap}}/N_{\text{sim}}$ is estimated as the trapping efficiency of our MOT.

We estimate the expected atomic loading rate L_{MOT} in the MOT for a given atomic 2D-MOT atomic flux $\Phi_{\text{ov}} = 5.8 \times 10^{14}$ atoms/s as previously evaluated in the Sec.3.2.5. The two factors can be linked each others with the following relation:

$$L_{\text{MOT}} = r\,\Phi_{\text{ov}} \tag{4.25}$$

where the parameter r expresses the single atom probability that starting form the oven it enters in the 2D-MOT region and goes towards the MOT region. According our simulation, we can only relate the parameter r_{MC} expressed in Eq.4.25 as a ratio between the number of the trajectories captured in our MC simulation N_{cap} with the number of the simulated trajectories N_{sim}. For a given atomic source configuration, in order to extract more efficiently a value r, we sample only atoms with initial velocity amplitude $v(t=0) < v_{\text{cutoff}}$. This means that our simulated capture ratio r is referred to a $\Phi_{\text{ov}}^{\text{cutoff}}$ instead of Φ_{ov}. The relation between the Φ_{ov}

and $\Phi_{\text{ov}}^{\text{cutoff}}$ is expressed as:

$$c = \frac{\Phi_{\text{ov}}^{\text{cutoff}}}{\Phi_{\text{ov}}} = \int_0^{v_{\text{cutoff}}} f(v)dv = 1.53 \times 10^{-3} \tag{4.26}$$

where $f(v)$ is the velocity distribution in the Eq.4.2. Using the c parameter expressed in Eq.4.26, we can relate the capture ratio computed with the MC simulation r_{MC} with the probability r of the Eq.4.25 as $r = r_{\text{MC}}c$ and so we can provide and estimation of the MOT loading rate as:

$$L_{\text{MOT}} = r_{\text{MC}}\, c\, \Phi_{\text{ov}} \tag{4.27}$$

The last equation related the expected MOT loading rate considering the atomic flux estimation of oven and the trapping efficiency given by the simulation results.

Chapter 5

Atomic source characterization

As already described in Ch.3, our atomic funnel generated by 2D-MOT and push beam is used as cold atomic beam source. Atomic source performance has to satisfy two requirements. The first is the ability to efficiently capture atoms in 2D-MOT region from a thermal atomic beam and this propriety is mainly related to the optical and magnetic proprieties of the 2D-MOT. The second requirement is to move efficiently atoms from a 2D-MOT toward the MOT region. This transfer process is regulated by the push beam proprieties. In this chapter, experimental characterizations of the atomic source are compared with numeric simulations explained in Ch.4. In this chapter it is also experimental demonstrated a novel trapping scheme used to enhance 2D-MOT loading by means of a sideband beam added to the 2D-MOT beams. Enhancement factor and the related propriety of this new trapping method are discussed in detail. We also report the first signature of MOT enhancement with the repumping lasers.

5.1 2D-MOT optimization

In following characterizations, the MOT fluorescence signal is used as tool for the atomic source optimization. During the optimization, we assume that the number of atoms captured in the MOT region is proportional to the number of atoms captured in the 2D-MOT region at fixed push beam parameters. Following these considerations, our strategy is to maximize the MOT signal changing independently the experimental parameters of 2D-MOT beams and then the push beam. Considering the number of atoms in the MOT, we study the sensitivity of the atomic source parameters as a function of the 2D-MOT beams dimensionality and its properties such as the saturation intensity and detuning. We also present the optimization of the push parameter as a function of its saturation intensity and detuning.

The position of the permanent magnets are fixed maximizing the MOT fluorescence signal. During the magnets alignment procedure, it was paid attention to the shape of the atom cloud trapped in the 2D-MOT region. The shape of the atomic cloud provided a direct information of the zero regions of the magnetic field, magnets were aligned in order to generate a cigar shape cloud along the push direction. In order to reduce the atom losses during the push transfer, the atomic cigar cloud was superimposed to the push beam and at the same time, put in a concentric way respect to the differential vacuum channel. At the optimized magnets positions, we estimated a magnetic gradient of $b_{\text{2D-MOT}} = 0.2\,\text{T/m}$. This procedure was difficult to replicate exactly and so we decided to perform the atomic source optimization at fixed magnetic gradient of the 2D-MOT. The same approach was adopted in [103, 104, 107]. In all the optimization above, we consider the MOT beam dimension $w_{\text{MOT}} = 6.2\,\text{mm}$, the total saturation intensity $s_{\text{MOT}} = 2.5$, the detuning $\Delta_{\text{MOT}}/\Gamma = -1.2$, the MOT magnetic gradient of $b_{\text{MOT}} = 0.4\,\text{T/m}$ and a resonant push with $s_{\text{push}} = 0.34$ and $w_{\text{push}} = 0.81\,\text{mm}$.

5.1.1 Beams geometry

As already pointed out in Ch.2, the capture efficiency of the 2D-MOT is related to the beams dimensionality. Eq.2.37 and Eq:2.39 show that the finite beams dimensionality affects the 2D-MOT capture velocity v_{capt} and its captured number of atoms N with the scaling relations $N \sim v_{\text{capt}}^4 \sim w^2$ where w is the 2D-MOT beams radius. In this section, the effect of the 2D-MOT beam dimensionality to the final number of atoms capture in the MOT is investigated.

The 2D-MOT beam size is set by a telescope of two convergent lenses. The position of the first lens of the telescope is chosen in order to increase the AOM diffraction efficiency while the second lens is used to enlarge the output beam to the target size. Knowing the waist of the input beam, it possible to compute the output beam size and the related beam divergence after the telescope considering each lenses positions and their focal power [218]. We used two different focal lenses in the final lens of the telescope component in order to study two different 2D-MOT waists. Their positions in the telescope are optimized in order to minimizing the output beam divergence. Using two different lenses, we study the effect of two different 2D-MOT e^{-2} beam radius on the atoms: $w_1 = 6.7\,\text{mm}$ and $w_2 = 9.5\,\text{mm}$. Because of the related Rayleigh ranges are larger than 300 m, we approximate the beam radius as the beam waist.

The Fig.5.1(a) reports the number of atoms captured by the MOT as a function of the 2D-MOT optical power considering the two different waist configurations w_1 (purple triangles) and w_2 (blue points). At fixed 2D-MOT power beam, the saturation intensity perceived by atoms in the 2D-MOT is estimated

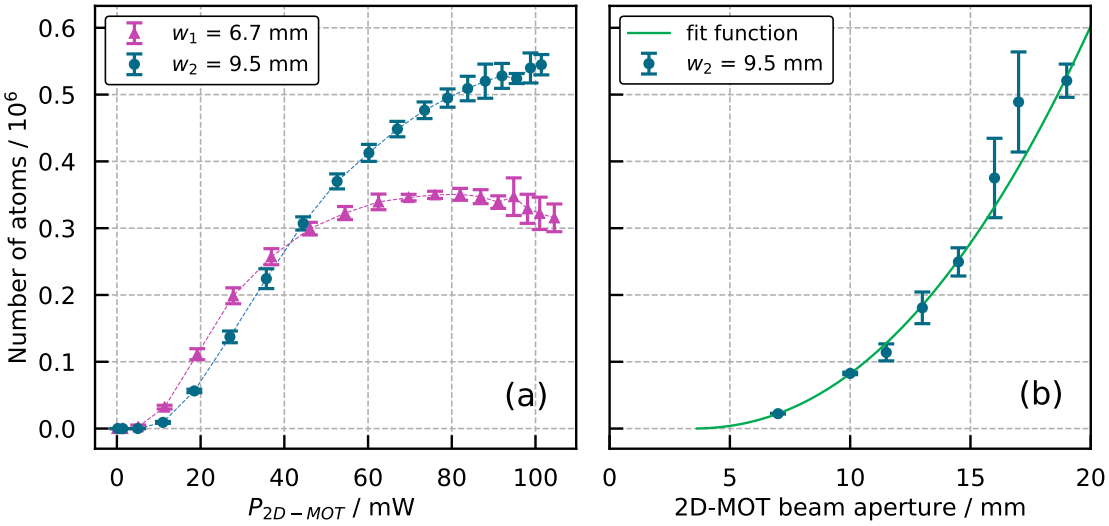

Figure 5.1: Effect of the beams dimension in the 2D-MOT **(a)** Number of atom in the MOT as a function of 2D-MOT optical power. The blue points (purple triangles) are the obtained with a 2D-MOT waist of $w_2 = 9.5\,\text{mm}$ ($w_1 = 6.7\,\text{mm}$). **(b)** Number of atoms in the MOT as a function of the 2D-MOT beam aperture. The blue points are obtained with a $w_{\text{2D-MOT}} = 9.5\,\text{mm}$ at fixed optical power $P_{\text{2D-MOT}} = 100\,\text{mW}$ which corresponds to a saturation level of $s = 3.3$. The green line is the associated fit function.

as $s = 2(2P_{\text{2D-MOT}}/\pi w^2)/I_0$, where $I_0 = 41\,\text{mW/cm}^2$ is the saturation intensity of $^1\text{S}_0 - ^1\text{P}_1$ transition, w is the 2D-MOT beam waist and the extra factor of 2 takes into account the retro-reflection component of the 2D-MOT beams. At $P_{\text{2D-MOT}} = 100\,\text{mW}$, the corresponding saturation parameters are $s_1 = 3.3$ and $s_2 = 6.9$. As shown in the Fig.5.1(a), the larger beam waist increases the 2D-MOT capture efficiency by a factor 1.7(1) at $P_{\text{2D-MOT}} = 100\,\text{mW}$. We also observe that the two waists curves w_2 and w_1 at $P_{\text{2D-MOT}} \simeq 50\,\text{mW}$ have the same capture efficiency with different gain slope. In the curve with a smaller waist w_1 it is possible observe a saturation in the capture efficiency due to the high intensity of the trapping beams while the in the curve with larger waist w_2 is still in the linear region of the capture efficiency gain. We do not investigate larger waist of w_2 because the related 2D-MOT beams were cut by various optical elements present in the 2D-MOT path. For these reasons we decided to keep the 2D-MOT beam waist at $w_{\text{2D-MOT}} = 9.5\,\text{mm}$

Another analysis related to the 2D-MOT beam dimensionality is reported in the Fig.5.1(b). In this analysis, we modify the 2D-MOT beam size by means of a iris diaphragm. At fixed 2D-MOT waist $w_{\text{2D-MOT}} = 9.5\,\text{mm}$ and power $P_{\text{2D-MOT}} = 100\,\text{mW}$, the number of atoms captured in the MOT is recorder as a function of the iris aperture a (blue point). With this analysis, we studied the effect of the finite

size 2D-MOT beams at fixed maximum saturation intensity perceived by atoms. In particularly, we study the effect of the Gaussian beam tails in the 2D-MOT capture process. The experimental point are fitted with function $N(a) = C(a - a_0)^n$, where a_0 is an aperture offset, n is the scaling factor between the capture number of atom and the beam size, and C is a conversion factor. After the fitting procedure we obtain $n = 2.1(1)$ and $a_0 = 3.4(5)$ mm. The fit result of n is in accordance with the expected scaling law discussed before in Sec.2.4.1. The aperture offset a_0 set a lower value of the 2D-MOT beam dimension useful for trapping. This can be explained considering a non perfect crossing of the 2D-MOT beams, and so a non perfect trapping configuration due to a small misalinement among the crossed 2D-MOT beams, push beam and zero magnetic field region.

5.1.2 Optical parameters

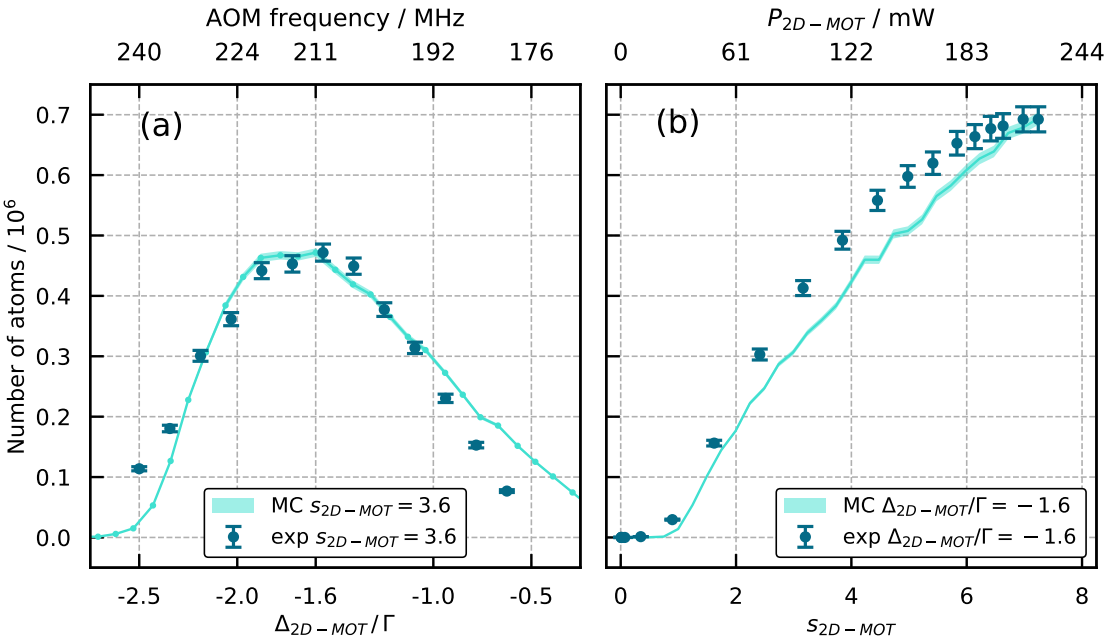

Figure 5.2: 2D-MOT experimental characterization. **(a)** Number of atoms in the MOT as a function of the 2D-MOT detuning at fixed saturation $s_{\text{2D-MOT}} = 3.6$. The blue points are the experimental values of the number of atoms in the MOT. The cyan regions are the MC simulations properly normalized to the experimental points. **(b)** Number of atoms in the MOT as a function of the 2D-MOT saturation at fixed $\Delta_{\text{2D-MOT}} = -1.6\,\Gamma$.

The 2D-MOT characterizations as a function of the optical beam proprieties are reported in Fig.5.2 MOT fluorescence is measured at oven temperature $T_{\text{ov}} = 460\,^{\circ}\text{C}$ and at resonant push intensity $s_{\text{push}} = 0.34$ and e^{-2} waist on the atoms is $w_{\text{push}} = 0.81$ mm. For a given total optical power $P_{\text{2D-MOT}}$, the saturation intensity

is computed considering the waist beams $w_{\text{2D-MOT}} = 9.5\,\text{cm}$.

The Fig.5.2(a) reports the measured MOT number of atoms as a function of 2D-MOT beam detuning (blue points) taken at fixed 2D-MOT intensities $s_{\text{2D-MOT}} = 3.6$. The experimental optimization shows an optimum value at $\Delta_{\text{2D-MOT}} = -1.6\,\Gamma$ with a FWHM of $1.5\,\Gamma$. Our experimental investigation (blue point) is compared with the result of our simulation (cyan dots). The maximum value of simulations are normalized to the experimental maximum point. We notice that simulations are in good agreement with the experimental data. Fig.5.2(b) reports the MOT number of atoms as a function of 2D-MOT saturation intensity (blue points) at fixed 2D-MOT detuning $\Delta_{\text{2D-MOT}} = -1.6\,\Gamma$. From the experimental characterization we observe that the MOT number of atoms increases as a function of the saturation intensity. At higher value of the saturation intensity, the experimental trend seems to saturate while the simulating one (cyan dots) does not show an equivalent trends. Also in this case, simulations overall predicts experimental trends.

5.1.3 Atomic transfer process

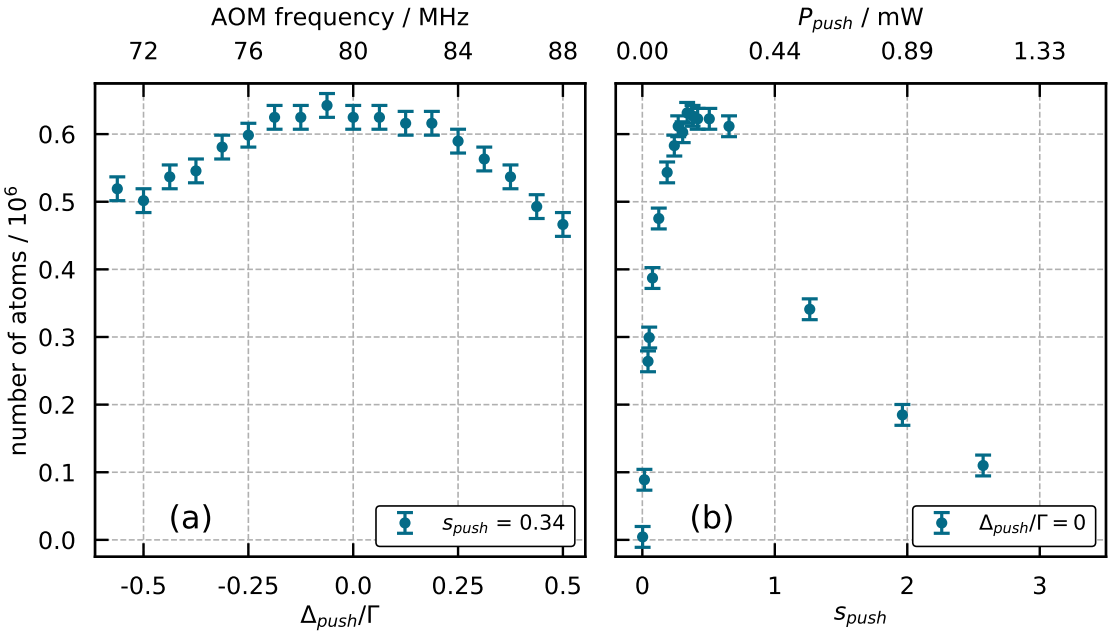

Figure 5.3: Push characterization. **(a)** Number of atoms in the MOT as a function of the push detuning at fixed saturation $s_{\text{push}} = 0.34$ **(b)** Number of atoms in the MOT as a function of the push saturation at $\Delta_{\text{push}}/\Gamma = 0$.

In this section we study the MOT capture efficiency as a function of the optical transfer parameters given by the push beam The measurements reported in Fig.5.3

were taken at $T_{ov} = 460\,°C$ and with $s_{2D\text{-}MOT} = 6.56, \Delta_{2D\text{-}MOT}/\Gamma = -1.6$. The push beam radius e^{-2} on the atoms is $\omega_{push} = 0.81\,mm$.

The Fig.5.3(a) shows the MOT number of atoms as a function of the push detuning beam at $s_{push} = 0.34$. From this plot we observe that the best transfer efficiency is obtained around the resonance condition of the push beam. Fig.5.3(b) reports the MOT number of atoms as a function of the push saturation parameter. These characterizations were taken with resonant push beam $\Delta_{push} = 0$. From the Fig.5.3(b) we observe that the maximum number of atoms is achieved at $s_{push} = 0.34$ which corresponds to an optical power of $0.15\,mW$. At higher push intensity, the transfer efficiency starts to decrease. A possible explanation to this behaviour is provided considering the possible mismatch between the atomic longitudinal velocity, given by the push beam, and the final MOT capture velocity, defined by the final trapping region. At higher push saturation parameter, the mean atomic velocity becomes larger than the MOT capture velocity and so generating a reduction of MOT trapping efficiency. This effects will be discussed in the next section.

5.2 Proprieties of cold atomic beam

In this section, the proprieties of the cold atomic beam generated from atomic source are studied. This experimental investigation is performed observing the fluorescence signal between the atomic beam generated from the atomic source and a probe beam. The probe beam is place perpendicularity to the atomic beam along the vertical direction of the MOT beam. The probe beam was aligned in order to maximize the collected fluorescence and slightly tilted in order to avoid the retro-reflection given by the vertical MOT mirror. This fluorescence detection procedure was employed in order to study the atomic beam proprieties without considering the perturbation induced by the MOT.

The reduction in the MOT atoms number at higher push intensity can be explained considering the velocity mismatch between the trapping velocity of the MOT and the longitudinal velocity of the cold atomic beam. If the push intensity increases, the velocity of the cold atomic beam will increases as well. In Fig.5.4, the push intensity characterization (blue points) is compared with the MC simulation (cyan dots). Considering the MOT beam dimension $w_{MOT} = 6.2\,mm$, the total saturation intensity $s_{MOT} = 2.5$, the detuning $\Delta_{MOT}/\Gamma = -1.2$ and the magnetic gradient $b_{MOT} = 0.4\,T/m$ we numerically estimate the MOT capture velocity of $v_{cap}^{MOT} \sim 60\,m/s$. With this parameter we performed a MC simulation considering

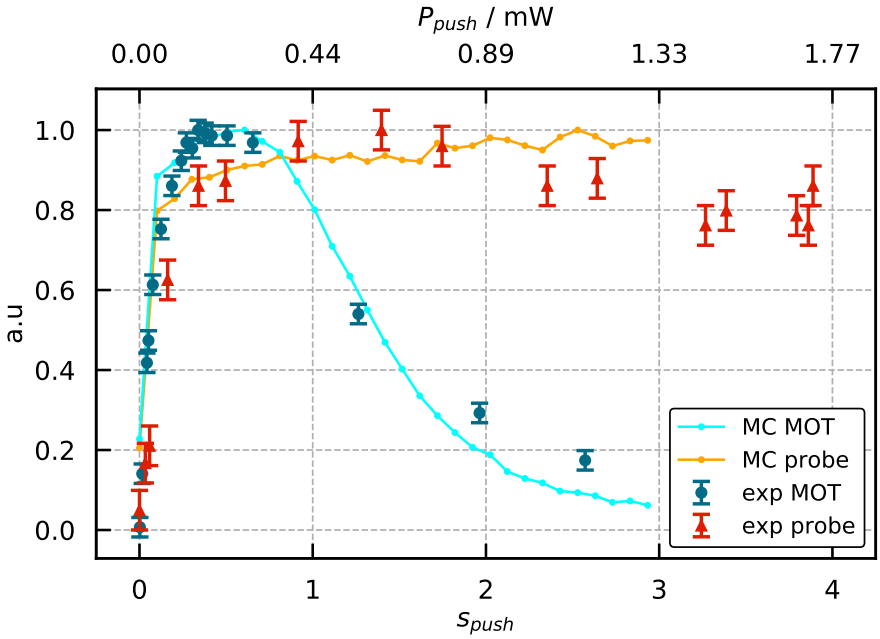

Figure 5.4: Comparison between MOT and probe collected fluorescences with their respective MC simulations. Blue points describe the number of atoms in the MOT as a function of the push intensity. Cyan dots are the associated MC simulation. In this simulation, a MOT capture velocity of $v_c = 60\,\mathrm{m/s}$ is imposed. Red triangles are the probe fluorescence as a function of s_{push}. Orange dots are the associated MC simulation. For comparison purpose, all the sets are normalize to their maximum values

the maximum longitudinal velocity admitted below of $v_{\mathrm{cap}}^{\mathrm{MOT}}$. Adding this restriction as a maximum longitudinal velocity admitted during the atomic transferring process, the simulation trend (cyan dots) well describes the experimental trend. To confirm the mismatch velocity hypothesis, we also measure the probe fluoresce signal as a function of the push saturation intensity s_{push} (red triangles) because this measure is not dependent on MOT capture velocity. In this case, a decreasing trend of the fluorescence signal as a function at higher push intensity is not observed. Removing the constraint of the MOT capture velocity in the MC simulation (orange dots) we correctly predict the experimental trend of probe fluorescence.

In conclusion, the Fig.5.4 shows us that the capture efficiency on the MOT region mainly depends on the longitudinal velocity of our cold atomic beam. At higher longitudinal velocity compare the MOT capture velocity, the MOT is not able to efficiently capture the flux coming from the atomic source.

5.2.1 Longitudinal velocity

The push beam is the parameter that control the transfer process of the atoms from the atomic source to the final MOT region. In this section we want to characterize the longitudinal velocity of the cold atomic flux emitted from the atomic source as a function of the push saturation intensity s_{push}.

Our experimental procedure is reported in Fig.5.5(a). We program an optical push impulse (red dashed line) with finite time duration by tuning the the RF signal injected to the push AOM. The optical push impulse interact with the atoms trapped in the 2D-MOT accelerating them toward the science cell. When the atoms reach the science cell they interact with the probe beam, the fluorescence light $f(t)$ generated is collected with the photodiode as a function of the time as show in the fig.5.5. In the Fig.5.5, we report different fluorescence traces as a function of the push saturation parameters. The total push pulse duration is $\Delta t_{\text{push}} = 5\,\text{ms}$. Apart from the amplitude of the collected fluorescence signal, no differences in the fluorescence profile $f(t)$ were observed changing to $\Delta_{\text{push}} = 2\,\text{ms}$ which means that deviations of the $f(t)$ caused by a longer push pulse is negligible. In this analysis, the possible role of the transverse velocity components are neglected. The trace $f(t)$ reported on Fig.5.5(a) is obtained after averaging 32 traces. The longitudinal velocity distribution is estimated knowing fluorescence time distribution $f(t)$ and the distance $d = 36.5(5)\,\text{cm}$ between the 2D-MOT center and interaction region of probe and cold atomic beam. In the Fig.5.5(b), we compute the longitudinal velocity distribution as $f(v) = f(d/t)$. From these profiles we extrapolate the maximum value v_L of $f(v)$ which is the most probable longitudinal velocity

Fig.5.5(b) reports the velocity distribution $f(v)$ obtained from $f(t)$ at different push saturation s_{push}. The signal $f(t)$ is sampled with a time step $\delta t = 0.1\,\text{ms}$ within a total time $T \simeq 100\,\text{ms}$. According our temporal sampling, we are able to detect a minimum velocity of $v_{\text{min}} = d/T = 3.65\,\text{m/s}$ and a maximum velocity of $v_{\text{max}} = \delta t/d = 3.65 \times 10^3\,\text{m/s}$. Information about the higher velocity components are limited by the photodetector and pre-amplifier characteristic time scale $\tau_{\text{PD}} = 6.5\,\text{ms}$ which give us $v_{\text{PD}} = d/\tau_{\text{PD}} = 56\,\text{m/s}$. This means that the estimate velocity distribution between $v_{\text{min}} < v < v_{\text{PD}}$ are not affected by our acquisition method. The obtained velocity are then corrected considering also a delay time induced by the acquisition system. The estimated delay time of acquisition method is $\tau_{\text{lag}} \simeq \tau_{\text{PD}}$ and longitudinal velocity is computed as $f(v) = f(d/(t - \tau_{\text{lag}}))$. The effect of the photodiode is also observe in the velocity profiles $f(v)$, at velocity larger than v_{PD} (which means at time-scale shorter than $t < \tau_{\text{PD}}$) the traces start to broaden generating a non symmetric signal for high velocities. This non symmetric broadening is neglected if all the signal information $f(v)$ is below the v_{PD}.

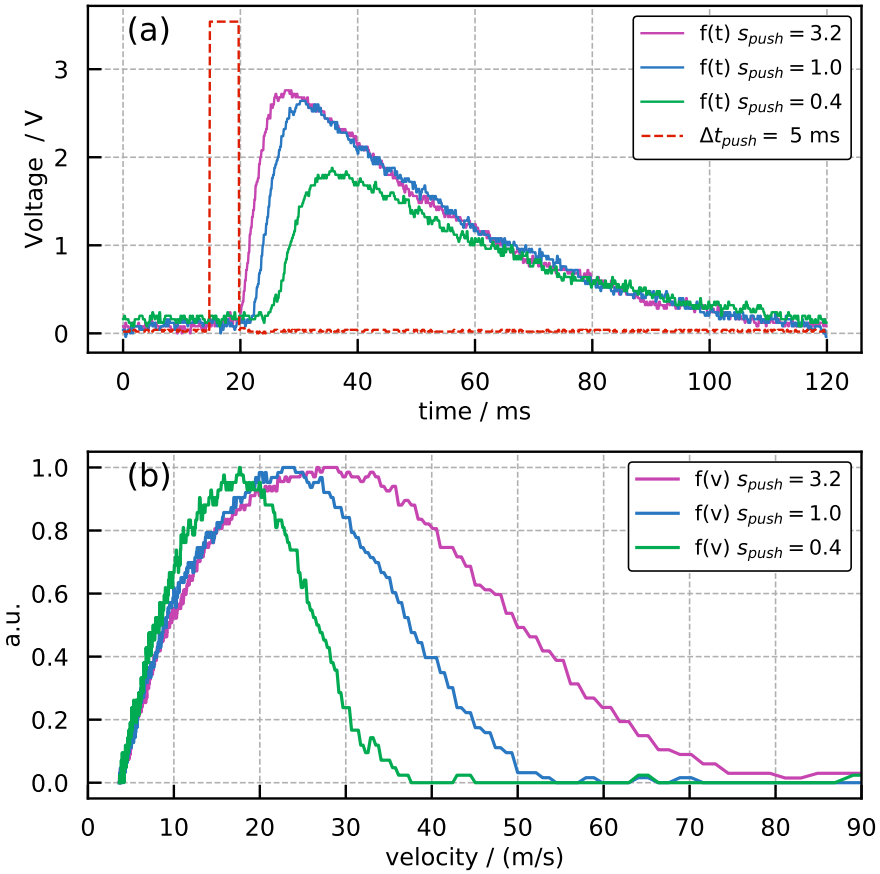

Figure 5.5: Measuring the longitudinal velocity. **(a)** Fluorescence time profile $f(t)$ (solid lines) respect to the push pulse (red dashed line). Push pulse has a time duration of $\Delta t_{\text{push}} = 5\,\text{ms}$ at different push saturation parameter s_{push}. **(b)** Velocity distribution $f(v)$ (solid lines)

Fig.5.6 compares experimental most probable velocities v_L (blue points) with the simulated ones (orange dots). The error bar is estimated considering the acquisition time interval δt which gives us a velocity uncertainty of $\delta v \simeq 6\,\text{m/s}$ for each point. Good agreement is found with the experimental data (red triangles) given by [107]. The experimental most probable velocity are fit with the function $v_L(s) = v_0 s^n$, where v_0 is a conversion factor and n a scaling factor. From the fit procedure we obtain $v_0 = 34.7(6)\,\text{m/s}$ and $n = 0.40(2)$. In the Fig.5.5, the Gaussian fit plot (blue line) is also reported. In the comparison with MC simulations, a large mismatch is observed between numerical prediction and the experimental values. Numerical longitudinal velocities are systematically higher that experimental ones. From simulating point of view, this discrepancy in the longitudinal velocity explained considering that in MC simulation we do not simulate the push pulse effect. In the MC simulation we are continuously loading the atoms in the MOT

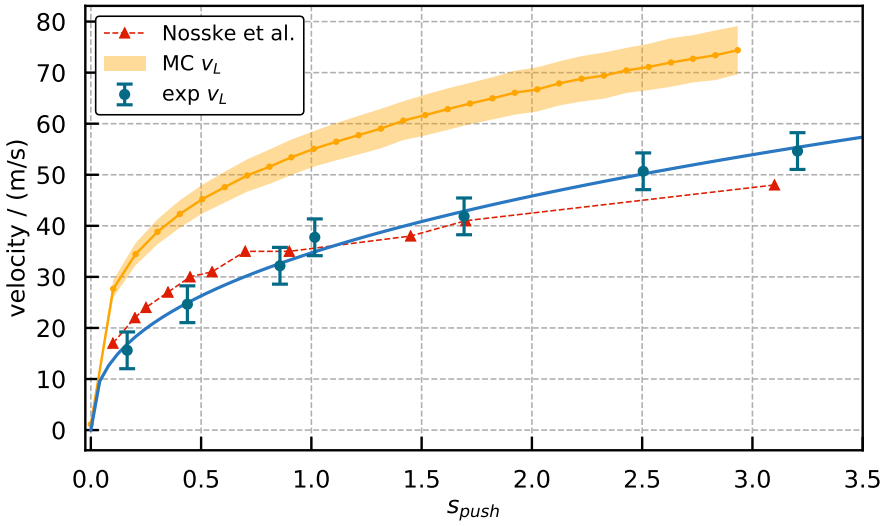

Figure 5.6: Comparison between experimental and simulated longitudinal velocity at different push saturation intensities. Blue points are experimental most probable longitudinal velocities. Red triangles are experimental most probable longitudinal velocities given by [107]. Orange dots are the MC simulated longitudinal velocities. The orange areas are the associated standard deviations

region by means of push beam and so they continuously increase their longitudinal velocity during the transfer process from the 2D-MOT region toward the final MOT. To simulate correctly the longitudinal velocity we would have simulate the atomic trajectory of atoms trapped in the 2D-MOT and accelerated by a finite time push interaction and then extract their longitudinal velocity distribution.

5.2.2 Temperature and divergence

In this section we estimate the transverse velocity of cold atomic beam emitted from the 2D-MOT region. At fixed push intensities $s_{\text{push}} = 0.34$, we collect the probe fluorescence signal at different probe detuning Δ_{probe} and fixed $s_{\text{probe}} = 0.1$ as reported in Fig.5.7. These measures are taken with total saturation parameter $s_{\text{2D-MOT}} = 6.6$.

As reported in Fig.5.15, the Voigt function is used as fitting function for the collected fluorescence signal. The Voigt profile is a convolution between the Lorentzian distribution and Gaussian distribution. This fitting function allow us to take into account the natural linewidth of the $^1S_0 - {}^1P_1$ transition of Sr together with the Doppler broadening of atomic beam transverse velocity [219]. Introducing a complex notation, the Voigt profile is analytically described according with the following

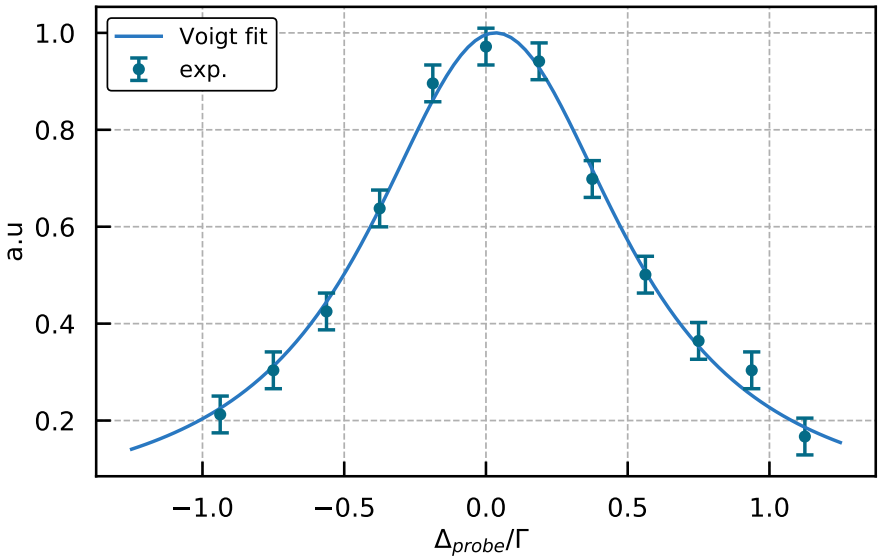

Figure 5.7: Transverse spectroscopy. Probe fluorescence signal as a function of probe detuning Δ_{probe}. Blue points are probe fluorescence signal of the atomic beam with its Voigt fit (blue line).

equation [220]:

$$f(z) = A\frac{\text{Re}[w(z)]}{\sigma_T\sqrt{2\pi}} \tag{5.1}$$

where z is a complex variable and $w(z)$ is also called Faddeeva function defined as:

$$z = \frac{(\Delta_{\text{probe}} - \Delta_0) + i\Gamma\sqrt{1+s_{\text{probe}}}}{\sqrt{2}\sigma_T} \qquad w(z) = \frac{2iz}{\pi}\int_0^\infty \frac{e^{-t^2}}{z^2-t^2}dt \tag{5.2}$$

where Γ and λ are the linewidth and the wavelength of the $^1\text{S}_0 - ^1\text{P}_1$ transition of Sr, $\Delta_{\text{probe}} = 0$ is the probe detuning and $s_{\text{probe}} = 0.1$ is the probe saturation parameter. The value $\sigma_T = v_T/\lambda$ is related to thermal Doppler broadening along the transverse direction and v_T is its corresponding transverse velocity. The related Experimental temperatures values are computed as $T = m_{\text{Sr}}v_T^2/2k_B$. Doppler broadening σ_T with corresponding transverse velocity v_T and temperature T are reported in Tab.5.2.

	σ_T/MHz	v_T/(m/s)	T / mK
2D-MOT	3.6(8)	1.7(4)	14(7)

Table 5.1: Voigt fit results. Doppler broadening and related transverse parameters of the cold atomic beam at $s_{\text{push}} = 0.34$, $s_{\text{2D-MOT}} = 6.6$ and $\Delta_{\text{2D-MOT}}/\Gamma = -1.6$.

According the transverse velocity fitted results in Tab.5.2, it is possible provide an estimation of the beam divergence. As show in Fig:5.6, at $s_{\text{push}} = 0.34$ the cold atomic beam has longitudinal most probable velocity of $v_L = 22.5(4)\,\text{m/s}$ with a transverse velocity of $v_T = 1.7(4)\,\text{m/s}$. This give us a beam divergence of $\theta_{\text{beam}} = v_T/v_L = 75(17)\,\text{mrad}$ which is slightly below the maximum admitted divergence $\theta_{\text{DPC}} = 88\,\text{mrad}$ imposed by the differential pressure channel constraint. This value of atomic divergence is in agreement with [107] and its uncertainty can be further improved with a better estimation of the transverse velocity of the atomic beam.

5.2.3 Atomic flux

Knowing the longitudinal velocity v_L and the transverse component v_T of the cold atomic beam, we can finally estimate the atomic flux emitted from the atomic source using Eq.3.33. Atomic flux Φ_{2D} emitted from the 2D-MOT region is detected by probing the cold atomic beam with the transverse probe beam.

For the flux detection we scan different saturation parameters of the 2D-MOT optical beam as reported in the Fig.5.8 while the push intensity and 2D-MOT detuning are fixed at $s_{\text{push}} = 0.34$ and $\Delta_{\text{2D-MOT}}/\Gamma = -1.6$. In this configuration, the transverse velocity of the cold atomic beam is $v_T = 3.6(8)\,\text{m/s}$ and leads a negligible Doppler contribution $F(v_T) \simeq 1$ in the fluorescence detection as defined in Eq.3.32. According to Eq:3.32, the Doppler contribution in the transverse velocity starts to have an effect when the radial velocity of the beam is larger that $v_T \sim \Gamma/k_L \sim 14\,\text{m/s}$ which is above the estimated radial velocity of our cold atomic beam. The best atomic flux is observed at $s_{\text{2D-MOT}} = 6.6$, $\Delta_{\text{side}}/\Gamma = -3.1$ and it is $\Phi_{\text{2D}} = 0.85(15) \times 10^8\,\text{atoms/s}$.

The theoretical prediction of the maximum atomic flux generated by the our atomic source is estimated according the following equation:

$$\Phi_{\text{2D}}^{\text{th}} = p_{\text{cap}} p_{\text{rad}} \Phi_{\text{ov}} \tag{5.3}$$

where $\Phi_{\text{ov}} = 1 \times 10^{14}\,\text{atoms/s}$ is the atomic flux exit from the capillary at $T_{\text{ov}} = 460\,^{\circ}\text{C}$, this flux is estimated according to the Eq.3.10 considering a capillary transmission efficiency of $20\,\%$. This efficiency factor takes into account the possible extra losses of flux divergence induced by a capillaries non perfect alignment. The factor p_{cap} is the probability that an atoms is captured from the thermal beam and transferred with the push beam toward the MOT region. This factor is estimated as the product $p_{\text{cap}} = r_{\text{MC}} c$, as explained in Eq.4.27. With the best 2D-MOT configuration we obtain a factor $r_{\text{MC}} \sim 0.2$ and so $p_{\text{cap}} = 4.5 \times 10^{-4}$. The factor p_{rad} is the probability that an atom during the trapping process does not decay in the metastable state $^3\text{P}_2$ and so it continues to interact with the trapping laser beams.

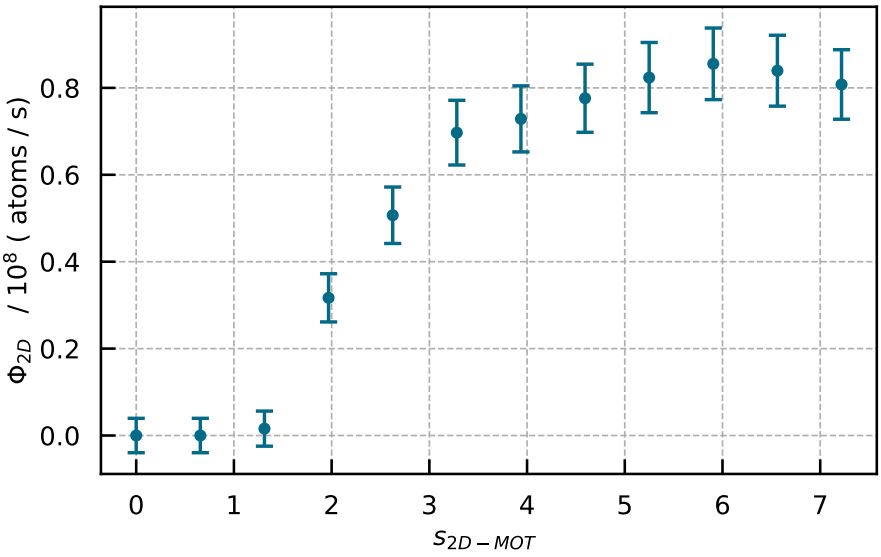

Figure 5.8: Atomic flux generated from the atomic source as a function of the 2D-MOT saturation parameter. This data are taken at $s_{\text{push}} = 0.34$, $\Delta_{\text{2D-MOT}}/\Gamma = -1.6$ and $\Delta_{\text{side}}/\Gamma = -3.1$

This probability is estimated as $p_{\text{rad}} = 1 - R\,\langle\tau_{\text{2D}}\rangle$, where $\langle\tau_{\text{2D}}\rangle$ is the average time that a trapped atoms spend in the 2D-MOT region before be moved by the push beam and R is the decay rate in the metastable state. According our MC simulation this time is estimated as $\langle\tau_{\text{2D}}\rangle = 2.9(6)\,\text{ms}$. The decay rate R is computed as [122]:

$$R = \frac{1}{2}\frac{s_{\text{tot}}}{1 + s_{\text{tot}} + 4\Delta/\Gamma^2}\Gamma_{^1\text{P}_1\rightarrow{}^1\text{D}_2}B_{^1\text{D}_2\rightarrow{}^3P_2} = 223(80)\,\text{s}^{-1} \tag{5.4}$$

where $s_{\text{tot}} = 6.5$ is the total saturation of the 2D-MOT perceived from atoms, $\Delta_{\text{2D-MOT}}/\Gamma = -1.6$ is the detuning of the 2D-MOT, $\Gamma_{^1\text{P}_1\rightarrow{}^1\text{D}_2} = 3.8(14)\times10^3\,\text{s}^{-1}$ [119] is the decay rate in the state $^1\text{D}_2$, and $B_{^1\text{D}_2\rightarrow{}^3\text{P}_2} = 1/3$ is the branching ratio for the state $^3\text{P}_2$. The probability that an atom does not decay in the state $^3\text{P}_2$ during the 2D-MOT trapping is estimated at $p_{\text{rad}} = 0.35(17)$. Merging all these considerations in the Eq.5.3 we finally obtain $\Phi_{\text{2D}}^{\text{th}} \simeq 6(3)\times10^9$ atoms/s providing a discrepancy of a factor ~ 70 between the theoretic estimation and the experimental results. Considering the fact that this estimation is only performed by theoretical arguments and numeric simulations, the result is in a reasonable agreement with the experimental observation. Some extra losses in the 2D-MOT region may also be induced by a non-perfect alignments of the zero magnetic field of the permanent magnets and push beam. This factor will further reduce the theoretical expectation on the atomic flux.

5.3 Oven temperature

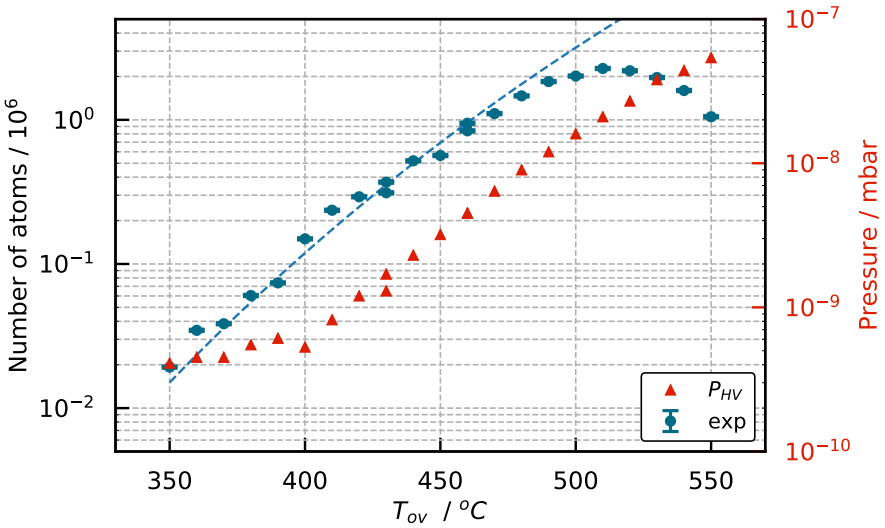

Figure 5.9: Oven temperature characterization. Blue points are MOT number of atoms as a function of the oven temperature T_{ov}. The dashed curve is the expected atomic flux power law $\Phi \simeq P_{\mathrm{Sr}}(T_{\mathrm{ov}})T_{\mathrm{ov}}^{-5/2}$. Red triangles are the atomic source pressure P_{HV} measured during the characterization at different oven temperatures.

The temperature of the oven is another parameter that can affect the performances of the atomic flux. The Fig.5.9 shows the collected MOT atomic number as a function of the oven temperature T_{ov} (blue points). This characterization is taken at fixed 2D-MOT parameters $\Delta_{\text{2D-MOT}} = -1.6\,\Gamma$ and $s_{\text{2D-MOT}} = 3.6$ and resonant push intensity $s_{\mathrm{push}} = 0.34$. Pressure values measured in the HV region P_{HV} by the NexTorr D-200 pump's driver is also reported in the figure (red triangle).

It is also interesting to predict the scaling law of the number of atoms captured in the MOT as a function of the oven temperature T_{ov}. Again, we are assuming the presence of a proportionality relation between the 2D-MOT loading rate and the MOT loading rate. According the calculations presented in Sec.3.2.5, the atomic flux generated by the oven scales with the oven temperature as $\Phi_{\mathrm{ov}} \sim n_{\mathrm{ov}} T_{\mathrm{ov}}^{-1/2}$. Considering the capture velocity of a 2D-MOT and its loading rate relation given by Eq.2.39, the loading rate scales with the oven temperature as $\Phi_{\mathrm{2D}} \sim n_{\mathrm{ov}} T_{\mathrm{ov}}^{-3/2}$. Remembering that $n_{\mathrm{ov}} \sim P_{\mathrm{Sr}}(T_{\mathrm{ov}})T_{\mathrm{ov}}^{-1}$, the scaling law of the 2D-MOT atomic flux can be written as:

$$\Phi_{\mathrm{2D}} \sim P_{\mathrm{Sr}}(T_{\mathrm{ov}}) \times T_{\mathrm{ov}}^{-5/2} \tag{5.5}$$

In the plot, we fit the experimental measurements with $N(T_{\mathrm{ov}}) = \alpha\Phi_{\mathrm{2D}}(T_{\mathrm{ov}})$ (dashed blue line), where α is a proportionality parameter. The scaling law is

in good agreement with the experimental results until $T_{ov} < 500\,°C$.

During the entire temperature ramp, the pressure in the atomic source region remains below than $P_{HV} < 1 \times 10^{-7}$ mbar. As already explained in the Eq.3.2, the maximum differential pressure sustainable by our differential channel is estimated to be $P_{UHV}/P_{HV} = 2.1 \times 10^{-4}$. This means that for all the temperatures explored, the pressure in the atomic source region affects the vacuum quality of the MOT region only at the level of $\Delta P_{UHV} \sim 10^{-11}$ mbar or below which is below the minimum detectable pressure of our ion pump drivers.

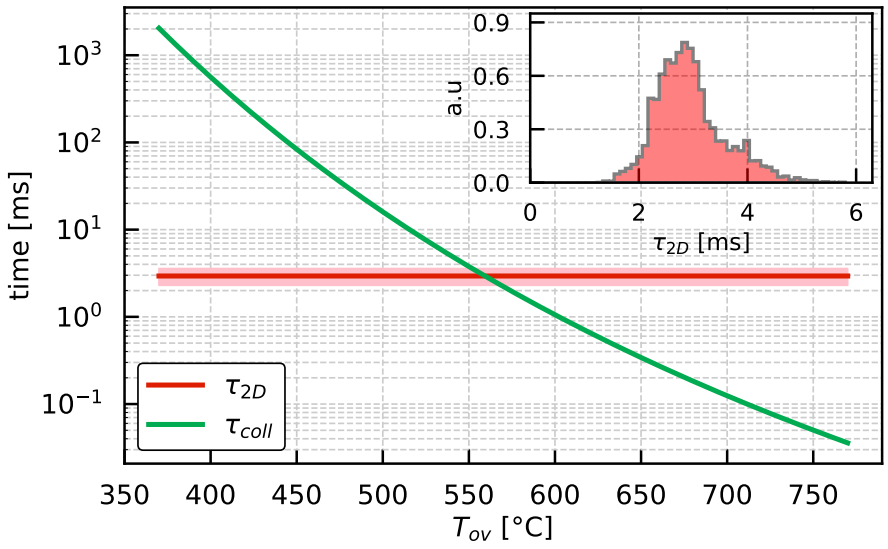

Figure 5.10: Time scales comparison as a function of the oven temperature T_{ov}. The green line is the estimated collision τ_{coll} time among atoms of thermal beam at different T_{ov}. The red line is the simulating time of atoms spent in the 2D-MOT interaction region defined by the beams dimensions. Inset shows the simulating time distribution τ_{2D} of $N \sim 3700$ trapped atomic trajectories.

As shown in the Fig.5.9, At $T_{ov} > 500\,°C$, the MOT number of atoms decreases even if the background pressure P_{HV} increases. A possible explanation is provided considering the collisions processes among the atoms in 2D-MOT with atoms in the thermal beam. We compared the expected collision time among hot atoms in the thermal beam with the time that a trappend atom spends in the 2D-MOT region. The green line in Fig.5.10 reports the collision time τ_{coll} among the atoms in the thermal beam as a function of the oven temperature. τ_{coll} is computed according to Eq.4.22. The red line in Fig.5.10 is the time spent by the atoms in the 2D-MOT interaction region τ_{2D} including the effect of the 2D-MOT beams and push beam. This time scale is estimated with MC simulations explained in Ch.4 and

considering the interaction region defined by the volume of the 2D-MOT beams dimension. The τ_{2D} distribution obtained from the simulation is reported as an inset in Fig.5.10. The mean value of the distribution is estimated as $\langle \tau_{2D} \rangle = 2.9(6)\,\text{ms}$. At oven temperature value from 350 °C and 550 °C the computed mean value τ_{2D} remain unaltered. According our calculation, at $T_{ov} \simeq 500\,°\text{C}$ the time spent in the 2D-MOT region is equal to the collision time among the atoms in the thermal beam hence resulting in a reduction of the MOT atomic flux. Another possible limiting factor is the presence of the capillaries array that may change the atomic flux regime at higher oven temperature. According Fig.3.8 at $T_{ov} > 500\,°\text{C}$, the capillary can no longer be considered as transparent and the flux emitted from the capillary is no more proportional to the pressure inside the oven [159, 160] hence reducing the overall atomic flux emitted.

5.4 Sideband enhancement

In this section we introduce a new trapping method used to enhance the atomic flux generated by the atomic source. This new trapping scheme employs an extra frequency component added to the standard 2D-MOT beam where the sideband beam is red-detuned compared to the 2D-MOT frequency. As already discussed in Sec.4.1.1, with these beams configuration it is possible to increase the atomic capture velocity of the 2D-MOT showing the possibility to increase the atomic flux provided by the atomic source. In this section, we present the experimental evidence of this method. In the literature, examples of these approach are given in the MOT [221] and 2D-MOT [102] by means of EOM modulation on the frequency of the trapping beams.

Our strategy adopted to find the best optical sideband configuration is to measure the number of atoms in the MOT as a function of different sibeband optical powers and detunings. During the sideband power and detuning mapping, the sideband radius e^{-2} beam is set equal to the 2D-MOT e^{-2} radius $w_{\text{2D-MOT}} = w_{\text{side}} = 9.5\,\text{mm}$ and we maintain the 2D-MOT detuning at its best value of trapping efficiency $\Delta_{\text{2D-MOT}} = -1.6\Gamma$ observed in the Fig.5.2(a). We perform such investigation keeping fixed the overall optical power $P_{\text{tot}} = P_{\text{2D-MOT}} + P_{\text{side}}$, and so also the total intensity perceived by atoms, and we redistribute the optical power among the sideband beam and the 2D-MOT beam observing the related MOT number of atoms. This procedure is repeated for different sideband detunings values.

In order quantify the performance of this trapping method, we introduce two numerical quantities. The first one is the gain G of the number of atom in the

MOT induced by the presence of sideband beams. This parameter is defined as:

$$G = \frac{N(s_{\text{side}} = s_{\text{tot}} - s_{\text{2D-MOT}}, \Delta_{\text{side}})}{N(s_{\text{2D-MOT}} = s_{\text{tot}} - s_{\text{side}})} \tag{5.6}$$

where N is the number of atoms trapped in the MOT with and without the sideband enhancing. This gain factor is easily measured by chopping the sideband beam and computing the ratio between the two MOT fluorescence levels with and without the sideband beam. Follow the definition of Eq.5.6, this G parameter compares the trapped number of atoms with different saturation parameters $s_{\text{side}} + s_{\text{2D-MOT}}$ and $s_{\text{2D-MOT}}$. If we want to measure the performance of the sideband trapping keeping constant the saturation parameter perceived by atoms, a second parameter is defined. We call this parameter η and we defined it as:

$$\eta = \frac{N(s_{\text{side}} = s_{\text{tot}} + s_{\text{2D-MOT}}, \Delta_{\text{side}})}{N(s_{\text{2D-MOT}} = s_{\text{tot}})} \tag{5.7}$$

This parameter compares two different trapping configurations with same saturation parameter perceived by atoms. For these reason, the η parameter is chosen for a fine optimization of the sideband configuration while the G parameter is used as a comparison between others enhancing methods spread in the literature. If $\eta > 1$ it means that the new trapping configuration is advantageous compare to the usual trapping configuration, the single frequency 2D-MOT. If $\eta \leq 1$, the new trapping configuration is not effective compared to the standard one. The adimensionality of η and G also allows to directly compare the numerical estimated η^{MC} with the experimental η^{exp} without any scaling factors. We optimize the sideband beam considering two optical power levels: $P_{\text{tot}} = 110\,\text{mW}$ and $P_{\text{tot}} = 200\,\text{mW}$. These power levels correspond to a total saturation parameters of $s_{\text{tot}} = 3.61$ and $s_{\text{tot}} = 6.56$

5.4.1 Complete sideband optimization

Fig.5.11(a) reports the experimental results while the Fig.5.11(b) reports the related simulation at $s_{\text{tot}} = 3.61$. MC simulation catches the main features of the experimental trends such as the optimum region where $\eta > 1$, and the no gain region $\eta < 1$. At $s_{\text{tot}} = 3.61$, the best enhancement factors measured is $\eta^{\text{exp}} = 1.48(7)$ while the computed one is $\eta^{\text{MC}} = 1.87(3)$. The best sideband configuration is reached around the values $s_{\text{side}} = 1.3$ and $\Delta_{\text{side}} = -3.1\,\Gamma$ which correspond to a AOM frequency of $-260\,\text{MHz}$ and a optical power level of $P_{\text{side}} = 40\,\text{mW}$.

Fig.5.12(a) shows the experimental enhancement factor η^{exp} as a function of $s_{\text{side}}, \Delta_{\text{side}}$ at fixed $s_{\text{tot}} = 6.56$. Fig.5.12(b) is the MC simulation of the η^{MC} at different s_{sat} and Δ_{side}. From these map plots we can see that our MC simulation

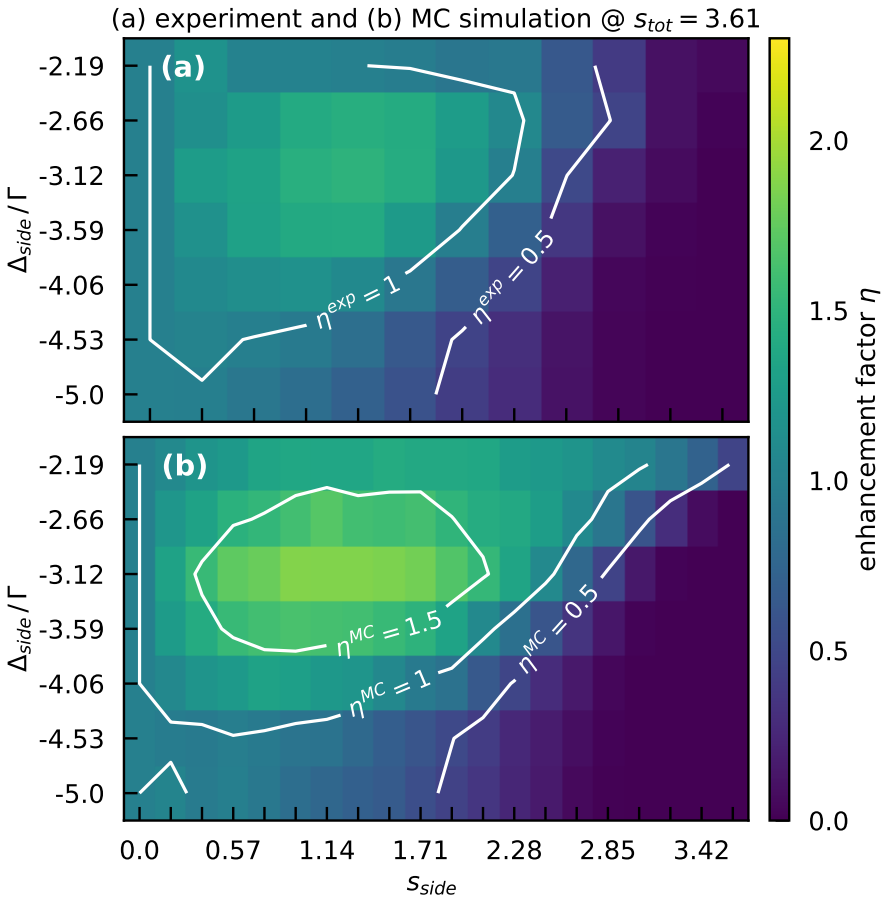

Figure 5.11: Enhancement factors η. Comparison at fixed total saturation parameter $s_{\text{tot}} = 3.61$ and $\Delta_{\text{2D-MOT}} = -1.6\,\Gamma$. **(a)** Experimental enhancement factor η^{exp}. **(b)** Numerical enhancement factor η^{MC} obtained by MC simulation.

catches the main features of the experimental measures such as the optimum peak region around the $s_{\text{side}} \simeq 3.1$, $\Delta_{\text{side}} \simeq -3.1\,\Gamma$ and the no gain region $0 < \eta < 1$ at $s_{\text{side}} > 5.2$. At $s_{\text{tot}} = 6.56$, the best enhancement factor measured is $\eta^{\text{exp}} = 2.3(1)$ while the simulated one is $\eta^{\text{MC}} = 2.13(4)$. All the maximum η values are reached around $s_{\text{side}} = 3.1$ and $\Delta_{\text{side}} = -3.1\,\Gamma$, which correspond to a AOM frequency of $-260\,\text{MHz}$ and a optical power level of $P_{\text{side}} = 90\,\text{mW}$.

Both numeric and experimental results reported in Fig.5.11 and in Fig.5.12, suggest to set a sidebad detuning at $\Delta_{\text{side}} \simeq -3.1\,\Gamma$ which is close to twice value of the 2D-MOT detuning $\Delta_{\text{2D-MOT}} = -1.6\,\Gamma$. The power redistribution between the sideband beam and the 2D-MOT beam depends on the total amount of power sent to the atoms. In the case of low total power $P_{\text{tot}} = 110\,\text{mW}$, the maximum enhancement value $\eta^{\text{exp}} = 1.48(7)$ is obtained distributing the optical power as 36 %

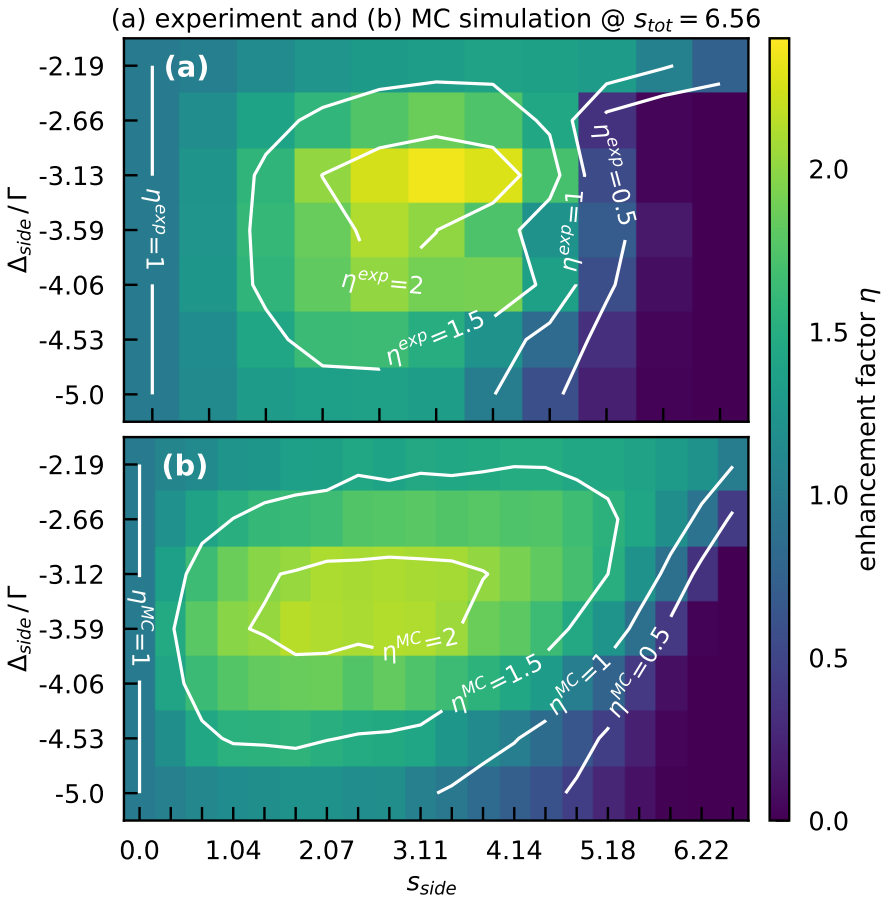

Figure 5.12: Enhancement factors η. Comparison at fixed total saturation parameter $s_{\text{tot}} = 6.56$ and $\Delta_{\text{2D-MOT}} = -1.6\,\Gamma$. **(a)** Experimental enhancement factor η^{exp}. **(b)** Numerical enhancement factor η^{MC} obtained by MC simulation.

on the standard 2D-MOT beams ($P_{\text{2D-MOT}} \simeq 70\,\text{mW}$) and the 64 % on the sideband beam ($P_{\text{side}} \simeq 40\,\text{mW}$). This power unbalance between the two beams is reduced at higher optical power $P_{\text{tot}} = 200\,\text{mW}$, where the 50 % is set to the sideband beam ($P_{\text{side}} = 100\,\text{mW}$) while the 50 % is set to the 2D-MOT beam ($P_{\text{2D-MOT}} = 10\,\text{mW}$) providing an enhancement factor of $\eta^{\text{exp}} = 2.3(1)$. This discrepancy reduction at higher power can be explained considering the saturation effect in the capture number of atom with the standard 2D-MOT configuration. As show in the Fig.5.2(b), at higher saturation parameter $s_{\text{2D-MOT}}$, the gain in the captured atoms as a function of saturation parameter starts to decrease. This implies that it is possible to subtract some optical power from the 2D-MOT beam without affecting the overall performance of the trapping. This power reduction is lower in the case of lower total optical power $s_{\text{tot}} = 3.1$, where the saturation effect in the efficiency trapping is not reached. In latter case, removing some optical power from the 2D-MOT

beam will reduce the efficiency trapping.

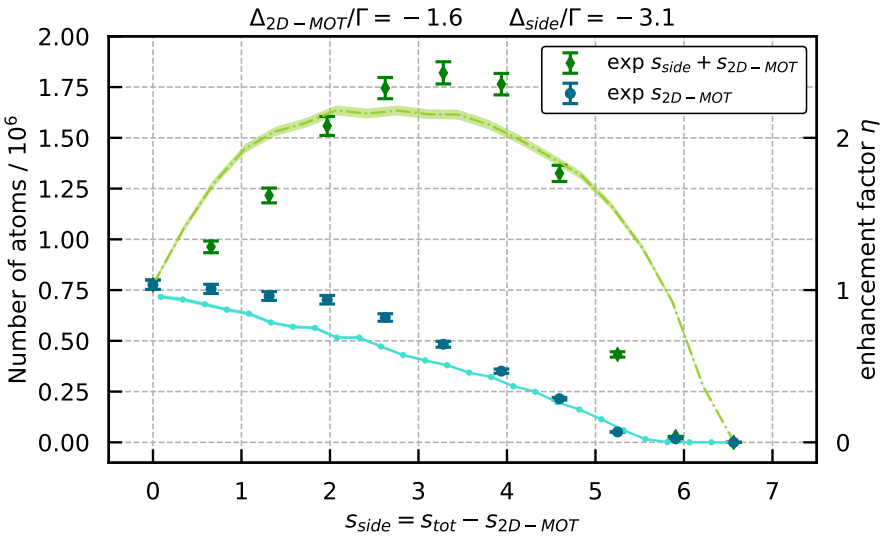

Figure 5.13: Number of atoms captured in the MOT region for different optical power redistributions. The $s_{\text{tot}} = 6.56$ is split with the sideband beam s_{side} and the 2D-MOT beam $s_{\text{2D-MOT}}$. All the values are computed at best 2D-MOT detuning configuration $\Delta_{\text{2D-MOT}} = -1.6\,\Gamma$. The green diamonds are the number of atom capture in the MOT region using the sideband enhancing. The experimental values are taken at fixed sideband detuning $\Delta_{\text{side}} = -3.13\,\Gamma$. The green filled area is associated MC simulation. The blue points describe the number of atom in the MOT region shutting the sideband beam.

After finding the optimized parameters reported in Fig.5.11 and Fig.5.12, the maximum enhancing factor $\eta^{\text{exp}} = 2.3(1)$ observed is obtained at $\Delta_{\text{side}} = -3.13\,\Gamma$ and $\Delta_{\text{2D-MOT}} = -1.6\,\Gamma$ at $s_{\text{tot}} = 6.56$. In Fig.5.13 we compare the number of atoms in the MOT as a function at different sideband power (green diamonds) with the number of atoms in MOT observing by shutting the sideband beam (blue points). One can also appreciate how the MC simulation well predicts the different enhancement regions reported by the experimental points. Shutting the sideband beam at $s_{\text{side}} \simeq 4$ we obtain a gain in number of atoms $G^{\text{exp}}_{\text{side}} \simeq 5$ as compared to the standard single frequency 2D-MOT.

5.4.2 Comparison with Zeeman Slower enhancing

Our first attempt to enhance the flux generated from the atomic source was to lunch a linear polarized *Zeeman slower* (ZS) beam toward the hot atoms flux generated by the oven. The ZS beam is far red-detuned respect to the 2D-MOT frequency and exploiting the tails of the magnetic field quadrupole of the 2D-MOT, the faster

atoms are slowed down along the ZS beam direction increasing their probability of being captured in the 2D-MOT region. This enhancing method was demonstrated to provide a gain efficiency of 12 for Na atoms [104] and a gain efficiency of 4 for Sr atoms [107].

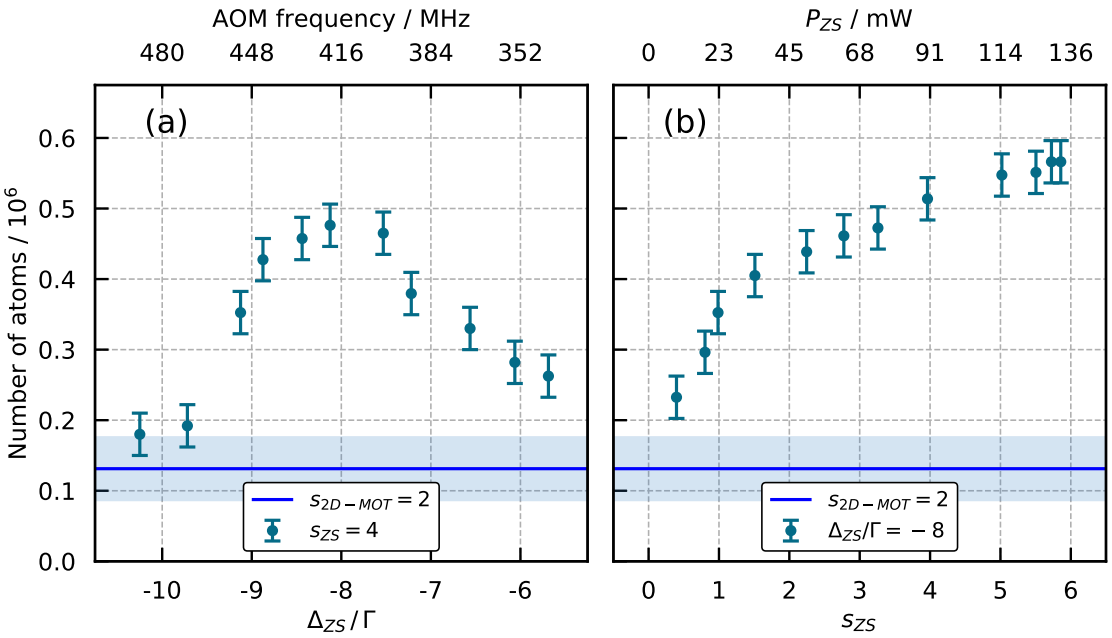

Figure 5.14: ZS optmization. Blue line show the MOT level without the ZS, the are region is the associated uncertainty. **(a)** Number of atom in the MOT as a function of ZS detuning. **(b)** Number of atom in the MOT as a function of ZS saturation parameter.

In Fig.5.14, the characterization of ZS beam is shown. We find the best configuration ZS configuration at $\Delta_{\mathrm{ZS}} = -8.1\,\Gamma$, $P_{\mathrm{ZS}} = 140\,\mathrm{mW}$, $P_{\text{2D-MOT}} = 36\,\mathrm{mW}$ and $\Delta_{\text{2D-MOT}} = -1.5\,\Gamma$. We set the ZS beam waist at $w_{\mathrm{ZS}} = 4.1\,\mathrm{mm}$. The distance between the ZS windows and the oven position is roughly 25 cm. Shutting the ZS beam, we observe a gain efficiency $G_{\mathrm{ZS}} = 4.3(6)$ in the number of atoms in MOT. This result is in agreement with ZS gain efficiency estimated in [107]. Unfortunately, we did not accomplish the full characterization of the ZS because of the drop in the trasmissivity in the ZS window which rapidly becomes metallized by Sr atoms. With this sever limitation, we were not able to produce a stable MOT during the day even if the ZS window was heated up to 350 °C. With this severe limitation we consider the sideband enhanced 2D-MOT as a viable alternative to ZS enhanced 2D-MOT. As reported in the Fig.5.13, with the sideband enhanced 2D-MOT we where able to measure a stable gain factor $G_{\mathrm{side}}^{\mathrm{exp}} = 5.31(1)$.

Even if G_{ZS} and G_{side} are the same order of magnitudes, the ZS enhancement for

the 2D-MOT loading has two experimental drawbacks considering the design of our atomic source. First of all, the quantization axis of the magnetic field along the hot atoms direction imposes that only one half of the linear polarized ZS light power has the correct circular polarization. This means that at least half of the ZS beam optical power is wasted in the slowing process. Secondly, the optical access of the ZS beam has to be constantly heated in order to avoid Sr metallization. A possible way to reduce Sr metallization is to increase the distance between oven and ZS window by means of vacuum extension and keeping heated the ZS windows. This solution is already implemented in [107] but it does not satisfy the compact vision of the atomic source. Another possibility is to insert a in-vacuum mirror and send the ZS beam along the orthogonal direction of the thermal atomic beam exploiting the reaming free optical access of the atomic source. Even if the reflection of the mirror it is not highly reduced in the short exposition time by Sr deposition, for a longer exposition time also in-vacuum mirror has to be replaced [222]. On the other hand, the sideband beams has a well defined polarization in the capture region and in addiction there is no needed of any vacuum extension or heating elements that keep clean the optical access. We also think that the approach of sideband enhancing is not limited to transversally loaded 2D-MOT atomic source but it can be reliably extended to any kind of atomic source that employ a 2D-MOT approach.

5.4.3 Cold atomic beam temperature

We are also interested in investigating the possible heating effect induced by sideband enhancing method. The extra heating induced by this method could increase the radial temperature of the cold atomic beam generated by the atomic source. The temperature estimation of the cold atomic beam is performed by repeating the analysis reported in Sec.5.2.2. At fixed push intensities $s_{\text{push}} = 0.34$, we collect the probe fluorescence signal at different probe detuning Δ_{probe} and fixed $s_{\text{probe}} = 0.1$ as reported in Fig.5.15. These measures were taken with and without the sideband enhancement at the optimum optical configuration found in the previous section where $s_{\text{2D-MOT}} = 3.5$, $\Delta_{\text{2D-MOT}}/\Gamma = -1.6$, $s_{\text{side}} = 3.1$, $\Delta_{\text{side}}/\Gamma = -3.1$.

The measure of the fluorescence signal of the probe is reported in Fig.5.15 (green triangles). These measures are also compared with the previous measures reported in Sec:5.2.2 taken without the sideband beam at the same total saturation parameter $s_{\text{tot}} = 6.6$. The Voigt function expressed with Eq.5.1 is used as fit function for the collected fluorescence signals. Tab.5.2 summarizes the fit results.

Fig.5.16 reports the 2D-MOT temperatures comparisons among experimental

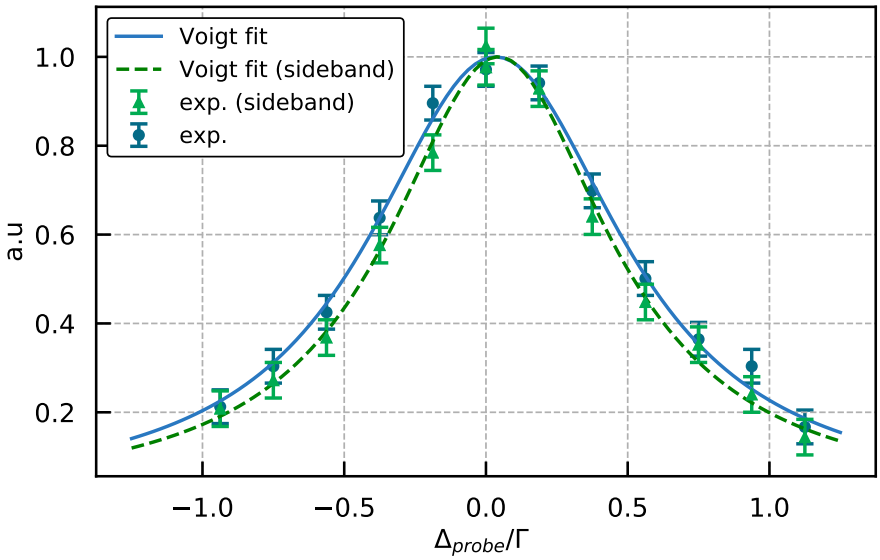

Figure 5.15: Transverse spectroscopy. Probe fluorescence signal as a function of probe detuning Δ_{probe}. Blue points are probe fluorescence signal of the atomic beam generated without the sideband enhancing with its Voigt fit (blue line). Green triangles are probe fluorescence signal of the atomic beam generate with the sideband enhancing with its Voigt fit (green dashed line).

	σ_T/MHz	v_T/(m/s)	T / mK
2D-MOT	3.6(8)	1.7(4)	14(7)
2D-MOT + sideband	0.8(3.0)	0.4(1.3)	0.7(5.0)

Table 5.2: Voigt fit results. Doppler broadening and related transverse parameters

investigations, numeric simulations and theory prediction. From laser cooling theory, the Doppler temperature T_D is computed as [85]:

$$T_D = \frac{\hbar\Gamma}{8k_B}\frac{1+s+4(\Delta/\Gamma)^2}{|\Delta|/\Gamma} = 2.14\,\text{mK} \tag{5.8}$$

where $s = 6.6$ is the total intensity saw by atoms in 2D-MOT interaction region, $\Delta = -1.6\,\Gamma$ is 2D-MOT detuning and Γ is the linewidth of $^1\text{S}_0 - ^1\text{P}_1$ transition of Sr.

From Fig.5.16, we observe that no extra-heating effect is induced by the sideband beam. Instead this method seems to reduce the temperature of the cold atomic beam produced from the atomic source. This effect reduction is observed in the numeric simulations. The temperature reduction with the presence of the sideband beam can be explained considering that a fraction of the power of the 2D-MOT, which it is closer to resonance of $^1\text{S}_0 - ^1\text{P}_1$ transition, is transferred to

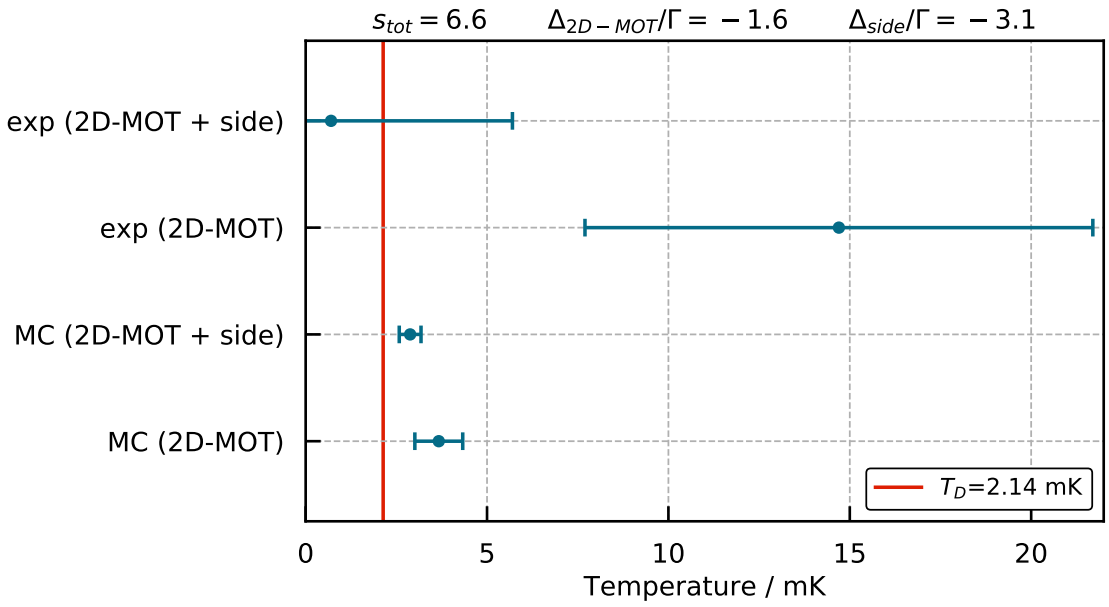

Figure 5.16: Radial temperature comparison with and without the sideband enhancing. Simulations, theory and experiment are compared

higher detuning hence reducing the induced heating. With the data and with the experimental method used in the Fig.5.16 it is not possible to claim that the atomic flux generated form the 2D-MOT sideband enhanced has a lower temperature of the atomic flux generated from the single 2D-MOT. As suggested in [214], a better estimation of the fit parameter of the Voigt profile can be obtained employing the $^1S_0 - ^3P_1$ transition instead of $^1S_0 - ^1P_1$ transition.

5.4.4 Atomic flux and comparison

As a final characterization, we measured the atomic flux generated from the atomic source by means of the sideband enhancing method at $s_{\text{tot}} = 6.56$. Keeping fixed the total saturation parameter $s_{\text{tot}} = 6.56$, $\Delta_{\text{2D-MOT}} = -1.6\,\Gamma$ and $\Delta_{\text{side}} = -3{,}1\,\Gamma$, we measure the atomic flux at different sideband saturation parameter. The Fig.5.17 reports flux generated from the atomic source with (green triangles) and without (blue points) the sideband enhancing.

At $s_{\text{side}} \simeq 3.2$, we measure an atomic flux of $\Phi_{\text{2D}} = 2.0(2) \times 10^8$ atoms/s. The related enhancing factor is $\eta = 2.3(4)$ and it is in agreement with all the experimental and numerical results reported in Sec.5.4. The value of $\Phi_{\text{2D}} = 2.0(2) \times 10^8$ atoms/s represents our best value for the atomic flux generated by sideband enhanced 2D-MOT with the experimental setting reported in the Tab.5.3 at $T_{\text{ov}} = 460\,^\circ\text{C}$ and

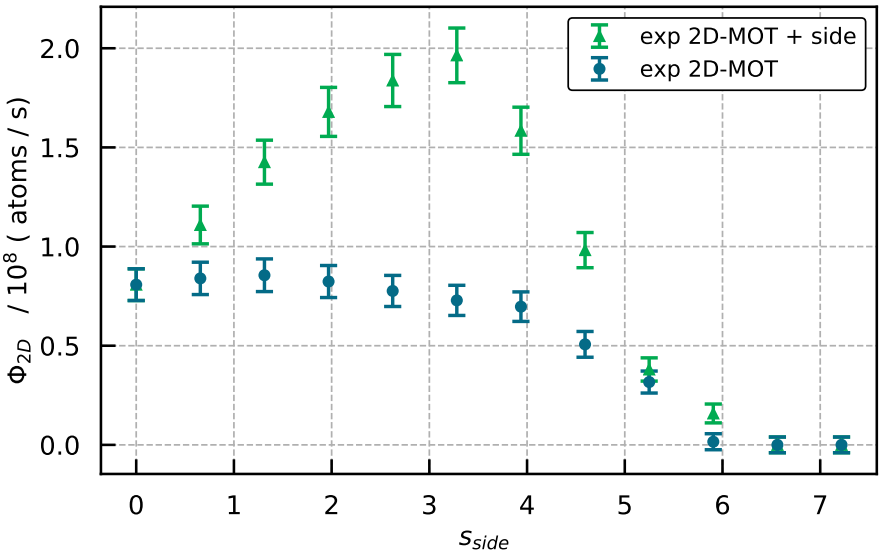

Figure 5.17: Atomic flux as a function of sideband saturation parameter. The total saturation parameter $s_{\text{tot}} = 6.56$ is split with the sideband beam and the 2D-MOT beam keeping fixed the $\Delta_{\text{2D-MOT}} = -1.6\,\Gamma$ and $\Delta_{\text{side}} = -3.2\,\Gamma$. Blue point are the atomic flux without the sideband enhancing. Green triangle are the point with the sideban enhancing

2D-MOT magnetic gradient of $b_{\text{2D-MOT}} = 0.2\,\text{T/m}$.

	Power/mW	f_{AOM}/MHz	radius/mm	s	Δ/Γ
spectroscopy	0.5	80†	0.37	0.11	0.0
2D-MOT	100	-210	9.50	3.28*	-1.6
sideband	100	-260	9.50	3.28*	-3.13
push	0.15	-80†	0.81	0.34	0.0
MOT	45	-200	6.20	2.49*	-1.2
probe	0.5	-80†	0.83	1.07	0.0

Table 5.3: Atomic source optimization. Detuning, power and optical e^{-2} radius interacting with Sr atoms. Total power of the blue laser source is around 600 mW (†) AOM is consider in double-pass configuration. (*) Calculation of the saturation intensity is performed considering the retro-reflection contribution. For the MOT beam we consider also the windows trasmittivity $T_{\text{w}} = 84(8)\%$.

Comparison with [107, 223]

Although our atomic flux generated form the 2D-MOT has the same order of the atomic flux reported in Nosske et.al work [107, 223] it is not fully comparable.

In particular, our flux estimation is about a factor 5 lower. There are some differences between our atomic source and the one reported in Nosske work like the presence of the capillary array, some differences regarding the trapping parameters of the 2D-MOT and possible underestimation of the atomic due to our fluorescence detection method.

The presence of the capillary array is the main difference. Here we try to estimate theoretically the expected flux capture in the 2D-MOT region with and without the presence of the capillaries. As described in the Eq.3.10, it is possible estimate the ratio R_{ov} between atomic flux produced by the oven with and without the presence of the capillaries as:

$$R_{\text{ov}} = \frac{\Phi_{\text{ov}}}{\Phi_{\text{ov}}(\text{no cap.})} = W\frac{S_{\text{cap}}}{S_{\text{ov}}} = 2.5 \times 10^{-3} \tag{5.9}$$

where $W \simeq 8r_{\text{cap}}/3L_{\text{cap}} = 2.62 \times 10^{-2}$ is the Clausing factor which describes the transmission probability of atoms through a single long capillary in the long tube approximation ($L_{\text{cap}} \gg r_{\text{cap}}$), $S_{\text{cap}} = N_{\text{cap}}\pi r_{\text{cap}}^2 = 1.88 \times 10^{-5}\,\text{m}^2$ is the total surface described by the capillaries array, $S_{\text{ov}} = \pi r_{\text{ov}}^2 = 2.01 \times 10^{-4}\,\text{m}^2$ is the oven surface aperture. We remember that $r_{\text{cap}} = 0.2\,\text{mm}$, $L_{\text{cap}} = 2\,\text{cm}$, $r_{\text{ov}} = 8\,\text{mm}$ and $N_{\text{cap}} = 150$. The Eq.5.9 indicates a reduction of the atomic flux because of the capillaries. On the other hand, the angular divergence between the two types of atomic fluxes are quite different. The collimation propriety of the thermal beam induced by capillary is estimated as $\Omega_{\text{cap}} = \pi a_{\text{cap}}^2/L_{\text{cap}}^2 = 1.25 \times 10^{-3}\,\text{sr}$ where $a_{\text{cap}} = 2r_{\text{cap}}$, while the solid angle of the 2D-MOT capture process is $\Omega_{\text{2D}} = \pi w_{\text{2D-MOT}}^2/x_0^2 = 1.73 \times 10^{-2}\,\text{sr}$ where $w_{\text{2D-MOT}} = 9.5\,\text{mm}$ is the 2D-MOT beam waist and $x_0 = 128\,\text{mm}$ is the distance between the oven aperture and the center of the 2D-MOT region. As expected, $\Omega_{\text{cap}} < \Omega_{\text{2D}}$ which means that all the thermal collimated beam generated by capillaries participates to the 2D-MOT loading process. With this consideration, it is legit to approximate the atomic flux captured by the 2D-MOT as $\Phi_{\text{2D}} \simeq \Phi_{\text{ov}}(v_c/v_{th})^4$ where v_c is the 2D-MOT capture velocity and v_{th} is the thermal velocity, while without the capillary presence the captured flux by 2D-MOT is estimated as $\Phi_{\text{2D-MOT}}(\text{no cap.}) \simeq \Phi_{\text{ov}}(\Omega_{\text{2D}}/2\pi)(v_c/v_{th})^4$. The flux ratio between the 2D-MOT capture rate with and without the presence of the capillary can be estimated as:

$$R_{\text{2D-MOT}} = \frac{\Phi_{\text{2D-MOT}}}{\Phi_{\text{2D-MOT}}(\text{no cap.})} = R_{\text{ov}}\frac{1}{\Omega_{\text{2D}}/2\pi} = 0.9 \tag{5.10}$$

which means that we aspect to find the same captured flux in the 2D-MOT with and without the presence of the capillary. From this point of view, the presence of the capillaries does not affect the performances of the atomic source , moreover they reduce the flux emitted from the oven increasing the atomic source lifetime. A non correct orientation of the capillaries or the a possible obstruction along the

capillary path are the majors drawbacks and they may reduce the performances of our atomic source compare to Nosske work.

Minor differences are also present in the trapping parameter of the 2D-MOT. In our system we send almost 220 mW in the 2D-MOT while in the Nosske work they employed 250 mW of blue power in the atomic source region. Another difference is the magnetic field gradient generated by the permanent magnets. In the Nosske work, they put the permanent magnets at distance of 7.5 cm and 8.8 cm of the 2D-MOT plane generating of 0.36 T/m. Because of the presence of the mechanical insert for the water cooling system of the atomic source, we are obliged to put the magnets position at larger distances as 9 cm and 11 cm of the 2D-MOT plane generating a 2D-MOT magnetic gradient of 0.2 T/m. This lower magnetic field gradient and the lower optical power employed in the 2D-MOT region can affect atomic flux generated from our atomic source. We also think that the motivation of this mismatch is not due to the low efficiency of the sibeband enhanced compared with the ZS ones. In fact, if we consider the ZS gain reported in the [107], it has the same gain compared to our ZS enhanced estimation and it is slightly lower compared to the sibenband enhanced gain.

Another possibility is the non correct calibration of the photodiode or the presence of some systematic errors not take into account in our fluorescence detection system. Employing a more sophisticated diagnostic system, like a imaging system by beam of CCD camera, it can provide us a better to estimation of the atomic flux provided by the atomic source and to the number of atoms capture in the final MOT.

5.5 MOT loading curves

The Fig.5.18 reports the MOT loading rates using the sideband enhancing method. The green line is the best MOT loading with the sideband beam while blue line represents the MOT loading by chopping the sideband beam. These loading curve are taken with the experimental configuration provided by Tab.5.3. MOT number of atoms N are fitted with the following function:

$$N(t) = N_{\mathrm{MOT}}(1 - e^{(t-t_0)/\tau})\Theta(t - t_0) + N_{\mathrm{offset}} \tag{5.11}$$

where $\Theta(t)$ is the heaviside function, N_{MOT} is the MOT number of atoms, t_0 is the time delay from the push pulse and τ is the loading time. Using the experimental parameters of Tab.5.3 we were able to reach $N_{\mathrm{MOT}} \simeq 2.3(2) \times 10^6$ atoms with a loading time $\tau \simeq 45(2)$ ms hence resulting in a MOT loading rate $L_{\mathrm{MOT}} = N_{\mathrm{MOT}}/\tau = 5.2(5) \times 10^7$ atoms/s. The error bar in the MOT number of atoms takes

into account also the systematic uncertainty of 10 % induced by the fluorescence calibration.

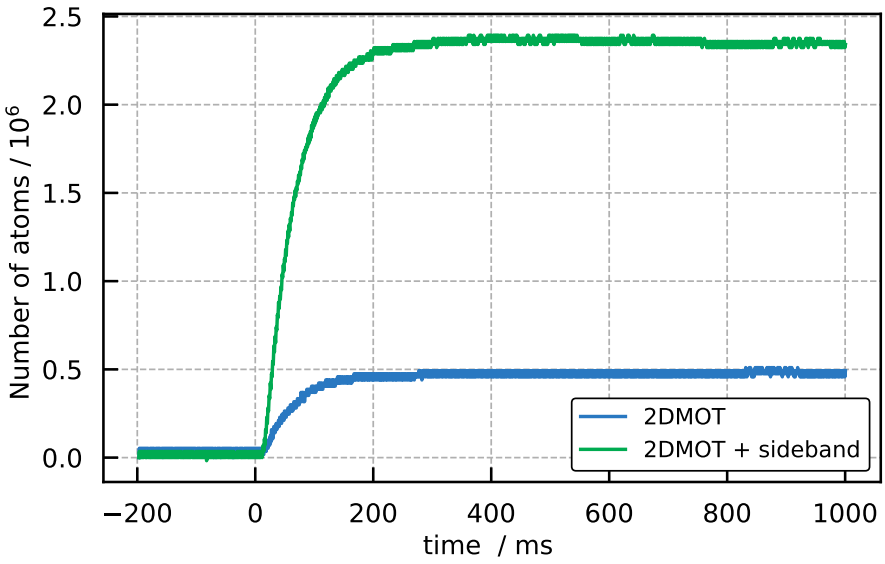

Figure 5.18: Loading curves. The green line is the MOT loading curve with experimental configuration reported in Tab.5.3. The total optical power in the 2D-MOT region is $P_{\text{tot}} = P_{\text{2D-MOT}} + P_{\text{side}} = 200\,\text{mW}$. The blue line is the MOT loading curve by chopping the sideband beam and so reducing the total optical power in the 2D-MOT region at $P_{\text{2D-MOT}} = 100\,\text{mW}$. The fitted MOT rising times $\tau = 47(1)\,\text{ms}$ are equals

	2D-MOT	2D-MOT + side
N_{MOT}/atoms	$1.0(1) \times 10^6$	$2.3(2) \times 10^6$
τ / ms	47(1)	45(1)
t_0 / ms	15.2(6)	16.3(1)
L_{MOT} / (atoms / s)	$2.2(2) \times 10^7$	$5.2(5) \times 10^7$
Φ_{2D} / (atoms / s)	$0.85(15) \times 10^8$	$2.0(2) \times 10^8$

Table 5.4: Atomic flux best values and MOT performances

The Tab.5.4 reports the final atomic source performances considering the atomic source settings reported in Tab.5.3. In the case of the sideband configuration, the estimated MOT capture efficiency is given by the ratio $L_{\text{MOT}}/\Phi_{\text{2D}} = 25(6)\,\%$. One possible reason of this losses can be motivated considering optical quality of the science cell windows. As stated previously, at $\lambda = 461\,\text{nm}$ the cell windows have and average transmittivity of $T_{\text{w}} = 84(8)\,\%$. Moreover, the transmission efficiencies among to all the windows are not the same hence inducing some power imbalance

from beams to beams and reduce the quality of the polarization. Another factor is related to the low diameter of the windows of 16 mm. In fact, as we explained in the Ch.2, the MOT beam diameter plays an important role in the capture efficiency, at larger MOT beam waist we aspect a lower losses.

As final calibration, the Fig.5.19 reports the MOT number of atoms as a function of the MOT gradient. The maximum number of atoms is reached at current value above $I = 7.5\,\mathrm{A}$. This calibration was taken without the sideband enhancing

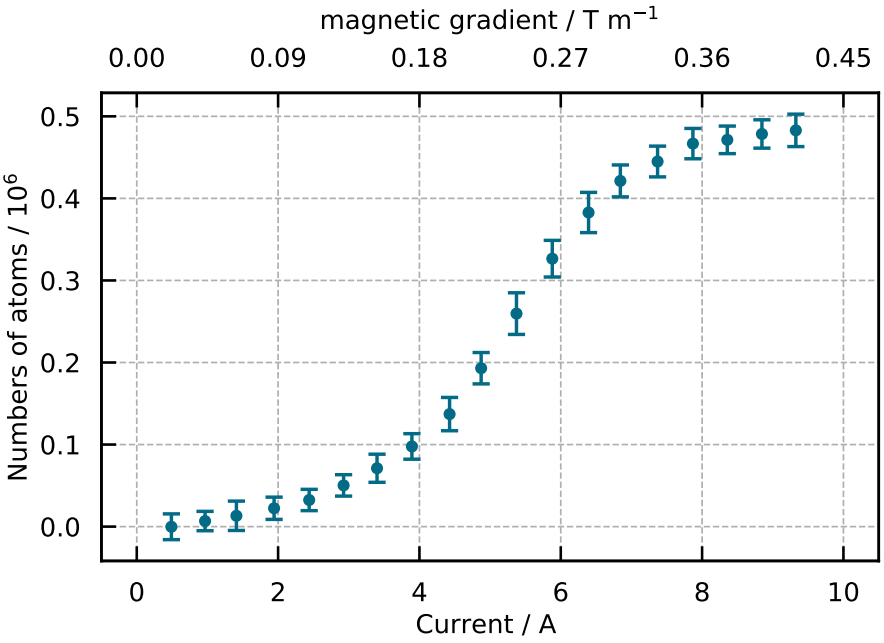

Figure 5.19: MOT number of atoms as a function of MOT coils current

Rempumpers

We also observe the first signature of the repumper effect in the MOT signal. The Fig.5.20 reports the number of atoms in MOT with different repumpers. As already discussed before, the loading rate of the MOT is $\tau = 47(1)\,\mathrm{ms}$. We first add the rempumper $\lambda = 707\,\mathrm{nm}$ in the MOT fluorescence signal. The repumper is superimposed to the MOT beams after the AOM of the MOT. We send a total power level to the atom of $P_{707} = 16.1\,\mathrm{mW}$. With this configuration we observed a gain factor in the number of atoms of the order of $G_{707} = 4.5(1)$ with a rising time $\tau_{707} = 55(1)\,\mathrm{ms}$. We also added the second rempumper at $\lambda = 679\,\mathrm{nm}$ in the MOT fluorescence with a total power of $P_{679} = 8.1\,\mathrm{mW}$. With the two rempuper configuration we observe a gain factor of $G_{707+679} = 9.6(2)$ with a rising time

$\tau_{679} = 69(1)\,\mathrm{ms}$.

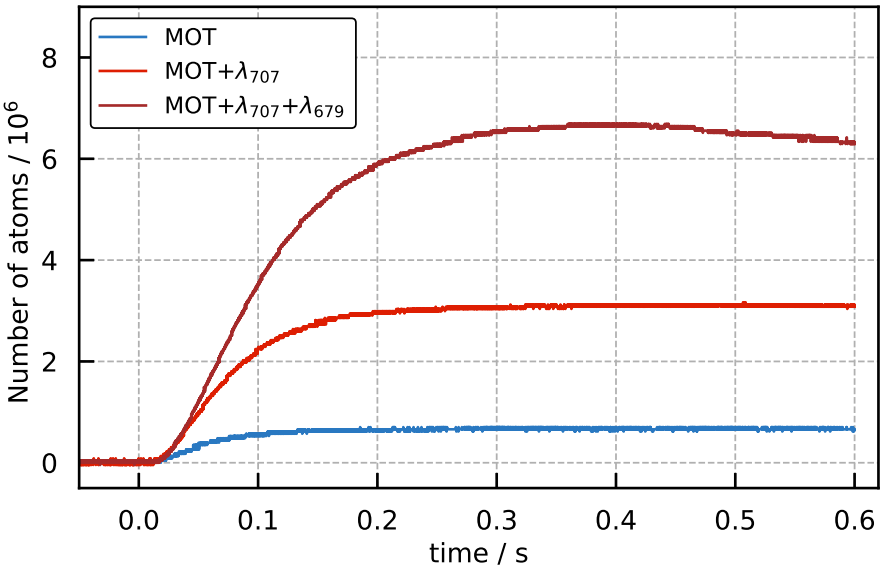

Figure 5.20: MOT number of atoms with repumper lasers

The gain on the steady-state atoms number are in agreement with the one reported in [122]. From Fig.5.20, the number of atoms decreases a function of the time in the case of double repumpers schemes. This is mainly due to a wavelength instability observe for the 679 nm repumper laser source, this problem can be solved opportunely chancing the voltage in the piezo of the master maximizing the MOT fluorescence signal. This instability is not observed in the single repumper scheme of 707 nm laser source. This laser source is able to maintain a constant number of atoms in the MOT even for a couple of hours without tuning the piezo of the master.

Chapter 6

Conclusions

The atomic source designed for our apparatus represent an innovative set-up conceived for optical lattice clock applications as well as for fundamental physics research. The atomic source is composed of a *two dimensional magnetic optical trap* (2D-MOT) which it is transversally loaded from a thermal beam of Sr atoms. The trapped atoms are then transferred to the final MOT by means of a push beam. This atomic source design features important advancements in metrological applications like a:

- complete optical control of the cold atomic flux generated by the atomic source by means of the 2D MOT and push beams;
- suppression of the hot-background collisions among atoms trapped in the optical lattice for the clock interrogation and the thermal beam. Thanks to the orthogonality between the loading beam in the 2D-MOT and the MOT loading axis these collisions are virtually eliminated;
- strong reduction of the black-body shift on the clock transition given that the oven (and the Zeeman slower window if used) is not in line of sight of the final science chamber

Once the optical lattice clock will be operated regularly, all these contributions on clock performance will be investigated in details. As reported in [148], the scientific target of this Sr clock is to explore the quantum frontiers of the frequency measurements exploiting state-of-the-art optical lattice clocks and systems where atoms are strongly coupled with electromagnetic radiation by means of a mechanical cavity.

The main contribution of my PhD work consist in the building of a novel atomic source for a new optical lattice clock with Sr atoms for the Time and frequency division at INRIM. Starting the project form a scratch, at the end of this PhD it is possible to generate a stable fluorescence signal of atoms trapped in a MOT. We also fully characterized the atomic source and we proposed a novel trapping

method to enhance the atomic flux from the source. During my PhD I spent the first period at UNITN where I started to assemble the main components of the experimental apparatus. At UNITN I also had the opportunity to participate in the construction of a new apparatus for the production of a Na Bose Einstein condensate. Both systems share common atomic source design and common hardware and software control system. I also developed preliminary numerical simulations in order to compare various trapping configurations maximizing the atomic source performances. Once obtained a stable MOT signal, the entire apparatus was moved to INRIM. At INRIM, a new trapping scheme employing a sideband enhanced 2D-MOT was studied and demonstrated, both numerically and experimentally, as a possible method to increase the atomic flux production of the atomic source. This method is a robust trapping method that preserves the compactness of the atomic source and avoids the introduction of any hot window elements typically used in the standard ZS enhancing method. This trapping scheme can be reliably extended to any kind of atomic source that employs a 2D-MOT approach. At INRIM we also assembled and characterized the laser sources for the second MOT cooling stage, repumping transitions and clock laser transition. Currently we are assembling the multi-wavelengths stabilization system in order to achieve a stable second MOT cooling stage. In the system we will lock all the cooling lasers and the optical dipole trap laser to an ultrastable cavity avoiding the need of the heatpipe element. At the same time we are preparing the opto-electronics system to realize the clock laser, exploiting the ultrastable laser and optical frequency comb already present at INRIM.

Once the Sr clock will operate, INRIM will have a set of optical lattice clocks composed of an already operating clock with neutral Yb atoms and a clock with neutral Cd atoms which is under construction, opening to the possibility of novel metrological and physical investigations. With this set of clocks it will be possible perform the evaluation and validation of different high accuracy atomic clocks, performing direct frequency measurements to test fundamental physics models. Another reason to employ a set of different clocks based on different atomic transition deals with the possible redefinition of the second based on the optical transition. One of the objective of this investigation is to figure out the best atomic transition candidate for the second redefinition considering the uncertainty reached and stability and robustness offered by different optical atomic clocks systems [224].

Bibliography

[1] SI. *The International System of Units*. 8th. BIPM. 2006. URL: https://www.bipm.org/en/publications/si-brochure/ (cit. on p. 1).

[2] SI. *The International System of Units (Draft)*. 9th. BIPM. May 2019. URL: https://www.bipm.org/en/measurement-units/rev-si/#communication (cit. on p. 1).

[3] Joint Committee for Guides in Metrology. *JCGM 100: Evaluation of Measurement Data - Guide to the Expression of Uncertainty in Measurement*. Tech. rep. JCGM, 2008. URL: https://www.bipm.org/utils/common/documents/jcgm/JCGM_100_2008_E.pdf (cit. on p. 2).

[4] D.W. Allan. "Statistics of atomic frequency standards". In: *Proceedings of the IEEE* 54.2 (1966), pp. 221–230. DOI: 10.1109/proc.1966.4634 (cit. on p. 2).

[5] David W. Allan. "Should the classical variance be used as a basic measure in standards metrology?" In: *IEEE Transactions on Instrumentation and Measurement* IM-36.2 (1987), pp. 646–654. DOI: 10.1109/tim.1987.6312761 (cit. on p. 2).

[6] W. M. Itano, J. C. Bergquist, J. J. Bollinger, J. M. Gilligan, D. J. Heinzen, F. L. Moore, M. G. Raizen, and D. J. Wineland. "Quantum projection noise: Population fluctuations in two-level systems". In: *Physical Review A* 47.5 (1993), pp. 3554–3570. DOI: 10.1103/physreva.47.3554 (cit. on p. 2).

[7] C. E. Cleeton and N. H. Williams. "Electromagnetic Waves of 1.1 cm Wave-Length and the Absorption Spectrum of Ammonia". In: *Physical Review* 45.4 (1934), pp. 234–237. DOI: 10.1103/physrev.45.234 (cit. on p. 3).

[8] Norman F. Ramsey. "A Molecular Beam Resonance Method with Separated Oscillating Fields". In: *Physical Review* 78.6 (1950), pp. 695–699. DOI: 10.1103/physrev.78.695 (cit. on p. 3).

[9] N.F. Ramsey. "History of Atomic Clocks". In: *Journal of Research of the National Bureau of Standards* 88.5 (1983), p. 301. DOI: 10.6028/jres.088.015 (cit. on p. 3).

[10] Harold Lyons. "Spectral lines as frequency standards". In: *Annals of the New York Academy of Sciences* 55.5 (1952), pp. 831–871. DOI: 10.1111/j.1749-6632.1952.tb26600.x (cit. on p. 3).

[11] L. Essen and J. V. L. Parry. "An Atomic Standard of Frequency and Time Interval: A Cæsium Resonator". In: *Nature* 176.4476 (1955), pp. 280–282. DOI: 10.1038/176280a0 (cit. on p. 3).

[12] Harold J. Metcalf and Peter van der Straten. *Laser Cooling and Trapping*. Springer New York, 1999. DOI: 10.1007/978-1-4612-1470-0 (cit. on pp. 3, 11, 48, 91, 96).

[13] Mark A. Kasevich, Erling Riis, Steven Chu, and Ralph G. DeVoe. "rf spectroscopy in an atomic fountain". In: *Physical Review Letters* 63.6 (1989), pp. 612–615. DOI: 10.1103/physrevlett.63.612 (cit. on p. 4).

[14] G. Santarelli, Ph. Laurent, P. Lemonde, A. Clairon, A. G. Mann, S. Chang, A. N. Luiten, and C. Salomon. "Quantum Projection Noise in an Atomic Fountain: A High Stability Cesium Frequency Standard". In: *Physical Review Letters* 82.23 (1999), pp. 4619–4622. DOI: 10.1103/physrevlett.82.4619 (cit. on p. 4).

[15] F. Levi, C. Calosso, D. Calonico, L. Lorini, E.K. Bertacco, A. Godone, G.A. Costanzo, B. Mongino, S.R. Jefferts, T.P. Heavner, and E.A. Donley. "Cryogenic fountain development at NIST and INRIM: preliminary characterization". In: *IEEE Transactions on Ultrasonics, Ferroelectrics and Frequency Control* 57.3 (2010), pp. 600–605. DOI: 10.1109/tuffc.2010.1453 (cit. on p. 4).

[16] J. Guena, M. Abgrall, D. Rovera, P. Laurent, B. Chupin, M. Lours, G. Santarelli, P. Rosenbusch, M. E. Tobar, Ruoxin Li, K. Gibble, A. Clairon, and S. Bize. "Progress in atomic fountains at LNE-SYRTE". In: *IEEE Transactions on Ultrasonics, Ferroelectrics and Frequency Control* 59.3 (2012), pp. 391–409. DOI: 10.1109/tuffc.2012.2208 (cit. on p. 4).

[17] Thomas P Heavner, Elizabeth A Donley, Filippo Levi, Giovanni Costanzo, Thomas E Parker, Jon H Shirley, Neil Ashby, Stephan Barlow, and S R Jefferts. "First accuracy evaluation of NIST-F2". In: *Metrologia* 51.3 (2014), pp. 174–182. DOI: 10.1088/0026-1394/51/3/174 (cit. on p. 4).

[18] S Weyers, V Gerginov, M Kazda, J Rahm, B Lipphardt, G Dobrev, and K Gibble. "Advances in the accuracy, stability, and reliability of the PTB primary fountain clocks". In: *Metrologia* 55.6 (2018), pp. 789–805. DOI: 10.1088/1681-7575/aae008 (cit. on p. 4).

[19] Andrew D. Ludlow, Martin M. Boyd, Jun Ye, E. Peik, and P. O. Schmidt. "Optical atomic clocks". In: *Reviews of Modern Physics* 87.2 (2015), pp. 637–701. DOI: 10.1103/revmodphys.87.637 (cit. on pp. 4, 30).

[20] Th. Udem, A. Huber, B. Gross, J. Reichert, M. Prevedelli, M. Weitz, and T. W. Hänsch. "Phase-Coherent Measurement of the Hydrogen 1S-2S Transition Frequency with an Optical Frequency Interval Divider Chain". In: *Physical Review Letters* 79.14 (1997), pp. 2646–2649. DOI: 10.1103/physrevlett.79.2646 (cit. on p. 4).

[21] Th. Udem, J. Reichert, R. Holzwarth, and T. W. Hänsch. "Accurate measurement of large optical frequency differences with a mode-locked laser". In: *Optics Letters* 24.13 (1999), p. 881. DOI: 10.1364/ol.24.000881 (cit. on p. 4).

[22] Scott A. Diddams, David J. Jones, Jun Ye, Steven T. Cundiff, John L. Hall, Jinendra K. Ranka, Robert S. Windeler, Ronald Holzwarth, Thomas Udem, and T. W. Hänsch. "Direct Link between Microwave and Optical Frequencies with a 300 THz Femtosecond Laser Comb". In: *Physical Review Letters* 84.22 (2000), pp. 5102–5105. DOI: 10.1103/physrevlett.84.5102 (cit. on p. 4).

[23] Th. Udem and F. Riehle. "Frequency combs applications and optical frequency standards". In: *La Rivista del Nuovo Cimento* 30.1 (2008), pp. 563–606. ISSN: 0393-697X. DOI: 10.1393/ncr/i2007-10027-5 (cit. on p. 5).

[24] G. Krame and W. Klische. "Extra high precision digital phase recorder". In: *18th European Frequency and Time Forum (EFTF 2004)*. IEE, 2004. DOI: 10.1049/cp:20040935 (cit. on p. 5).

[25] U. Sterr, T. Legero, T. Kessler, H. Schnatz, G. Grosche, O. Terra, and F. Riehle. "Ultrastable lasers: new developments and applications". In: *Time and Frequency Metrology II*. Ed. by Tetsuya Ido and Derryck T. Reid. SPIE, 2009. DOI: 10.1117/12.825217 (cit. on p. 5).

[26] F. Diedrich, J. C. Bergquist, Wayne M. Itano, and D. J. Wineland. "Laser Cooling to the Zero-Point Energy of Motion". In: *Physical Review Letters* 62.4 (1989), pp. 403–406. DOI: 10.1103/physrevlett.62.403 (cit. on p. 5).

[27] Wolfgang Paul. "Electromagnetic traps for charged and neutral particles". In: *Reviews of Modern Physics* 62.3 (1990), pp. 531–540. DOI: 10.1103/revmodphys.62.531 (cit. on p. 5).

[28] N. Huntemann, C. Sanner, B. Lipphardt, Chr. Tamm, and E. Peik. "Single-Ion Atomic Clock with 3×10^{-18} Systematic Uncertainty". In: *Physical Review Letters* 116.6 (2016). DOI: 10.1103/physrevlett.116.063001 (cit. on p. 6).

[29] Charles F. A. Baynham, Rachel M. Godun, Jonathan M. Jones, Steven A. King, Peter B. R. Nisbet-Jones, Fred Baynes, Antoine Rolland, Patrick E. G. Baird, Kai Bongs, Patrick Gill, and Helen S. Margolis. "Absolute frequency measurement of the optical clock transition in with an uncertainty of using a frequency link to international atomic time". In: *Journal of Modern Optics* 65.5-6 (2017), pp. 585–591. DOI: 10.1080/09500340.2017.1384514 (cit. on p. 6).

[30] Bin Jian, Pierre Dube, and Alan A. Madej. "Quantum projection noise limited stability and blackbody radiation shift uncertainty of NRC's Sr^+ atomic clock". In: *2016 Conference on Precision Electromagnetic Measurements (CPEM 2016)*. IEEE, 2016. DOI: 10.1109/cpem.2016.7540548 (cit. on p. 6).

[31] C. Chou, D. Hume, J. Koelemeij, D. Wineland, and T. Rosenband. "Frequency Comparison of Two High-Accuracy Al^+ Optical Clocks". In: *Physical Review Letters* 104.7 (2010). DOI: 10.1103/physrevlett.104.070802 (cit. on p. 6).

[32] S. M. Brewer, J. S. Chen, A. M. Hankin, E. R. Clements, C. W. Chou, D. J. Wineland, D. B. Hume, and D. R. Leibrandt. "An $^{27}Al^+$ quantum-logic clock with systematic uncertainty below 10^{-18}". In: (Feb. 20, 2019). arXiv: http://arxiv.org/abs/1902.07694v1 [physics.atom-ph] (cit. on p. 6).

[33] W. H. Oskay, S. A. Diddams, E. A. Donley, T. M. Fortier, T. P. Heavner, L. Hollberg, W. M. Itano, S. R. Jefferts, M. J. Delaney, K. Kim, F. Levi, T. E. Parker, and J. C. Bergquist. "Single-Atom Optical Clock with High Accuracy". In: *Physical Review Letters* 97.2 (2006). DOI: 10.1103/physrevlett.97.020801 (cit. on p. 6).

[34] Kensuke Matsubara, Hidekazu Hachisu, Ying Li, Shigeo Nagano, Clayton Locke, Asahiko Nogami, Masatoshi Kajita, Kazuhiro Hayasaka, Tetsuya Ido, and Mizuhiko Hosokawa. "Direct comparison of a Ca^+ single-ion clock against a Sr lattice clock to verify the absolute frequency measurement". In: *Optics Express* 20.20 (2012), p. 22034. DOI: 10.1364/oe.20.022034 (cit. on p. 6).

[35] J. von Zanthier, Th. Becker, M. Eichenseer, A. Yu. Nevsky, Ch. Schwedes, E. Peik, H. Walther, R. Holzwarth, J. Reichert, Th. Udem, T. W. Hänsch, P. V. Pokasov, M. N. Skvortsov, and S. N. Bagayev. "Absolute frequency measurement of the In^+ clock transition with a mode-locked laser". In: *Optics Letters* 25.23 (2000), p. 1729. DOI: 10.1364/ol.25.001729 (cit. on p. 6).

[36] Hidetoshi Katori, Masao Takamoto, V. G. Pal'chikov, and V. D. Ovsiannikov. "Ultrastable Optical Clock with Neutral Atoms in an Engineered Light Shift Trap". In: *Physical Review Letters* 91.17 (2003). DOI: 10.1103/physrevlett.91.173005 (cit. on pp. 6, 30, 35).

[37] Masao Takamoto, Feng-Lei Hong, Ryoichi Higashi, and Hidetoshi Katori. "An optical lattice clock". In: *Nature* 435.7040 (2005), pp. 321–324. DOI: 10.1038/nature03541 (cit. on pp. 6, 35).

[38] St Falke, H Schnatz, J S R Vellore Winfred, Th Middelmann, St Vogt, S Weyers, B Lipphardt, G Grosche, F Riehle, U Sterr, and Ch Lisdat. "The ^{87}Sr optical frequency standard at PTB". In: *Metrologia* 48.5 (2011), pp. 399–407. DOI: 10.1088/0026-1394/48/5/022 (cit. on pp. 6, 35).

[39] R. Le Targat, L. Lorini, Y. Le Coq, M. Zawada, J. Guéna, M. Abgrall, M. Gurov, P. Rosenbusch, D. G. Rovera, B. Nagórny, R. Gartman, P. G. Westergaard, M. E. Tobar, M. Lours, G. Santarelli, A. Clairon, S. Bize, P. Laurent, P. Lemonde, and J. Lodewyck. "Experimental realization of an optical second with strontium lattice clocks". In: *Nature Communications* 4.1 (2013). DOI: 10.1038/ncomms3109 (cit. on pp. 6, 35).

[40] Daisuke Akamatsu, Hajime Inaba, Kazumoto Hosaka, Masami Yasuda, Atsushi Onae, Tomonari Suzuyama, Masaki Amemiya, and Feng-Lei Hong. "Spectroscopy and frequency measurement of the ^{87}Sr clock transition by laser linewidth transfer using an optical frequency comb". In: *Applied Physics Express* 7.1 (2013), p. 012401. DOI: 10.7567/apex.7.012401 (cit. on p. 6).

[41] Ichiro Ushijima and Masao Takamoto and Manoj Das and Takuya Ohkubo and Hidetoshi Katori. "Cryogenic optical lattice clocks". In: *Nature Photonics* 9.3 (2015), pp. 185–189. DOI: 10.1038/nphoton.2015.5 (cit. on pp. 6, 63).

[42] Marcin Bober and Piotr Morzyński and Agata Cygan and Daniel Lisak and Piotr Masłowski and Mateusz Prymaczek and Piotr Wcisło and Piotr Ablewski and Mariusz Piwiński and Szymon Wójtewicz and Katarzyna Bielska and Dobrosława Bartoszek-Bober and Ryszard S Trawiński and Michał Zawada and Roman Ciuryło and Jerzy Zachorowski and Marcin Piotrowski and Wojciech Gawlik and Filip Ozimek and Czesław Radzewicz. "Strontium optical lattice clocks for practical realization of the metre and secondary representation of the second". In: *Measurement Science and Technology* 26.7 (2015), p. 075201. DOI: 10.1088/0957-0233/26/7/075201 (cit. on p. 6).

[43] Takuya Kohno, Masami Yasuda, Kazumoto Hosaka, Hajime Inaba, Yoshiaki Nakajima, and Feng-Lei Hong. "One-Dimensional Optical Lattice Clock with a Fermionic ^{171}Yb Isotope". In: *Applied Physics Express* 2 (2009), p. 072501. DOI: 10.1143/apex.2.072501 (cit. on p. 6).

[44] Chang Yong Park, Dai-Hyuk Yu, Won-Kyu Lee, Sang Eon Park, Eok Bong Kim, Sun Kyung Lee, Jun Woo Cho, Tai Hyun Yoon, Jongchul Mun, Sung Jong Park, Taeg Yong Kwon, and Sang-Bum Lee. "Absolute frequency measurement of $^1S_0(F = 1/2) - ^3P_0(F = 1/2)$ transition of ^{171}Yb atoms in a one-dimensional optical lattice at KRISS". In: *Metrologia* 50.2 (2013), pp. 119–128. DOI: 10.1088/0026-1394/50/2/119 (cit. on p. 6).

[45] N. Hinkley, J. A. Sherman, N. B. Phillips, M. Schioppo, N. D. Lemke, K. Beloy, M. Pizzocaro, C. W. Oates, and A. D. Ludlow. "An Atomic Clock with 10^{-18} Instability". In: *Science* 341.6151 (2013), pp. 1215–1218. DOI: 10.1126/science.1240420 (cit. on p. 6).

[46] B. J. Bloom, T. L. Nicholson, J. R. Williams, S. L. Campbell, M. Bishof, X. Zhang, W. Zhang, S. L. Bromley, and J. Ye. "An optical lattice clock with accuracy and stability at the 10^{-18} level". In: *Nature* 506.7486 (2014), pp. 71–75. DOI: 10.1038/nature12941 (cit. on p. 6).

[47] Marco Pizzocaro, Pierre Thoumany, Benjamin Rauf, Filippo Bregolin, Gianmaria Milani, Cecilia Clivati, Giovanni A Costanzo, Filippo Levi, and Davide Calonico. "Absolute frequency measurement of the $^1S_0$–$^3P_0$ transition of ^{171}Yb". In: *Metrologia* 54.1 (2017), pp. 102–112. DOI: 10.1088/1681-7575/aa4e62 (cit. on pp. 6, 78).

[48] M. Schioppo, R. C. Brown, W. F. McGrew, N. Hinkley, R. J. Fasano, K. Beloy, T. H. Yoon, G. Milani, D. Nicolodi, J. A. Sherman, N. B. Phillips, C. W. Oates, and A. D. Ludlow. "Ultrastable optical clock with two cold-atom ensembles". In: *Nature Photonics* 11.1 (2016), pp. 48–52. DOI: 10.1038/nphoton.2016.231 (cit. on p. 6).

[49] H. Hachisu, K. Miyagishi, S. G. Porsev, A. Derevianko, V. D. Ovsiannikov, V. G. Pal'chikov, M. Takamoto, and H. Katori. "Trapping of Neutral Mercury Atoms and Prospects for Optical Lattice Clocks". In: *Physical Review Letters* 100.5 (2008). DOI: 10.1103/physrevlett.100.053001 (cit. on p. 6).

[50] L. Yi, S. Mejri, J. J. McFerran, Y. Le Coq, and S. Bize. "Optical Lattice Trapping of ^{199}Hg and Determination of the Magic Wavelength for the Ultraviolet $^1S_0$–$^3P_0$ Clock Transition". In: *Physical Review Letters* 106.7 (2011). DOI: 10.1103/physrevlett.106.073005 (cit. on p. 6).

[51] A. P. Kulosa, D. Fim, K. H. Zipfel, S. Rühmann, S. Sauer, N. Jha, K. Gibble, W. Ertmer, E. M. Rasel, M. S. Safronova, U. I. Safronova, and S. G. Porsev. "Towards a Mg Lattice Clock: Observation of the $^1S_0$–$^3P_0$ Transition and Determination of the Magic Wavelength". In: *Physical Review Letters* 115.24 (2015). DOI: 10.1103/physrevlett.115.240801 (cit. on p. 6).

[52] Yushi Kaneda, J. M. Yarborough, Yevgeny Merzlyak, Atsushi Yamaguchi, Keitaro Hayashida, Noriaki Ohmae, and Hidetoshi Katori. "Continuous-wave, single-frequency 229 nm laser source for laser cooling of cadmium atoms". In: *Optics Letters* 41.4 (2016), p. 705. DOI: 10.1364/ol.41.000705 (cit. on p. 6).

[53] S. L. Campbell, R. B. Hutson, G. E. Marti, A. Goban, N. Darkwah Oppong, R. L. McNally, L. Sonderhouse, J. M. Robinson, W. Zhang, B. J. Bloom, and J. Ye. "A Fermi-degenerate three-dimensional optical lattice clock". In: *Science* 358.6359 (2017), pp. 90–94. DOI: 10.1126/science.aam5538 (cit. on p. 6).

[54] E. Oelker, R. B. Hutson, C. J. Kennedy, L. Sonderhouse, T. Bothwell, A. Goban, D. Kedar, C. Sanner, J. M. Robinson, G. E. Marti, D. G. Matei, T. Legero, M. Giunta, R. Holzwarth, F. Riehle, U. Sterr, and J. Ye. "Optical clock intercomparison with 6×10^{-19} precision in one hour". In: (Feb. 7, 2019). arXiv: http://arxiv.org/abs/1902.02741v1 [physics.atom-ph] (cit. on p. 6).

[55] Jacopo Grotti, Silvio Koller, Stefan Vogt, Sebastian Häfner, Uwe Sterr, Christian Lisdat, Heiner Denker, Christian Voigt, Ludger Timmen, Antoine Rolland, Fred N. Baynes, Helen S. Margolis, Michel Zampaolo, Pierre Thoumany, Marco Pizzocaro, Benjamin Rauf, Filippo Bregolin, Anna Tampellini, Piero Barbieri, Massimo Zucco, Giovanni A. Costanzo, Cecilia Clivati, Filippo Levi, and Davide Calonico. "Geodesy and metrology with a transportable optical clock". In: *Nature Physics* 14.5 (2018), pp. 437–441. DOI: 10.1038/s41567-017-0042-3 (cit. on p. 6).

[56] Tanja E Mehlstäubler, Gesine Grosche, Christian Lisdat, Piet O Schmidt, and Heiner Denker. "Atomic clocks for geodesy". In: *Reports on Progress in Physics* 81.6 (2018), p. 064401. DOI: 10.1088/1361-6633/aab409 (cit. on p. 6).

[57] W. F. McGrew, X. Zhang, R. J. Fasano, S. A. Schäffer, K. Beloy, D. Nicolodi, R. C. Brown, N. Hinkley, G. Milani, M. Schioppo, T. H. Yoon, and A. D. Ludlow. "Atomic clock performance enabling geodesy below the centimetre level". In: *Nature* 564.7734 (2018), pp. 87–90. DOI: 10.1038/s41586-018-0738-2 (cit. on pp. 6, 39).

[58] Christian Sanner, Nils Huntemann, Richard Lange, Christian Tamm, Ekkehard Peik, Marianna S. Safronova, and Sergey G. Porsev. "Optical clock comparison for Lorentz symmetry testing". In: *Nature* 567.7747 (2019), pp. 204–208. DOI: 10.1038/s41586-019-0972-2 (cit. on p. 6).

[59] Cédric Delaunay, Roee Ozeri, Gilad Perez, and Yotam Soreq. "Probing atomic Higgs-like forces at the precision frontier". In: *Physical Review D* 96.9 (2017). DOI: 10.1103/physrevd.96.093001 (cit. on p. 6).

[60] P. Wcisło, P. Morzyński, M. Bober, A. Cygan, D. Lisak, R. Ciuryło, and M. Zawada. "Experimental constraint on dark matter detection with optical atomic clocks". In: *Nature Astronomy* 1.1 (2016), p. 0009. DOI: 10.1038/s41550-016-0009 (cit. on p. 6).

[61] N. Huntemann, B. Lipphardt, Chr. Tamm, V. Gerginov, S. Weyers, and E. Peik. "Improved Limit on a Temporal Variation of m_p/m_e from Comparisons of Yb^+ and Cs Atomic Clocks". In: *Physical Review Letters* 113.21 (2014). DOI: 10.1103/physrevlett.113.210802 (cit. on p. 6).

[62] Q-Clocks. *Cavity-Enhanced Quantum Optical Clocks*. URL: https://www.quantera.eu/calls-for-proposals/funded-projects/49-q-clocks (cit. on p. 6).

[63] Claude Cohen-Tannoudji, Jacques Dupont-Roc, and Gilbert Grynberg. *Atom-Photon Interactions*. Wiley-VCH Verlag GmbH, 1998. DOI: 10.1002/9783527617197 (cit. on pp. 6, 11, 12).

[64] D G Matei, T Legero, Ch Grebing, S Häfner, Ch Lisdat, R Weyrich, W Zhang, L Sonderhouse, J M Robinson, F Riehle, J Ye, and U Sterr. "A second generation of low thermal noise cryogenic silicon resonators". In: *Journal of Physics: Conference Series* 723 (2016), p. 012031. DOI: 10.1088/1742-6596/723/1/012031 (cit. on pp. 7, 78).

[65] R. H. Dicke. "Coherence in Spontaneous Radiation Processes". In: *Physical Review* 93.1 (1954), pp. 99–110. DOI: 10.1103/physrev.93.99 (cit. on p. 7).

[66] M. Gross and S. Haroche. "Superradiance: An essay on the theory of collective spontaneous emission". In: *Physics Reports* 93.5 (1982), pp. 301–396. DOI: 10.1016/0370-1573(82)90102-8 (cit. on p. 7).

[67] D. Meiser, Jun Ye, D. R. Carlson, and M. J. Holland. "Prospects for a Millihertz-Linewidth Laser". In: *Physical Review Letters* 102.16 (2009). DOI: 10.1103/physrevlett.102.163601 (cit. on p. 7).

[68] Matthew A. Norcia, Matthew N. Winchester, Julia R. K. Cline, and James K. Thompson. "Superradiance on the millihertz linewidth strontium clock transition". In: *Science Advances* 2.10 (2016), e1601231. DOI: 10.1126/sciadv.1601231 (cit. on p. 7).

[69] Audrey Quessada, Richard P Kovacich, Ir ne Courtillot, Andr Clairon, Giorgio Santarelli, and Pierre Lemonde. "The Dick effect for an optical frequency standard". In: *Journal of Optics B: Quantum and Semiclassical Optics* 5.2 (2003), S150–S154. DOI: 10.1088/1464-4266/5/2/373 (cit. on p. 7).

[70] Onur Hosten, Nils J. Engelsen, Rajiv Krishnakumar, and Mark A. Kasevich. "Measurement noise 100 times lower than the quantum-projection limit using entangled atoms". In: *Nature* 529.7587 (2016), pp. 505–508. DOI: 10.1038/nature16176 (cit. on p. 8).

[71] Vittorio Giovannetti, Seth Lloyd, and Lorenzo Maccone. "Quantum Metrology". In: *Physical Review Letters* 96.1 (2006). DOI: 10.1103/physrevlett.96.010401 (cit. on p. 8).

[72] J. Appel, P. J. Windpassinger, D. Oblak, U. B. Hoff, N. Kjaergaard, and E. S. Polzik. "Mesoscopic atomic entanglement for precision measurements beyond the standard quantum limit". In: *Proceedings of the National Academy of Sciences* 106.27 (2009), pp. 10960–10965. DOI: 10.1073/pnas.0901550106 (cit. on p. 8).

[73] Zilong Chen, Justin G. Bohnet, Shannon R. Sankar, Jiayan Dai, and James K. Thompson. "Conditional Spin Squeezing of a Large Ensemble via the Vacuum Rabi Splitting". In: *Physical Review Letters* 106.13 (2011). DOI: 10.1103/physrevlett.106.133601 (cit. on p. 8).

[74] R. N. Bisset, S. Serafini, E. Iseni, M. Barbiero, T. Bienaimé, G. Lamporesi, G. Ferrari, and F. Dalfovo. "Observation of a spinning top in a Bose-Einstein condensate". In: *Physical Review A* 96.5 (2017). DOI: 10.1103/physreva.96.053605 (cit. on p. 8).

[75] G. Colzi, E. Fava, M. Barbiero, C. Mordini, G. Lamporesi, and G. Ferrari. "Production of large Bose-Einstein condensates in a magnetic-shield-compatible hybrid trap". In: *Physical Review A* 97.5 (2018). DOI: 10.1103/physreva.97.053625 (cit. on pp. 8, 26, 38, 59).

[76] T.W. Hänsch and A.L. Schawlow. "Cooling of gases by laser radiation". In: *Optics Communications* 13.1 (1975), pp. 68–69. DOI: 10.1016/0030-4018(75)90159-5 (cit. on p. 11).

[77] D. Wineland and H. Dehmelt. "Proposed $1014\delta\nu/\nu$ laser fluorescence spectroscopy on Tl^+ mono-ion oscillator III (side band cooling)". In: *Bull. Am. Phys. Soc. 20, 637 (1975)* (1975) (cit. on p. 11).

[78] J. Dalibard. In: *Helsinki workshop on laser manipulation of atoms, (unpublished)*. 1986 (cit. on p. 11).

[79] E. L. Raab, M. Prentiss, Alex Cable, Steven Chu, and D. E. Pritchard. "Trapping of Neutral Sodium Atoms with Radiation Pressure". In: *Physical Review Letters* 59.23 (1987), pp. 2631–2634. DOI: 10.1103/physrevlett.59.2631 (cit. on pp. 11, 18).

[80] C.J. Foot and D.P.C.J. Foot. *Atomic Physics*. Oxford Master Series in Physics. OUP Oxford, 2005. ISBN: 9780198506959. URL: https://books.google.it/books?id=_CoSDAAAQBAJ (cit. on pp. 11, 13, 55).

[81] David Guery-Odelin Claude Cohen-Tannoudji. *Advances In Atomic Physics: An Overview*. World Scientific Publishing Co Pte Ltd, Sept. 5, 2011. 796 pp. ISBN: 9812774971. URL: https://www.ebook.de/de/product/11434066/claude_cohen_tannoudji_david_guery_odelin_advances_in_atomic_physics_an_overview.html (cit. on pp. 11, 13, 27).

[82] V I Balykin, V G Minogin, and V S Letokhov. "Electromagnetic trapping of cold atoms". In: *Reports on Progress in Physics* 63.9 (2000), pp. 1429–1510. DOI: 10.1088/0034-4885/63/9/202 (cit. on pp. 12, 13).

[83] W. Ketterle, D. S. Durfee, and D. M. Stamper-Kurn. "Making, probing and understanding Bose-Einstein condensates". In: (Apr. 2, 1999). arXiv: http://arxiv.org/abs/cond-mat/9904034v2 [cond-mat] (cit. on p. 13).

[84] A. Ashkin. "Trapping of Atoms by Resonance Radiation Pressure". In: *Physical Review Letters* 40.12 (1978), pp. 729–732. DOI: 10.1103/physrevlett.40.729 (cit. on p. 14).

[85] P. D. Lett, W. D. Phillips, S. L. Rolston, C. E. Tanner, R. N. Watts, and C. I. Westbrook. "Optical molasses". In: *Journal of the Optical Society of America B* 6.11 (1989), p. 2084. DOI: 10.1364/josab.6.002084 (cit. on pp. 15, 17, 18, 94, 123).

[86] J. P. Gordon and A. Ashkin. "Motion of atoms in a radiation trap". In: *Physical Review A* 21.5 (1980), pp. 1606–1617. DOI: 10.1103/physreva.21.1606 (cit. on pp. 16, 17).

[87] T. W. Hodapp, C. Gerz, C. Furtlehner, C. I. Westbrook, W. D. Phillips, and J. Dalibard. "Three-dimensional spatial diffusion in optical molasses". In: *Applied Physics B Laser and Optics* 60.2-3 (1995), pp. 135–143. DOI: 10.1007/bf01135855 (cit. on p. 16).

[88] J Dalibard and C Cohen-Tannoudji. "Atomic motion in laser light: connection between semiclassical and quantum descriptions". In: *Journal of Physics B: Atomic and Molecular Physics* 18.8 (1985), pp. 1661–1683. DOI: 10.1088/0022-3700/18/8/019 (cit. on p. 17).

[89] Y. Castin, H. Wallis, and J. Dalibard. "Limit of Doppler cooling". In: *Journal of the Optical Society of America B* 6.11 (1989), p. 2046. DOI: 10.1364/josab.6.002046 (cit. on p. 17).

[90] J. Dalibard and C. Cohen-Tannoudji. "Laser cooling below the Doppler limit by polarization gradients: simple theoretical models". In: *Journal of the Optical Society of America B* 6.11 (1989), p. 2023. DOI: 10.1364/josab.6.002023 (cit. on p. 17).

[91] P. J. Ungar, D. S. Weiss, E. Riis, and Steven Chu. "Optical molasses and multilevel atoms: theory". In: *Journal of the Optical Society of America B* 6.11 (1989), p. 2058. DOI: 10.1364/josab.6.002058 (cit. on p. 17).

[92] David S. Weiss, Erling Riis, Yaakov Shevy, P. Jeffrey Ungar, and Steven Chu. "Optical molasses and multilevel atoms: experiment". In: *Journal of the Optical Society of America B* 6.11 (1989), p. 2072. DOI: 10.1364/josab.6.002072 (cit. on p. 17).

[93] Kurt E. Gibble, Steven Kasapi, and Steven Chu. "Improved magneto-optic trapping in a vapor cell". In: *Optics Letters* 17.7 (1992), p. 526. DOI: 10.1364/ol.17.000526 (cit. on p. 20).

[94] D. Haubrich, A. Höpe, and D. Meschede. "A simple model for optical capture of atoms in strong magnetic quadrupole fields". In: *Optics Communications* 102.3-4 (1993), pp. 225–230. DOI: 10.1016/0030-4018(93)90387-k (cit. on p. 21).

[95] K. Lindquist, M. Stephens, and C. Wieman. "Experimental and theoretical study of the vapor-cell Zeeman optical trap". In: *Physical Review A* 46.7 (1992), pp. 4082–4090. DOI: 10.1103/physreva.46.4082 (cit. on p. 21).

[96] Muhammad Anwar, Daniel V Magalhães, Stella T Müller, Muhammad Faisal, Muhammad Nawaz, and Mushtaq Ahmed. "Revisiting the capture velocity of a cesium magneto-optical trap: model, simulation and experiment". In: *Laser Physics* 24.12 (2014), p. 125502. DOI: 10.1088/1054-660x/24/12/125502 (cit. on p. 23).

[97] Mariusz Gajda and Jan Mostowski. "Three-dimensional theory of the magneto optical trap: Doppler cooling in the low-intensity limit". In: *Physical Review A* 49.6 (1994), pp. 4864–4875. DOI: 10.1103/physreva.49.4864 (cit. on p. 23).

[98] O. N. Prudnikov, A. V. Taichenachev, and V. I. Yudin. "Three-dimensional theory of the magneto-optical trap". In: *Journal of Experimental and Theoretical Physics* 120.4 (2015), pp. 587–594. DOI: 10.1134/s1063776115040147 (cit. on p. 23).

[99] W. Wohlleben, F. Chevy, K. Madison, and J. Dalibard. "An atom faucet". In: *The European Physical Journal D* 15.2 (2001), pp. 237–244. DOI: 10.1007/s100530170171 (cit. on pp. 25, 26, 38, 85).

[100] J. Schoser, A. Batär, R. Löw, V. Schweikhard, A. Grabowski, Yu. B. Ovchinnikov, and T. Pfau. "Intense source of cold Rb atoms from a pure two-dimensional magneto-optical trap". In: *Physical Review A* 66.2 (2002). DOI: 10.1103/physreva.66.023410 (cit. on p. 26).

[101] J. Catani, P. Maioli, L. De Sarlo, F. Minardi, and M. Inguscio. "Intense slow beams of bosonic potassium isotopes". In: *Physical Review A* 73.3 (2006). DOI: 10.1103/physreva.73.033415 (cit. on pp. 26, 85, 96).

[102] Jae Hoon Lee and Jongchul Mun. "Optimized atomic flux from a frequency-modulated two-dimensional magneto-optical trap for cold fermionic potassium atoms". In: *Journal of the Optical Society of America B* 34.7 (2017), p. 1415. DOI: 10.1364/josab.34.001415 (cit. on pp. 26, 116).

[103] T. G. Tiecke, S. D. Gensemer, A. Ludewig, and J. T. M. Walraven. "High-flux two-dimensional magneto-optical-trap source for cold lithium atoms". In: *Physical Review A* 80.1 (2009). DOI: 10.1103/physreva.80.013409 (cit. on pp. 26, 38, 59, 102).

[104] G. Lamporesi, S. Donadello, S. Serafini, and G. Ferrari. "Compact high-flux source of cold sodium atoms". In: *Review of Scientific Instruments* 84.6 (2013), p. 063102. DOI: 10.1063/1.4808375 (cit. on pp. 26, 38, 59, 102, 121).

[105] Sören Dörscher, Alexander Thobe, Bastian Hundt, André Kochanke, Rodolphe Le Targat, Patrick Windpassinger, Christoph Becker, and Klaus Sengstock. "Creation of quantum-degenerate gases of ytterbium in a compact 2D-/3D-magneto-optical trap setup". In: *Review of Scientific Instruments* 84.4 (2013), p. 043109. DOI: 10.1063/1.4802682 (cit. on p. 26).

[106] S. Saskin, J. T. Wilson, B. Grinkemeyer, and J. D. Thompson. "Narrow-Line Cooling and Imaging of Ytterbium Atoms in an Optical Tweezer Array". In: *Physical Review Letters* 122.14 (2019). DOI: 10.1103/physrevlett.122.143002 (cit. on p. 26).

[107] Ingo Nosske and Luc Couturier and Fachao Hu and Canzhu Tan and Chang Qiao and Jan Blume and Y. H. Jiang and Peng Chen and Matthias Weidemüller. "Two-dimensional magneto-optical trap as a source for cold strontium atoms". In: *Physical Review A* 96.5 (2017). DOI: 10.1103/physreva.96.053415 (cit. on pp. 26, 38, 59, 102, 109, 110, 112, 121, 122, 125, 127).

[108] A. Burchianti, C. D'Errico, S. Rosi, A. Simoni, M. Modugno, C. Fort, and F. Minardi. "Dual-species Bose-Einstein condensate of ^{41}K and ^{87}Rb in a hybrid trap". In: *Physical Review A* 98.6 (2018). DOI: 10.1103/physreva.98.063616 (cit. on p. 26).

[109] Steven Chu, J. E. Bjorkholm, A. Ashkin, and A. Cable. "Experimental Observation of Optically Trapped Atoms". In: *Physical Review Letters* 57.3 (1986), pp. 314–317. DOI: 10.1103/physrevlett.57.314 (cit. on p. 26).

[110] Rudolf Grimm, Matthias Weidemüller, and Yurii B. Ovchinnikov. "Optical Dipole Traps for Neutral Atoms". In: *Advances In Atomic, Molecular, and Optical Physics*. Elsevier, 2000, pp. 95–170. DOI: 10.1016/s1049-250x(08)60186-x (cit. on p. 27).

[111] R. H. Dicke. "The Effect of Collisions upon the Doppler Width of Spectral Lines". In: *Physical Review* 89.2 (1953), pp. 472–473. DOI: 10.1103/physrev.89.472 (cit. on p. 29).

[112] Hidetoshi Katori. "Spectroscopy of Strontium Atoms in the Lamb-Dicke Confinement". In: *Frequency Standards and Metrology*. WORLD SCIENTIFIC, 2002. DOI: 10.1142/9789812777713_0036 (cit. on p. 30).

[113] Hidetoshi Katori, V. D. Ovsiannikov, S. I. Marmo, and V. G. Palchikov. "Strategies for reducing the light shift in atomic clocks". In: *Physical Review A* 91.5 (2015). DOI: 10.1103/physreva.91.052503 (cit. on p. 31).

[114] Nils Nemitz, Asbjørn Arvad Jørgensen, Ryotatsu Yanagimoto, Filippo Bregolin, and Hidetoshi Katori. "Modeling light shifts in optical lattice clocks". In: *Physical Review A* 99.3 (2019). DOI: 10.1103/physreva.99.033424 (cit. on p. 31).

[115] M. Takamoto, H. Katori, S. I. Marmo, V. D. Ovsiannikov, and V. G. Pal'chikov. "Prospects for Optical Clocks with a Blue-Detuned Lattice". In: *Physical Review Letters* 102.6 (2009). DOI: 10.1103/physrevlett.102.063002 (cit. on p. 31).

[116] J. E. Sansonetti and G. Nave. "Wavelengths, Transition Probabilities, and Energy Levels for the Spectrum of Neutral Strontium (SrI)". In: *Journal of Physical and Chemical Reference Data* 39.3 (2010), p. 033103. DOI: 10.1063/1.3449176 (cit. on pp. 31, 32, 50).

[117] S. B. Nagel, P. G. Mickelson, A. D. Saenz, Y. N. Martinez, Y. C. Chen, T. C. Killian, P. Pellegrini, and R. Côté. "Photoassociative Spectroscopy at Long Range in Ultracold Strontium". In: *Physical Review Letters* 94.8 (2005). DOI: 10.1103/physrevlett.94.083004 (cit. on p. 32).

[118] Masami Yasuda, Tetsuo Kishimoto, Masao Takamoto, and Hidetoshi Katori. "Photoassociation spectroscopy of ^{88}Sr: Reconstruction of the wave function near the last node". In: *Physical Review A* 73.1 (2006). DOI: 10.1103/physreva.73.011403 (cit. on p. 32).

[119] L. R. Hunter, W. A. Walker, and D. S. Weiss. "Observation of an atomic Stark–electric-quadrupole interference". In: *Physical Review Letters* 56.8 (1986), pp. 823–826. DOI: 10.1103/physrevlett.56.823 (cit. on pp. 32, 113).

[120] Masami Yasuda and Hidetoshi Katori. "Lifetime Measurement of the $^3P_2$ Metastable State of Strontium Atoms". In: *Physical Review Letters* 92.15 (2004). DOI: 10.1103/physrevlett.92.153004 (cit. on p. 33).

[121] Andrei Derevianko. "Feasibility of Cooling and Trapping Metastable Alkaline-Earth Atoms". In: *Physical Review Letters* 87.2 (2001). DOI: 10.1103/physrevlett.87.023002 (cit. on p. 33).

[122] Xinye Xu, Thomas H. Loftus, John L. Hall, Alan Gallagher, and Jun Ye. "Cooling and trapping of atomic strontium". In: *Journal of the Optical Society of America B* 20.5 (2003), p. 968. DOI: 10.1364/josab.20.000968 (cit. on pp. 33, 34, 64, 113, 130).

[123] Hidetoshi Katori and Tetsuya Ido and Yoshitomo Isoya and Makoto Kuwata-Gonokami. "Magneto-Optical Trapping and Cooling of Strontium Atoms down to the Photon Recoil Temperature". In: *Physical Review Letters* 82.6 (1999), pp. 1116–1119. DOI: 10.1103/physrevlett.82.1116 (cit. on pp. 33, 64).

[124] Thomas H. Loftus, Tetsuya Ido, Andrew D. Ludlow, Martin M. Boyd, and Jun Ye. "Narrow Line Cooling: Finite Photon Recoil Dynamics". In: *Physical Review Letters* 93.7 (2004). DOI: 10.1103/physrevlett.93.073003 (cit. on p. 33).

[125] Tommaso Mazzoni. "Laser cooling and trapping of ^{87}Sr and ^{88}Sr atoms". MA thesis. Università degli Studi di Firenze, 2012. URL: coldatoms.lens.unifi.it/index.php/ultra-cold-strontium/documents/31-documents/79-intrappolamento-e-raffreddamento-laser-di-atomi-di-87sr-e-88sr.html (cit. on p. 33).

[126] Timothy P. Dinneen, Kurt R. Vogel, Ennio Arimondo, John L. Hall, and Alan Gallagher. "Cold collisions of Sr*–Sr in a magneto-optical trap". In: *Physical Review A* 59.2 (1999), pp. 1216–1222. DOI: 10.1103/physreva.59.1216 (cit. on p. 33).

[127] N. Poli, R. E. Drullinger, G. Ferrari, J. Léonard, F. Sorrentino, and G. M. Tino. "Cooling and trapping of ultracold strontium isotopic mixtures". In: *Physical Review A* 71.6 (2005). DOI: 10.1103/physreva.71.061403 (cit. on pp. 34, 83).

[128] N. Poli, G. Ferrari, M. Prevedelli, F. Sorrentino, R.E. Drullinger, and G.M. Tino. "Laser sources for precision spectroscopy on atomic strontium". In: *Spectrochimica Acta Part A: Molecular and Biomolecular Spectroscopy* 63.5 (2006), pp. 981–986. DOI: 10.1016/j.saa.2005.10.024 (cit. on p. 34).

[129] Simon Stellmer and Florian Schreck. "Reservoir spectroscopy of $5s5p\,^3P_2$–$5snd\,^3D_{1,2,3}$ transitions in strontium". In: *Physical Review A* 90.2 (2014). DOI: 10.1103/physreva.90.022512 (cit. on p. 34).

[130] P G Mickelson, Y N Martinez de Escobar, P Anzel, B J DeSalvo, S B Nagel, A J Traverso, M Yan, and T C Killian. "Repumping and spectroscopy of laser-cooled Sr atoms using the $(5s5p)^3P_2$–$(5s4d)^3D_2$ transition". In: *Journal of Physics B: Atomic, Molecular and Optical Physics* 42.23 (2009), p. 235001. DOI: 10.1088/0953-4075/42/23/235001 (cit. on p. 34).

[131] Fachao Hu, Ingo Nosske, Luc Couturier, Canzhu Tan, Chang Qiao, Peng Chen, Y. H. Jiang, Bing Zhu, and Matthias Weidemüller. "Analyzing a single-laser repumping scheme for efficient loading of a strontium magneto-optical trap". In: (Dec. 4, 2018). arXiv: http://arxiv.org/abs/1812.01258v2 [physics.atom-ph] (cit. on p. 34).

[132] Takayuki Kurosu and Fujio Shimizu. "Laser Cooling and Trapping of Alkaline Earth Atoms". In: *Japanese Journal of Applied Physics* 31.Part 1, No. 3 (1992), pp. 908–912. DOI: 10.1143/jjap.31.908 (cit. on p. 34).

[133] Xavier Baillard, Mathilde Fouché, Rodolphe Le Targat, Philip G. Westergaard, Arnaud Lecallier, Yann Le Coq, Giovanni D. Rovera, Sebastien Bize, and Pierre Lemonde. "Accuracy evaluation of an optical lattice clock with bosonic atoms". In: *Optics Letters* 32.13 (2007), p. 1812. DOI: 10.1364/ol.32.001812 (cit. on p. 35).

[134] Tomoya Akatsuka, Masao Takamoto, and Hidetoshi Katori. "Optical lattice clocks with non-interacting bosons and fermions". In: *Nature Physics* 4.12 (2008), pp. 954–959. DOI: 10.1038/nphys1108 (cit. on p. 35).

[135] Piotr Morzyński and Marcin Bober and Dobrosława Bartoszek-Bober and Jerzy Nawrocki and Przemysław Krehlik and Łukasz Śliwczyński and Marcin Lipiński and Piotr Masłowski and Agata Cygan and Piotr Dunst and Michał Garus and Daniel Lisak and Jerzy Zachorowski and Wojciech Gawlik and Czesław Radzewicz and Roman Ciuryło and Michał Zawada. "Absolute measurement of the $^1S_0$–$^3P_0$ clock transition in neutral 88Sr over the 330 km-long stabilized fibre optic link". In: *Scientific Reports* 5.1 (2015). DOI: 10.1038/srep17495 (cit. on pp. 35, 63).

[136] S. Origlia, M. S. Pramod, S. Schiller, Y. Singh, K. Bongs, R. Schwarz, A. Al-Masoudi, S. Dörscher, S. Herbers, S. Häfner, U. Sterr, and Ch. Lisdat. "Towards an optical clock for space: Compact, high-performance optical lattice clock based on bosonic atoms". In: *Physical Review A* 98.5 (2018). DOI: 10.1103/physreva.98.053443 (cit. on p. 35).

[137] Y. B. Band and A. Vardi. "Collisional shifts in optical-lattice atom clocks". In: *Physical Review A* 74.3 (2006). DOI: 10.1103/physreva.74.033807 (cit. on p. 35).

[138] Sergey G. Porsev and Andrei Derevianko. "Hyperfine quenching of the metastable $^3P_{0,2}$ states in divalent atoms". In: *Physical Review A* 69.4 (2004). DOI: 10.1103/physreva.69.042506 (cit. on p. 35).

[139] I. Courtillot, A. Quessada-Vial, A. Brusch, D. Kolker, G. D. Rovera, and P. Lemonde. "Accurate spectroscopy of Sr atoms". In: *The European Physical Journal D* 33.2 (2005), pp. 161–171. DOI: 10.1140/epjd/e2005-00058-0 (cit. on p. 35).

[140] Xiaoji Zhou, Xia Xu, Xuzong Chen, and Jingbiao Chen. "Magic wavelengths for terahertz clock transitions". In: *Physical Review A* 81.1 (2010). DOI: 10.1103/physreva.81.012115 (cit. on p. 35).

[141] P. G. Westergaard, J. Lodewyck, L. Lorini, A. Lecallier, E. A. Burt, M. Zawada, J. Millo, and P. Lemonde. "Lattice-Induced Frequency Shifts in Sr Optical Lattice Clocks at the 10^{-17} Level". In: *Physical Review Letters* 106.21 (2011). DOI: 10.1103/physrevlett.106.210801 (cit. on p. 35).

[142] Hidekazu Hachisu, Gérard Petit, and Tetsuya Ido. "Absolute frequency measurement with uncertainty below 1×10^{-15} using International Atomic Time". In: *Applied Physics B* 123.1 (2016). DOI: 10.1007/s00340-016-6603-9 (cit. on p. 35).

[143] Christian Grebing and Ali Al-Masoudi and Sören Dörscher and Sebastian Häfner and Vladislav Gerginov and Stefan Weyers and Burghard Lipphardt and Fritz Riehle and Uwe Sterr and Christian Lisdat. "Realization of a timescale with an accurate optical lattice clock". In: *Optica* 3.6 (2016), p. 563. DOI: 10.1364/optica.3.000563 (cit. on p. 35).

[144] Jérôme Lodewyck, Sławomir Bilicki, Eva Bookjans, Jean-Luc Robyr, Chunyan Shi, Grégoire Vallet, Rodolphe Le Targat, Daniele Nicolodi, Yann Le Coq, Jocelyne Guéna, Michel Abgrall, Peter Rosenbusch, and Sébastien Bize. "Optical to microwave clock frequency ratios with a nearly continuous strontium optical lattice clock". In: *Metrologia* 53.4 (2016), pp. 1123–1130. DOI: 10.1088/0026-1394/53/4/1123 (cit. on p. 35).

[145] Hidekazu Hachisu, Gérard Petit, Fumimaru Nakagawa, Yuko Hanado, and Tetsuya Ido. "SI-traceable measurement of an optical frequency at the low 10^{-16} level without a local primary standard". In: *Optics Express* 25.8 (2017), p. 8511. DOI: 10.1364/oe.25.008511 (cit. on p. 35).

[146] Fritz Riehle, Patrick Gill, Felicitas Arias, and Lennart Robertsson. "The CIPM list of recommended frequency standard values: guidelines and procedures". In: *Metrologia* 55.2 (2018), pp. 188–200. DOI: 10.1088/1681-7575/aaa302 (cit. on p. 35).

[147] Consultative Committee for Time and Frequency (CCTF). *Recommendation CCTF 2 (2017).* Tech. rep. 21st meeting pag 49. Bureau International des Poids et Mesures, June 2017. URL: https://www.bipm.org/utils/common/pdf/CC/CCTF/CCTF21.pdf (cit. on p. 35).

[148] M. G. Tarallo, D. Calonico, F. Levi, M. Barbiero, G. Lamporesi, and G. Ferrari. "A strontium optical lattice clock apparatus for precise frequency metrology and beyond". In: *2017 Joint Conference of the European Frequency and Time Forum and IEEE International Frequency Control Symposium (EFTF/IFC).* IEEE, 2017. DOI: 10.1109/fcs.2017.8089020 (cit. on pp. 37, 131).

[149] Erling Riis, David S. Weiss, Kathryn A. Moler, and Steven Chu. "Atom funnel for the production of a slow, high-density atomic beam". In: *Physical Review Letters* 64.14 (1990), pp. 1658–1661. DOI: 10.1103/physrevlett.64.1658 (cit. on p. 38).

[150] T Middelmann, C Lisdat, S Falke, J S R Vellore Winfred, F Riehle, and U Sterr. "Tackling the Blackbody Shift in a Strontium Optical Lattice Clock". In: *IEEE Transactions on Instrumentation and Measurement* 60.7 (2011), pp. 2550–2557. DOI: 10.1109/tim.2010.2088470 (cit. on p. 38).

[151] M. S. Safronova, M. G. Kozlov, and C. W. Clark. "Blackbody radiation shifts in optical atomic clocks". In: *IEEE Transactions on Ultrasonics, Ferroelectrics and Frequency Control* 59.3 (2012), pp. 439–447. DOI: 10.1109/tuffc.2012.2213 (cit. on p. 38).

[152] Kurt Gibble. "Scattering of Cold-Atom Coherences by Hot Atoms: Frequency Shifts from Background-Gas Collisions". In: *Physical Review Letters* 110.18 (2013). DOI: 10.1103/physrevlett.110.180802 (cit. on p. 39).

[153] Rebecca Grinham and Dr Andrew Chew. "A Review of Outgassing and Methods for its Reduction". In: *Applied Science and Convergence Technology* 26.5 (2017), pp. 95–109. DOI: 10.5757/asct.2017.26.5.95 (cit. on p. 41).

[154] Ruwan Senaratne, Shankari V. Rajagopal, Zachary A. Geiger, Kurt M. Fujiwara, Vyacheslav Lebedev, and David M. Weld. "Effusive atomic oven nozzle design using an aligned microcapillary array". In: *Review of Scientific Instruments* 86.2 (2015), p. 023105. DOI: 10.1063/1.4907401 (cit. on p. 44).

[155] R Calder and G Lewin. "Reduction of stainless-steel outgassing in ultra-high vacuum". In: *British Journal of Applied Physics* 18.10 (1967), pp. 1459–1472. DOI: 10.1088/0508-3443/18/10/313 (cit. on p. 45).

[156] A Berman. "Water vapor in vacuum systems". In: *Vacuum* 47.4 (1996), pp. 327–332. DOI: 10.1016/0042-207x(95)00246-4 (cit. on p. 45).

[157] Manoj Kumar Gupta, Abhinav Priyadarshi, and Ziauddin Khan. "Hydrogen in Stainless Steel as Killing Agent for UHV: A Review". In: *Materials Today: Proceedings* 2.4-5 (2015), pp. 1074–1081. DOI: 10.1016/j.matpr.2015.07.011 (cit. on p. 45).

[158] M. Bernardini, S. Braccini, R. De Salvo, A. Di Virgilio, A. Gaddi, A. Gennai, G. Genuini, A. Giazotto, G. Losurdo, H. B. Pan, A. Pasqualetti, D. Passuello, P. Popolizio, F. Raffaelli, G. Torelli, Z. Zhang, C. Bradaschia, R. Del Fabbro, I. Ferrante, F. Fidecaro, P. La Penna, S. Mancini, R. Poggiani, P. Narducci, A. Solina, and R. Valentini. "Air bake-out to reduce hydrogen outgassing from stainless steel". In: *Journal of Vacuum Science &*

Technology A: Vacuum, Surfaces, and Films 16.1 (1998), pp. 188–193. DOI: 10.1116/1.580967 (cit. on p. 47).

[159] J. A. Giordmaine and T. C. Wang. "Molecular beam formation by long parallel tubes". In: *Journal of Applied Physics* 31.3 (1960), pp. 463–471. DOI: 10.1063/1.1735609 (cit. on pp. 48, 116).

[160] H. C. W. Beijerinck and N. F. Verster. "Velocity distribution and angular distribution of molecular beams from multichannel arrays". In: *Journal of Applied Physics* 46.5 (1975), pp. 2083–2091. DOI: 10.1063/1.321845 (cit. on pp. 48, 49, 116).

[161] C. B. Alcock, V. P. Itkin, and M. K. Horrigan. "Vapour Pressure Equations for the Metallic Elements: 298–2500 K". In: *Canadian Metallurgical Quarterly* 23.3 (1984), pp. 309–313. DOI: 10.1179/cmq.1984.23.3.309 (cit. on p. 48).

[162] Manjeera Mantina, Adam C. Chamberlin, Rosendo Valero, Christopher J. Cramer, and Donald G. Truhlar. "Consistent van der Waals Radii for the Whole Main Group". In: *The Journal of Physical Chemistry A* 113.19 (2009), pp. 5806–5812. DOI: 10.1021/jp8111556 (cit. on p. 49).

[163] BEC-Trento. *exp-control*. https://github.com/BEC-Trento/exp-control. 2018 (cit. on p. 50).

[164] Daniel J. Thompson and Robert E. Scholten. "Narrow linewidth tunable external cavity diode laser using wide bandwidth filter". In: *Review of Scientific Instruments* 83.2 (2012), p. 023107. DOI: 10.1063/1.3687441 (cit. on p. 51).

[165] E. M. Bridge, J. Millen, C. S. Adams, and M. P. A. Jones. "A vapor cell based on dispensers for laser spectroscopy". In: *Review of Scientific Instruments* 80.1 (2009), p. 013101. DOI: 10.1063/1.3036980 (cit. on p. 54).

[166] M. Schioppo, N. Poli, M. Prevedelli, St. Falke, Ch. Lisdat, U. Sterr, and G. M. Tino. "A compact and efficient strontium oven for laser-cooling experiments". In: *Review of Scientific Instruments* 83.10 (2012), p. 103101. DOI: 10.1063/1.4756936 (cit. on pp. 54, 68, 69).

[167] Alexei A. Tonyushkin, Adam D. Light, and Michael D. Di Rosa. "Phase-locked scanning interferometer for frequency stabilization of multiple lasers". In: *Review of Scientific Instruments* 78.12 (2007), p. 123103. DOI: 10.1063/1.2818773 (cit. on p. 54).

[168] A. Rossi, V. Biancalana, B. Mai, and L. Tomassetti. "Long-term drift laser frequency stabilization using purely optical reference". In: *Review of Scientific Instruments* 73.7 (2002), pp. 2544–2548. DOI: 10.1063/1.1487895 (cit. on p. 54).

[169] Luc Couturier, Ingo Nosske, Fachao Hu, Canzhu Tan, Chang Qiao, Y. H. Jiang, Peng Chen, and Matthias Weidemüller. "Laser frequency stabilization using a commercial wavelength meter". In: *Review of Scientific Instruments* 89.4 (2018), p. 043103. DOI: 10.1063/1.5025537 (cit. on p. 54).

[170] T. W. Hänsch, M. D. Levenson, and A. L. Schawlow. "Complete Hyperfine Structure of a Molecular Iodine Line". In: *Physical Review Letters* 26.16 (1971), pp. 946–949. DOI: 10.1103/physrevlett.26.946 (cit. on p. 54).

[171] A. L. Schawlow. "Spectroscopy in a New Light". In: *Science* 217.4554 (1982), pp. 9–16. DOI: 10.1126/science.217.4554.9 (cit. on p. 54).

[172] K. B. MacAdam, A. Steinbach, and C. Wieman. "A narrow-band tunable diode laser system with grating feedback, and a saturated absorption spectrometer for Cs and Rb". In: *American Journal of Physics* 60.12 (1992), pp. 1098–1111. DOI: 10.1119/1.16955 (cit. on pp. 54, 69).

[173] David S. Bomse, Alan C. Stanton, and Joel A. Silver. "Frequency modulation and wavelength modulation spectroscopies: comparison of experimental methods using a lead-salt diode laser". In: *Applied Optics* 31.6 (1992), p. 718. DOI: 10.1364/ao.31.000718 (cit. on p. 54).

[174] James M. Supplee, Edward A. Whittaker, and Wilfried Lenth. "Theoretical description of frequency modulation and wavelength modulation spectroscopy". In: *Applied Optics* 33.27 (1994), p. 6294. DOI: 10.1364/ao.33.006294 (cit. on pp. 54, 55).

[175] Todd P. Meyrath. *Electromagnet Design Basics for Cold Atom Experiments*. 2004. URL: http://citeseerx.ist.psu.edu/viewdoc/download?doi=10.1.1.505.4652&rep=rep1&type=pdf (cit. on p. 61).

[176] Engineering ToolBox. May 2001. URL: https://www.engineeringtoolbox.com (cit. on p. 62).

[177] Piotr Ablewski, Marcin Bober, and Michal Zawada. "Reducing blackbody radiation shift uncertainty in optical lattice clocks". In: *2018 European Frequency and Time Forum (EFTF)*. IEEE, 2018. DOI: 10.1109/eftf.2018.8409067 (cit. on p. 63).

[178] K. Beloy, N. Hinkley, N. B. Phillips, J. A. Sherman, M. Schioppo, J. Lehman, A. Feldman, L. M. Hanssen, C. W. Oates, and A. D. Ludlow. "Atomic Clock with 1×10^{-18} Room-Temperature Blackbody Stark Uncertainty". In: *Physical Review Letters* 113.26 (2014). DOI: 10.1103/physrevlett.113.260801 (cit. on p. 63).

[179] T.L. Nicholson, S.L. Campbell, R.B. Hutson, G.E. Marti, B.J. Bloom, R.L. McNally, W. Zhang, M.D. Barrett, M.S. Safronova, G.F. Strouse, W.L. Tew, and J. Ye. "Systematic evaluation of an atomic clock at 2×10^{18} total uncertainty". In: *Nature Communications* 6.1 (2015). DOI: 10.1038/ncomms7896 (cit. on p. 63).

[180] F. Sorrentino, G. Ferrari, N. Poli, R. Drullinger, and G. M. Tino. "Laser cooling and trapping of atomic strontium for ultracold atom physics, high-precision spectroscopy and quantum sensors". In: *Modern Physics Letters B* 20.21 (2006), pp. 1287–1320. DOI: 10.1142/s0217984906011682 (cit. on p. 64).

[181] John David Jackson. *Classical Electrodynamics*. John Wiley & Sons Inc, July 27, 1998. 832 pp. ISBN: 047130932X. URL: https://www.ebook.de/de/product/3240907/john_david_jackson_classical_electrodynamics.html (cit. on p. 69).

[182] Daniel A. Steck. "Quantum and Atom Optics". 2019. URL: http://steck.us/teaching (cit. on p. 69).

[183] L. Ricci, M. Weidemüller, T. Esslinger, A. Hemmerich, C. Zimmermann, V. Vuletic, W. König, and T.W. Hänsch. "A compact grating-stabilized diode laser system for atomic physics". In: *Optics Communications* 117.5-6 (1995), pp. 541–549. DOI: 10.1016/0030-4018(95)00146-y (cit. on p. 69).

[184] K. Petermann. *Laser Diode Modulation and Noise*. Springer Netherlands, 1988. DOI: 10.1007/978-94-009-2907-4 (cit. on p. 69).

[185] Ye Cunyun. *Tunable External Cavity Diode Lasers*. WORLD SCIENTIFIC, 2004. DOI: 10.1142/5694 (cit. on pp. 69, 71).

[186] A. L. Schawlow and C. H. Townes. "Infrared and Optical Masers". In: *Physical Review* 112.6 (1958), pp. 1940–1949. DOI: 10.1103/physrev.112.1940 (cit. on p. 71).

[187] M. Osinski and J. Buus. "Linewidth broadening factor in semiconductor lasers–An overview". In: *IEEE Journal of Quantum Electronics* 23.1 (1987), pp. 9–29. DOI: 10.1109/jqe.1987.1073204 (cit. on p. 71).

[188] M. Fleming and A. Mooradian. "Spectral characteristics of external-cavity controlled semiconductor lasers". In: *IEEE Journal of Quantum Electronics* 17.1 (1981), pp. 44–59. DOI: 10.1109/jqe.1981.1070634 (cit. on p. 71).

[189] C. Henry. "Theory of the linewidth of semiconductor lasers". In: *IEEE Journal of Quantum Electronics* 18.2 (1982), pp. 259–264. DOI: 10.1109/jqe.1982.1071522 (cit. on p. 71).

[190] Pasquale Maddaloni. *Laser-Based Measurements for Time and Frequency Domain Applications*. CRC Press, Apr. 25, 2013. 764 pp. ISBN: 1439841519. URL: https://www.ebook.de/de/product/19119714/pasquale_maddaloni_laser_based_measurements_for_time_and_frequency_domain_applications.html (cit. on p. 71).

[191] Huanqian Loh, Yu-Ju Lin, Igor Teper, Marko Cetina, Jonathan Simon, James K. Thompson, and Vladan Vuletić. "Influence of grating parameters on the linewidths of external-cavity diode lasers". In: *Applied Optics* 45.36 (2006), p. 9191. DOI: 10.1364/ao.45.009191 (cit. on p. 71).

[192] Sebastian Häfner, Stephan Falke, Christian Grebing, Stefan Vogt, Thomas Legero, Mikko Merimaa, Christian Lisdat, and Uwe Sterr. "8×10^{-17} fractional laser frequency instability with a long room-temperature cavity". In: *Optics Letters* 40.9 (2015), p. 2112. DOI: 10.1364/ol.40.002112 (cit. on p. 78).

[193] Garrett D. Cole, Wei Zhang, Bryce J. Bjork, David Follman, Paula Heu, Christoph Deutsch, Lindsay Sonderhouse, John Robinson, Chris Franz, Alexei Alexandrovski, Mark Notcutt, Oliver H. Heckl, Jun Ye, and Markus Aspelmeyer. "High-performance near- and mid-infrared crystalline coatings". In: *Optica* 3.6 (2016), p. 647. DOI: 10.1364/optica.3.000647 (cit. on p. 78).

[194] Christian Hagemann, Christian Grebing, Thomas Kessler, Stephan Falke, Nathan Lemke, Christian Lisdat, Harald Schnatz, Fritz Riehle, and Uwe Sterr. "Providing 10^{-16} Short-Term Stability of a 1.5 μm Laser to Optical Clocks". In: *IEEE Transactions on Instrumentation and Measurement* 62.6 (2013), pp. 1556–1562. DOI: 10.1109/tim.2013.2242597 (cit. on p. 78).

[195] Hajime Inaba, Kazumoto Hosaka, Masami Yasuda, Yoshiaki Nakajima, Kana Iwakuni, Daisuke Akamatsu, Sho Okubo, Takuya Kohno, Atsushi Onae, and Feng-Lei Hong. "Spectroscopy of ^{171}Yb in an optical lattice based on laser linewidth transfer using a narrow linewidth frequency comb". In: *Optics Express* 21.7 (2013), p. 7891. DOI: 10.1364/oe.21.007891 (cit. on p. 78).

[196] Daniele Nicolodi, Bérengère Argence, Wei Zhang, Rodolphe Le Targat, Giorgio Santarelli, and Yann Le Coq. "Spectral purity transfer between optical wavelengths at the 10^{-18} level". In: *Nature Photonics* 8.3 (2014), pp. 219–223. DOI: 10.1038/nphoton.2013.361 (cit. on p. 78).

[197] Piero Barbieri, Cecilia Clivati, Marco Pizzocaro, Filippo Levi, and Davide Calonico. "Spectral purity transfer with 5×10^{-17} instability at 1 s using a multibranch Er:fiber frequency comb". In: *Metrologia* (2019). DOI: 10.1088/1681-7575/ab2b0f (cit. on p. 78).

[198] Shayne Bennetts, Gordon D. McDonald, Kyle S. Hardman, John E. Debs, Carlos C. N. Kuhn, John D. Close, and Nicholas P Robins. "External cavity diode lasers with 5 kHz linewidth and 200 nm tuning range at 1.55 µm and methods for linewidth measurement". In: *Optics Express* 22.9 (2014), p. 10642. DOI: 10.1364/oe.22.010642 (cit. on p. 79).

[199] Gianmaria Milani, Benjamin Rauf, Piero Barbieri, Filippo Bregolin, Marco Pizzocaro, Pierre Thoumany, Filippo Levi, and Davide Calonico. "Multiple wavelength stabilization on a single optical cavity using the offset sideband locking technique". In: *Optics Letters* 42.10 (2017), p. 1970. DOI: 10.1364/ol.42.001970 (cit. on p. 83).

[200] J. I. Thorpe, K. Numata, and J. Livas. "Laser frequency stabilization and control through offset sideband locking to optical cavities". In: *Optics Express* 16.20 (2008), p. 15980. DOI: 10.1364/oe.16.015980 (cit. on p. 83).

[201] James M. Kohel, Jaime Ramirez-Serrano, Robert J. Thompson, Lute Maleki, Joshua L. Bliss, and Kenneth G. Libbrecht. "Generation of an intense cold-atom beam from a pyramidal magneto-optical trap: experiment and simulation". In: *Journal of the Optical Society of America B* 20.6 (2003), p. 1161. DOI: 10.1364/josab.20.001161 (cit. on pp. 85, 94).

[202] Saptarishi Chaudhuri, Sanjukta Roy, and C. S. Unnikrishnan. "Realization of an intense cold Rb atomic beam based on a two-dimensional magneto-optical trap: Experiments and comparison with simulations". In: *Physical Review A* 74.2 (2006). DOI: 10.1103/PhysRevA.74.023406 (cit. on p. 85).

[203] K.-A. Brickman, M.-S. Chang, M. Acton, A. Chew, D. Matsukevich, P. C. Haljan, V. S. Bagnato, and C. Monroe. "Magneto-optical trapping of cadmium". In: *Physical Review A* 76.4 (2007). DOI: 10.1103/physreva.76.043411 (cit. on p. 85).

[204] Asaf Szulc. "Simulating atomic motion in a magneto-optical trap". MA thesis. Ben-Gurion University of the Negev, 2016 (cit. on p. 85).

[205] Ryan K. Hanley, Paul Huillery, Niamh C. Keegan, Alistair D. Bounds, Danielle Boddy, Riccardo Faoro, and Matthew P. A. Jones. "Quantitative simulation of a magneto-optical trap operating near the photon recoil limit". In: *Journal of Modern Optics* 65.5-6 (2017), pp. 667–676. DOI: 10.1080/09500340.2017.1401679 (cit. on p. 85).

[206] R. W. Mu, Z. L. Wang, Y. L. Li, X. M. Ji, and J. P. Yin. "A controllable double-well optical trap for cold atoms (or molecules) using a binary π-phase plate: experimental demonstration and Monte Carlo simulation". In: *The European Physical Journal D* 59.2 (2010), pp. 291–300. DOI: 10.1140/epjd/e2010-00148-x (cit. on p. 85).

[207] M. Chalony, A. Kastberg, B. Klappauf, and D. Wilkowski. "Doppler Cooling to the Quantum Limit". In: *Physical Review Letters* 107.24 (2011). DOI: 10.1103/physrevlett.107.243002 (cit. on p. 85).

[208] Daniel Comparat. "Molecular cooling via Sisyphus processes". In: *Physical Review A* 89.4 (2014). DOI: 10.1103/physreva.89.043410 (cit. on p. 85).

[209] M R Tarbutt. "Magneto-optical trapping forces for atoms and molecules with complex level structures". In: *New Journal of Physics* 17.1 (2015), p. 015007. DOI: 10.1088/1367-2630/17/1/015007 (cit. on p. 85).

[210] A. D. Bounds, N. C. Jackson, R. K. Hanley, R. Faoro, E. M. Bridge, P. Huillery, and M. P. A. Jones. "Rydberg-Dressed Magneto-optical Trap". In: *Physical Review Letters* 120.18 (2018). DOI: 10.1103/physrevlett.120.183401 (cit. on p. 85).

[211] F James. "Monte Carlo theory and practice". In: *Reports on Progress in Physics* 43.9 (1980), pp. 1145–1189. DOI: 10.1088/0034-4885/43/9/002 (cit. on p. 88).

[212] John von Neumann. "Various techniques used in connection with random digits". In: *Monte Carlo Method*. Ed. by A.S. Householder, G.E. Forsythe, and H.H. Germond. Washington, D.C.: U.S. Government Printing Office: National Bureau of Standards Applied Mathematics Series, 12, 1951, pp. 36–38 (cit. on p. 90).

[213] P T Greenland, M A Lauder, and D J H Wort. "Atomic beam velocity distributions". In: *Journal of Physics D: Applied Physics* 18.7 (1985), pp. 1223–1232. DOI: 10.1088/0022-3727/18/7/009 (cit. on p. 91).

[214] F. Gao, H. Liu, P. Xu, X. Tian, Y. Wang, J. Ren, Haibin Wu, and Hong Chang. "Precision measurement of transverse velocity distribution of a strontium atomic beam". In: *AIP Advances* 4.2 (2014), p. 027118. DOI: 10.1063/1.4866983 (cit. on pp. 91, 124).

[215] W. H. Enright. "The Numerical Analysis of Ordinary Differential Equations: Runge–Kutta and General Linear Methods (J. C. Butcher)". In: *SIAM Review* 31.4 (1989), pp. 693–693. DOI: 10.1137/1031147 (cit. on p. 94).

[216] David M. Lubman, Charles T. Rettner, and Richard N. Zare. "How isolated are molecules in a molecular beam?" In: *The Journal of Physical Chemistry* 86.7 (1982), pp. 1129–1135. DOI: 10.1021/j100396a017 (cit. on p. 96).

[217] Numba. *Numba: A High Performance Python Compiler*. 2018. URL: http://numba.pydata.org/ (cit. on p. 98).

[218] Jérôme Lodewyck. *GaussianBeam*. 2013. URL: https://sourceforge.net/projects/gaussianbeam/ (cit. on p. 102).

[219] Wolfgang Demtröder. *Atoms, Molecules and Photons*. Springer Berlin Heidelberg, 2010. DOI: 10.1007/978-3-642-10298-1 (cit. on p. 110).

[220] F. Schreier. "The Voigt and complex error function: A comparison of computational methods". In: *Journal of Quantitative Spectroscopy and Radiative Transfer* 48.5-6 (1992), pp. 743–762. DOI: 10.1016/0022-4073(92)90139-u (cit. on p. 111).

[221] Brian P. Anderson and Mark A. Kasevich. "Enhanced loading of a magneto-optic trap from an atomic beam". In: *Physical Review A* 50.5 (1994), R3581–R3584. DOI: 10.1103/physreva.50.r3581 (cit. on p. 116).

[222] J. Huckans, W. Dubosclard, E. Maréchal, O. Gorceix, B. Laburthe-Tolra, and M. Robert de Saint-Vincent. "Note on the reflectance of mirrors exposed to a strontium beam". In: (Feb. 23, 2018). arXiv: http://arxiv.org/abs/1802.08499v2 [physics.atom-ph] (cit. on p. 122).

[223] Ingo Nosske, Luc Couturier, Fachao Hu, Canzhu Tan, Chang Qiao, Jan Blume, Y. H. Jiang, Peng Chen, and Matthias Weidemüller. "Erratum: Two-dimensional magneto-optical trap as a source for cold strontium atoms [Phys. Rev. A 96 , 053415 (2017)]". In: *Physical Review A* 97.3 (2018). DOI: 10.1103/physreva.97.039901 (cit. on p. 125).

[224] Fritz Riehle. "Towards a redefinition of the second based on optical atomic clocks". In: *Comptes Rendus Physique* 16.5 (2015), pp. 506–515. DOI: 10.1016/j.crhy.2015.03.012 (cit. on p. 132).

This Ph.D. thesis has been typeset by means of the TEX-system facilities. The typesetting engine was pdfLATEX. The document class was `toptesi`, by Claudio Beccari, with option `tipotesi=scudo`. This class is available in every up-to-date and complete TEX-system installation.